Effect of Pre-Bending and Hydroforming Parameters on the Formability of Advanced High Strength Steel Tube

by

Alexander Bardelcik

A thesis
presented to the University of Waterloo
in fulfilment of the
thesis requirement for the degree of
Master of Applied Science
in
Mechanical Engineering

Waterloo, Ontario, Canada, 2006

I hereby declare that I am the sole author of this thesis. This is a true copy of the thesis, including any required final revisions, as accepted by my examiners.

I understand that my thesis may be made electronically available to the public.

ABSTRACT

With increasing fuel costs and the current drive to reduce greenhouse gas emissions and fuel consumption, a need to reduce vehicle weight is apparent. Weight reduction can be achieved by replacing conventionally stamped structural members with hydroformed parts. The weight reduction can be further enhanced by reducing the thickness of the hydroformed members through the use of advanced high strength steel (AHSS). A primary limitation in hydroforming AHSS, is the limited ductility or formability of these materials. This limitation becomes acute in multi-stage forming operations in which strain path changes become large making it difficult to predict formability. Thus, the focus of the current work is to study the effects of pre-bending on the subsequent hydroformability of Dual-Phase DP600 steel tubes. As part of this effort, the effect of key bending and hydroforming process parameters, bending boost and hydroforming end-feed, have been studied in a parametric fashion.

Multi-step pre-bending and hydroforming experiments were performed on 76.2 mm (3.0") OD tubes with a wall-thickness of 1.85mm (DP600). Experiments were also performed on 1.74mm Interstitial Free (IF) steel tube, which provided a low strength, high formability baseline material for comparison purposes. A fully instrumented servo-hydraulic mandrel-rotary draw tube bender was used in the pre-bending experiments in which various levels of boost were applied. The results showed that increased boost reduced the major (tensile) strain and thinning at the outside of the bend. At the inside of the bend, the compressive minor strain became larger and thickening increased.

Hydroforming of the straight and pre-bent tubes was conducted using various levels of load-control end-feed (EF). For both straight and pre-bend tube hydroforming, an increase in hydroforming EF resulted in increased burst pressure and corner-fill expansion (CFE). The effect of bending boost on CFE was also measured. For a given hydroforming EF case, a tube bent with greater boost achieved a higher burst pressure and consequently a greater CFE which increased the hydroformability of the material. Pre-bending was shown to consume a considerable amount of the formability of the tube in the hydroforming experiments. For the

same EF case, the pre-bent tubes could only achieve a fraction of the straight tube CFE at burst.

The pre-bending and hydroforming experiments were complimented by finite element simulation in the hope of providing additional insight into these processes. The finite element (FE) models were able to accurately predict the strain and thickness changes imposed during pre-bending. The models were able to accurately predict the CFE, EF displacement, and strain and thickness distributions after hydroforming.

The extended stress-based forming limit curve (XSFLC) failure criterion was applied to predict failure (onset of necking) during hydroforming, which was measured as the burst pressure in the experiments. For straight tube hydroforming, the XSFLC predicted the correct failure pressure *versus* hydroforming EF load trend, but over predicted the failure pressures. In pre-bend hydroforming, the models were able to capture the effect of bending boost and hydroforming EF on the hydroformability of the tubes. The XSFLC was able to capture the drop in formability for bending *versus* straight tube hydroforming, but was unable to capture the failure pressure *versus* hydroforming EF load trend or magnitude. Further work is required to make the XSFLC applicable to straight and pre-bend hydroforming.

ACKNOWLEDGEMENTS

To my parents,

For giving my sister and I the opportunity of a better life in Canada

TABLE OF CONTENTS

LIST OF TABLES

LIST OF FIGURES

CHAPTER 1

INTRODUCTION

1.1 Tube Bending and Hydroforming Overview

With the current drive for reduced greenhouse gas emissions and fuel conservation, a need to improve automobile efficiency through weight reduction is apparent. One method through which this can be realized is through the use of hydroforming to manufacture conventional automobile components. Hydroforming is a relatively young technology that has seen industrial application since the late 1960's for plumbing and automotive components (Dohman and Hartl, 1997). Before a component is hydroformed, a straight thin-walled tube is usually pre-formed by bending (typically CNC mandrel-rotary draw tube bending). The tube is then placed into the hydroforming die. The hydroforming process is shown in Figure 1 and consists of pressurizing the tube and thereby expanding it to conform to the cross-section of the die.

a)   b)   c)
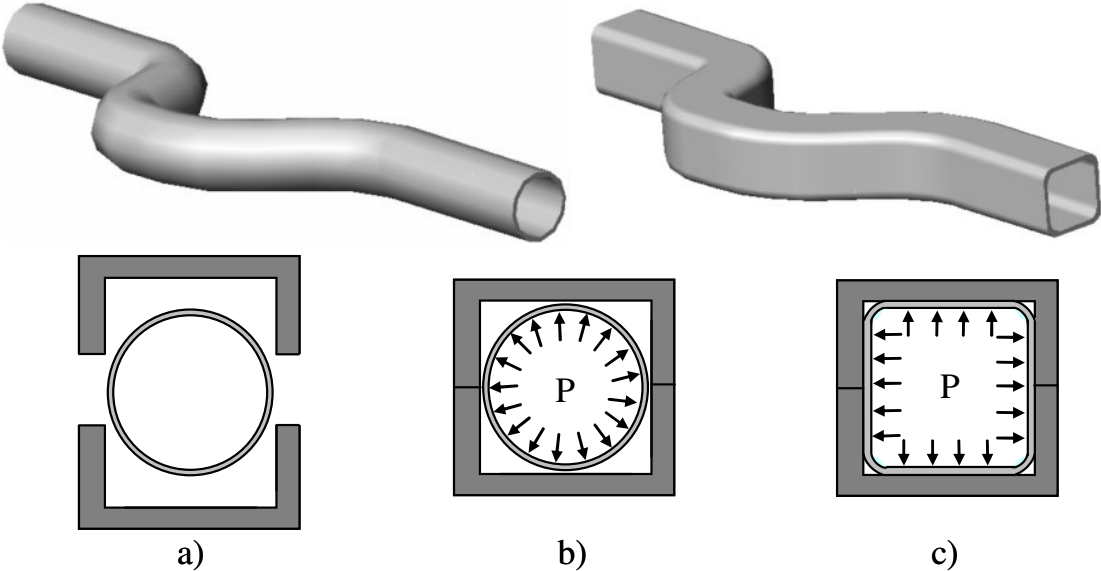
Figure 1: Hydroforming Process (Dyment, 2004)

The process of hydroforming an automotive structural component from a continuously bent steel tube possesses the following advantages over traditional manufacturing processes, which include stamping and welding (Dohman and Hartl, 1997; Zhang, 1999; Mortimer, 2001; Fretty, 2001; Rípodas Agudo, 2003):

- • Weight reduction for improved fuel efficiency
- • Improved strength and stiffness due to work hardening
- • Part consolidation
- • Reduced scrap
- • Better dimensional accuracy

Currently, hydroforming is being used by the automotive industry to manufacture the structural components shown in Figure 2. Other hydroformed components that are not shown include body structures such as instrument panel supports, radiator supports, roof rails, pillars, power-train components and exhaust pipes.
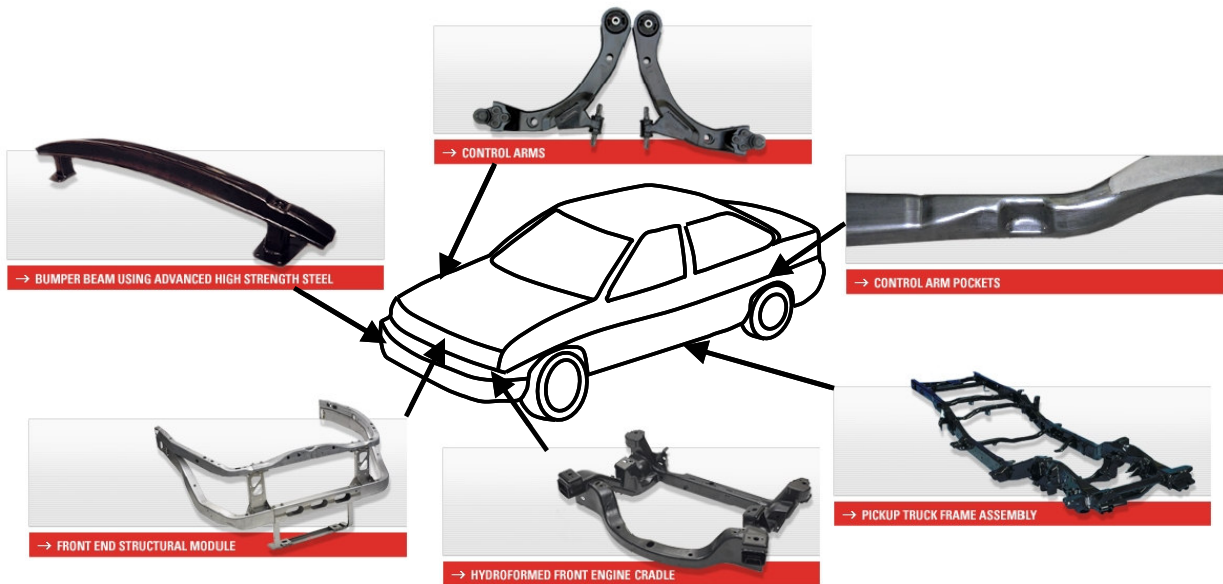
Figure 2: Typical hydroformed structural components (Photographs from Cosma International, http://www.cosma.com)

Vehicle weight reduction is the greatest benefit that hydroforming offer over conventional manufacturing methods. Fretty (2001) compared a conventionally manufactured steel engine cradle to a hydroformed steel and aluminum engine cradle. He showed that the weight savings of a hydroformed steel engine cradle (compared to a conventional steel engine cradle) is 17%, while the weight reduction of a hydroformed aluminum engine cradle (compared to a conventional steel engine cradle) is 41%. Mortimer (2002) reported that BMW's hydroformed A-pillar resulted in a reduction in the part count requirement (over the conventional process) by 44% with an increase in the part strength of 70%.

The main advantage of the use of hydroformed components, that is increased fuel efficiency, can be further enhanced through the use of high-strength steels (HSS) and advanced high-strength steels (AHSS). Since the density of all steels is approximately the same, components made of higher strength steels can be manufactured with thinner gauge steel while maintaining component strength and crash properties. The main challenge encountered when producing hydroformed high-strength steels parts is the limited ductility/formability of these materials. The low formability of high-strength steels limits the corner-fill expansion (CFE) achievable during hydroforming due to fracture (burst), which results in an impractical part. Figure 3 shows the different grades of steels based on their tensile strength and total elongation. It can be seen that formability (total elongation) decreases as the tensile strength of the steel increases. The AHSS group of steels are gaining popularity in automotive applications because they are easier to form than high-strength low alloy (HSLA) grades with similar initial yield strengths, but have a much higher final part strength (Advanced High-Strength Steels, 2006). This is particularly true for Dual-Phase (DP) steels which are the main focus of this thesis.
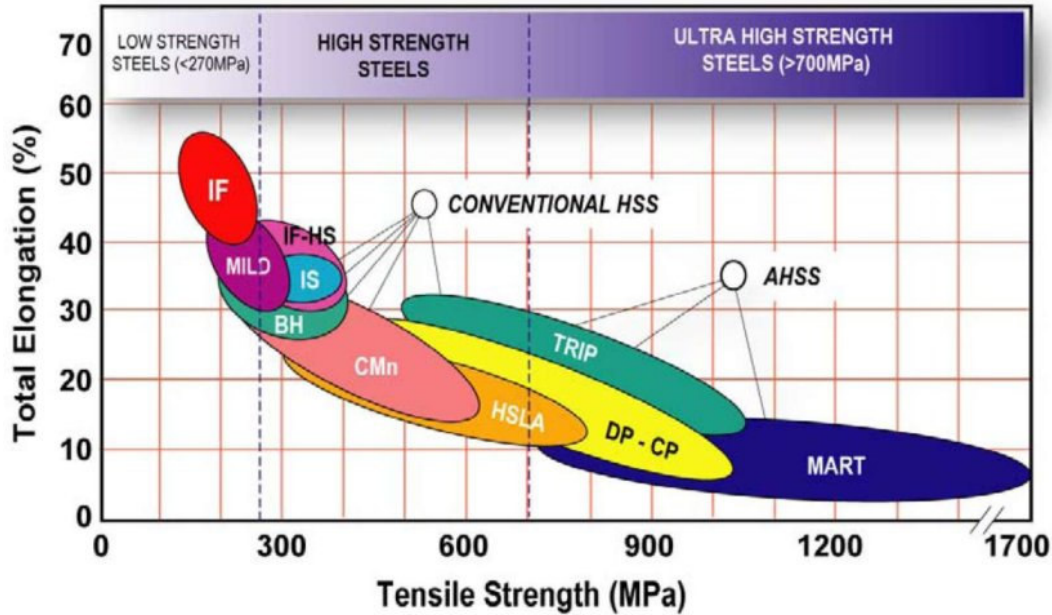
Figure 3: Grades of steel (International Iron and Steel Institute, 2005)

DP steel possesses characteristics that are desirable to the automotive industry in their pursuit for vehicle weight reduction. The microstructure of DP steel consists of about 20% hard martensite particles dispersed in a soft ductile ferrite matrix. When compared to equivalent strength HSLA steels, the characteristics of DP steels include a more continuous yielding behavior, a lower yield strength to tensile strength ratio, a higher work hardening rate and higher total elongation (Speich, 1990; Rege *et al.*, 2002).

Located in the low tensile strength range of Figure 3 is Interstitial-Free (IF) steel. This steel was also considered in the current study to compare the formability of DP steel to a low strength steel. IF steels possess very high formability which is attributed to a very low carbon content and an addition of titanium and/or niobium microalloying elements. These characteristics result in steel with no interstitial atoms in the crystal lattices (Interstitial Free (IF) Steel, 2005; Gupta and Kumar, 2006). As shown in Figure 3, IF steels possess remarkable formability, but at the cost of reduced strength.

The establishment of the first theoretical work on tubular hydroforming dates back to the 1940's, while the use of Finite Element Analysis (FEA) for modeling of the hydroforming

process is now a standard development tool, after investigations and validations conducted by many researchers since the early 1990's (Koc, 2001). An accurate and validated FE model is an indispensable tool to industry as a cost and time saving tool. Of the two methods, FEA has been shown to accurately predict pre-bending with subsequent hydroforming, which is the focus of the current work (Yang *et al.*, 2001; Dwyer *et al.*, 2002; Dyment, 2004; Gholipour *et al.*, 2004).

The focus of this thesis is the investigation of methods that may potentially improve the formability of pre-bent DP600 steel tubes during hydroforming. The two methods which will be explored are pre-bending boost and end-feed (EF) during hydroforming. Although bending boost has been measured experimentally and predicted using finite element analysis (FEA), no published work on the effects of bending boost on formability during hydroforming exists. Hydroforming of pre-bent steel tubes has also been published, but does not consider the effect of EF during hydroforming of a 90° pre-bent tube. In the current work, pre-bending and hydroforming experiments will be conducted on DP600 and IF tubes. A fully instrumented mandrel-rotary draw tube bender will be used to pre-bend (90°) the tubes at various boost levels. The pre-bent tubes (along with straight tubes) will be subsequently hydroformed with various levels of end-feed (EF) using a 1,000Ton hydroforming press with hydraulic EF actuators. After pre-bending and hydroforming, the strain and thickness will be measured to assess the effects of bending boost and hydroforming EF on the tubes formability. The corner-fill expansion during hydroforming will also be measured and used to assess hydroformability. To compliment the experimental work, the bending and hydroforming process will be modeled using the finite element method (FEM), which will be validated with the experimental results. A new stress-based failure criterion will be evaluated in terms of its ability to predict failure (burst) during hydroforming. The twist compression test will be used to measure the coefficient of friction (COF) by simulating the pre-bending and hydroforming friction conditions. The measured COF results will be used as input to the FE models.

1.2 Tube Bending

Tubes possesses the combination of light weight and high stiffness, which has attracted many applications in the aerospace, automobile, oil and other industries (Altan, 1999). Tube bending has previously been viewed as a craft, in which work was largely done by skilled labourers who had honed their skills over a period of many years (Al-Qureshi, 1999). In the past 30 years, research into tube bending has increased to build a stronger knowledge base as the technology has become more prevalent. In addition to experimental studies, analytical and finite element (FE) models have been successfully validated to help better understand tubular deformation in bending and are discussed in this chapter. This thesis is focused on the mandrel-rotary draw tube bending method (Inoue and Mellor, 1979). Other methods of tube bending include pure bending (Tang, 2000; Wang and Cao, 2001), stretch bending (Paulsen and Welo, 1996) and shear/extrusion bending (Al-Qureshhi, 1999; Goodarzi *et al.*, 2005). The mandrel-rotary draw tube bending method has been shown to be an accurate and repeatable method of pre-bending for components that are to be hydroformed (Dwyer *et al.*, 2002; Asnafi *et al.*, 2003). The focus of this work is on circular cross-section tubes. Other cross-sections capable of being mandrel-rotary draw bent include rectangular (Paulsen and Welo, 1996; Utsumi and Sakaki, 2002) and oval (Hokook *et al.*, 2005) shapes.

Figure 4 shows the tools and steps involved in mandrel-rotary draw tube bending. The bend die and clamp die act to grip the end of the tube and rotate together to draw the tube around the bend die. The pressure die reacts the moment created on the tube during bending and also pushes the tube axially into the bend. A flexible mandrel (post and balls) supports the tube and prevents collapse of the tube during bending. The wiper die prevents wrinkling of the tube on the inside of the bend and reacts part of the pressure die clamp force (Dyment, 2004). Bending boost, centre-line radius (CLR) of the bend to tube diameter (R/D) ratio and lubrication affect tube deformation and process variables during mandrel-rotary draw tube bending and are discussed in this review.

External Tooling	Internal Tooling (external tooling and tube shown with their top halves removed for clarity)
Bend Die, Wiper Die, CLR, Clamp Die, Pressure Die **Step 1:** -The tube is slid overtop mandrel and is positioned in-between other tooling	Mandrel Post, Mandrel Balls
Step 2: -The clamp die and pressure die are closed by applying normal loads to the tube	
Step 3: -The bend die and clamp die rotate and pull the tube around the bend, while the pressure die translates forward and pushes material into the bend. -The mandrel balls pivot to prevent tube collapse.	

Figure 4: Mandrel-rotary draw tube bending process (Dyment, 2004)

The two main failure modes encountered in mandrel-rotary draw tube bending include wrinkling and ovalization/collapse. Wrinkling occurs due to insufficient pressure die clamp load during bending. Wrinkles occur at the inside of the bend region where large compressive strains in the axial direction are encountered. By increasing the pressure die clamp load, wrinkles can be suppressed. The wiper die also aids in preventing wrinkling.

Ovalization during bending can also occur due to large plastic deformation. Without the support of an internal mandrel, a tube will ovalize to the point where the cross-section collapses. Different types of internal mandrels exist and all have their advantages and disadvantages. For a more detailed review on wrinkling and ovalization, refer to Dyment (2004). In addition to wrinkling and ovalization/collapse, springback during bending is a problem for maintaining bending geometric tolerances. Li *et al.* (1994) and Lou and Stelson (2001a, 2001b) conducted experimental and statistical studies into springback of mandrel-rotary draw bent tubes. Both studies were able to formulate an algorithm for accurate bending that agreed very well with experimental tests.

1.2.1 Bending Boost

In mandrel-rotary draw tube bending, one objective is to reduce thinning at the outside of the bend region, which naturally occurs due to bending strain. By reducing thinning in a bent tube, a possibility of improved formability during hydroforming exists. One method to reduce the thinning phenomenon in rotary-draw tube bending is to apply "boost" during the pre-bending process. Bending boost is defined by,

$$\%Boost = \frac{PRESSURE\ DIE\ DISPLACEMENT}{ARC\ LENGTH\ SWEPT\ BY\ CLR} \times 100\% \tag{1}$$

Figure 5 shows how more boost is achieved by increasing the pressure die displacement during bending. The increased pressure die displacement produces a greater compressive axial force on the tube during the bending process, forcing more material to flow into the bend region, and thus reducing thinning. Dwyer *et al.* (2002) and Dyment (2004) found that high bending boost caused the tube to slip relative to the pressure die. The solution to this problem was a rigidly attached boost block at the end of the pressure die (Figure 5).
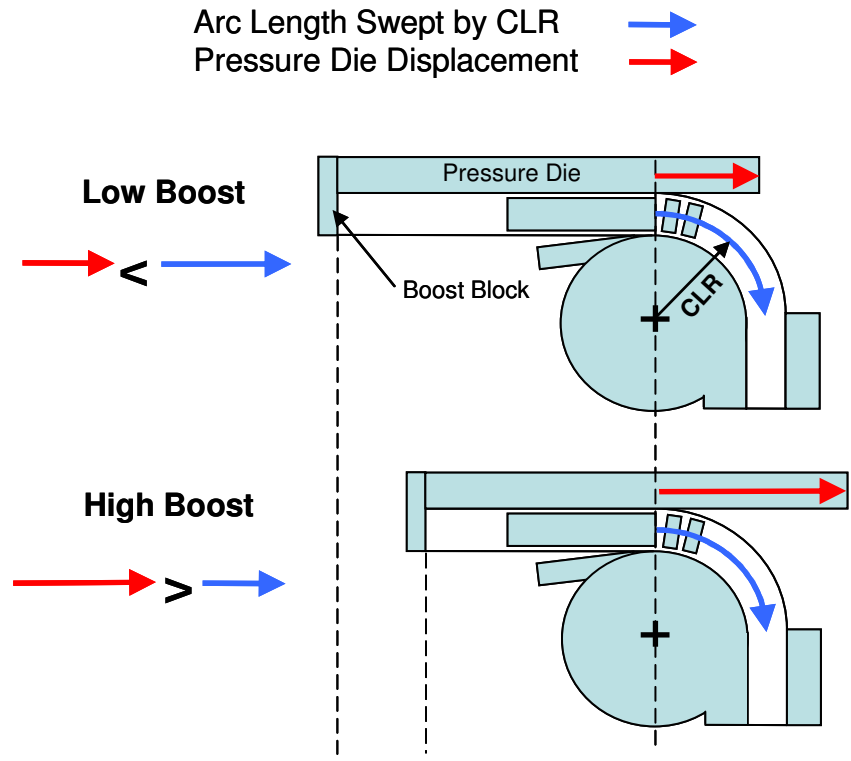
Figure 5: Bending boost schematic

Early experimental work on stainless steel tube by Inoue and Mellor (1979) showed that application of a boost force on the pressure die with an independent ram, reduced axial strain by shifting the strain distribution in the tube downward, as shown in Figure 6 (a). Thinning at the outside of the bend was also reduced with the application of boost, as shown in Figure 6 (b). The bending process parameters were also affected by boost. It was shown that the mandrel load and bend head torque were both reduced with the application of boost. More recent experimental studies into the application of boost have shown the same results for steel (Rodriguez and Schlatter, 1999; Dyment, 2003) and for aluminum (Dwyer *et al.,* 2002; Gholipour *et al.,* 2004).
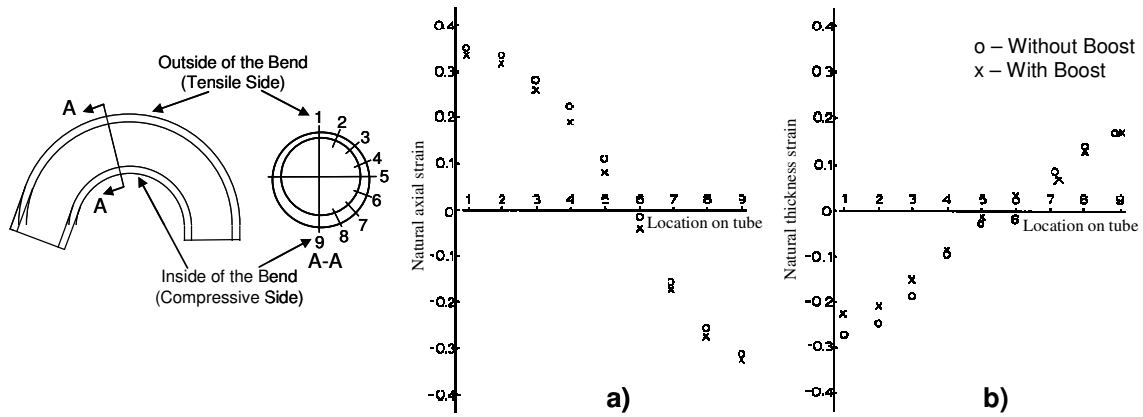
Figure 6: Effect of boost on strain distribution (Inoue and Mellor, 1979)

Dyment's (2004) experiments on 90° pre-bent AKDQ steel tubes showed that by increasing boost from 95% to 100%, the major tensile strain at the outside of the bend, decreased from approximately 0.23 to 0.20 and the thinning reduced roughly 0.03mm (2.0%) (Figure 7).
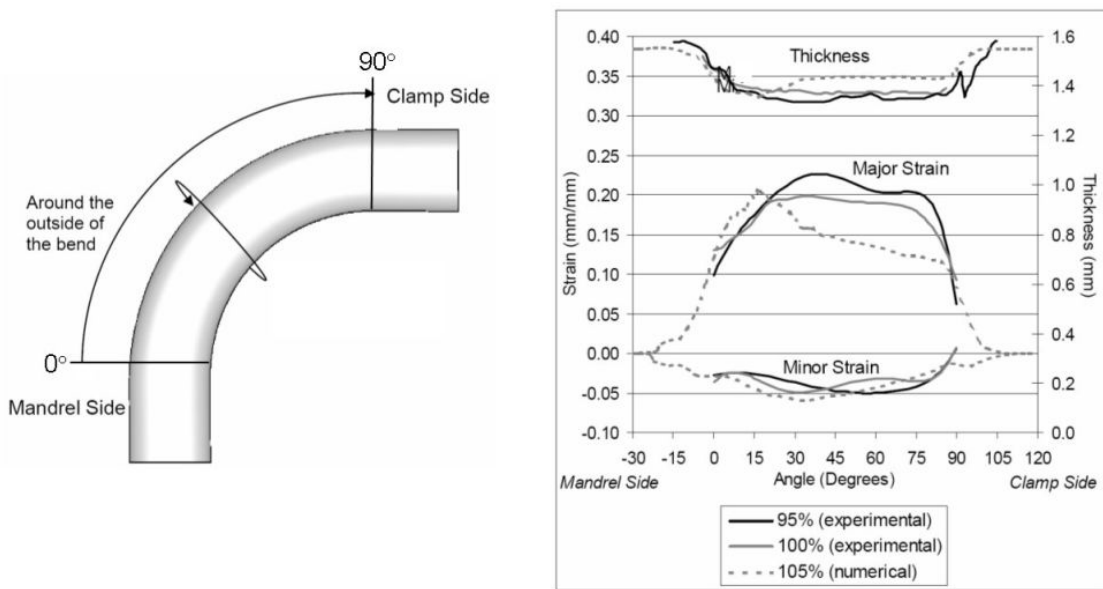
Figure 7: Effect of boost on the outside of the bend for AKDQ steel tubes (Dyment, 2004)

10

1.2.2 R/D Ratio

The R/D ratio in tube bending refers to the ratio of the center-line radius (CLR) of the tube to the tube diameter. Decreasing R/D ratios represent increasing bend severity. This affects the deformation of the tube and results in changes in strain and thickness distributions. Inoue and Mellor (1979) and Dyment (2004) both showed that for steel tubes, a decrease in R/D ratio increased the major tensile axial strain and thinning around the outside of the bend region. Also, the inside of the bend region experienced greater axial compressive strain and increased thickening (Figure 8).
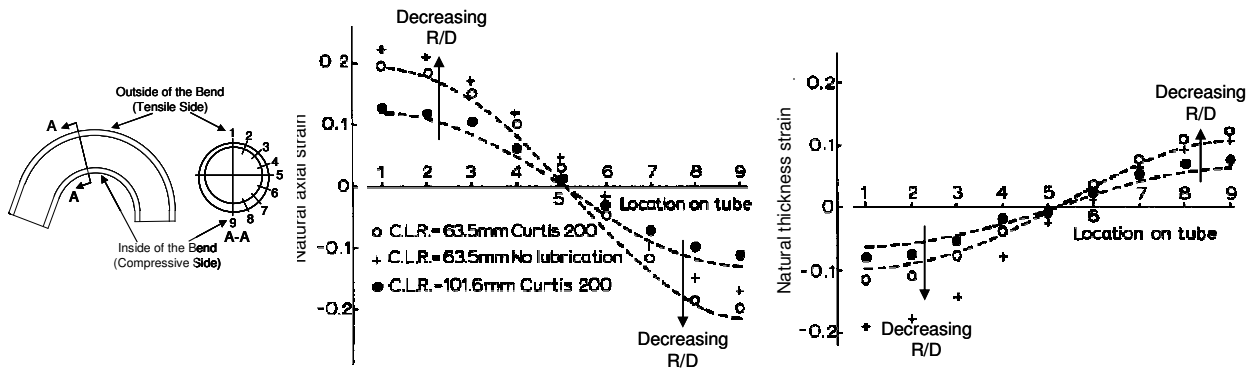
Figure 8: Effect of R/D ratio on strain distribution (Inoue and Mellor, 1979)

The bending process parameters involved in mandrel-rotary draw tube bending are also affected by R/D ratio. Both Inoue and Mellor (1979) and Dyment (2004) showed that decreasing the R/D ratio requires an increase in the required mandrel load and bend die torque during bending.

Toyoda *et al.* (2004) conducted a tube bending study on three grades of steel tubes (UTS = 440, 590, 780MPa). For each grade of tube, there were three variations of the mechanical properties which were described as rolled, normalized and specially processed "HISTORY" (high-speed tube welding and optimum reducing technology) tubes. They found that it was possible to successfully bend the high-strength (UTS = 780MPa) steel tubes to an R/D of 1.1, with the HISTORY tubes (Figure 9). This finding is significant because it shows

11

that very high-strength steel alloys are bendable to a tight bend radii, allowing more complex pre-bent part geometries to be hydroformed.

TS grade (MPa)	Tubes	Bending radius, ρ/D			
		2.0	1.5	1.0	Remarks
440	HISTORY	○	○	○	–
	Normalized ERW	○	○	○	–
	As rolled ERW	○	○	○	–
590	HISTORY	○	○	○	–
	Normalized ERW	○	○	○	–
	As rolled ERW	○	○	×	–
780	HISTORY	○	○	×	1.1: ○
	Normalized ERW	○	○	×	1.3: ○
	As rolled ERW	○	△	×	–

○ : Without split, △ : Necked, × : Split
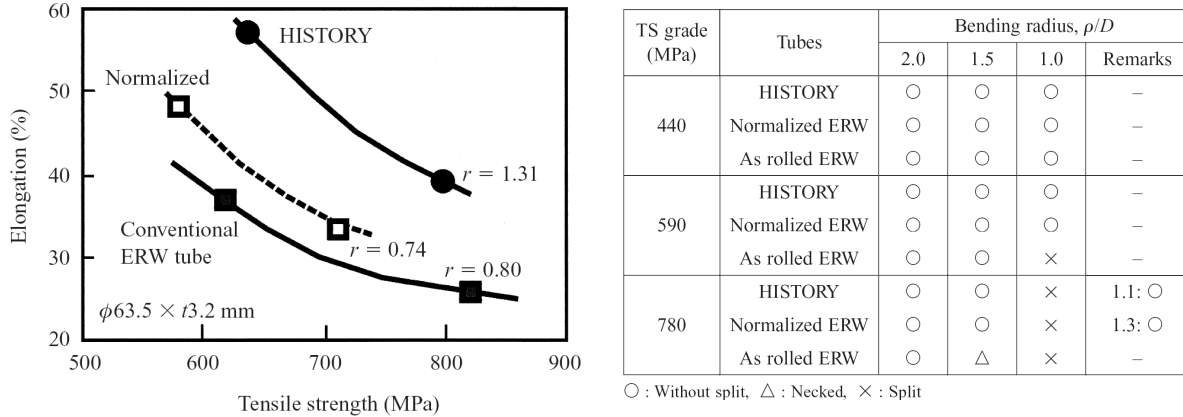
Figure 9: Effect of R/D on bendability of various grades of steel tube (Toyoda *et al.*, 2004)

1.2.3 Tribology in Tube Bending

A typical automotive structural member undergoes multiple process steps before a final part is made by hydroforming. Tube bending is usually one of the steps involved and due to the deformation the tube undergoes, a considerable amount of the material ductility is consumed. This bending pre-strain plays a big role in subsequent deformation steps, such as hydroforming, where the formability of pre-bent tubes is considerably lower than straight members (Dwyer *et al.*, 2002; Dyment, 2004). Therefore, the goal in tube bending is to minimize the high thinning and strain levels along the tube. In addition to the application of boost, good lubrication during mandrel-rotary draw tube bending can help to minimize thinning and ductility loss. In addition to improved formability, good lubrication can also reduce tube bending load requirements and improve the appearance and quality of the tube surface finish.

Oliveira *et al.* (2005) conducted a study on the effects of different lubricants in mandrel-rotary draw tube bending of steel and aluminum tubes. Figure 10 (a) shows that a good lubricant for AKDQ steel tubes resulted in less thinning at the outside of the bend. Increased thickening at the inside of the bend region was also observed. Also, for steel and

aluminum, good lubrication reduced forces, such as mandrel load and bend die torque (Figure 10 b and c), and improved the surface finish of the as-bent tubes. Inoue and Mellor (1979) considered lubrication effects also and found the same trends of reduced thinning and strain levels in better lubricated tubes (Figure 8). Using FE models of mandrel-rotary draw tube bending of stainless steel, Gao and Strano (2004) found that a lower coefficient of friction resulted in less thinning at the outside of the bend and more thickening at the inside of the bend.
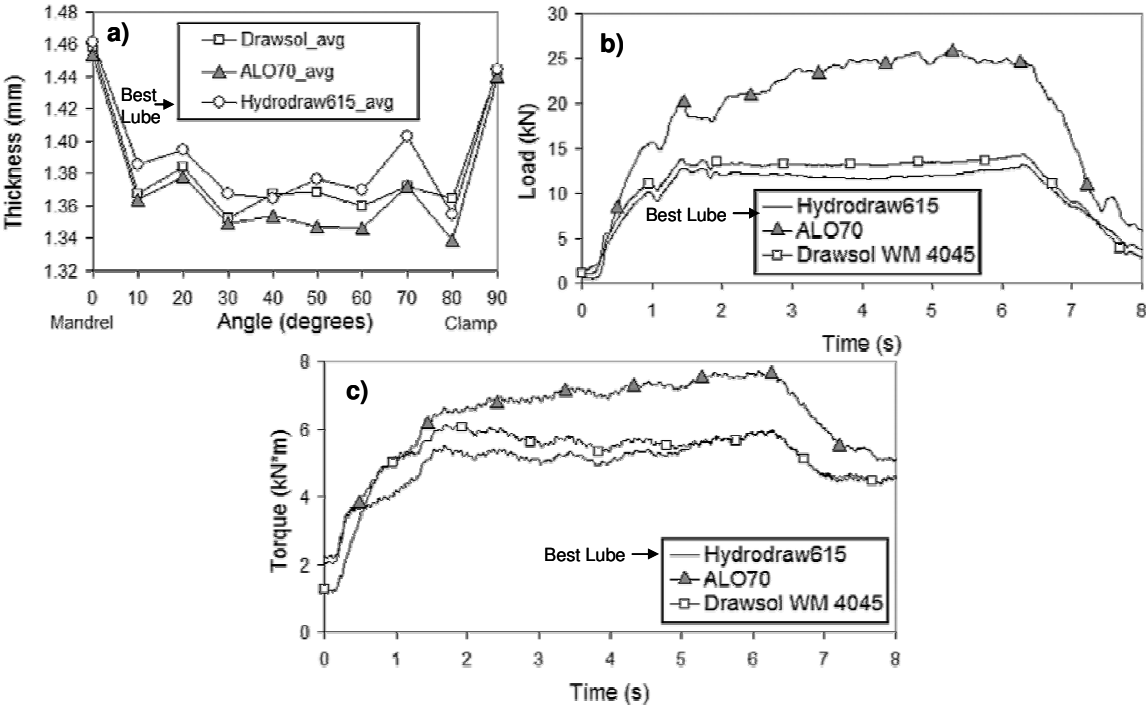
Figure 10: Effect of lubrication on AKDQ steel tubes a) Thickness around the outside of the bend region (see Figure 7 for measurement location) b) Mandrel load c) Bend die torque (Oliveira *et al.*, 2005)

1.2.4 Finite Element and Analytical Modeling of Tube Bending

Finite element (FE) and analytical models of the tube bending process have been shown to accurately predict the deformation of tubular members. With the rapid development of computers, the use of FE and analytical models allows simulations to be used to optimize a bending process for a given part. These models also provide a predictive tool for designing

and optimizing tooling parameters. In order to ensure confidence in FE and analytical models, validation of the methods with experiments is necessary.

FE simulation of mandrel-rotary draw tube bending using explicit dynamic codes has been successfully validated by researchers at the University of Waterloo and elsewhere. For steel and aluminum tubes Rodriguez and Schlatter (1999), Dwyer *et al.* (2002), Dyment (2003, 2004), Gholipour *et al.* (2004) and Bardelcik and Worswick (2006) used the commercial code, LS-DYNA to simulate the mandrel-rotary draw tube bending process. The common validation method in the above studies was based on comparison of the strain and thickness distributions along the longitudinal and circumferential directions of a bent tube. Figure 11 shows measured and predicted strain and thickness distributions along a bent tube. The error bars represent the experimental scatter of the strain measurement method. The predicted strains show good agreement with the experiments. In addition to strain and thickness, the predicted process variables (mandrel load and bend die torque) show good agreement with those measured during the experiments (Bardelcik and Worswick, 2006). Similar simulations for steel tubes using the code PAM-STAMP were successfully validated for strain and thickness by Yang *et al.* (2001). It has been shown by the above authors that accurate mandrel-rotary draw bending models require careful consideration of the tube material properties, friction between tools and tube, boundary conditions, mesh quality and dimensional accuracy of the mandrel-rotary draw bending tools.
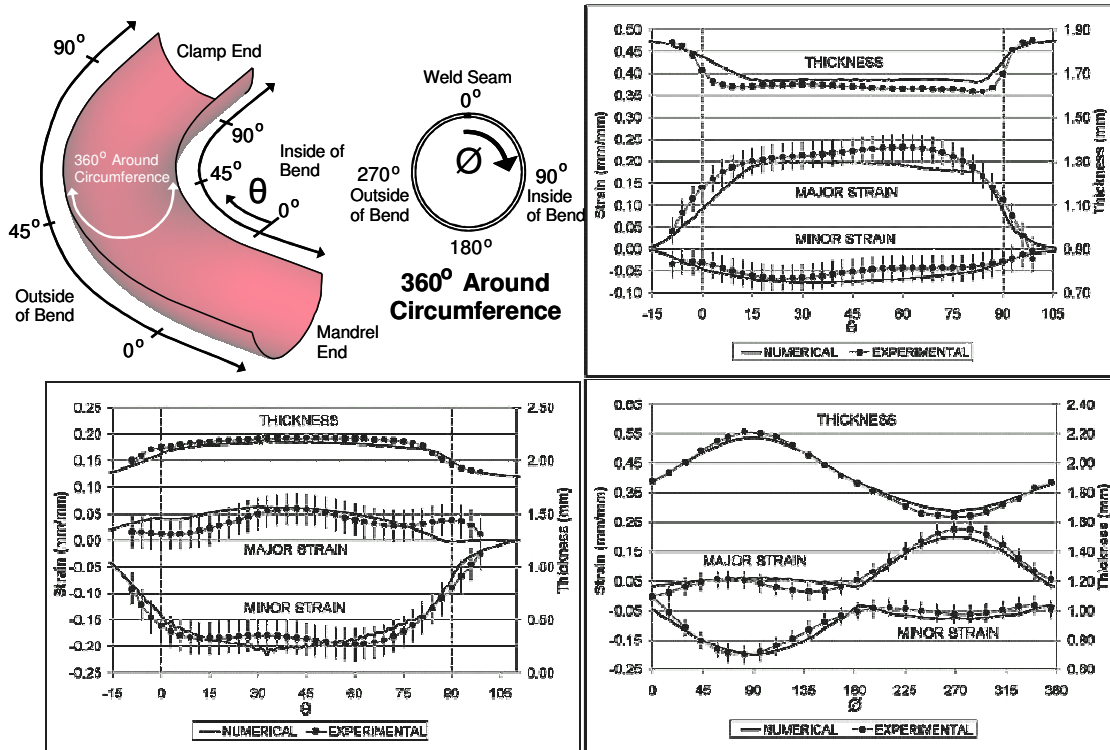
Figure 11: Validated FE tube bending simulations (Bardelcik and Worswick, 2006)

Paulsen and Welo (1996) successfully validated their FE mandrel-rotary draw bending models of rectangular aluminum-alloy profiles with the FE code MARC. In addition to validating strain and thickness, they also validated springback, buckling depth, ram force and deflection of flange. Their work showed that anisotropy of the material was the main material factor influencing the cross-sectional distortion of bent thin-walled extrusions. Utsumi and Sakaki (2002) also modeled draw-bending of extruded aluminum square tubes using LS-DYNA. They were able to predict wrinkling and shape distortion for hollow and internally ribbed square tubes. Zhan *et al.* (2002) developed a 3D rigid-plastic FE software named TBS-3D, used to simulate mandrel-rotary draw tube bending. They found that the strain distribution and tube deformations were similar to existing experimental findings.

Analytical models have the advantage of reduced computational requirements compared to FE simulations which makes them attractive. Normani (2004) developed an elastic-plastic model which predicted the strain and thickness distribution of a bent tube (Figure 12). The model performed well and was able to predict boost effects also. Tang

(2000) developed an analytical method based on plastic deformation theory and was able to validate (with experiments) the stress, wall thickness change, shrinkage rate at the tube section, deviation of neutral axis, feed preparation length of the bend, bending moment and flattening. Al-Qureshi (1999) also modeled tube bending using elastic-plastic theory. His model considered tube bending by pressing/extruding a tube with an internal elastomer rod into a 90° die. Compared to experimental work, springback and residual stress distributions were in good agreement. Wang and Cao (2001) developed an energy approach model to predict the minimum bending radius that does not result in wrinkling.
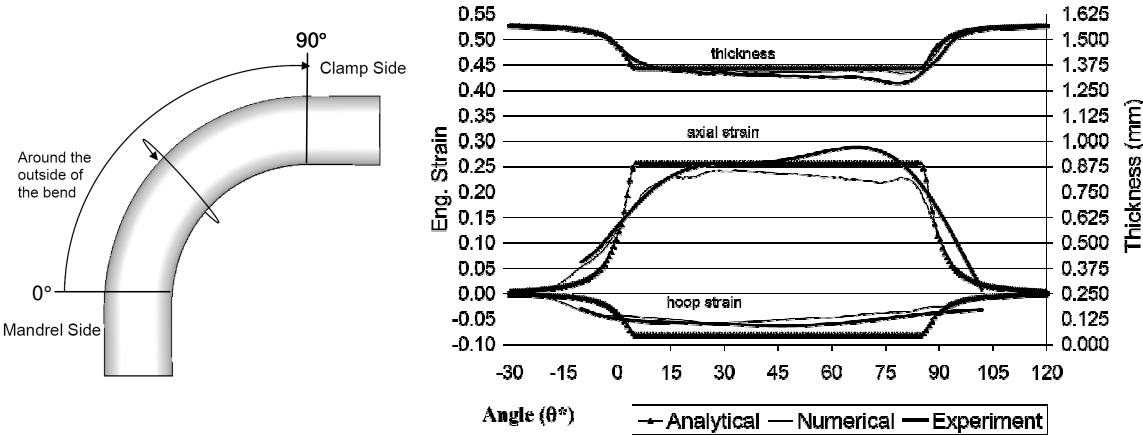
Figure 12: Analytical, numerical and experimental comparison of strain and thickness distribution along the outside of the bend (see Figure 7 for measurement location) (Normani, 2004)

1.3 Hydroforming

Extensive literature exists for both unsupported and supported tubular hydroforming of axial members, but little work has been done on supported hydroforming of pre-bent members with end-feed, which is a focus of this thesis. Numerical methods used to predict tubular deformation during hydroforming have been successfully validated and are reviewed in the following sections.

1.3.1 Unsupported Bulge Forming of Axial Members

Free expansion of tubes by hydroforming serves little use in the manufacture of practical components; rather, it is used to evaluate material formability for more practical hydroforming applications. Also, unsupported bulge forming allows one to identify the effects of material properties such as strain hardening exponent (n) and anisotropy (r-value) on the formability of a tube. Due to the simplicity and symmetry (axisymmetry) of this process, accurate and validated analytical methods are available. In recent times, FE codes have also been successfully validated for unsupported bulge forming.

The typical tooling used to conduct unsupported bulge forming can be seen in Figure 13. In this process, a straight section of the tube is sealed at both ends with a ram and contained in an open die (a). Figure 13 (b) shows the tooling setup for the zero axial force unsupported bulging process. Here, one end of the die is fixed in place while the other is allowed to translate. This allows the free end to move towards the fixed end during bulging without inducing axial forces due to the natural draw-in of the material during expansion.
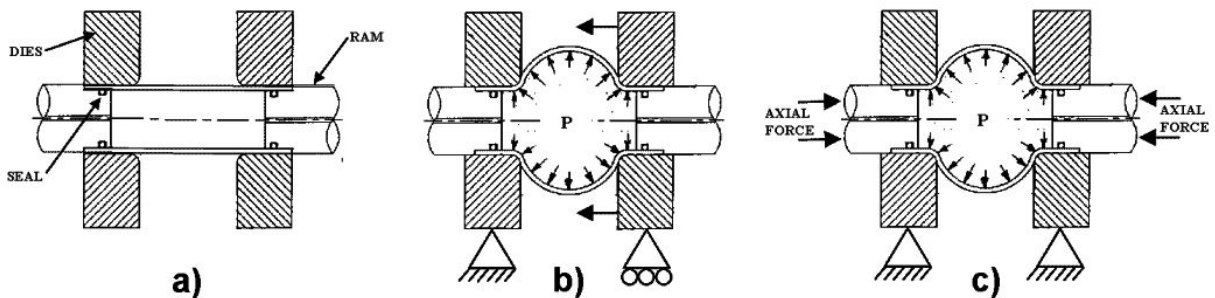
Figure 13: Unsupported bulge forming tooling (modified figure) (Thiruvarudchelvan, 1996)

Figure 13 (c) shows the unsupported bulging process with the addition of force in the axial direction of the tube. In this case, the die halves are stationary and the rams displace based on a load or displacement-control sequence.

The three dominant failure modes encountered during hydroforming are fracture (burst), wrinkling and buckling, as shown in Figure 14 (Manabe *et al.*, 1984; Dohmann and Hartl, 1997; Ahmetoglu *et al.*, 2000; Singh, 2003). Fracture (burst) is caused by excessive

tensile membrane stress on the tube due to high internal pressure. At some pressure, necking initiates which is followed by fracture. Wrinkling and buckling are due to high axial loading on the tube and usually occur when there is insufficient internal pressure or excessive axial compression.

Fracture   **Wrinkling**   **Buckling**
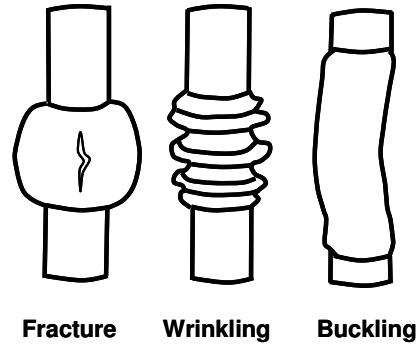
Figure 14: Typical failure modes in hydroforming

The early work done by Woo (1973) and Woo and Lua (1978) focused on developing and validating a theoretical solution for modeling unsupported bulge forming. Strain incremental theory, combined with Hill's (1947) theory of plastic anisotropy, was used for the investigation. The work considered copper tube and a tooling setup as shown in Figure 13 (c). The results of the work shows the importance of including the effect of material anisotropy when modeling tube bulging. Anisotropy is often characterized using the Lankford coefficient or "r-value", given by,

$$r = \frac{\varepsilon_w}{\varepsilon_t} \tag{2}$$

where (ε_w) is the width strain and (ε_t) is the thickness strain measured in a tensile test (both strains are measured as true strains). When considering the strain distribution along the axial direction of a bulged tube Woo and Lua found that the accuracy of the theoretical strain prediction improved when anisotropy is included in the analysis.

Building on the above work, Fuchizawa (1987) focused on the effect of anisotropy (in the circumferential (r_θ) and longitudinal (r_ϕ) directions) on the expansion (formability), stress-

strain distribution and internal pressure at burst. The study was purely analytical and based on deformation theory and Hill's theory of plastic anisotropy. He showed that with an increasing r_ϕ, the critical expansion radius increased (Figure 15 a), tube wall thinning reduced and maximum burst pressure decreased. For increasing r_θ, critical expansion decreased (Figure 15 b) and maximum internal pressure increased. For transverse isotropy ($r_\phi = r_\theta \neq 1$), the maximum internal pressure and critical expansion radius increase for $r_\phi = r_\theta > 1$ (Figure 15 c).
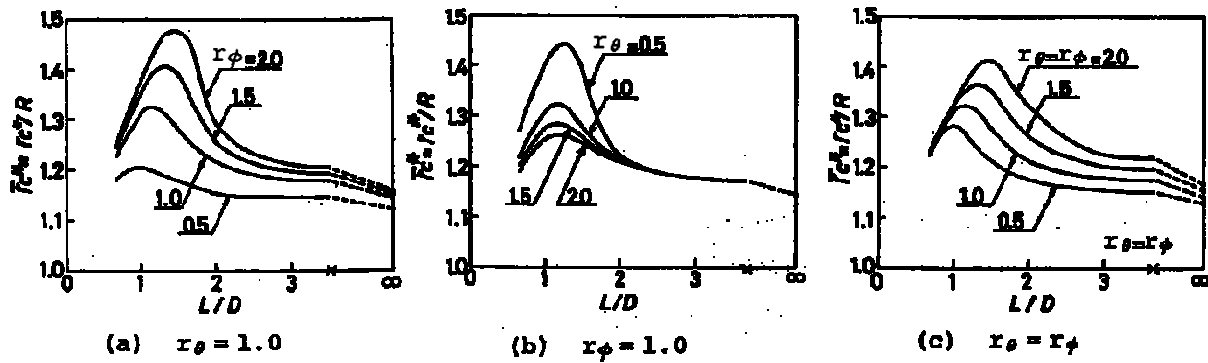
Figure 15: Effect of anisotropy on critical expansion radius, $\bar{r}_c^{\,*}$ (L/D = Length/Diameter of tube) (Fuchizawa, 1987)

In the 1980's, work done by Manabe and Nishimura (1983) and Fuchizawa (1984) explored the effect of strain hardening exponent (n) on unsupported bulge forming. The strain hardening exponent, n, is a variable used in the Power Law,

$$\sigma = K\varepsilon^n \tag{3}$$

Fuchizawa's analysis was strictly numerical and considered both incremental strain theory and strain total theory. The results of Fuchizawa's study are shown in Figure 16. The general trends indicate a reduction in failure (burst) pressure and increase in radial expansion at failure for increasing values of n.

19
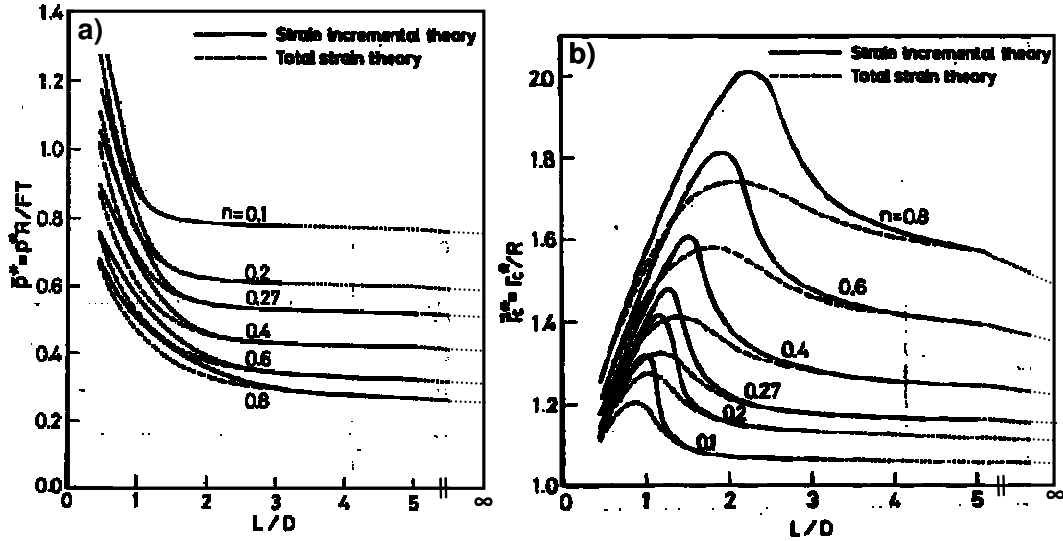
Figure 16: a) Effect of strain hardening exponent on maximum internal pressure, $\bar{p}^*$ and b) Critical expanding radius, $\bar{r}_c^*$ (L/D = Length/Diameter of tube) (Fuchizawa, 1984)

Recently, the analytical work done by Chow and Yang (2002) on unsupported bulge forming using the incremental theory of plasticity for anisotropic materials resulted in the same trends described above for changing *n* and r-value. Xia (2001) used the deformation theory of plasticity for anisotropic materials and showed increased formability with increased r-value. Kim and Kim (2002) used Hill's quadratic yield criterion for anisotropic materials and the equivalent plastic work theory to show that burst pressure was higher with an increased anisotropic parameter (*r*-value) and lower strain-hardening exponent. Carleer *et al.* (2000) performed experimental, analytical calculations and FE simulations for unsupported bulging. Their study was conducted on six grades of steel tube which ranged in ultimate tensile strength from 295 MPa to 517 MPa. Again, the advantage of increased r-value and *n* on formability was shown in the results for the experimental, analytical and FE work which all agreed fairly well with each other. Figure 17 a) shows that increasing *r*-value reduces localized deformation and more evenly distributes strain along the expanded region while allowing more material flow during the process (due to increased axial draw-in of the tube). The strain-path of an element can be easily observed in FE simulations. Figure 17 b) shows that an increasing *r*-value causes the strain-path to shift left and become more linear in major and minor strain

20

space. This is advantageous for increased formability because the path is less likely to intersect the material forming limit curve at lower pressures.
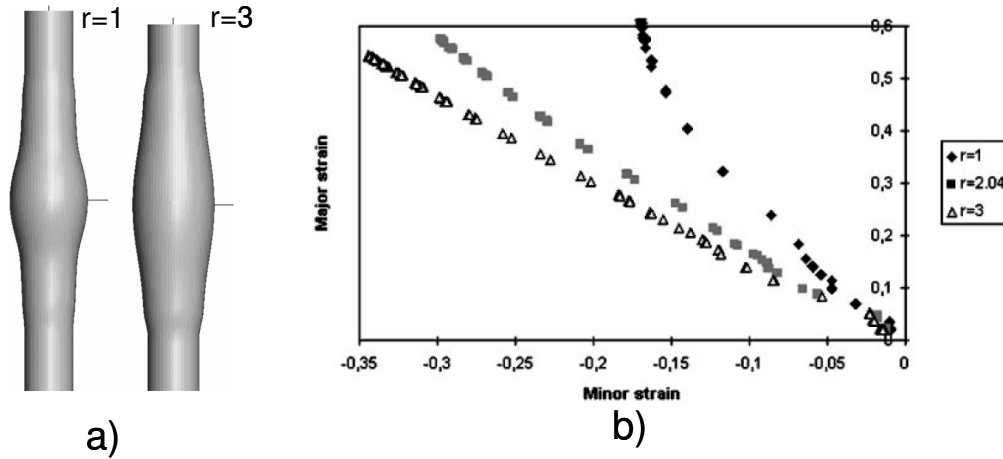
Figure 17: Effect of *r*-value on a) the predicted geometry and b) the predicted FLD strain-path of unsupported bulge forming (Carleer *et al.*, 2000)

An experimental study on free expansion was conducted by Konieczny *et al.* (2005) for seven different steel tube grades of the same thickness. The lowest tubular tensile strength material was IF steel (301MPa), which showed the best formability by achieving a 40% expansion ratio at burst. The DP590 tubes had a tensile strength of 650MPa and failed at an expansion ratio of 23%, while a higher strength TRIP590 tube with a tensile strength of 708MPa failed at an expansion ratio of 31%. The reported tensile strengths were measured through uniaxial tension tests of tubular samples oriented at 90° from the weld. This result agrees with Figure 3, which shows the increased benefits of formability that more exotic AHSS, like TRIP steels offer for processes like hydroforming.

The addition of an axial compressive force during unsupported bulge forming has been shown to greatly improve the formability (radial expansion) of a tube. Experimentally, Woo and Hawkes (1968) found that with the addition of an axial force during forming, greater radial expansion was achieved at burst, Figure 18 (a).
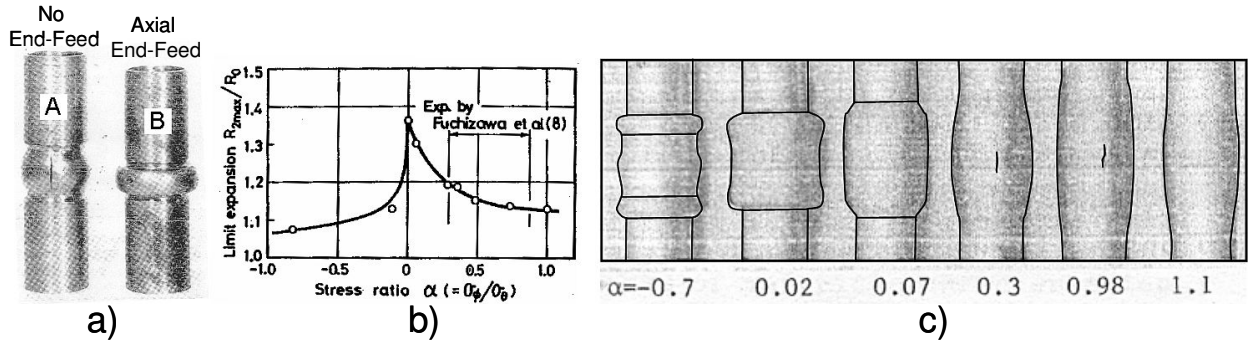
Figure 18: a) Effect of axial load on the deformation on unsupported bulge forming (Woo and Hawkes, 1968) b) & c) Sequential increase in axial force in hydroforming (Manabe *et al.*, 1984)

Fuchizawa and Takeyama (1979) and Manabe *et al.* (1984) conducted experiments on aluminum tubes with varying circumferential (σ_θ) and longitudinal (σ_ϕ) stress ratios during unsupported bulge forming. They defined the stress ratio in the experiments as,

$$\alpha = \frac{\sigma_\phi}{\sigma_\theta} \tag{4}$$

The results of their study are shown in Figure 18 (b) and (c). As α approaches zero from 1.0, the compressive force in the axial direction increases, as does the radial expansion of the tube. When α becomes negative, excessive levels of axial force cause the tube to buckle. The deformed geometry of the tube as a function of stress ratio can be seen in Figure 18 (c). Tirosh *et al.* (1995) confirmed, both experimentally and analytically, that for optimal forming of unsupported tube bulging $-1/5 < \alpha < 0$.

1.3.2 Supported Bulge Forming of Axial Members in a Die

Supported bulge forming is similar to the unsupported bulge forming method with the exception of having a closed die that limits the expansion of the tube to the die cavity geometry. The most simple hydroformed shape is an axisymmetric tube, as shown in Figure 19 (a). This type of hydroforming is far more practical than the unsupported case because it

allows one to design a component with flat sections. Many of the components formed within a die are asymmetric due to their design. One such extreme part is the T or Y-branch, as shown in Figure 19 (b) and (c). Friction plays a large role in supported hydroforming since the tube is in contact with the die walls during the forming process. Contact between the tube and die wall induces frictional forces that retard material flow, causing uneven wall-thickness distributions that, in turn, promote failure due to tensile instability (fracture). The onset of failure can be delayed with good lubrication to reduce frictional effects, in addition to the application of an axial compressive force during hydroforming, as in the unsupported bulge forming case.
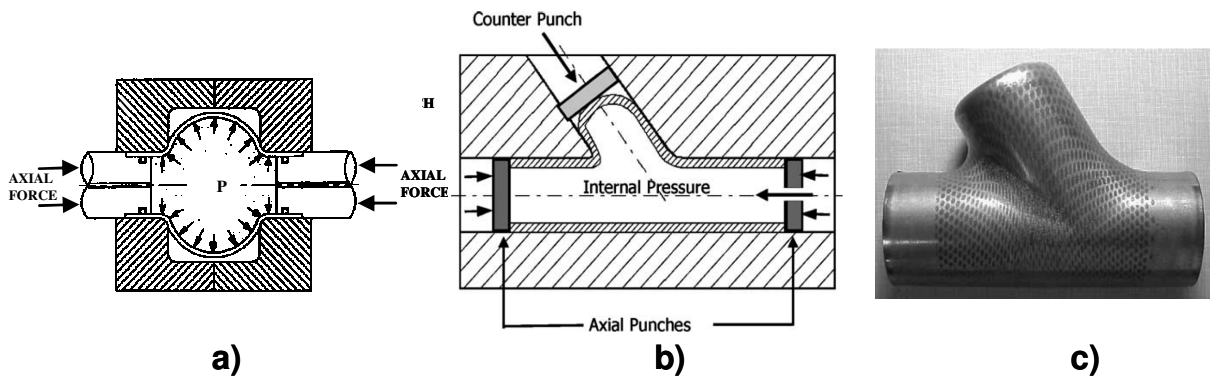
Figure 19: (a) Axisymmetric (Thiruvarudchelvan, 1996) and (b) and (c) Asymmetric supported bulge forming (Jiratearanat, 2004)

The work of Grey *et al.* (1939) on the manufacturing of seamless copper fittings with T-branches was one of the first implementations of hydroforming to an industrially manufactured part (Koc and Altan, 2001). Limb *et al.* (1976) conducted experiments on T-branches and reported that the softer materials in their study (copper and aluminum) were formed with little or no wall thinning, whereas the stronger materials (brass and steel) showed considerable thinning in the branch wall thickness. They also showed that bulge height of the T-branch increased for materials with decreasing strength. FE analysis (with experimental validation) of the Y-branch forming process (Figure 19 b and c) was conducted by Jiratearanat *et al.* (2004). Their FE simulations predicted a thickness distribution along the bulge of the Y branch that was in very close agreement with that from the experiments. The main finding of the study showed that the bulge height of the Y branch increased for decreasing initial straight tube lengths. The effect was due to increased sliding friction along the longer tube section.

Koc (2003a) looked at the effect of strain hardening exponent on the thickness distribution in a production-scale structural frame part (Figure 20 a). He intentionally altered the material properties of the low carbon steel tubes by heat treatment. Figure 20 (b) shows that the heat treatment did not drastically change the flow stress curves of the altered materials, but in (c) the strain hardening value is seen to be altered by heat treatment. The results of the thickness measurements (average of regions B, C and D) showed that n did not have an affect on the thickness distribution in hydroforming.
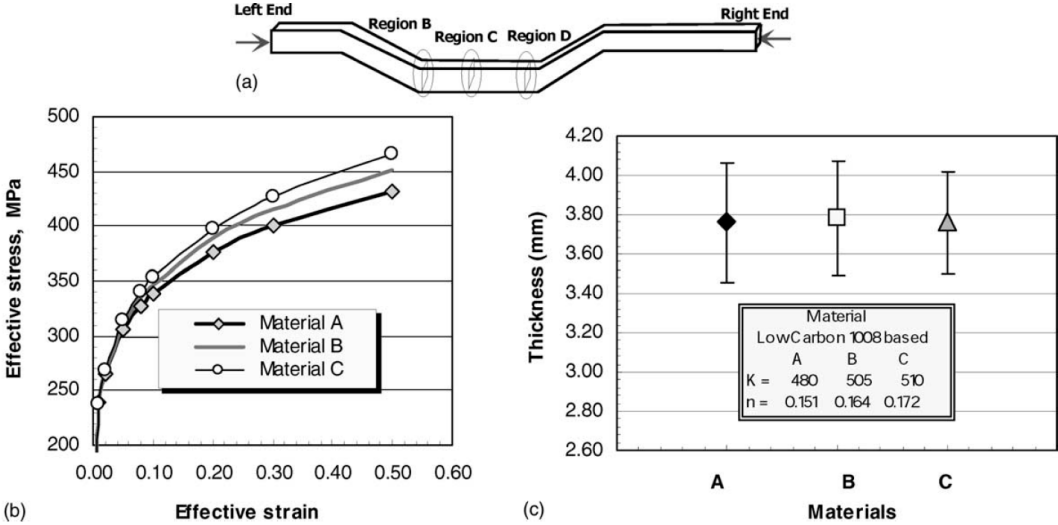
Figure 20: Effect of strain hardening exponent (n) on thickness distribution (Koc, 2003)

Lei *et al.* (2000) and Xing and Makinouchi (2001) developed their own FE codes to simulate hydroforming of a differential gear box casing. Both FE codes were successfully validated with experiments and used to further investigate the optimal manufacturing of the part. A fixed-type and sliding-type die were investigated by Lei *et al.* (Figure 21 a). It was shown that the sliding type-die produced a superior part because it produced a more evenly distributed wall thickness. Xing and Makinouchi showed that pre-forming with a ring tool and then fully hydroforming to the desired shape resulted in a final part with a more evenly distributed thickness.
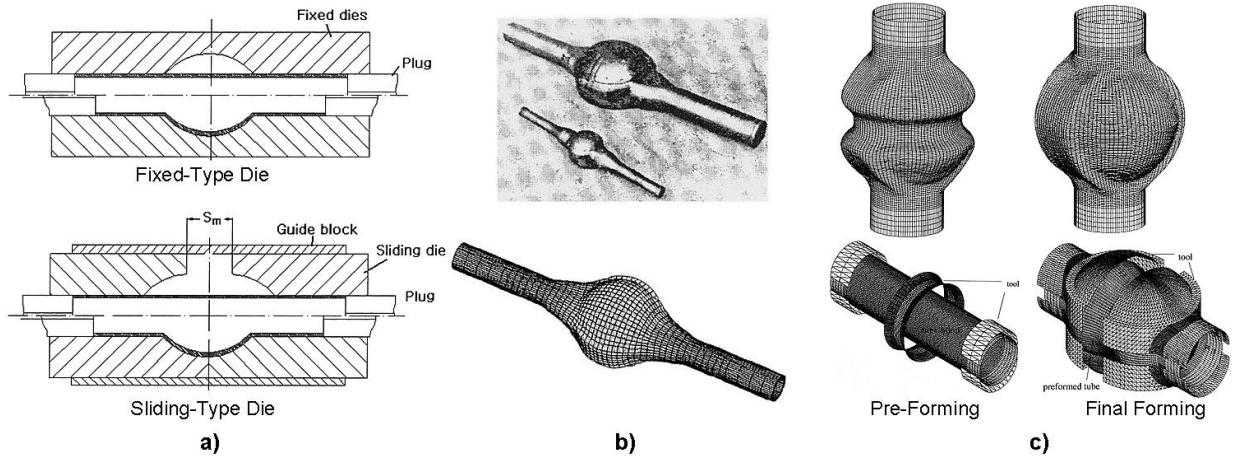
Figure 21: (a) Fixed and sliding-type dies (Lei *et al.*, 2000) (b) experimental/FE simulated parts (Lei *et al.*, 2000) and (c) pre-forming/final forming FE simulations (Xing and Makinouchi, 2001)

For analysis of hydroformed tubular cross-sections, 2D FE codes are simple and efficient. Kridli *et al.* (2003) modeled the expansion of a tube within a square die using ABAQUS/Standard. They were able to accurately predict the wall thickness distribution measured in the experiments. The predicted failure region (based on thickness reduction) was shown to be at the transition between the tube/die contact and free-expansion zone. Simulation showed that materials with a larger strain-hardening exponent (*n*) could be formed to a smaller corner radius. Chen *et al.* (2005) also modeled the 2D cross-sectional corner-fill expansion of a round tube into a square die using ABAQUS/Standard. They successfully predicted the internal pressure vs. corner-fill expansion, but were not able to predict the burst pressure with the plastic strain criterion or forming limit diagram approach (strain- and stress-based). It was concluded that tube contact with the die contributed to the erroneous predictions of the two methods since this was the location of failure in the experiments.

1.3.3 Supported Hydroforming of Pre-Bent Tubes in a Die

Automotive structural components such as engine cradles, lower arms and s-rails have been manufactured using the hydroforming technology. These components begin as straight tubular (circular) sections which undergo tube bending and possibly other pre-forming processes such as crushing in a die before hydroforming. As mentioned in the tube bending

section, much of the ductility of the tube is consumed by the large deformation a tube undergoes during the bending process which affects the formability of the material during the subsequent hydroforming process. The effects of bending process parameters, such as boost and R/D ratio, have been studied numerically and experimentally by only a small number of researchers, thus providing only a limited knowledge base. In addition to bending boost, the major parameter to improve formability of pre-bent tube is the application of end-feed, which is discussed later in this review.

Dyment (2004) conducted an extensive experimental and numerical study into the effects of tube bending parameters on the hydroformability of AKDQ steel tubes for zero end-feed hydroforming. Experimentally, he showed that for straight tube hydroforming in a square cross-section die, the corner-fill expansion (CFE) at burst (25MPa) was 8.0mm. The average CFE for a pre-bent tube in a square cross-section die was only 1.5mm at burst (23MPa). Annealing the pre-bent tube resulted in a dramatic improvement in CFE. Due to the experimental measurement resolution and variability in the study, the effect of boost and R/D ratio on formability could not be measured. The experimental study was numerically modeled using LS-DYNA with shell elements. The failure criterion used to predict fracture (burst) in the hydroforming models was element instability which is representative of necking; however, this criterion was unable to accurately predict the measured burst pressures.

Using an in-house Gurson-Tvergaard-Needleman (GTN) constitutive model coded into LS-DYNA, Gholipour (2006) was able to accurately predict the failure location and pressure for straight and pre-bent (R/D=2.5) aluminum tubes.

Another FE study conducted by Gao and Strano (2004) investigated two grades of stainless steel (SS304 and SS409) and two geometries of pre-bent tube. Figure 22 shows the dimensions of the hydroforming die which has a circular cross-section that is greater in diameter than the tube. In pre-bending, the SS304 material exhibits less thinning and a more uniform thickness distribution than the SS409. The large expansion cavity of the hydroforming die allowed for a modified (greater R/D ratio) pre-bent tube to be hydroformed.

Thinning at the outside of the bend region reduced from 27.9% to 24.9% for the modified pre-bent tube due to lower strains imposed by the larger R/D bend.
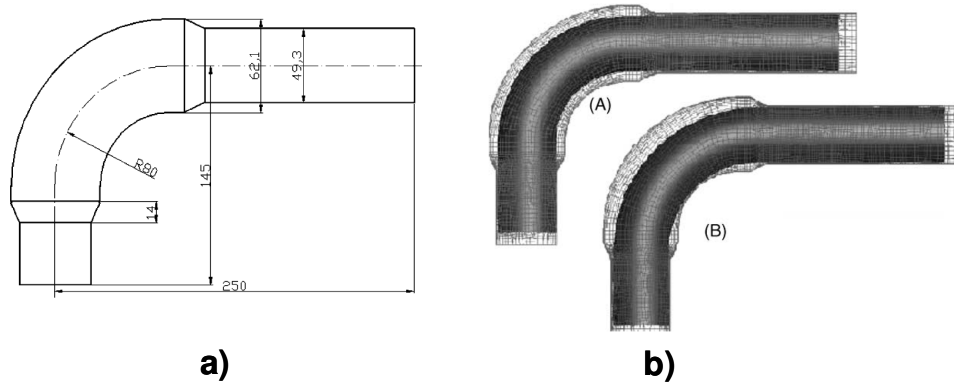
Figure 22: Pre-Bent hydroforming (a) die dimensions (b) Normal (A) and Modified (B) pre-bent tube (Gao and Strano, 2004)

1.3.4 Effect End-Feed on Hydroforming

The effects of end-feed (EF) on unsupported hydroforming of axial members was partially discussed in Section 1.3.1. It was shown that for unsupported hydroforming of axial member, insufficient axial compressive force during hydroforming leads to fracture (burst) of the tube, while excessive axial force results in buckling or wrinkling (Figure 14). Due to the simple geometry of this process, it is straightforward to experimentally and analytically derive a general process diagram for axial force (or EF displacement) and internal pressure (Figure 23). FE models could also be used to derive process diagrams, but only with a validated failure criterion. Problems arise for generating the process diagram of supported axial and pre-bent hydroforming because of the influence of the tube-die contact conditions (mainly friction) and any previous work hardening of the material due to a process such as pre-bending. For this reason, an in-die process limit diagram must be experimentally derived for each die geometry. The two methods used to apply EF during hydroforming are displacement- and load-control. Displacement-control requires the user to input an EF actuator displacement *versus* internal pressure curve to the hydroforming control system. In this case, the load on the EF actuators is automatically adjusted to achieve the prescribed EF actuator displacement.

Similarly, load-control requires the user to input an EF actuator load *versus* internal pressure curve to the hydroforming control system. The displacement of the EF actuators is then automatically adjusted to meet the demand of the prescribed EF actuator load.
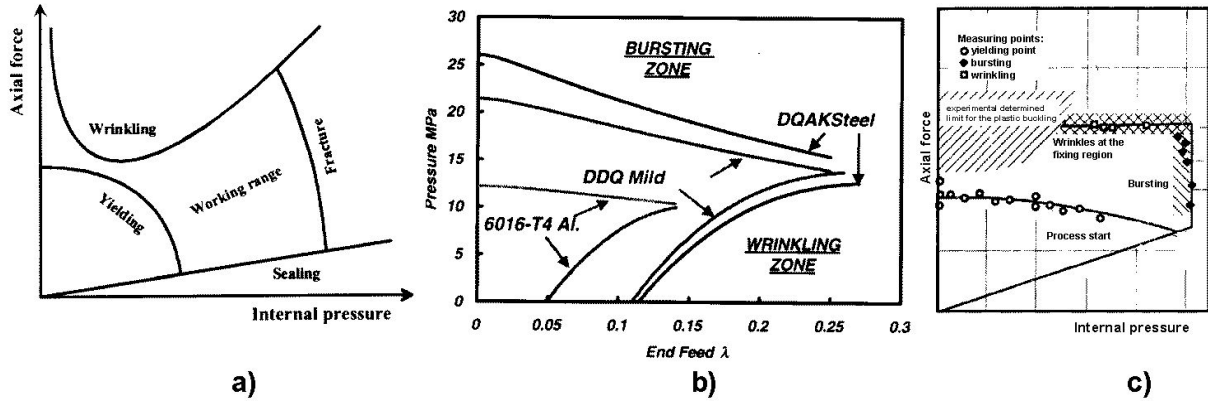
Figure 23: Internal pressure and end-feed diagrams (a) General (Asnafi, 1999) (b) Analytical (Xia, 2001) (c) Experimental (Dohman and Hartl, 1997)

The majority of the work conducted on hydroforming EF is on simple axial and T-branch members, for which no pre-forming operations such as pre-bending have taken place. Manabe and Amino (2002) experimentally and numerically (LS-DYNA) studied hydroforming of steel tubes into an axial square cross-section die. Using a prescribed stress ratio (axial stress/circumferential stress) they varied the EF under a load-control condition. The resulting EF load *versus* internal pressure curves were linear and varied in slope for each stress ratio. Their results showed that by increasing the stress ratio (more negative), the uniformity of the wall thickness of the hydroformed part increased. Koc (2000) used the FE code PAM-STAMP to simulate axial hydroforming of low carbon steel tubes into a bulge die. Displacement-control EF was used to simulate hydroforming with 15.9mm and 17.5mm (10% increase) of EF. He found that maximum thinning was reduced by 12% and internal pressure increased by 18% for the higher EF case. Koc (2003a) also modeled T-branch hydroforming of stainless steel (SS309) tube. Displacement-control was used and it was shown that an EF increase from 30mm to 38mm, resulted in an increase in bulge height of the T-branch from 25mm to 32mm. Thinning was unchanged for both cases. Johnson *et al.* (2004) developed a numerical control method to predict the combined end-feed and pressure loads for stable

deformation and maximum formability during tubular hydroforming. The algorithm uses the material stress-strain curve and the deformation theory of plasticity with Hill's criterion (1948) to relate the incremental stress and strain component to the increments in the applied loads for a given constant ratio of axial-to-hoop plastic strain (β=-0.40, -0.55 and -0.60). The incremental stress and strain is determined from an FE model. To validate this method, a simple tube bulging process within a conical die was examined using 6061-T4 aluminum tubes. Figure 24 (a) shows the predicted EF displacement *versus* internal pressure curves for the different strain ratios. After hydroforming, the predicted and measured EF load *versus* internal pressure curves showed good agreement (Figure 24 b). The geometry and thickness of the experimental and FE model predictions are shown in Figure 24 (c) and agree with each other well. The study also identified that the accuracy of the method was very sensitive to the lubrication condition between the tube and the die. A more simple approach was taken by Rimkus *et al*. (2000) to derive formulas and diagrams for the estimation of load parameters required to hydroform steel tubes in a radial expansion hydroforming die.
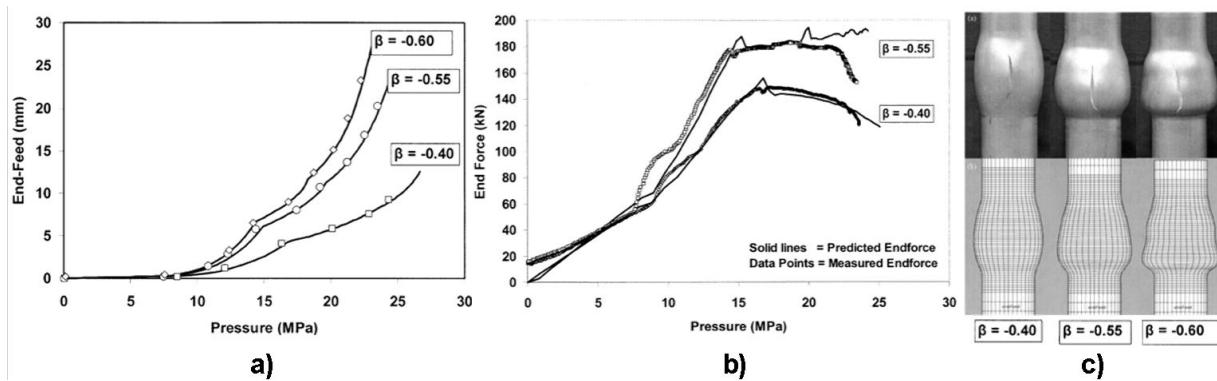
Figure 24: Numerical process control hydroforming method a) Predicted EF displacement vs. internal pressure b) Predicted and experimental EF force vs. internal pressure c) Experimental and FE results (Johnson *et al.*, 2004)

In an experimental hydroforming study on the effect of EF for a large automotive structural frame rail (Figure 25 a), Koc (2003a) used an analytical prediction to derive two loading curves (Case A and B) shown in Figure 25 (b). After hydroforming, the thickness of the part for regions B, C and D were averaged and are shown in Figure 25 c). Even though the EF displacement for case A was greater than case B, the resultant thickness of the part with

less EF was greater. This is due to the lower EF case always having a lower internal pressure than the higher EF case at a given time, except at the end of the test. A lower internal pressure produces less friction between the tube and die, allowing a more uniform axial EF of the entire tube. Another process advantage of EF case B is that there is less variation in thickness and EF.
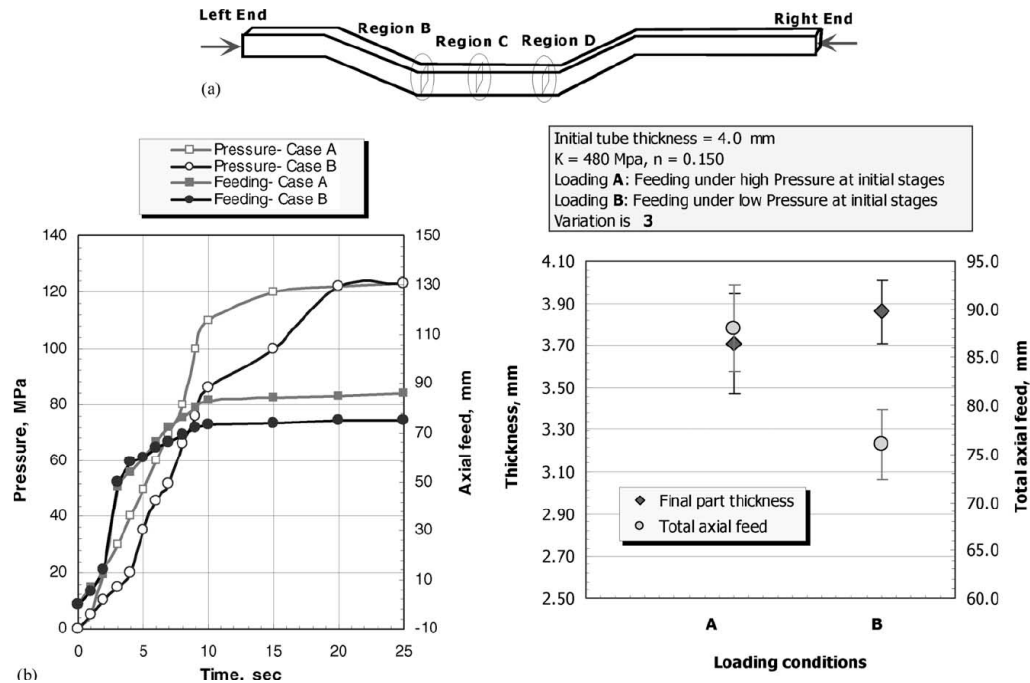
Figure 25: Effect of EF on thickness distribution of a large structural frame rail (Koc, 2003a)

Kim *et al.* (2003) found that a pre-bent tube used to hydroform an automobile lower arm, benefited from increased displacement-control EF during hydroforming by displaying better formability (corner-fill expansion). This study was purely numerical and based on their in-house 3D FE code, HydroFORM-3D. Gao and Strano (2004) observed that excessive thinning (element instability) occurred for small levels of EF during FE hydroforming simulations (PAM-STAMP) of pre-bent stainless steel tubes. For higher EF levels, wrinkling of the inside radius occurred. Sorine *et al.* (2006) conducted a similar study on HSS and AHSS tubes. In this study, load-control was applied to the hydroforming simulations for pre-bent and straight tubes. The same trends of increased formability for greater EF were observed. The most significant finding was that increased levels of EF allowed the less ductile and higher strength DP600 steel tubes to achieve the same levels of corner-fill expansion as the

more ductile and lower strength DDQ tubes (zero EF case). Another finding of the study was the lift-off phenomenon, which caused the inside radius of the tube to move away from the inside of the bend die until the internal pressure was high enough to form the tube against the inside of the bend region of the die. This behaviour was also observed in the work of Dyment (2004) and Bardelcik and Worswick (2006).

1.3.5 Tribology in Hydroforming

Due to the nature of the deformation involved in tubular hydroforming within a die, friction between the tube and die play a major role. Koc (2003b) identifies the following elements and factors of the hydroforming tribological system: (1) surface conditions of tube and die, (2) contact area and associated state of stress, (3) pressure, (4) sliding velocity, (5) tube and die materials and their mechanical properties, (6) die coating, (7) position of the parting line and (8) lubricant. Lubricant selection is critical to industrial hydroforming because it can often determine whether a part can be successfully produced. Industrially, a robust hydroforming process is also sought to ensure good part quality in a high throughput manufacturing environment. Poor lubrication conditions retard the flow of material into the die cavity during hydroforming expansion and typically cause failure (burst) due to excessive tensile strains. Part thickness is also affected by the lubrication condition and must be repeatable. In addition to proper lubricant selection, it is vital to accurately measure the lubricant coefficient of friction (COF) if the process is to be modeled numerically. The three main friction zones found in hydroforming are the guide, transition and expansion zones (Vollertsen and Plancak, 2002; Koc, 2003b; Costello and Riff, 2005). Laboratory tests are available to measure the COF for these different friction zones and are discussed in the following sections.

The early experimental work of Limb *et al.* (1976) investigated the effect of lubricant on the protrusion height during T-branch hydroforming. They found that for copper, brass, aluminum and steel tube, the protrusion height increased approximately 12.7mm (33% increase) when the lubricant condition was changed from the poor lube to the best lube. Koc (2003b) conducted an extensive lubricant study on a large automotive structural frame rail

part. In his study of a large hydroformed automotive frame rail, four different lubricants were used. Two different initial tube thicknesses were also evaluated (3mm and 4mm) and post hydroforming thickness was measured. Lubricants 1 and 3 were a wet type, 2 was an air dried lube and 4 was a paste. Figure 26 shows the average thickness measurement results for the three different sections and for each initial tube thickness. For the 4mm initial thickness tubes, lubricant 2 resulted in the least amount of thinning for all three cross-sections. Lubricant 2 also had the least amount of variation in thickness with respect to the other lubes. This attribute is important and representative of one component of a robust production process. The same trends are also evident for the 3mm initial thickness tube, but to a lesser degree. The total end-feed displacement (sum of the displacements of both actuators) was the greatest for lube 2 and the EF load requirements were the least for lube 2 also. Using the thickness measurements in Figure 26, Koc used LS-DYNA to back-calculate the COF for the four lubricants. His methodology assumed a COF for the FE model which resulted in a predicted thickness for the three sections measured in the experiments. The predicted thickness was compared to the experimental results. If the predicted thickness was not within 5-10% of the experimental thickness, the simulation was run again using another value for the COF. This procedure was repeated until the predicted thickness was within the tolerance. The resulting predictions are listed in the table within Figure 26.

Lube	Type	Predicted μ
1	Wet	0.08 - 0.09
2	Dry	0.04 - 0.05
3	Wet	0.12 - 0.14
4	Paste	0.19 – 0.22
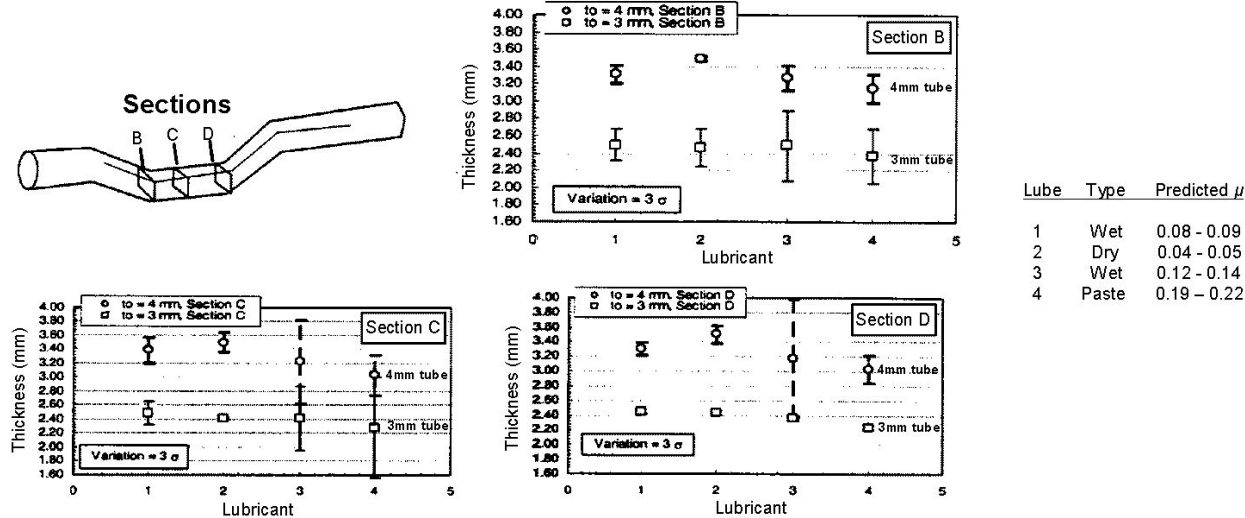
Figure 26: Effect of lubricant on thickness of a large structural frame rail and predicted COF (Koc, 2003b)

32

Kim *et al.* (2002) validated their in-house FE code HydroFORM-3D for a hydroformed automobile lower arm structure and conducted a purely numerical study into the effect of μ during hydroforming. They showed that the lowest value of COF resulted in improved formability by allowing more material feed into the possible failure regions. Higher values of COF increased the occurrence of wrinkles and burst locations. Manabe and Amino (2002) found results similar to the findings of Kim *et al.* (2002) for an axial tube hydroformed into a square cross-section die. They conducted experiments and FE simulations and found that a tube achieved a greater corner-fill expansion with a low COF lubricant.

The guiding zone (Figure 27 a) is region within the die where the undeformed tube is fed into the forming zone. There are high frictional forces encountered between the tube and die because the entire tubular surface area is in contact with the die. The movement (displacement) of the tube relative to the die can be relatively high for applications where end-feed (EF) is utilized. A low COF is required to allow undeformed material to be fed into the expansion region of the die. High frictional forces prevent sufficient material feed and cause excessive thinning in the transition and expansion zones which eventually lead to fracture (burst). In addition to promoting failure, high frictional forces require larger capacity EF actuators. The guiding zone test (Prier and Schmoeckel, 2003) was developed to experimentally measure the COF and evaluate the performance of lubricants (Figure 27 b). A circular section of tube is pressurized within a die and is axially displaced a given distance with a certain velocity. The axial load is measured and given the internal pressure and surface area of the tube OD, the COF can be calculated.
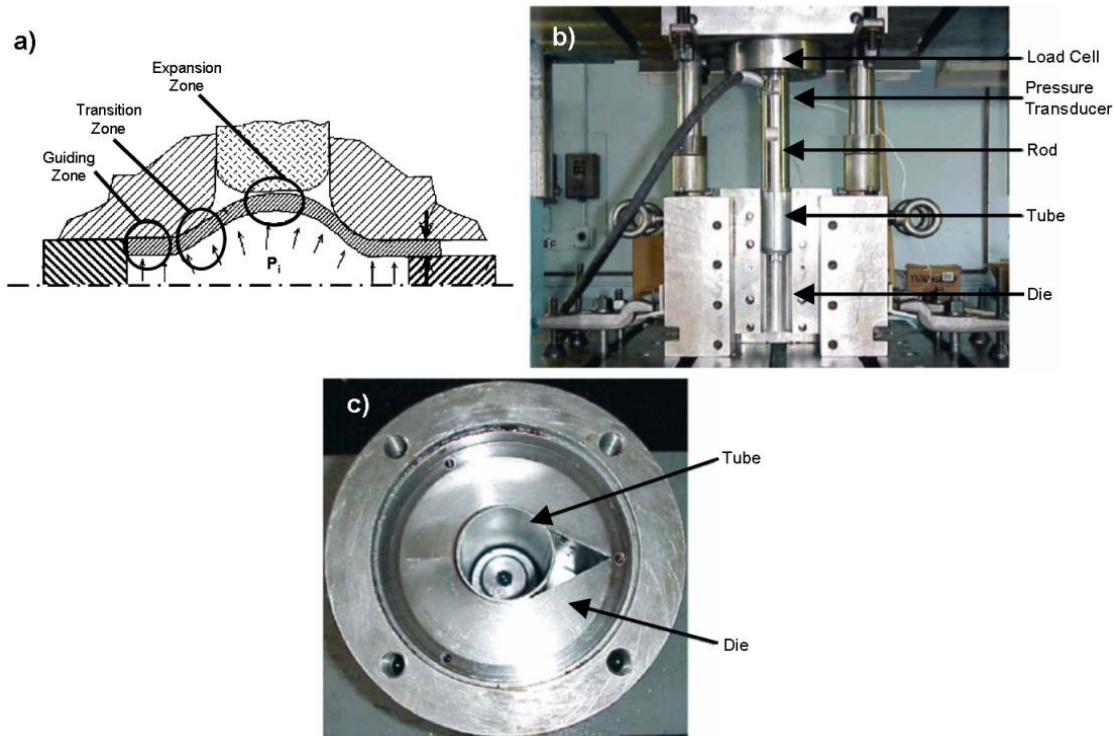
Figure 27: (a) Three main friction zones (Koc, 2003b) (b) Guiding zone test (Costello and Riff, 2005) (c) Expansion zone test (Costello and Riff, 2005)

The transition zone is the area between the guide and expansion zones. In this zone, the tube deforms and is under a tri-axial state of stress due to the contact with the die. The displacement and velocity of the tube are non-zero within this zone, but are often lower than in the guide zone. This area requires a low COF much like the guide zone.

In the expansion zone, the tube is under biaxial loading with little to no effect of axial feeding. The tube material displacement relative to the die is minor and in the circumferential direction, with negligible sliding velocity. An expansion zone test (Ngaile *et al.*, 2004a, 2004b) is shown in Figure 27 (c). A tube is expanded into the triangular (or other shaped) cavity until failure (burst) is reached. Different lubricants are applied and based on their COF, the height from the apex of the triangle to the deformed protrusion height of the tube will change. Better lubricants will allow greater protrusion heights, since they allow more material to flow along the triangular cavity wall. There is no quantitative measure of COF, but with the use of FE simulations, the experiment can be modeled with various values for COF. The

model which most accurately predicts the protrusion height gives a good approximation of the actual COF of the lubricant.

Another frictional test that was utilized for the work presented in this thesis is the twist-compression test (TCT), which was developed by Schey (1990). The first version of this test was an alternative to the pin-on-disk test and was developed by Kawai and Dohda (1987) to simulate the following fundamental friction conditions in metal forming: (1) the amount of plastic deformation, (2) interface pressure, (3) sliding distance, (4) sliding velocity, (5) compatibility between the contacting materials and (6) temperature. For this test, two flat annular sections (indenters) are loaded against a flat lubricated sheet metal specimen (Figure 28 a). The load is adjusted to produce a specific interfacial pressure between the tool and sheet sample. The tool specimen is rotated against the fixed sheet for half a turn (Figure 28 b). The torque imposed on the sheet specimen is measured and with the given normal load, the COF is calculated as per Figure 28 (c). The test was able to capture the static and dynamic COF, but failed to capture the breakdown of the lubrication due to the limited sliding distance (half turn). Kawai and Dohda also showed that their results were dependent on the length of the indenter sections. The indenter geometry exhibited the undesirable effect of gouging and rubbing against the sheet materials. Another study by Dohda and Kawai (1990) compared their TCT against three existing tribological tests. These tests included the four ball test, ironing type test and cup deep drawing test. They concluded that there was a relatively good correlation between the indices measured, but only under similar frictional conditions, and that care should be taken to choose test conditions which embody the same frictional conditions as are expected in the forming process. The version of the TCT that was used for the current thesis work was the same as Kawai and Dohda's, but incorporated a continuous annular contact surface for the tool (Figure 28 a). This modification was the work of Schey and Nautiyal (1990) and Nautiyal and Schey (1990) for experiments on aluminum sheet with steel tools. The new tool geometry allowed lubricant breakdown to be studied by measuring the COF for multiple revolutions of the tool and reduced gouging caused by the non-continuous indenter contact face. The TCT replicates the conditions found in metal forming in which the lubricant supply is limited and sliding under high pressure is enforced. Even though there is little plastic deformation (of sheet specimen), good correlation has been found between the test

results and lubricant performance in such operations as ironing and cold extrusion. Also, since the TCT does not simulate any single metal forming process, it is a valuable tool for ranking and screening lubricants. The controlled interfacial pressure and sliding movement of the TCT, makes it a viable test for measuring the COF in the hydroforming process. In more recent work, the COF determined by the TCT correlated well with experimental results for a hydroforming lubricant evaluation study conducted by Khodayari *et al.* (2002). Costello and Riff (2005) conducted a study of hydroforming lubricants using the guide zone test, expansion test and TCT. They concluded that for the TCT, the initial COF displayed a low correlation with the guiding zone test, while the failure (total lubricant break-down) time displayed a mild correlation with the expansion zone test. Although some correlations can be made between the tests, there is not a single test that completely replicates the complex tribological conditions found in hydroforming. It is the experimentalist's discretion to select the test that they feel best represents the forming process that is being examined.
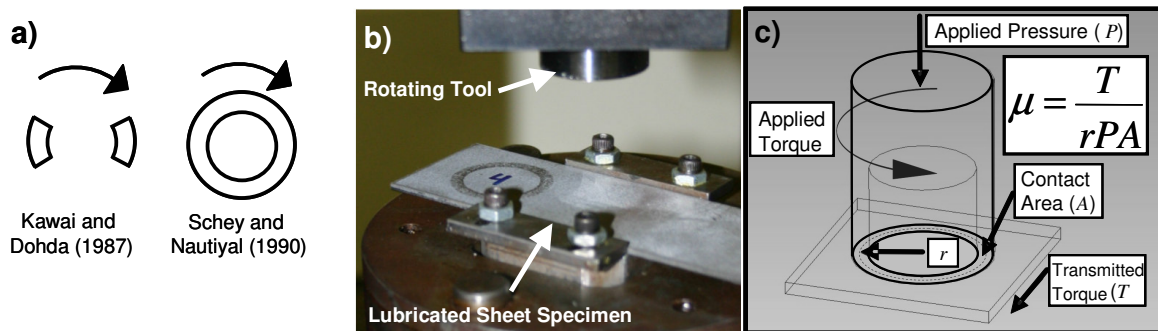
Figure 28: Twist-compression test (a) contact surface, (b) test equipment, (c) specimen loading condition

1.4 Sheet Metal Forming Failure Criteria

The most widely used sheet metal forming failure criterion was developed in the mid 1960's by Keeler and Backhofen (1964) and Goodwin (1968). Their strain-based Forming Limit Diagram (εFLD) gauges the forming severity with respect to necking during sheet metal forming. Through a series of dome height tests, sheet metal is formed under various

monotonic strain-path ratios until necking occurs. The strain at necking is plotted as data points and a line is curve-fit to define the forming limit curve (εFLC) shown in Figure 29 (a).
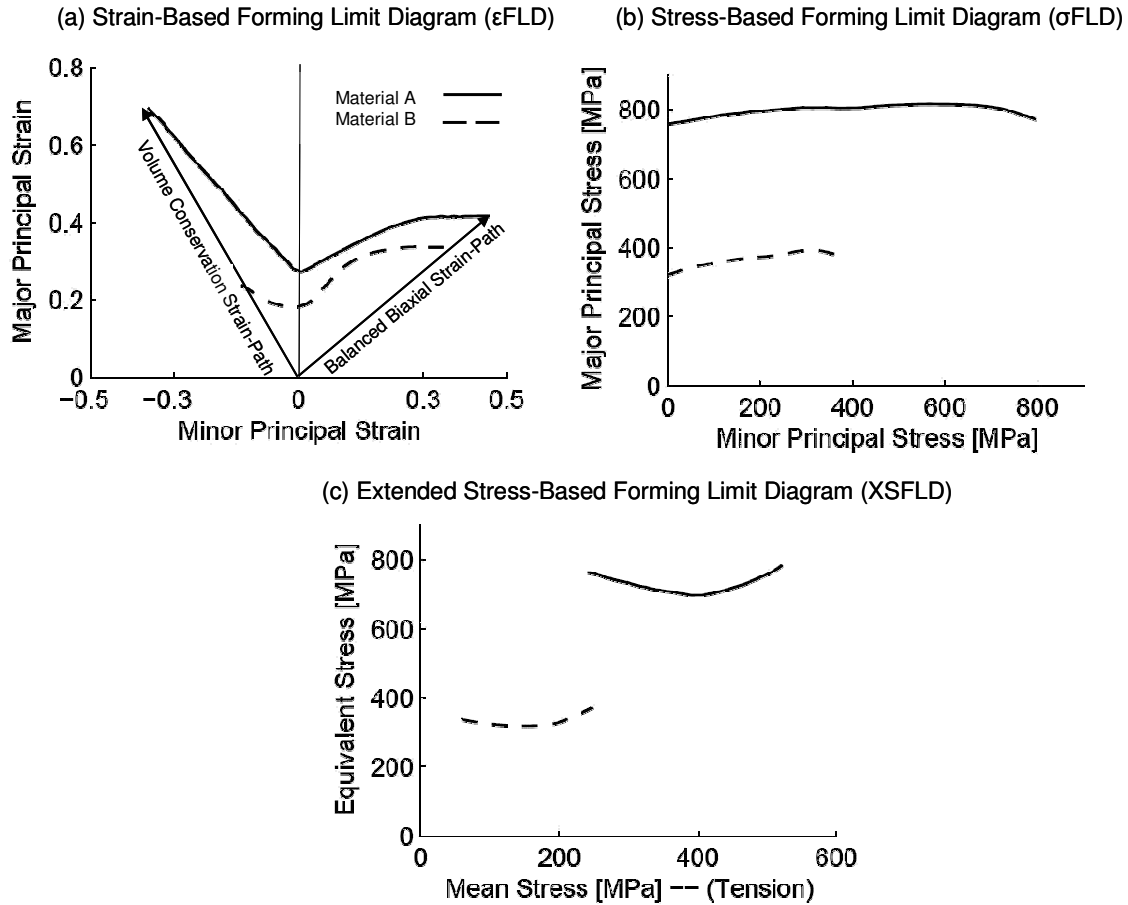
Figure 29: (a) Strain based (b) Stress based and (c) Extended stress-based forming limit diagrams (Simha *et al.*, 2006)

The work of Kleemola and Pelkkikangan (1977), Arrieux *et al.* (1982) and Graf and Hosford (1994) examined the effect of pre-strain on the εFLC. Both groups found that the εFLC shifted in strain space due to the amount of pre-strain imposed on the sheet. This finding was significant because it showed that the εFLD failure criterion was invalid for processes where the strain-path was not monotonic. An example of a non-monotonic sheet metal forming process is the pre-bending of tubes (longitudinal direction deformation) that are subsequently hydroformed (hoop direction deformation). The effect of pre-strain on the εFLC was the motivation for the development of the Stress-Based Forming Limit Diagram (σFLD)

by Stoughton (2000). Stoughton used the work of Kleemola and Pelkkikangan (1977), Arrieux *et al.* (1982) and Graf and Hosford (1994) to show that the shifted εFLC's converged onto a single curve in principal stress-space Figure 29 (b). His method was based on a plane-stress assumption which did not account for all three principal stress components. This criterion was validated for free-expansion experiments (tube expands freely and does not conform to a die) with AKDQ steel tubes (Green and Stoughton, 2004) and showed excellent agreement.

Hydroforming experiments conducted at the University of Waterloo have consistently shown that the fracture (burst) location for hydroformed tubes is at the tube/die contact area and not in the free-expansion zone. This observation was the motivation behind the development of the new Extended Stress-Based Forming Limit Curve (XSFLC) failure criterion by Simha *et al.* (2005, 2006), which is a fully three-dimensional stress-based failure criterion. The XSFLC method converts the σFLD principal stress components into the invariants equivalent stress and mean stress (Figure 29 c), with the main assumption that the equivalent and mean stress that characterize the formability limit under plane-stress loading are representative of the formability limit under three-dimensional stress states. To evaluate the predictive ability of the XSFLC, it will be implemented in the numerical modeling portion of this work.

1.5 Current Work

The preceding literature review has shown that the pre-bending process imposes a great deal of strain on a tube, which leads to a considerably more complex deformation than experienced by a straight tube in subsequent hydroforming. Also, the application of bending boost has been shown to reduce the overall thinning of a tube during pre-bending. To date, there has been no successful experimental work that has shown the effect of bending boost on the burst pressure during hydroforming. End-feed (EF) during hydroforming has been shown to increase the burst pressure and formability (corner-fill expansion) during straight tube hydroforming. Little published work exists on the effect of hydroforming end-feed on formability of pre-bent tubes. To expand on the existing published literature, this thesis will

focus on the effects of pre-bending boost and hydroforming EF on the hydroformability of straight and pre-bent steel tubes.

For this work, a mandrel-rotary draw tube bender will be used to bend 76.2mm (3.0") O.D. steel tubes to an R/D of 2.0. DP600 and IF steel provide a contrast between a high strength and moderate formability steel (DP600) to a low strength and very formable steel (IF). Different levels of bending boost will be applied during bending. The resulting strain and thicknesses will be measured to show how they change according to bending boost. Also, the bending process parameters will be compared for the two steels and boost levels. Square cross-section dies (straight and pre-bend) will be used to hydroform straight and pre-bent tubes to failure. In hydroforming, formability will be measured as the corner-fill expansion within the die cavity. Various levels of end-feed (EF) load will be applied to the ends of the straight and pre-bent tubes during hydroforming. Finite element models of the tube bending and subsequent hydroforming process will be created and validated. The extended stress-based forming limit curve (XSFLC) failure criterion will be implemented and validated with the experiments.

The balance of the thesis is organized as follows: material and friction characterization; the experimental procedure; experimental results of the pre-bending and straight tube hydroforming operations; and, the assessment of FE models of the pre-bending and hydroforming processes. Conclusions and recommendations complete the thesis.

CHAPTER 2

MATERIAL AND FRICTION CHARACTERIZATION

This chapter describes the equipment and methods used to characterize constitutive and frictional properties of the DP600 and IF steel tubes. This property data is used as input for the numerical models that are used to simulate the bending and hydroforming operations.

2.1 Tube Properties

2.1.1 Wall Thickness

The sheet materials studied in this work were manufactured by Stelco and were "tubed" by Nova Tube Ontario using a roll forming process with electric resistance seam welding (ERW). The thickness of the tubes was measured for two random samples using a micrometer at 45° increments around the circumference with the weld seam at 0°/360° (Figure 30). The thickness at the weld is not shown in the figure because it is considerably larger (the DP600 weld thickness is 2.02mm compared to 1.94mm for the IF tubes). The average thickness of the tubes away from the weld was calculated as 1.85mm for the DP600 and 1.74mm for the IF tubes. These average values were used in simulations of pre-bending and hydroforming operations.
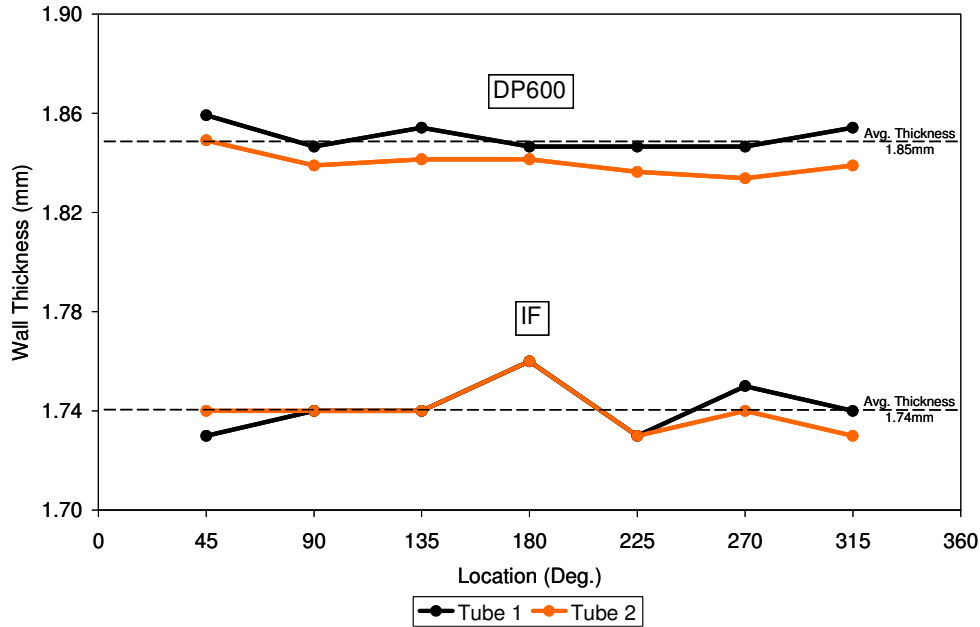
Figure 30: Tubular wall thickness measurements

2.1.2 Mechanical Properties

The mechanical properties of the tubular materials were measured using standard uniaxial tensile testing. The test specimens were cut along the longitudinal direction of the tube from three different orientations (3, 6 and 9 o'clock) around the circumference (Figure 31). For the tension test, flat grips were used to clamp the ends of the specimens, such that the curved shape of the specimen ends was crushed flat. Dyment (2004) used curved grip adaptors for his tension tests of tubular specimens and found no difference when comparing the results to those of the flat grips. Engineering stress-strain curves were generated and are shown in Figure 31 for the DP600 steel and Figure 32 for the IF steel. It was found that specimens from the 3 and 9 o'clock positions resulted in identical curves while the 6 o'clock position showed a slightly higher yield stress due to additional work hardening from the roll forming process (Singh, 2003). For DP600, three tension tests were completed at each of the three positions around the circumference (nine tests in total), while for the IF material, two tests were done at each position (six tests in total).

41

Using the uniaxial test results shown in Figure 31 for the DP600 steel and Figure 32 for IF steel, the 0.2% offset method was used to determine the average yield strength (YS) of the two materials. The average YS (from all tests) of the DP600 samples was 415MPa compared to 234MPa for the IF steel. The average ultimate tensile strength (UTS) was 559MPa and 296MPa for the DP600 and IF steel samples, respectively. It should be noted that the YS and UTS ratio (of DP600 to IF steel) is 1.8 and 2.1, respectively. The engineering stress-strain curves were converted into true stress-strain curves and averaged for the results around the circumference of the tube to generate a single average true stress-strain curve. This averaged curve was then converted into the true stress *versus* plastic strain, or flow stress curve, that is used as an input for the numerical models. The DP600 flow stress curve was linearly extrapolated from a strain level of 0.15 and the IF flow stress curve was extrapolated from a strain of 0.25, which corresponds roughly to the strain at the UTS for each material. Figure 33 shows both the DP600 and IF flow stress curves to contrast their difference in strength. The data points shown for the flow stress curves are used as input for the numerical models. Figure 33 also shows the DP600 flow stress curve of the original DP600 sheet material that was used to form the tubes (Winkler *et al.*, 2005). The sheet material shows a lower YS but an overall higher strength than the tubed material.
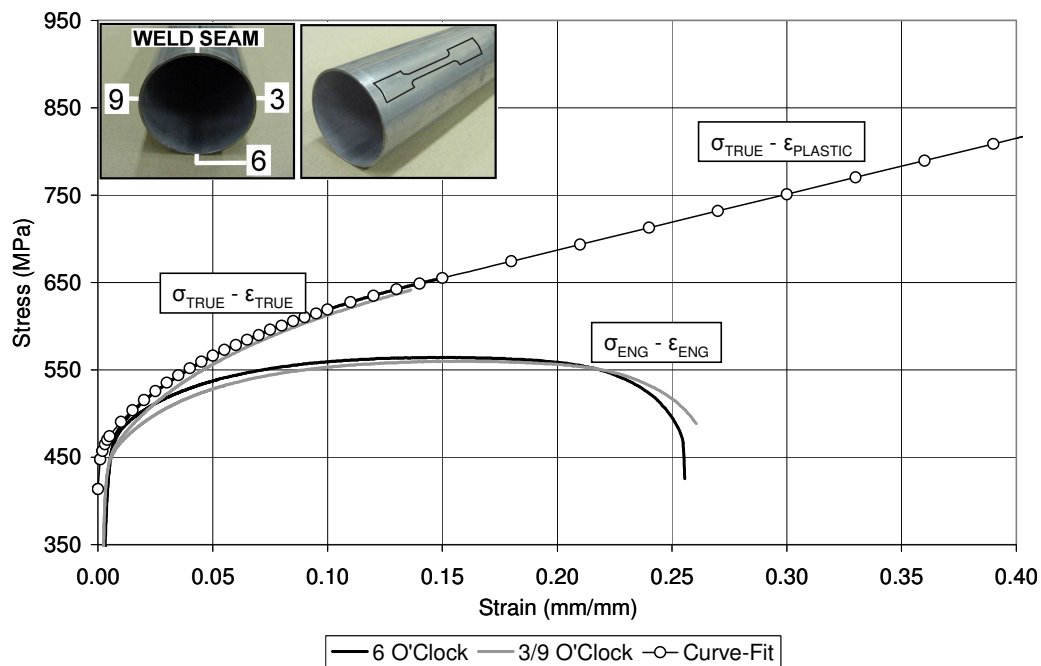
Figure 31: Uniaxial results from tensile testing of DP600 tubes

42
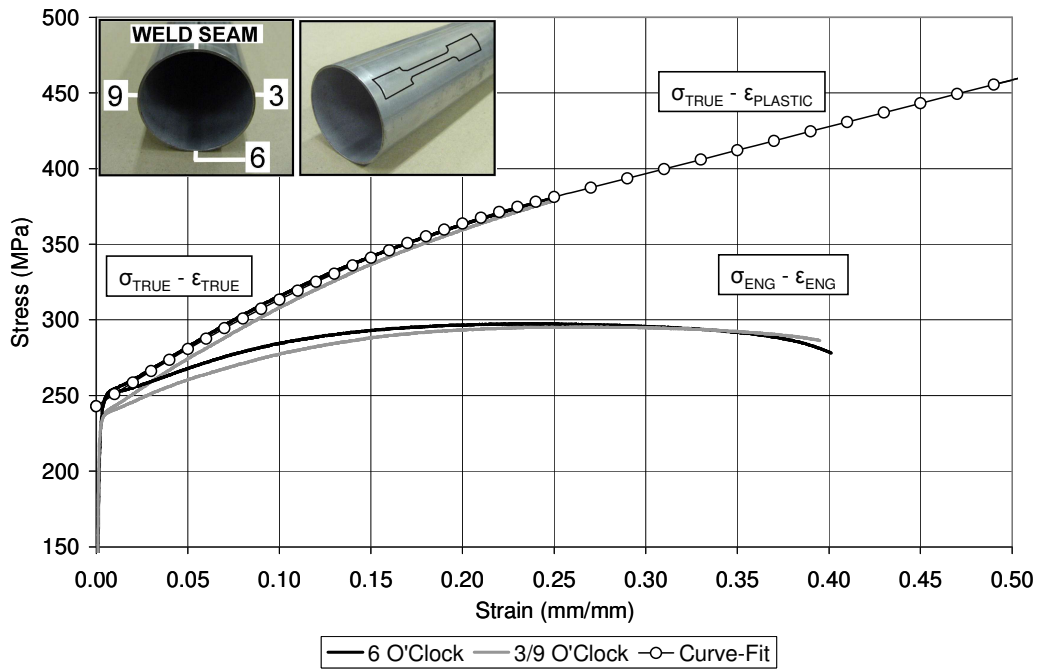
Figure 32: Uniaxial results from tensile testing of IF tubes
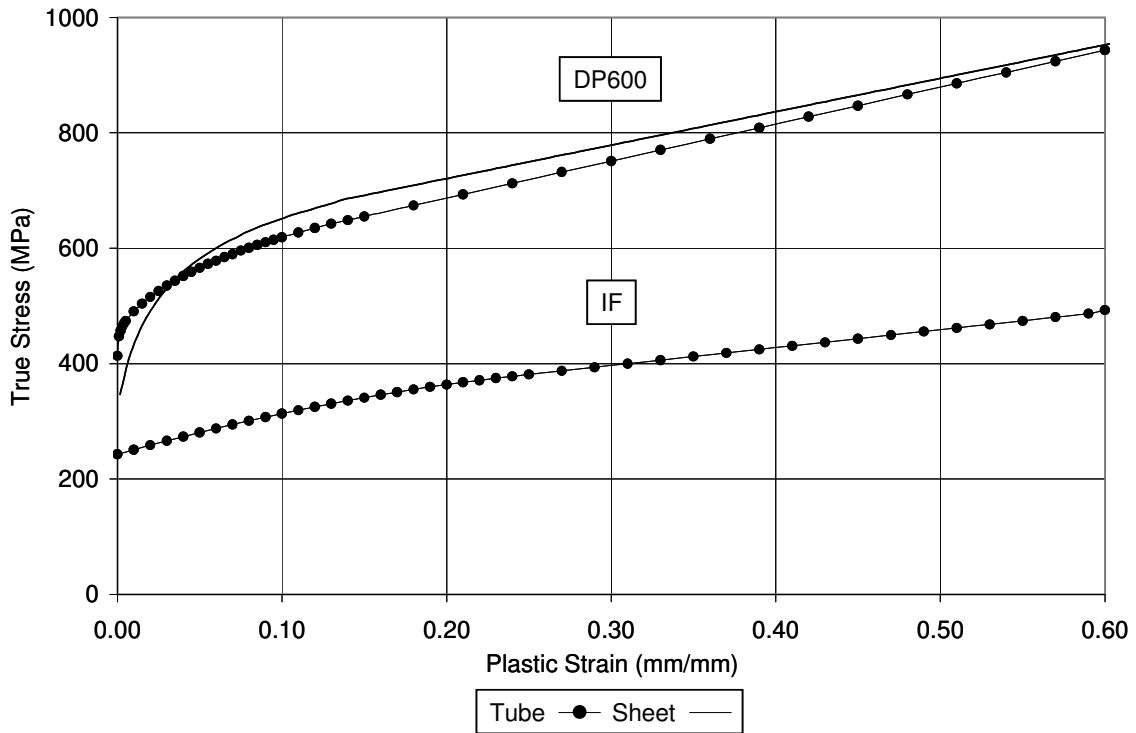
Figure 33: DP600 and IF tubular flow stress curves and DP600 sheet flow stress curve

43

The true stress-strain curves were fit with the power law function which is shown in equation (3). In the power law function, the true stress (σ) is a function of the strength coefficient (K), the true strain (ε) and strain-hardening exponent (n), a measure of the work hardening rate and an index to overall ductility. For DP600, the power law function was fit to each of the nine tensile tests, using data between the 0.2% offset yield strain to the strain at UTS (0.15). The nine K and n values were then averaged to obtain a single power law curve, that is shown in Figure 34.
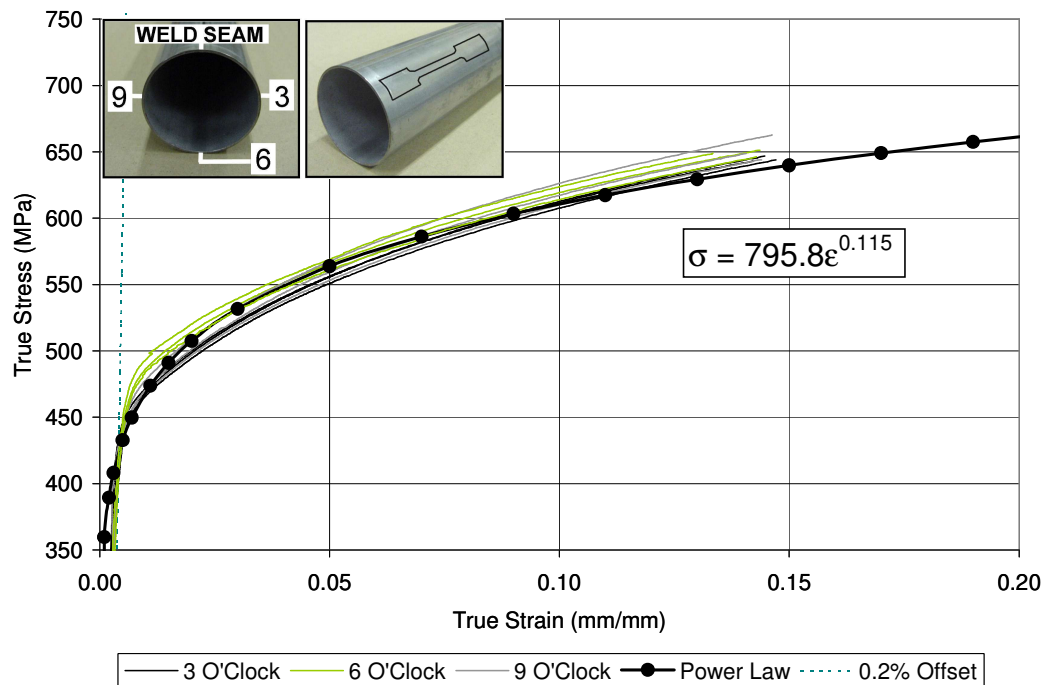
Figure 34: Power law curve fit for DP600

Rege *et al.* (2002) reported the range of strain hardening exponent varies greatly from about 0.12 to 0.22 for DP600 sheet steels. The range was a result of an extensive experimental study into the effects of chemical composition, processing parameters and microstructure on the family of DP600 materials. The average *n* value from the power law curve fit in Figure 34 is 0.115 which is on the low end of the range, a consequence of the pre-strain during tubing reported by Rege *et al.* (2002).

Due to the high formability of the IF material, the power law curve fit was not able to capture the true stress-strain response from 0.2% offset strain to the strain at UTS (0.25). The power law fit was applicable from a strain of 0.05 to strain at UTS and resulted in a strain hardening exponent of 0.205 and a strength coefficient of 500.8 (Figure 35). To fit the entire curve, the six true stress-strain curves were converted into true stress vs. plastic strain (flow stress), for which a single average second order polynomial was able to capture the material response. The second order polynomial curve was used to generate the IF flow stress curve shown in Figure 32 and Figure 33.
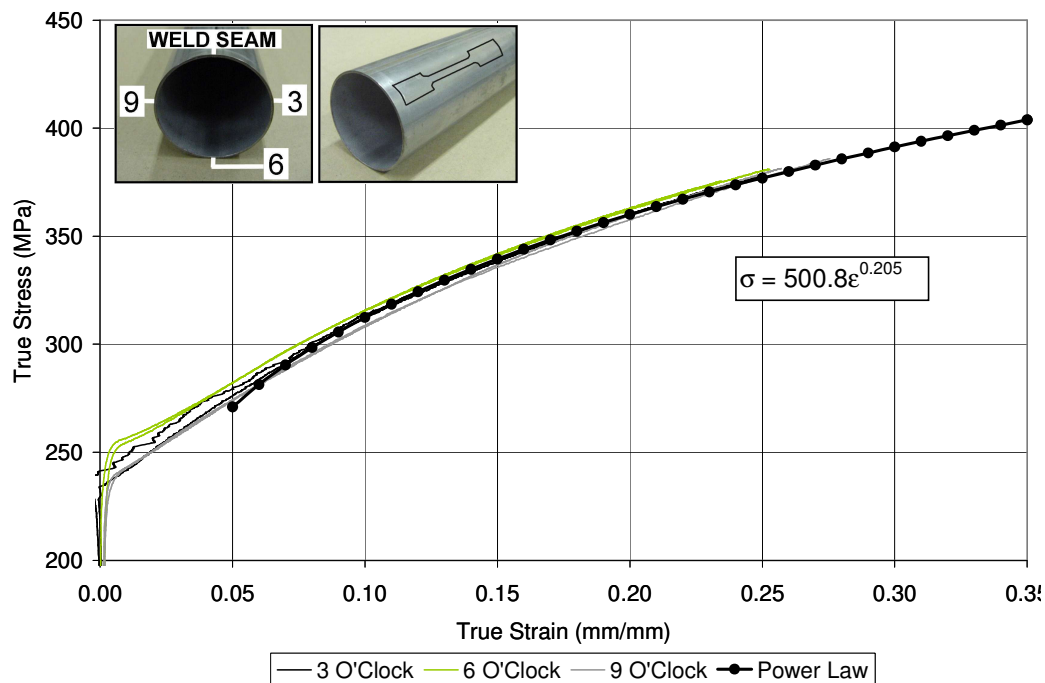
Figure 35: Polynomial curve fit for IF

2.1.3 Forming Limit Diagrams

The strain-space forming limit curve (εFLC) for the DP600 and IF tubular materials is used as input for the extended stress-based forming limit curve (XSFLC) failure criterion that will be implemented for this work. Because tubular materials are considered, the standard dome height test (used to generate sheet εFLC) does not apply and burst tests (used to generate tubular εFLC) were not available. To approximate the tubular εFLC, the Keeler-Brazier

45

(1975) approximation is used. Keeler and Brazier found that for various low-carbon steels, the shape of the εFLC was similar, but the plain-strain intercept (FLC_0, for $\varepsilon_2 = 0$) shifted along the major strain axis according to the following approximation,

$$FLC_o = (23.3 + 14.14t)\left(\frac{n}{21.0}\right) \tag{5}$$

where t is the sheet (or tube in this case) thickness in mm, and n is the strain-hardening exponent from the power law equation. Given the thickness and strain-hardening exponents found for the DP600 and IF tubes in Section 2.1.2, the corresponding FLC_0 was 0.27 for DP600 and 0.47 for IF. The FLC shape was scanned from the Keeler and Brazier (1975) publication, digitized and shifted to the corresponding FLC_0 (Figure 36).
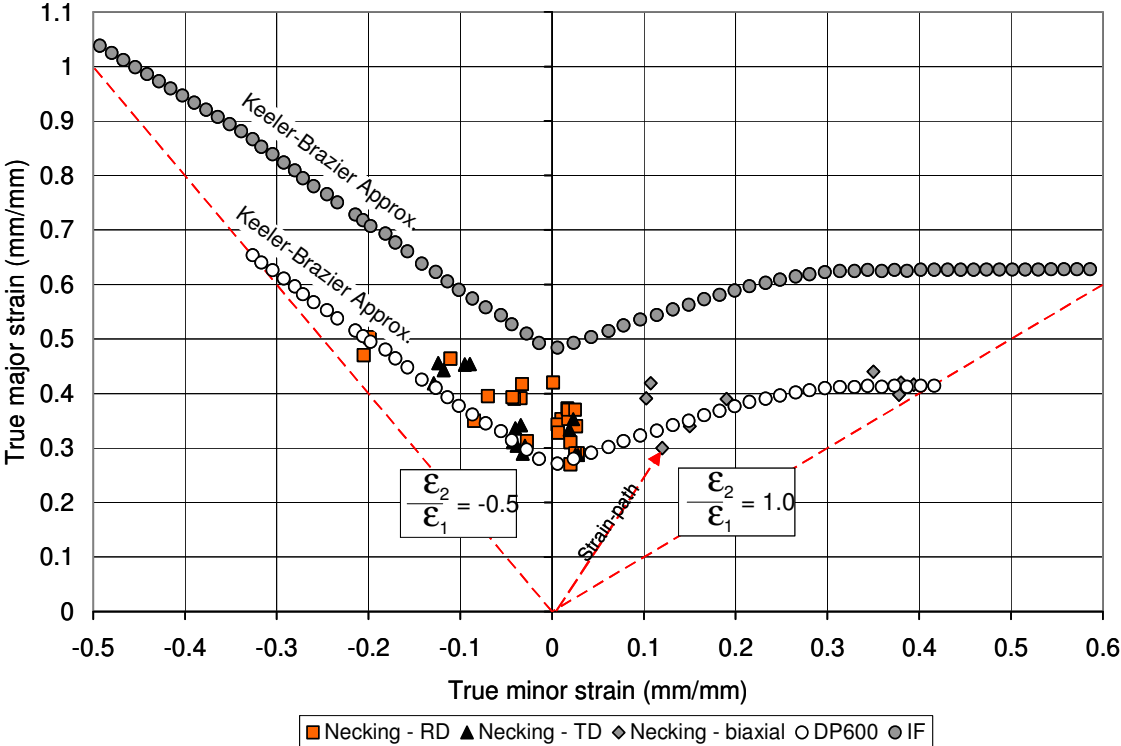
Figure 36: Experimental (dome height tests) DP600 εFLC and approximated (DP600 and IF) εFLC

The εFLC for the DP600 sheet metal (which was used to form the tubes) was measured by Yuri Ososkov at McMaster University and is shown as the necking data points in Figure 36. The test was conducted using the hemispherical dome height testing apparatus. The IF εFLC was not determined experimentally. Figure 36 shows that the DP600 sheet metal εFLC matches well with the approximated (Keeler-Brazier) tubular εFLC.

2.2 Friction Characterization

The twist compression apparatus at the University of Waterloo was used to measure the coefficient of friction between the tube and tools used in the pre-bending and hydroforming experiments.

2.2.1 Twist Compression Apparatus

The twist compression test (TCT) was designed and built at the University of Waterloo by Schey (1990) and is shown in Figure 37. An axial hydraulic cylinder provides up to 110kN (25kip) of normal load. Based on the annular contact area of the tool, the maximum interfacial pressure is 496MPa (72ksi). A hydraulic motor is used to rotate the tool at a maximum torque and speed (variable) of 1000Nm and 60RPM respectively. Data acquisition is done through a desktop PC with an in-house custom LabVIEW program. The data acquisition system measures the load from the transmitted torque and computes the coefficient of friction (COF) as a function of contact pressure and angle of rotation.
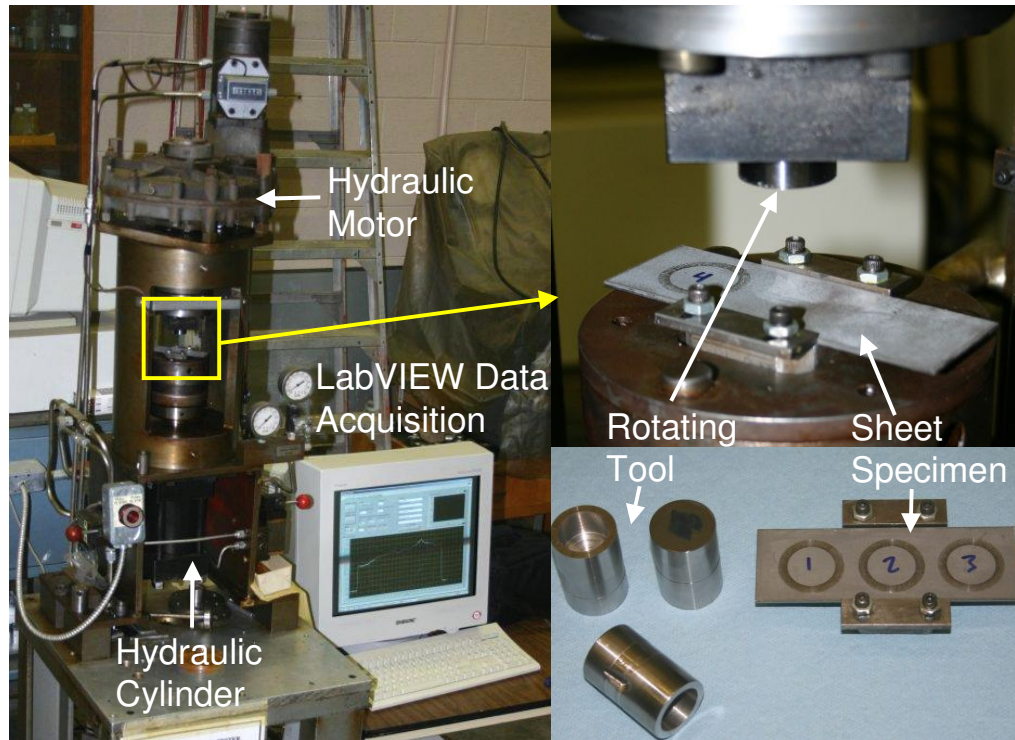
Figure 37: University of Waterloo twist compression apparatus

2.2.2 Experimental Parameters and Results

The tool steels used for the TCT were manufactured from the same materials (and heat treatments) used for the bend and hydroforming dies (Table 1). The lubricants used are also shown in the table. It should be noted that for the twist compression test, pre-bending and hydroforming experiments, the lubricants were applied in excess and the amount of applied lubricant was not measured. The rotational speed (RPM) of the TCT was set to approximate the sliding velocity experienced in the tube bending and hydroforming experiments (Table 1). To determine the range of interfacial pressures, finite element (FE) models and approximations based on known bending and hydroforming parameters were used to calculate the expected interfacial pressure during the tube bending and hydroforming experiments.

Table 1: Twist compression test parameters and results

Tool	Material and Hardening	Lubricant, Viscosity (cps), Specific Gravity	Expected Interfacial Pressure, MPa (psi)	Sliding Distance between tool and tube, mm	Rotational Speed, RPM (mm/sec)	Coefficient of Friction (COF), dynamic
Wiper Die	4130, Unhardened	Hydrodraw 615, 8,000 (@22°C), 1.02	34 (5,000)	180	19.2 (22.4)	0.040
Mandrel	8620, Ammonia nitride (60Rc), hard-chrome	Hydrodraw 615, 8,000 (@22°C), 1.02	NA	NA	NA	0.060
Bend, Pressure, Clamp Die	4130, Ammonia nitride (60Rc)	None	17-28 (2,500–4,000)	0	4 (4.7)	0.080
Hydroforming Die	P20, Unhardened	Hydrodraw 625, dry-film	0-83 (0–12,000)	25	4 (4.7)	0.035

Each tool was tested for a range of interfacial pressures, with three repeat tests at each pressure. The three repeat tests were averaged to produce a single static and dynamic COF at each pressure. The static COF was measured as the peak value at the beginning of the test and the dynamic COF was the average (after the static values) calculated over the expected sliding distance.

To illustrate the TCT results, Figure 38, Figure 39 and Figure 40 show the sliding distance *versus* COF for three tools that were tested at 55MPa (8,000psi) interfacial pressure. Appendix A contains the complete set of sliding distance *versus* COF plots for all TCT tests. Note that tests of the mandrel tool were not performed because hard-chrome plating of the tool contact surface was unsuccessful due to inconsistent chrome deposition. Figure 41 summarizes the complete set of experiments and shows the COF (static and dynamic) *versus* interfacial pressure for the three tools. From these curves, the COF used in the FE models (Table 1) was based on the dynamic COF curve (Figure 41) at the expected interfacial pressure shown in Table 1.
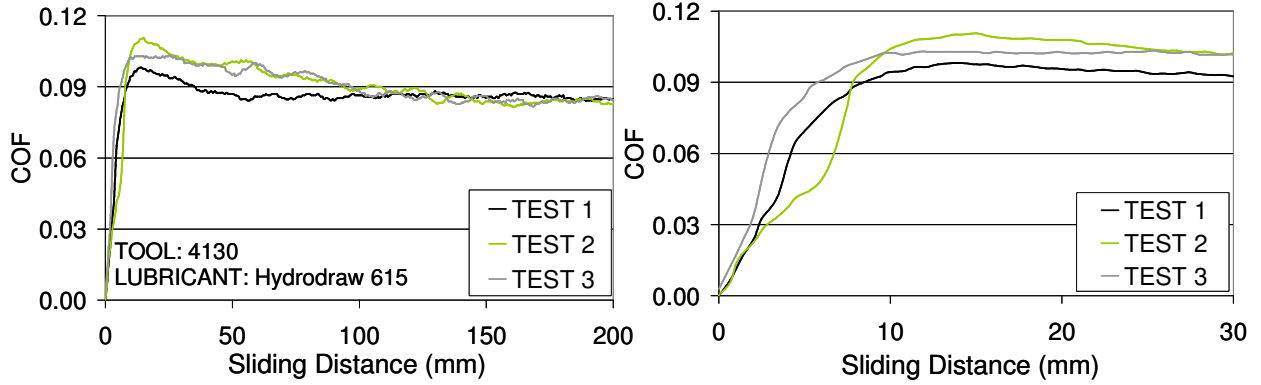
Figure 38: TCT results for wiper tool at 55MPa (8,000psi) interfacial pressure
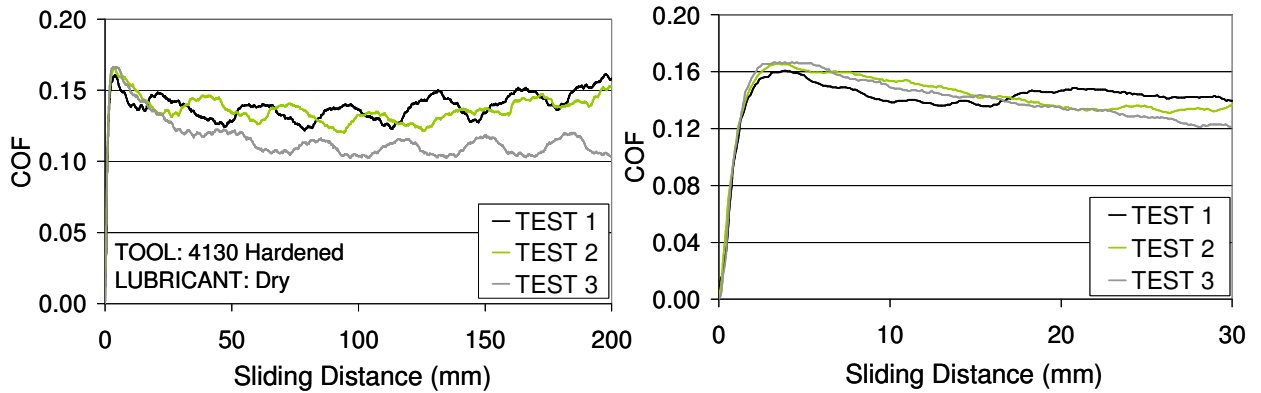
Figure 39: TCT results for bend, pressure and clamp tool at 55MPa (8,000psi) interfacial pressure
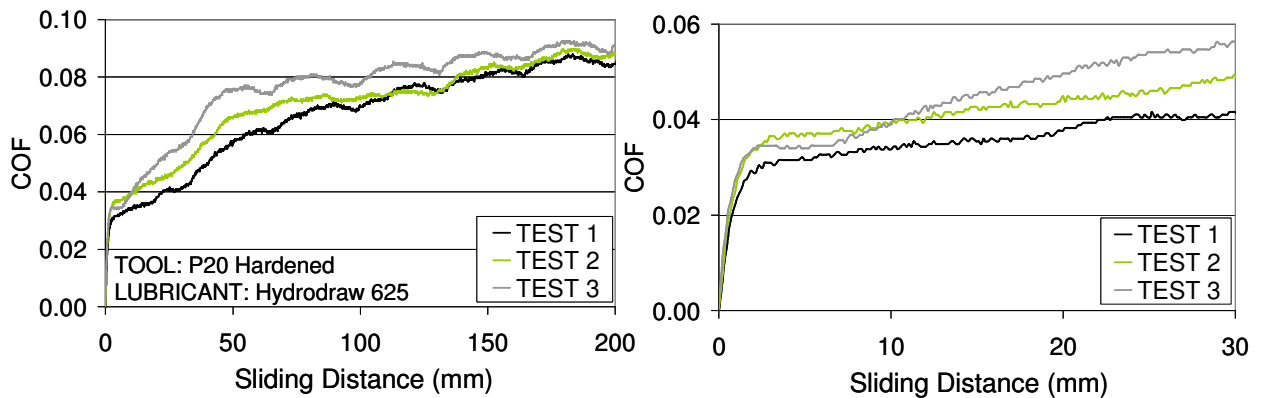
Figure 40: TCT results for hydroforming tool at 55MPa (8,000psi) interfacial pressure
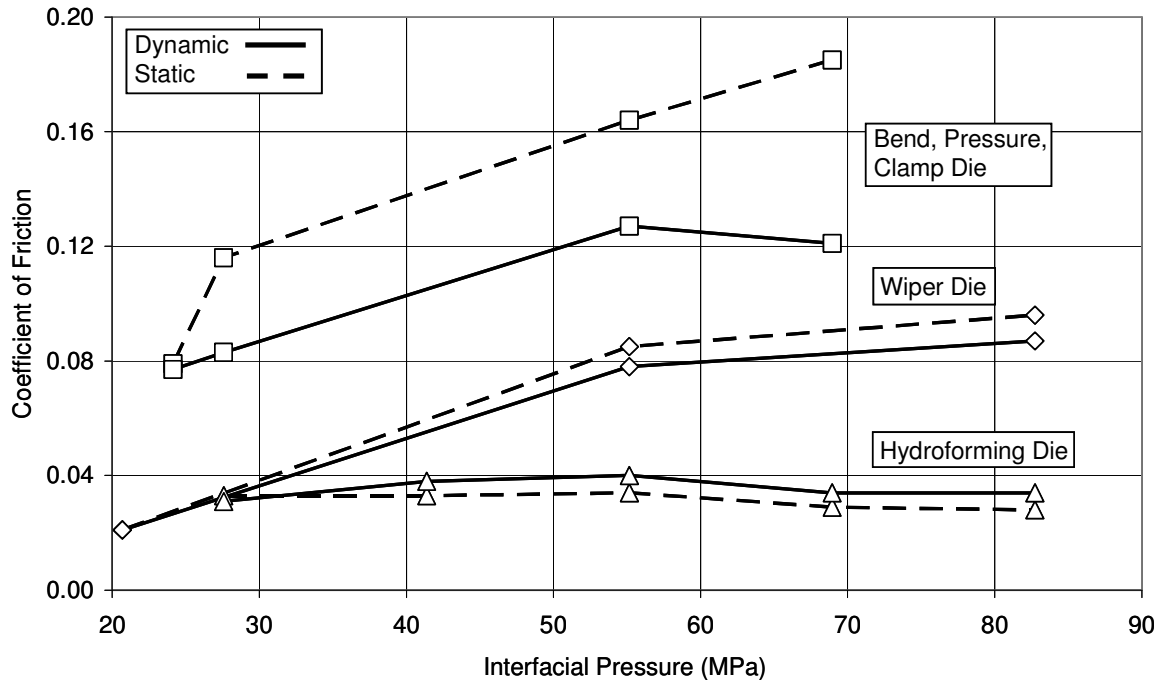
Figure 41: Interfacial pressure *versus* coefficient of friction results from twist compression test

The wiper results showed good repeatability at all of the test pressures (4130-Hydrodraw 615 results in Figure 38). The maximum variability in the COF from repeat tests was ±0.006, which occurred for the 55MPa interfacial pressure tests (Figure 38). The sliding distance between the tube and wiper during tube bending is approximately 180mm. The strong initial peak in the data represents the static COF, while the steady-state portion is the dynamic COF.

Tests on the bend, pressure and clamp die were conducted dry (4130-dry results in Figure 39). In the tube bending experiments, these tools experience little sliding distance if any. The repeatability was fairly good throughout the entire test with a maximum variability of the repeat tests being ±0.016 (COF) for the 55MPa interfacial pressure tests (Figure 39). As the interfacial pressure increased, the variability was reduced to ±0.005 (COF) for the 69MPa interfacial pressure tests (Appendix A). Again, a static COF peak was observed and a steady-state dynamic COF region.

Tests on the P20 tool steel behaved differently from the 4130 results. The lubricant progressively broke down as the sliding distance between the tool and sheet increased. Flaking and wear of the solid-film lubricant indicates breakdown during the test. A breakdown response is evident in Figure 40, corresponding to the progressive increase in COF with sliding distance. The breakdown phenomenon was consistent between tests. The static COF is not defined by a peak in this case, but rather the first COF reading after the initial increase. The average sliding distance during the hydroforming experiments is approximately 25mm and the dynamic COF was measured as the average COF over this sliding distance. Within this sliding distance, the maximum variability between tests was ±0.007 (COF) which occurred at the 83MPa interfacial pressure tests (Appendix A). The lubricant performed exceptionally well by adhering to the surface of the sheet metal. Even at high interfacial pressure, the lubricant film was present after the 25mm sliding distance.

CHAPTER 3

EXPERIMENTAL PROCEDURE

This chapter describes the experimental equipment and methods used to conduct the mandrel-rotary draw tube bending and hydroforming experiments.

3.1 Mandrel-Rotary Draw Tube Bending Experiments

3.1.1 Instrumented Laboratory Tube Bender

An Eagle Precision Technologies EPT-75 hydraulic mandrel-rotary draw tube bender at the University of Waterloo was used to conduct all of the bending experiments for this work. Figure 42 (a), (b) and (c) shows the EPT-75 tube bender and tooling. This industrial grade tube bender was retrofit with a closed-loop servo-hydraulic controls system that is run with a PC-based control and data acquisition system (Dyment, 2004). Five MTS 406 servo-hydraulic PID controllers are used. A custom in-house LabVIEW program, TubeBend version 1.93 (Dyment, 2002), was used to control the instrumented tube bender. Load and displacement sensors are coupled to each of the tools to enable accurate closed-loop control and allow real-time monitoring of the tools during bending. The tooling sensors are shown in a schematic (Figure 42 d) and in Table 2. A more detailed description of the control system, is provided by Dyment (2004).
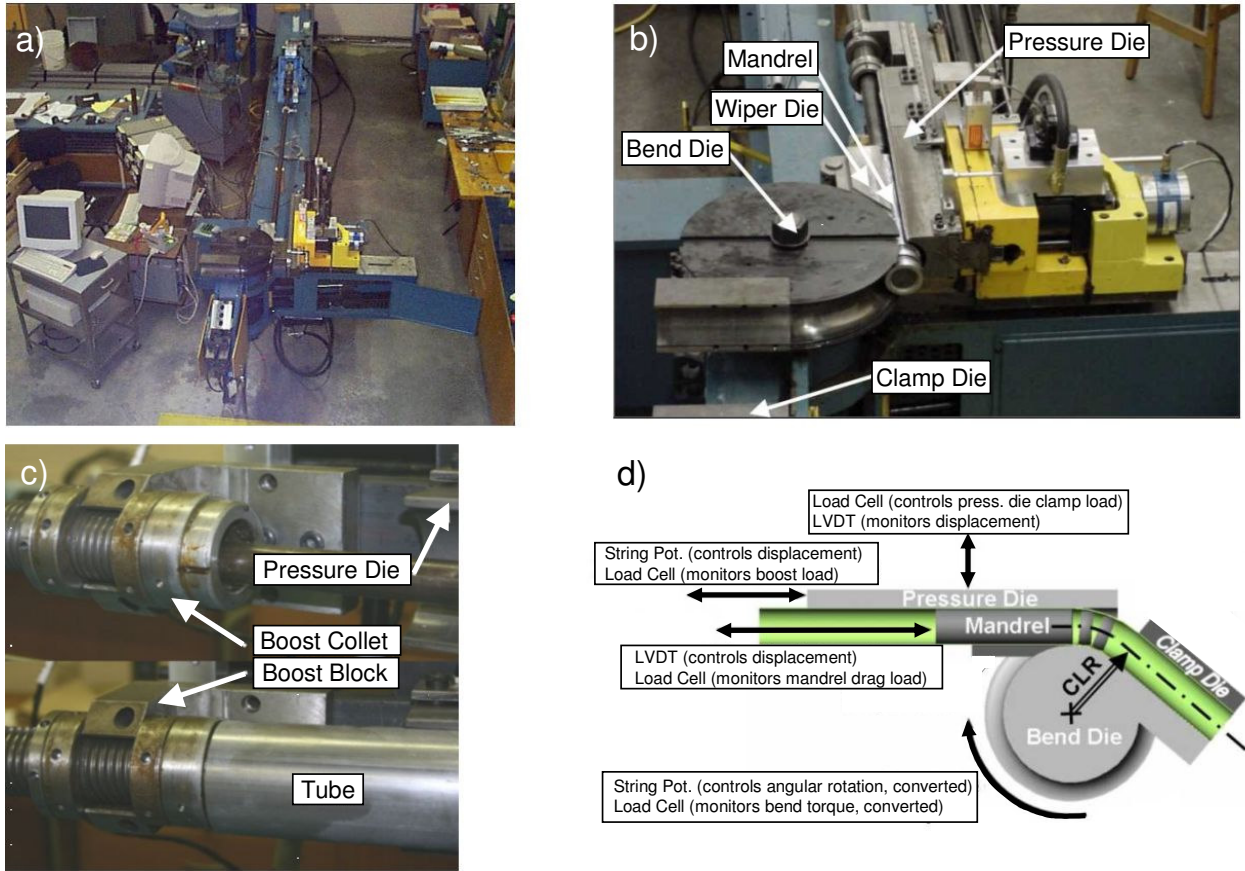
Figure 42: a) EPT-75 Bender b) laboratory bender tooling c) boost block assembly d) load and displacement sensors.

Table 2: Instrumented tube bender sensor and actuator details (Dyment, 2004)

Tool	PID Controller	Actuator Control Mode	Sensor (Control)	Sensor (Monitor)
Bend Die	MTS 406	Displacement	String Potentiometer (converted to angular rotation)	Load Cell on chain drive (converted to torque)
Pressure Die Boost	MTS 406	Displacement	String Potentiometer	Pressure Transducer
Pressure Die Clamp	MTS 406	Load	LVDT	Load Cell
Mandrel	MTS 406	Displacement	LVDT	Load Cell
Clamp Die	MTS 406	None (open/close)	none	none

The mandrel-rotary draw tube bending process is explained in Section 1.2. Figure 43 shows the tooling dimensions for an R/D=2.0 bending setup. To compensate for springback, the bend die radius or centre line radius (CLR) was undercut from the nominal 152.4mm (6") to 150.4mm (5.921"). A two-ball flexible mandrel, with a post diameter of 71.80mm and ball diameter of 71.95mm was used for the DP600 tubes, while the IF tube two-ball flexible mandrel post diameter was 72.13mm and ball diameter of 72.30mm. Given the average thickness of the tubes (Section 2.1.1), the radial clearance between the radius of the mandrel and the inside radius of the DP600 tube is 0.28mm (balls) and 0.35mm (post). The radial clearance for the IF tubes is 0.21mm (balls) and 0.30mm (post). A two-piece wiper was used with replaceable wiper tips. The material properties and heat treatments of the tools are given in Table 1.

A boost block assembly was used for all bending experiments and is shown in Figure 42 (c) and Figure 43. The end of the tube fits over the boost collet which is rigidly attached to the pressure die. The purpose of the boost block is to ensure that the tube does not slip relative to the pressure die and thereby attain boost levels greater than 100% (see Section 1.2.1). The straight tube sections are cut to a 1016mm (40") length with a cut-off saw and deburred around each edge.
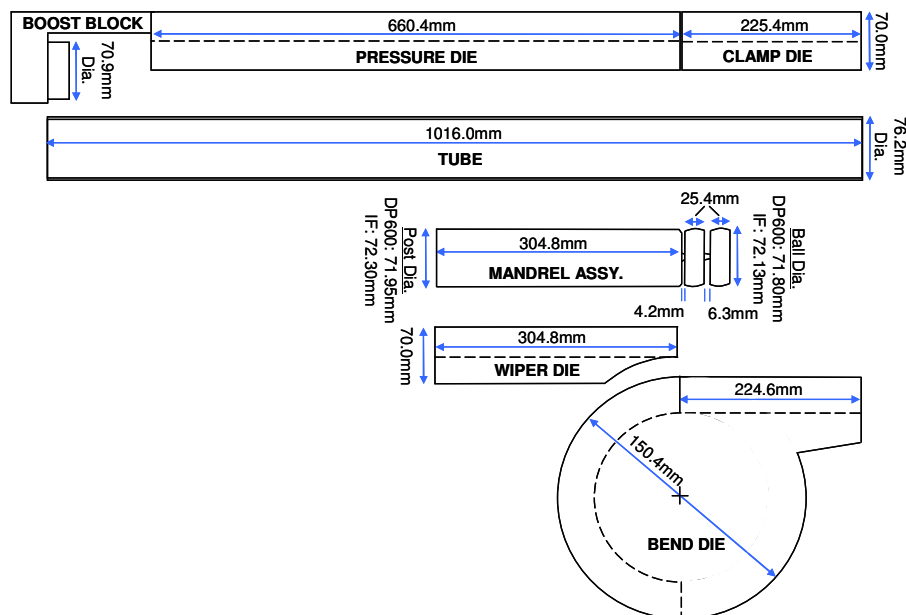
Figure 43: R/D=2.0 tooling dimensions

3.1.2 Bending Parameters

The bending parameters used in this study are summarized in Table 3. With the exception of the wiper rake angle, these parameters were input directly into the TubeBend v.1.93 program. Experience and trials were used to determine these optimal parameters.

Table 3: Bending Tool Setup and Parameters

	DP600		IF		
Boost Condition	LB	MB	LB	MB	HB
Boost Prescribed, %	95	100	95	100	105
Wiper Rake Angle, Degrees	0.3-0.4		0.3-0.4		
Mandrel Position behind Tangency, mm	3.0	0	0		
Bend Angle (account for springback), Degrees	93.0		91.0		
Pressure Die Clamp Force, kN (kip)	89 (18)	80 (20)	55.6 (12.5)		
Time for Bend, sec	8.0		8.0		
Start of Mandrel Retract, Degrees of Bend	85		85		
Mandrel Retract Displacement, mm	30		30		

The boost condition parameter was described in Section 1.2.1 and is calculated using equation (1). The bender control system prescribes pressure die displacement and bend die angular displacement to achieve the specified boost. Note that the boost levels for the DP600 tubes are 95% (LB) and 100% (MB), while the boost levels for the IF tubes are 95% (LB), 100% (MB) and 105% (HB). The bender did no have an adequate pressure die force and bend die torque capacity of achieve a boost of 105% for the high strength DP600 tubes.

Wiper rake angle is critical in preventing wrinkling and ensuring a smooth surface condition on the inside of the bend. The wiper position was adjusted manually until good bends were produced and the angle was then measured. Similarly, the mandrel position at the start of the bend was manually adjusted until good bends resulted. Incorrect mandrel position creates a hump and local thinned spot in the tube. Figure 44 is a schematic showing the rake angle, mandrel position and defects caused by incorrect wiper and mandrel settings.
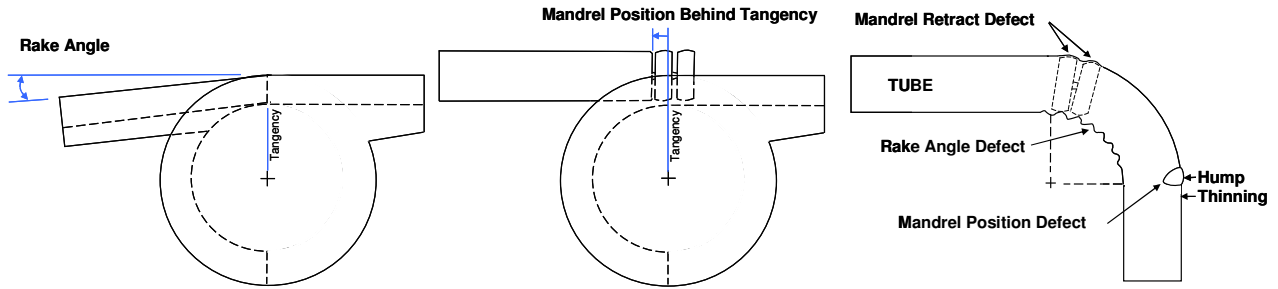
Figure 44: Rake angle and mandrel position behind tangency

The total bend angle was prescribed to account for springback of the tubes and was determined experimentally. After each bend experiment, the bent tubes were placed into a machined steel template die (Figure 45) to ensure that a 90° bend was achieved and that the sample would fit into the hydroforming die. Due to the higher strength of the DP600 tube, the bend angle was greater than that for the IF tube to compensate for the more severe springback. Similarly, the higher strength DP600 tube required a greater pressure die clamp force than the IF tubes to prevent opening of the pressure die which would result in wrinkles. At a given angle during bending, the mandrel is retracted from the inside of the tube so the mandrel assembly is not within the bend region. If the mandrel assembly is not retracted, the excessive tensile strain at the outside of the bend causes the tube to stretch around the balls, creating humps (Figure 44).

Figure 45: 90° bend template die

3.1.3 Bending Sequence

The following steps were followed for every tube that was bent for this study (including set-up tubes),

1. Using acetone, manually cleanse the pressure, clamp, wiper and bend die of any lubricant.
2. Prepare a tube by manually cleaning it with acetone.
3. Apply lubricant (Hydrodraw 615) to the outside of the tube where the wiper tip makes contact.
4. Slide the tube over the mandrel until the end of the tube engages the boost block. Orient the weld seam vertically on the neutral axis of the bend.
5. Turn on the laboratory hydraulics.
6. Using the LabVIEW program TubeBend v.1.93,
   a. Close the clamp die and apply the required pressure die clamp load.
   b. Pump lubricant (Hydrodraw 615) through the mandrel by pressing the lubricant pump switch.
   c. Begin bending sequence with the input parameters shown in Table 3.
   d. After bending, retract the mandrel fully.
   e. Open the clamp die, then the pressure die and advance the mandrel to the starting position for that sequence.
7. Turn off the laboratory hydraulics.
8. Remove tube.

3.1.4 Strain and Thickness Measurement of Pre-Bent Tubes

The 1016mm (40") DP600 and IF tubes were electrochemically etched with circular grids that were used to measure the strain imposed by bending and hydroforming. To prepare the tubes for etching, Lectroetch Formula 1 – All Purpose Cleaner was used prior to etching the grids using an in-house apparatus. The apparatus used Lectrotech Formula 112A etchant. After etching, a Lectrotech cleaner was used to clean excess etchant from the tube. The circle grids had a diameter of 2.5mm

The strain grid measurement system uses a micro-CCD video camera to capture still images of the deformed (post bending or hydroforming) circle grids. Due to deformation, the circle grids become ellipitical which allows one to measure the major and minor engineering strain. A custom PC-based program was used to manually fit an ellipse to the deformed circle grids and calculate the major and minor engineering strains. The accuracy of the strain grid measurement system is ±0.03 strain. A more detailed description of the etching and measurement system is provided by Lee (2001).

Thickness distributions were measured using a StressTel TM1-CD ultrasonic thickness gauge. A sample of known thickness DP600 and IF steel tube was used to calibrate the gauge. The ultrasonic thickness gauge is accurate to 0.001mm.
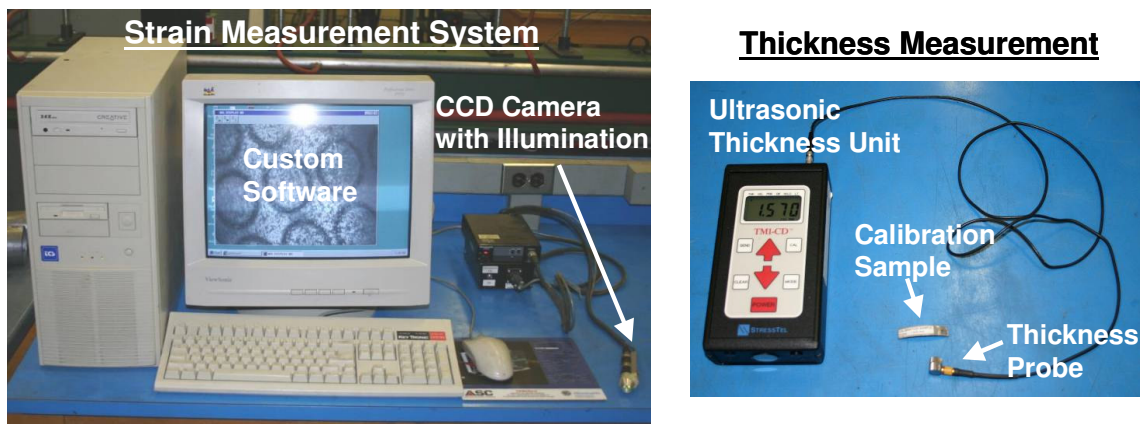
Figure 46: Strain and thickness measurement systems (Dyment, 2004)

The strain and thickness distributions along a bent tube were measured according the schematic shown in Figure 47. For an as-bent tube, the measurement angle start position (θ=0°) is at mandrel tangency and the position at the clamp-end tangency location is θ=90°. Measurement outside of the bend region, which corresponds to θ<0° and θ>90°, do not represent an actual angle; rather they are shown for completeness. At θ=45°, the strain and thickness is measured 360° around the circumference of the tube, starting at the weld seam ($\varnothing$=0°), as shown in Figure 47.
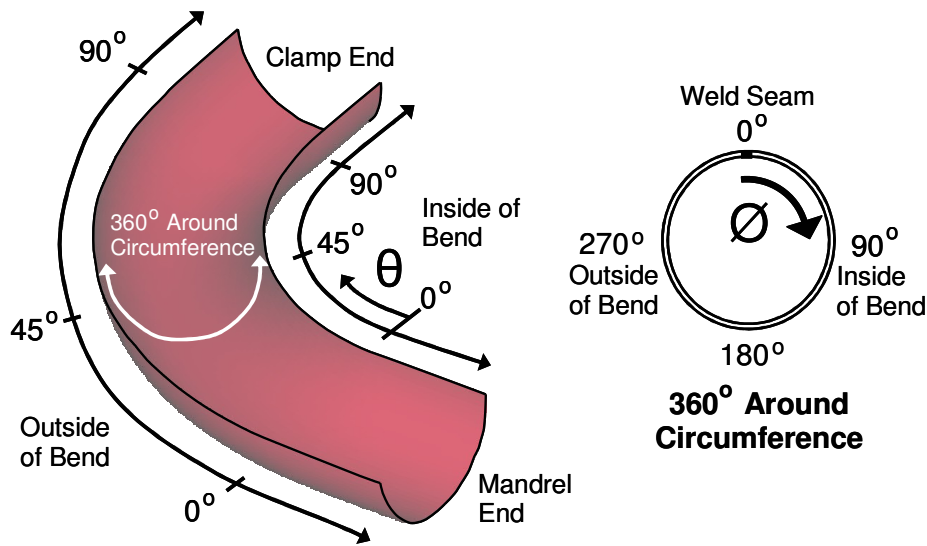
Figure 47: Strain and thickness measurement schematic for as-bent tubes

3.2 Tube Hydroforming Experiments

Two different hydroforming experiments were performed in this research, refered to as straight tube and pre-bend tube hydroforming experiments, respectively. Of key importance in this research is the effect of pre-bending on formability in hydroforming. Also of importance is the effect of end-feed (EF) during hydroforming. The hydroforming die design, controls system and experimental methods are described in the following sections.

3.2.1 Laboratory Hydroforming Press and End-Feed Actuators

All hydroforming experiments were performed at the University of Waterloo, using the 1,000Ton (2 million lbf) Macrodyne press shown in Figure 48. The maximum clamping load of the press is achieved by intensifying the laboratory hydraulic pressure to 69MPa (10ksi) inside the press cylinder. A detailed CAD drawing of the press can be found in Appendix B. To generate the internal pressure required for hydroforming, a high pressure intensifier is used to intensify the laboratory water to a maximum pressure of 414MPa (60ksi).

End-feed (EF) actuators are used to seal the tube and apply an axial EF load during hydroforming. The cylinders used for the EF actuators are Parker Series 3H large bore high pressure hydraulic cylinders that are manufactured by Parker Corporation. The EF actuators each have a capacity of 1,112kN (250kip) and are supplied by the 21MPa (3,000psi) laboratory hydraulics. The actuators are situated on an adjustable frame which allows them to be moved and adjusted manually for different die sets. Two mounting holes on each actuator are used to fasten them to the hydroforming dies with 2" UNF Grade 8 bolts. For all hydroforming tests, the EF rams are inserted into the ends of the tube until the shoulder engages the edge of the tube (Figure 48). A polymeric o-ring is used to created a seal between the inside diameter of the tube and the EF ram. The leading edge of the o-ring expands radially upon application of pressure from the inside of the tube. A teflon ring is used as a back up seal by expanding radially when compressed by the o-ring.
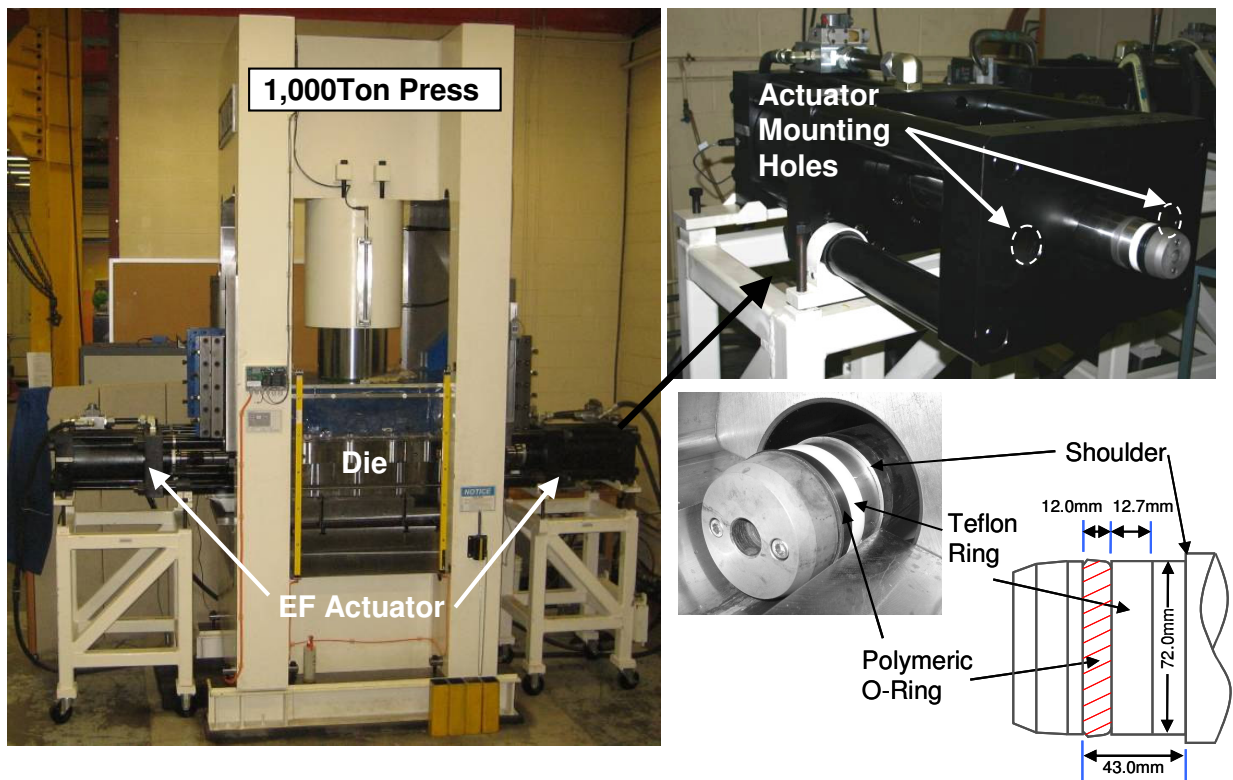
Figure 48: University of Waterloo laboratory hydroforming press and end-feed actuators

3.2.2 Hydroforming Controls System

The controls system and instrumentation used for the hydroforming press was developed in-house at the University of Waterloo. A PC-based LabView interface is used to control the hydroforming process and is coupled to four PID servo-hydraulic controllers via an analog/digital data acquisition card. The details of the hydroforming actuators and sensors are shown in Table 4 and the laboratory controls cabinet and sensor schematic are shown in Figure 49. All four processes (Table 4) are supplied by the 21MPa (3,000psi) laboratory hydraulics. The press clamp vertical displacement is controlled with an LVDT displacement transducer. During an experiment, the press clamp closes and the pressure inside of the cylinder is increased to 69MPa (10,000psi) with a Simplex PI2 four-way hydraulic intensifier that is monitored with a pressure transducer. A single pressure transducer is used to control and monitor the water pressure during hydroforming. The EF actuators are under displacement-control using an externally mounted string potentiometer. The load on the actuator is monitored using an externally mounted strain gauge bridge circuit. In addition to the four main processes controlled via the LabVIEW interface, a series of pneumatic valves are also controlled at various stages of the initial filling of the tube with water.

Table 4: Hydroforming process sensors and actuator details

Process	PID Controller	Actuator Control Mode	Sensor (Control)	Sensor (Monitor)
Press Clamp	MTS 406	Displacement	LVDT	Pressure Transducer
Pressure Intensifier	MTS 406	Pressure	Pressure Transducer	Pressure Transducer
End-Feed Actuator #1	MTS FlexTest SE	Displacement	String Potentiometer	Strain Gauge (Measures End-Feed Load)
End-Feed Actuator #2	MTS FlexTest SE	Displacement	String Potentiometer	Strain Gauge Measures End-Feed Load)
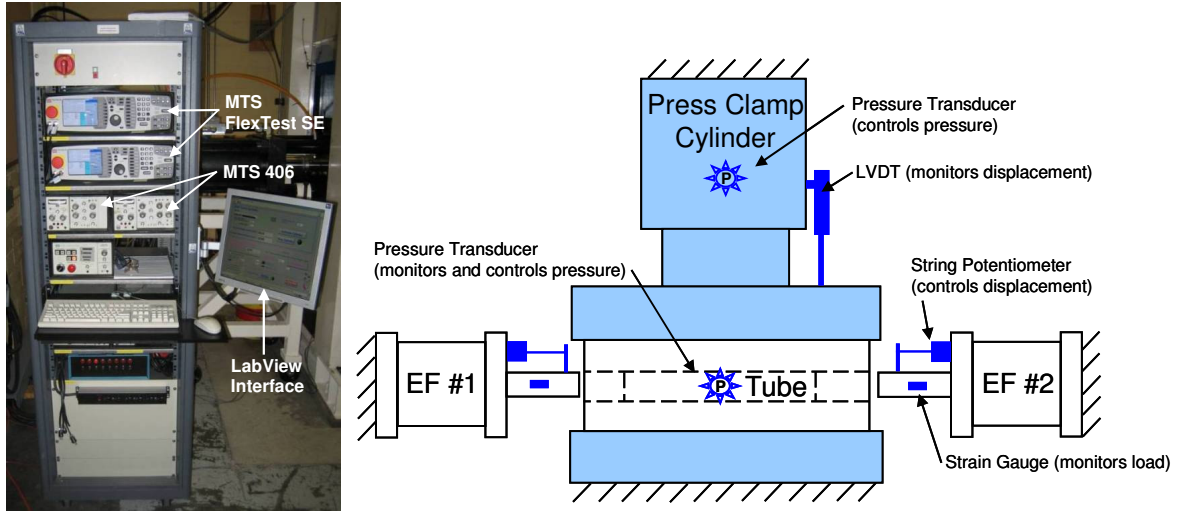
Figure 49: Laboratory controls cabinet and sensor schematic

3.2.3 End-Feed Loading Schedule

Straight and pre-bend tube hydroforming was conducted with four different levels of end-feed (EF) to observe the effect of EF on the formability of the tubes during hydroforming. The EF load schedule was determined through a numerical investigation of the hydroforming process before the die and press were available. The numerical investigation resulted in four different levels of EF for the straight and pre-bend experiments. The four levels of corresponding EF, and the test cases which they were applied to, are shown in Table 5. Table 5 also shows the EF stress ratio for each material and EF combination. The stress ratio is defined here as the ratio of the axial stress on the tube due to EF (σ_{axial}) to the yield strength of the material (σ_{yield}) which was presented in Section 2.1.2.

Table 5: DP600 and IF hydroforming end-feed test cases

Material	Hydroforming Case	Zero End-Feed	67kN (15kip) End-Feed	133kN (30kip) End-Feed	200kN (45kip) End-Feed
DP600	EF Stress Ratio ($\sigma_{axial}/\sigma_{yield}$)	NA	0.09	0.19	0.28
	Straight	Yes	Yes	Yes	Yes
	Pre-Bend	Yes	Yes	Yes	No
IF	EF Stress Ratio ($\sigma_{axial}/\sigma_{yield}$)	NA	0.18	0.35	0.53
	Straight	Yes	No	No	No
	Pre-Bend	Yes	Yes	No	No

Figure 50 shows the EF load *versus* internal pressure curves that were used as input for the hydroforming tests. In the zero EF case, the EF rams remain stationary during internal pressurization of the tube and the EF load applied to each ram is just enough to counteract the internal pressure of the water on the face of the ram. Due to corner-fill expansion (CFE), the tubes draw-in off the stationary rams during hydroforming. To measure the EF displacement for the zero EF case, the change in length (shorter) of the tube was measured manually after the die was opened.

For the EF cases that are greater than zero, load-control EF was used. For a given internal pressure, the required EF load is applied to the rams according to the curves in Figure 50. The control algorithm proceeds in steps and when the prescribed internal pressure and EF load are satisfied by the system (for a given step), the algorithm proceeds to the next step (next combination of internal pressure and EF load). For the DP600 67kN, 133kN and 200kN EF cases, the load curves shown in Figure 50 are the same as the zero EF case up to 35MPa (5,000psi). 35MPa is considered the "pre-pressurization" pressure which is used to support the thin-walled tube and prevent buckling when the additional EF load is applied. The "pre-pressurization" pressure is just below the pressure at which the tube yields. From 35MPa to 38MPa (5,500psi), the additional 67kN, 113kN or 200kN of EF load is applied. For the single EF case applied to the pre-bent IF tubes (Table 5), the EF load is applied between 20MPa (3,000psi) and 23MPa (3,500psi). In this case the "pre-pressurization" pressure is 20MPa because the low strength IF tube yields at a lower pressure than the DP600 tube. For all EF cases, the internal pressure was increased until failure (burst) of the tube occurred. A series of burst tests is repeated to establish the average burst pressure of the tube. Interrupted tests were then performed up to 70% and 90% of the average burst pressures.
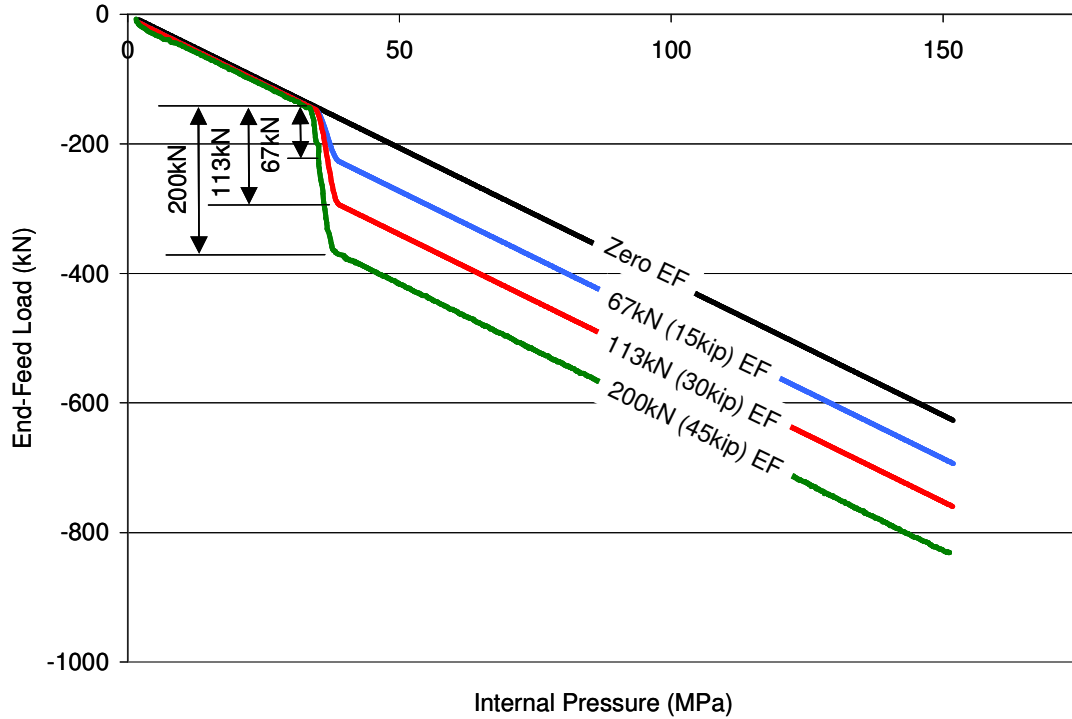
Figure 50: End-feed load *versus* internal pressure schedule

3.2.4 Straight Tube Hydroforming

An existing hydroforming die was used for the straight tube hydroforming experiments. The major dimensions and cross-sections of the die are shown in the solid model drawing of the lower die, given in Figure 52. At either end of the die, a 241.3mm (9.5") straight section with a circular cross-section is followed by a 50.8mm (2") transition cross-section which changes from circular to square, as shown in Figure 52. The square cross-section has a total length of 431mm (17"). All cross-sections have an outside dimension of 76.7mm (3.02") which allows a total diametrical clearance of 0.5mm (0.02") between the OD of the tube and the die wall. The die is self aligning through a series of wear plates (alignment faces) that mate during die closure. For the tests, a 1016mm (40") straight tube is cut and placed in the center of the die.
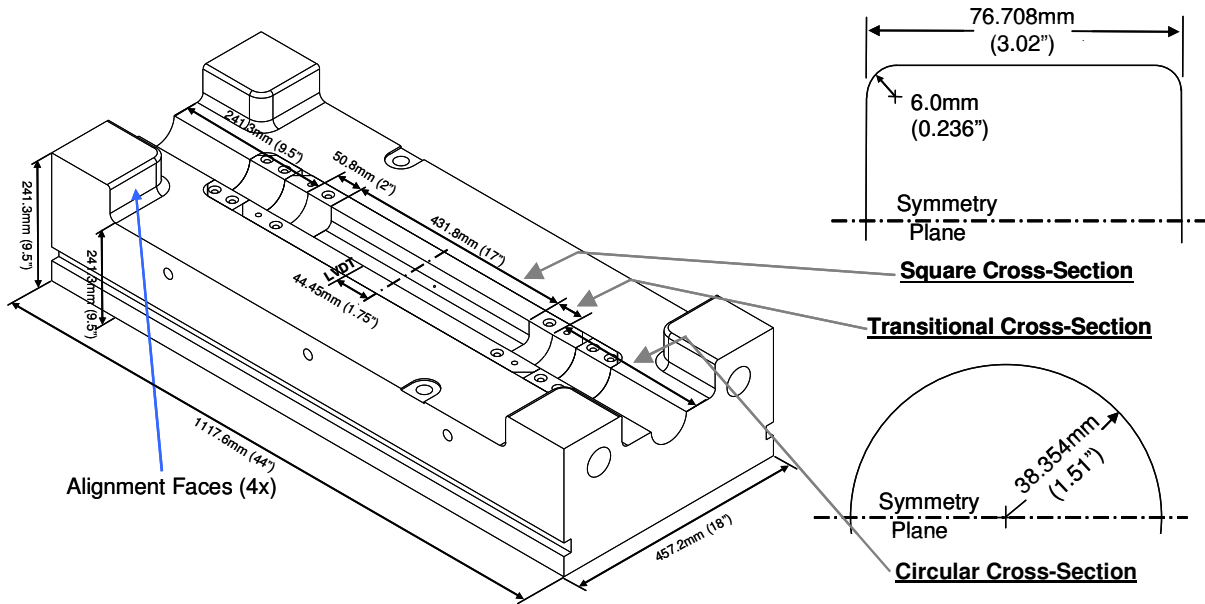
Figure 51: Straight tube hydroforming die

3.2.5 Pre-Bend Tube Hydroforming

As part of this research, a pre-bend hydroforming die was designed and fabricated. SolidWorks 2004 was used to create the three-dimensional solid model of the two-piece die. The detailed CAD drawings used to machine the dies can be found in Appendix B while the solid model of the lower die half is shown in Figure 52. At either end of the die, a 203.2mm (8") straight section exists which contains circular, transition and square cross-sections. The cross-sections have an outside dimension of 76.7mm (3.02") which allows a total clearance of 0.5mm (0.02") as for the straight tube die. After the straight section, the bent section begins which has a center line radius (CLR) of 152.4mm (6") and a center line arc length of 239.39mm (9.42"). The die is self aligning through a series of alignment faces that mate during die closure. For the tests, the pre-bent tube is cut so that the edge of the tube is flush with the ends of the die.
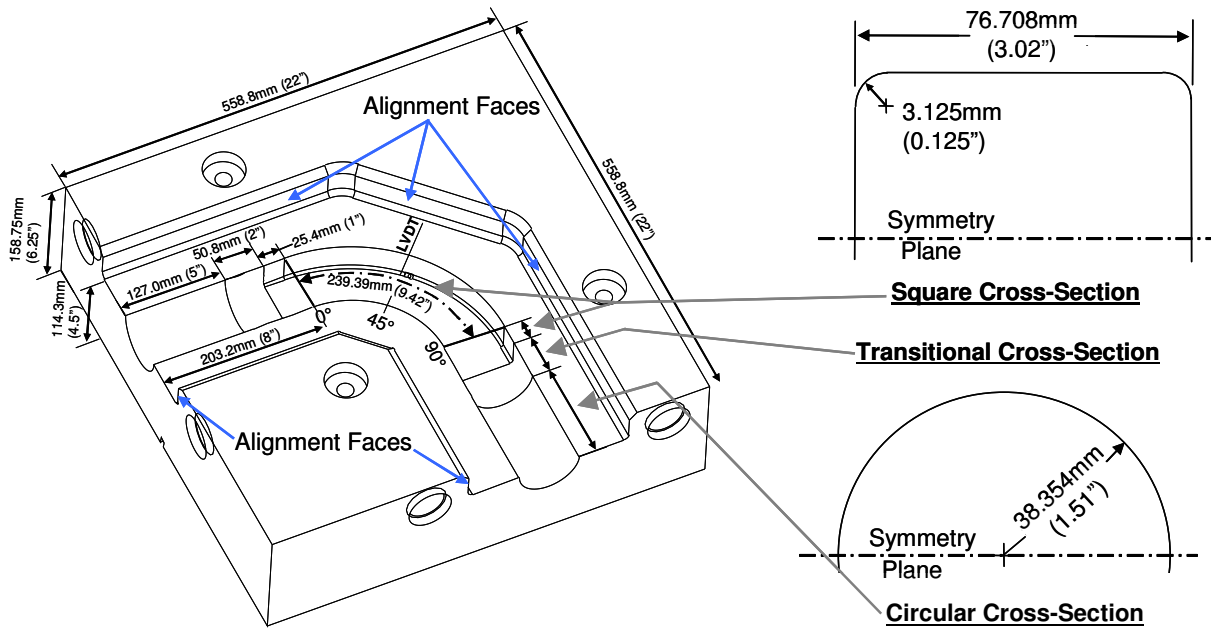
Figure 52: Pre-bend hydroforming die

3.2.6 Corner-Fill Expansion

To record the expansion and formability of the tube during hydroforming, the corner-fill expansion (CFE) is measured through a series of LVDT displacement transducers that are imbedded into the dies, as shown in the solid models in Figure 53. CFE is measured as the distance that the tube expands (δ) from a perfectly circular 76.2mm (3") OD tube. As the tube expands during hydroforming, δ increases from zero. It should be noted, that CFE can be negative in some cases if the tube has ovalized during pre-bending or shifts during hydroforming. Due to symmetry, the straight die only requires one LVDT, while the pre-bend die requires two. In the case of the pre-bend die, CFE is measured at the outside and inside of the bend regions because pre-bending affects the amount of expansion in these two regions.
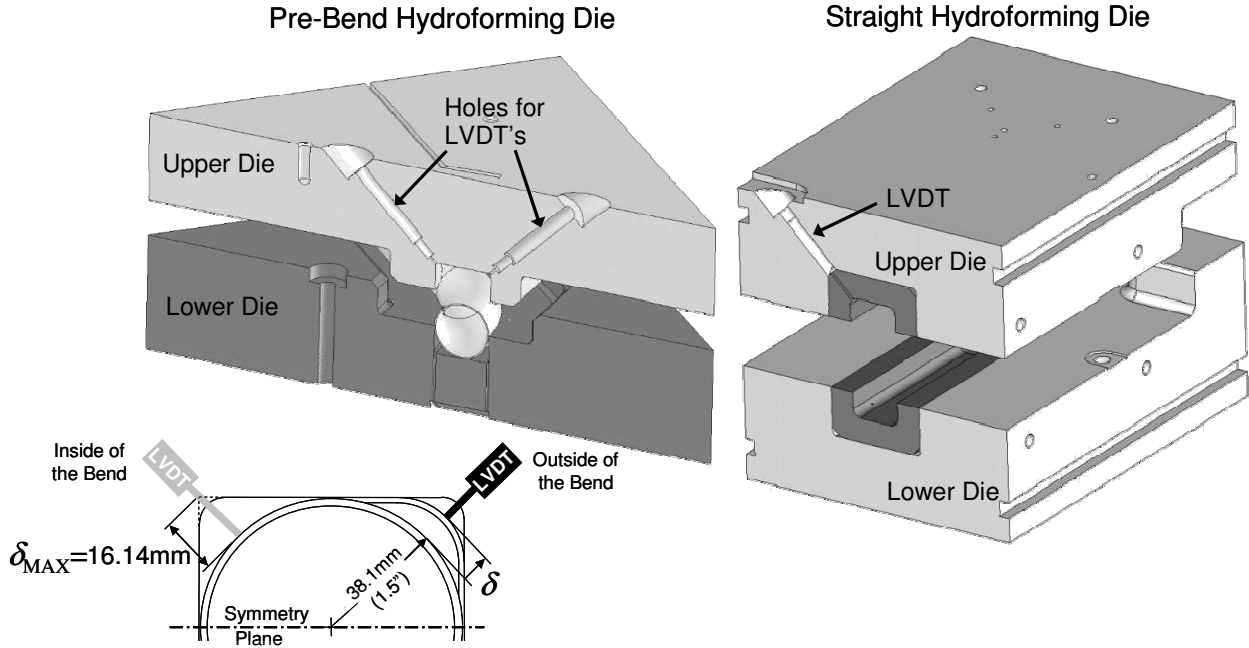
Figure 53: Sections through hydroforming dies showing LVDT locations

Figure 53 shows δ_{MAX}, which is the distance from a circular tube to the corner of a square cross-section. This value is used to express CFE in terms of the percent of expansion to a perfect square and is calculated as follows,

$$\%CFE = \frac{\delta}{\delta_{MAX}} \times 100\% = \frac{\delta}{16.14mm} \times 100\% \tag{6}$$

Due to the symmetry of the straight die, equation (6) can be applied, but due to the non-symmetrical CFE at the inside and outside of the bend regions within the pre-bend die, the overall %CFE is the average of the inside and outside %CFE, and is calculated as follows,

$$Average\ \%CFE = \frac{\%CFE_{inside} + \%CFE_{outside}}{2} \tag{7}$$

Given the fillet radius of the square cross-section for the straight and pre-bend dies (Figure 51 and Figure 52), the maximum achievable %CFE is 84.3% (δ=13.66mm) and 92.0% (δ=14.85mm), respectively.

3.2.7 Strain and Thickness Measurement of Hydroformed Tubes

For straight tube hydroforming, the tubes were electrochemically etched using the same procedure described in Section 3.1.4. After hydroforming, the straight tubes were cut in half and a stencil is used to mark $\varnothing=5°$ increments about the cross-section of the tube. The increments start at the neutral axis ($\varnothing=0°$) and continue to $\varnothing=180°$ (Figure 54). For the pre-bent hydroformed tubes, the measurement convention is the same as shown for the as-bent tubes (360° around circumference) in Section 3.1.4. A stencil is used to mark $\varnothing=10°$ increments which start at the neutral axis ($\varnothing=0°$) and continued to $\varnothing=360°$, as shown in Figure 54.
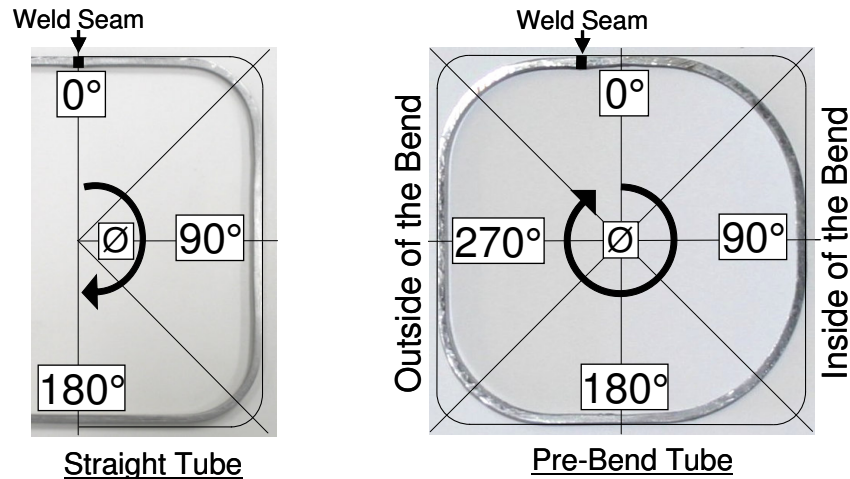
Figure 54: Straight and pre-bent tube strain and thickness measurements

3.2.8 Hydroforming Sequence

The following steps were followed for all straight and pre-bend hydroforming experiments. A more detailed description of the entire hydroforming test procedure can be found in Appendix C,

1. Prepare a tube by cleaning it with acetone and placing it into the die.
2. LabView: Close the press clamp/die.
3. LabView: Advance each EF actuator ram into the tube until the shoulder engages the edge of the tube.

4. LabView: Open and close valves to prepare for filling the tube with water (automated).

5. Create a vacuum inside of the tube with the vacuum pump.

6. LabView: Open and close valves to fill the tube with water.

7. Manually intensify the pressure inside of the press clamp cylinder to reach a clamping force of 1,000Ton (1Mlbf)

8. LabView: Set the test variables and load the appropriate EF *versus* internal pressure curve file and begin the hydroforming test.

9. LabView: Relieve the hydroforming pressure from the system and retract the EF actuators.

10. LabView: Open the press and remove the tube.

CHAPTER 4

EXPERIMENTAL RESULTS: TUBE BENDING

The results of the tube bending experiments are presented in this chapter. The process variable data is presented and summarized. Also, the strain and thickness after pre-bending are measured and summarized.

4.1 Process Variables

The bending process variables that are considered in this section are the pressure die boost load, mandrel load and torque. The distributions of these variables are plotted for the different boost cases and for the two materials (DP600 and IF). A summary presents the effect of boost level and material properties (DP600 and IF) on the pre-bending process variables

4.1.1 Process Data

Although the bending parameters shown in Table 3 were applied to the bending study, the measured values (after bending) for boost and bend angle are slightly different because of the bender control system response. The results are an average from the entire bending study for both materials and are shown in Table 6. The results for the individual experiments can be found in the Appendix D.

Table 6: Average process data

Material	Boost	Number of Tubes Bent	Avg. Measured Boost (%)	Avg. Bend Angle (°)	Avg. Clamp Slip (mm)	Avg. Actual Boost (%)
DP600	LB	12	95.9	93.0	12.9	95.8
	MB	36	99.5	93.0	7.0	99.5
IF	LB	12	95.4	90.8	9.8	95.4
	MB	36	100.3	90.9	2.1	100.3
	HB	12	104.4	90.8	0.5	104.4

Dyment (2004) suggested that the actual boost achieved during bending is a function of the slip that occurs at the bend die, not just the pressure and bend die displacements. The boost calculated strictly using the pressure and bend die displacements is represented by the average measured boost in Table 6. Slip at the bend die occurs due to insufficient clamp die pressure and is illustrated in Figure 55. During the bending experiments, clamp die slip was measured manually after every bend. Slip did not occur relative to the pressure die because the boost block was used for all bends. For the equivalent boost conditions (LB and MB), the amount of slip was greater for DP600 than IF and is a result of the higher strength of the DP600, which requires higher clamp loads during tube bending.
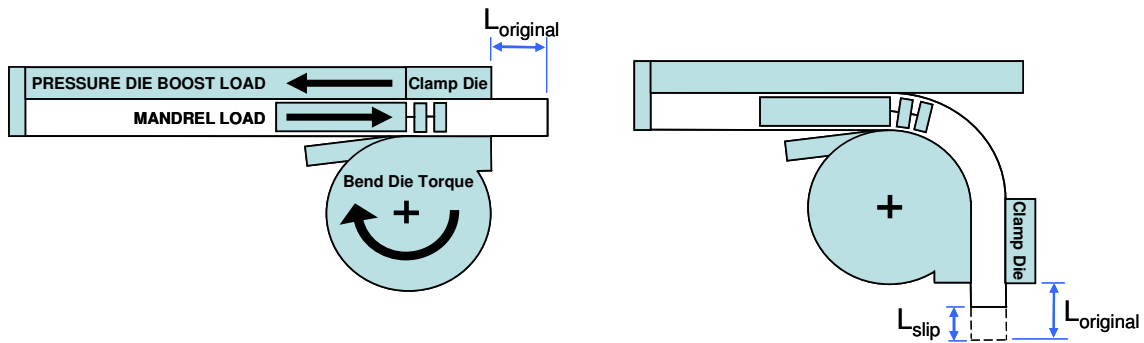
Figure 55: Tube bending slip and process variable schematic

Given the clamp slip, the actual boost was calculated as follows (Dyment, 2004),

$$\% Boost_{Actual} = \frac{Pressure\,Die\,Displacement - L_{slip}}{Arc\,Length\,Swept\,by\,CLR} \times 100\%$$

$$= \% Boost_{Measured} - \frac{L_{slip}}{Arc\,Length\,Swept\,by\,CLR} \times 100\%$$

$$(8)$$

The actual boost (*%Boost$_{Actual}$*) is a function of the measured boost (*%Boost$_{Measured}$*), the *Arc Length Swept by CLR* (based on bend angle) and the clamp slip (L$_{slip}$). These variables are

presented in Table 6. Only in the case of the DP600 LB bends, where the slip was greatest, the actual boost was 0.1% less than the measured boost.

During bending, the three main tools that are controlled and monitored are the pressure, mandrel and bend dies. These tools are controlled through displacement sensors and monitored/measured by load cells (mandrel and bend die) and a pressure sensor (pressure die) as per the schematic shown in Figure 42 c). The pressure die boost load, mandrel load and bend die torque are shown in Figure 55 with the arrow pointing in the positive measuring direction (reaction loads on tools). These bending process variables are used to evaluate their effect, as well as the effect of tube materials, on the pre-bending process and to validate the numerical models of pre-bending.

Figure 56 shows the pressure die boost load, mandrel load and bend die torque for all of the DP600 MB bends performed. The repeatability of the curves is typical for all other bending cases. In order to facilitate comparison of process data from the two different materials and their respective boost cases, an average curve is constructed from the process variables corresponding to the tubes that were used for subsequent hydroforming (not all of the bent tubes shown in column three of Table 6. The average curves for the DP600 MB bends are shown as the data points in Figure 56. The vertical dashed lines indicate the boundaries where the bending process is considered to be at steady-state (i.e. constant tool velocity). During ramp up, the tools are accelerated to their steady-state velocity and decelerated during ramp down. The proceeding sections provide a more detailed analysis of the three main bending process variables. For each material and boost level, the average pressure die boost load, average mandrel load and average bend die torque curves are created from the set of raw bending data (constructed as those in Figure 56).
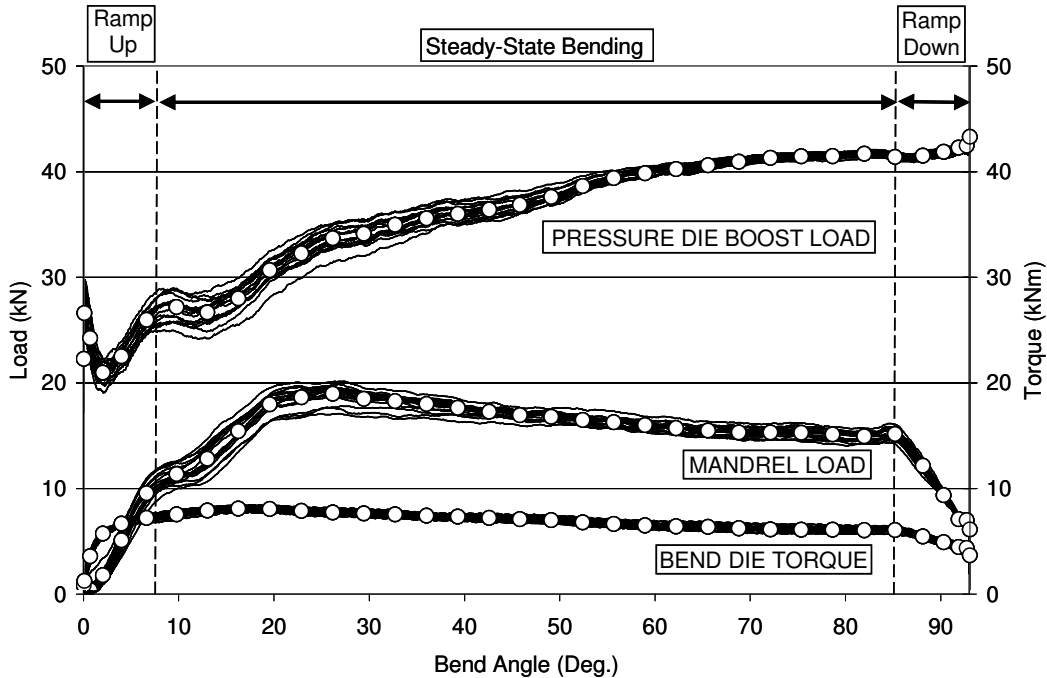
Figure 56: Process variable data for DP600 MB bends

4.1.2 Process Variable: Pressure Die Boost Load

During bending, an axial displacement is prescribed in the longitudinal direction of the tube via the pressure die. The force required to meet the prescribed displacement is applied by the pressure die hydraulic cylinder which has a maximum capacity of 43kN. The pressure die pushes the tube into the bend region via the frictional contact between the tube and die and from direct contact through the boost block assembly. Figure 57 shows the average pressure die boost loads for the DP600 and IF bends. Appendix D shows the measured results for the DP600 and IF tubes separately. To measure the frictional losses of the pre-bending process, a "calibration test" was conducted without a tube. The resultant calibration pressure die boost load is shown by the dashed line.
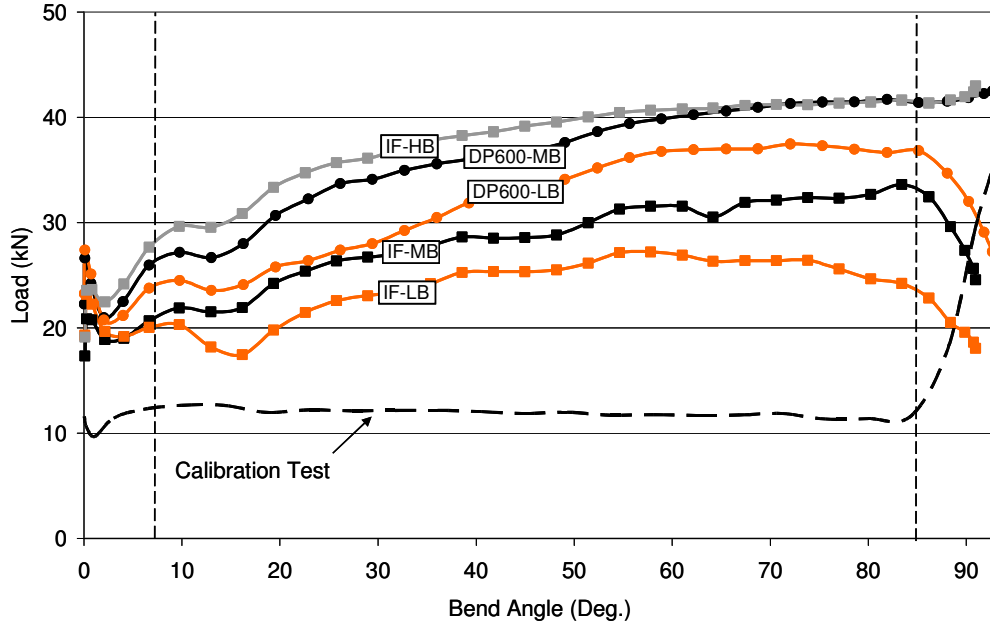
Figure 57: Average DP600 and IF pre-bending pressure die boost loads

For the DP600 tubes, the boost force for the MB case is greater than the LB case because the tube is being pushed more rapidly into the bend region (Section 1.2.1). For the MB case, the maximum capacity of the pressure die boost cylinder was reached at the end of the bend. For this reason, boost levels greater than 100% were not tested for DP600. The trend indicates an increase in the boost load as the bend progresses. The same trends for increasing boost levels are observed for the IF bends. Again, the pressure die boost cylinder was at maximum capacity for the HB bending case. Comparing the two materials, the higher strength DP600 tubes required greater pressure die boost loads than the IF tubes. It should also be noted that the as-received DP600 tubes are approximately 6% thicker than the IF tubes. The "calibration test" curve suggests that pressure die displacement requires approximately 11.8kN of boost load to overcome internal friction.

4.1.3 Process Variable: Mandrel Load

The mandrel is used to internally support the tube during bending. It is lubricated to reduce frictional drag between the tube and mandrel. A load cell was used to measure the drag

75

load on the mandrel during bending. Figure 58 shows the results for the two materials, while Appendix D shows the measured results for the DP600 and IF tubes separately.
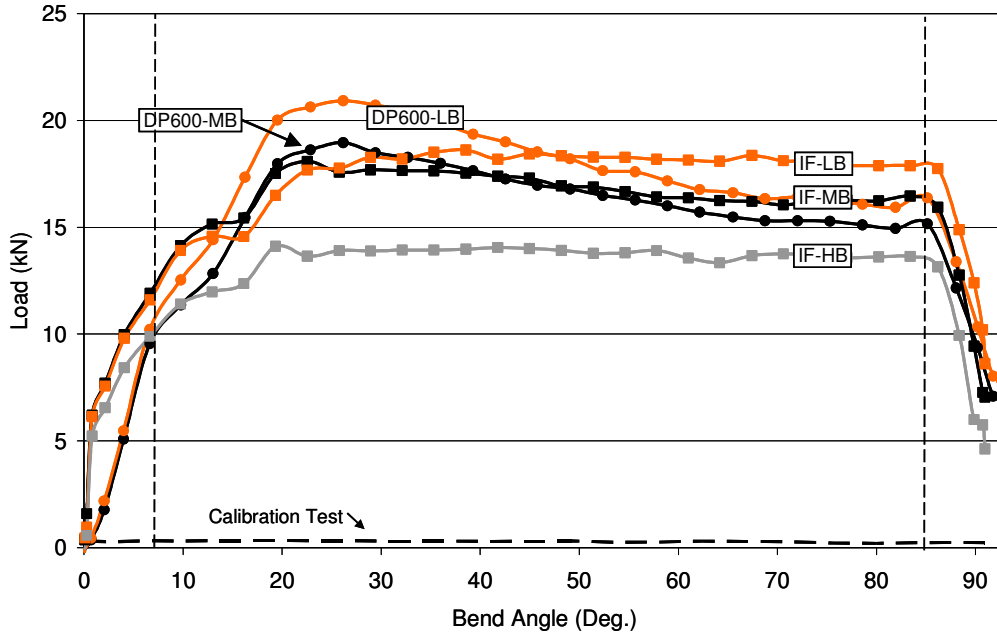
Figure 58: Average DP600 and IF pre-bending mandrel loads

For both the DP600 and IF tubes, an increase in boost results in a decrease in mandrel load. The trends indicate a peak in mandrel load for the DP600 and a relatively flat steady-state mandrel load for the IF tubes. An explanation for the difference in curve shape between the DP600 and IF tubes may be a result in the difference in radial clearance between the mandrel and tube. The DP600 tubes have a slightly greater radial clearance than the IF tubes, which may affect the lubrication condition during bending. Also, the frictional response between the mandrel and two different strength steels could affect the mandrel load. The "calibration test" mandrel load is insignificant.

4.1.4 Process Variable: Bend Die Torque

The bend die torque required to bend a tube was measured and is shown in Figure 59. Appendix D shows the measured results for the DP600 and IF tubes separately.

76
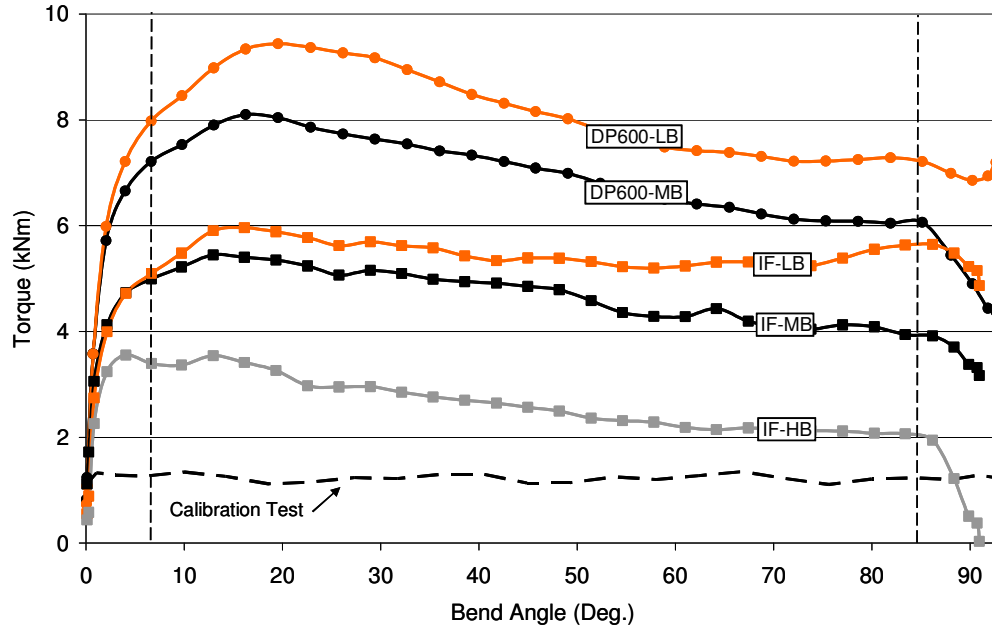
Figure 59: Average DP600 and IF pre-bending bend die torque

For both materials, the bend die torque reduces for increasing levels of boost. This trend is due to the additional axial force on the tube exerted by the pressure die for increasing boost levels. As the pressure die pushes more material into the bend region (at higher boost), some of the bend die torque is relieved. Although the thickness of the IF tube is slightly less, there is a large difference in bend die torque between the two steels due to the greater strength of the DP600 tube, which reflects the strength ratio of 1.67. The "calibration test" experiment shows that approximately 1.2kNm of torque is required to overcome the friction encountered during bend die rotation.

4.1.5 Summary

Table 6 summarizes the average steady-state values of pressure die boost load, mandrel load and bend die torque. The average steady-state values are calculated as the average of the data points as shown in Figure 56. In addition to the average steady-state values, the maximum value within the steady-state region is shown in square brackets. Figure 60 presents the average steady-state values (from Table 7) in a bar chart to illustrate the trends in the results.

Table 7: Average measured steady-state process variable summary

Material	Boost	Average Steady-State Pressure Die Boost Load (kN), [max]	Average Steady-State Mandrel Load (kN), [max]	Average Steady-State Bend Die Torque (kNm), [max]
DP600	LB	31.7 [37.5]	17.5 [20.9]	8.2 [9.4]
	MB	35.9 [41.7]	16.1 [19.0]	7.1 [8.1]
IF	LB	23.9 [27.2]	17.4 [18.6]	5.5 [6.0]
	MB	28.0 [33.6]	16.5 [18.1]	4.8 [5.4]
	HB	37.4 [41.6]	13.4 [14.1]	2.7 [3.5]
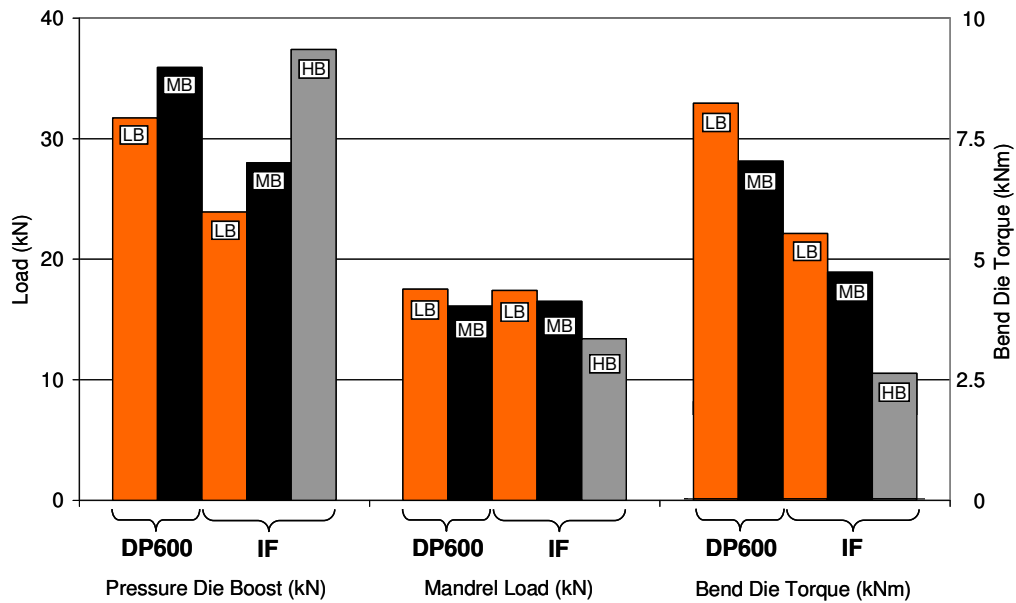
Figure 60: Average bending process variable bar graph

The most dramatic change in process variable occurs in the pressure die boost load. For DP600, a change from LB to MB required a pressure die boost load increase of 47%, while a 58% increase in boost force was required between the IF LB and HB bends. The mandrel loads show a decreasing trend for increased boost levels, with an 8% reduction for DP600 (LB to MB) and 23% for IF (LB to HB). Bend die torque is influenced by the amount of boost load applied by the pressure die, therefore increasing levels of boost reduce the amount of bend die torque required. For DP600 (LB to MB), the bend die torque was reduced by 15% while for IF (LB to HB), a reduction of 53% was measured.

4.2 Strain and Thickness Measurements

The strain and thickness distributions for the different boost cases and materials (DP600 and IF) are presented in this section. A summary presents the effect of boost level and material properties (DP600 and IF) on the strain and thickness distributions of the tubes.

4.2.1 Interpretation of Strain and Thickness Measurement

To evaluate the amount of deformation a tube undergoes during bending, the strain and thickness distributions were analyzed. Quantifying the effect of bending boost on the strain and thickness after pre-bending is the motivation behind this part of the work. Also, these measurements provide validation data for the numerical models.

As described in Section 3.1.4, strain grid measurement along the outside of the bend, inside of the bend and around the circumference was performed. Figure 61 shows the measured major and minor strain data for three different DP600 (MB) tubes.
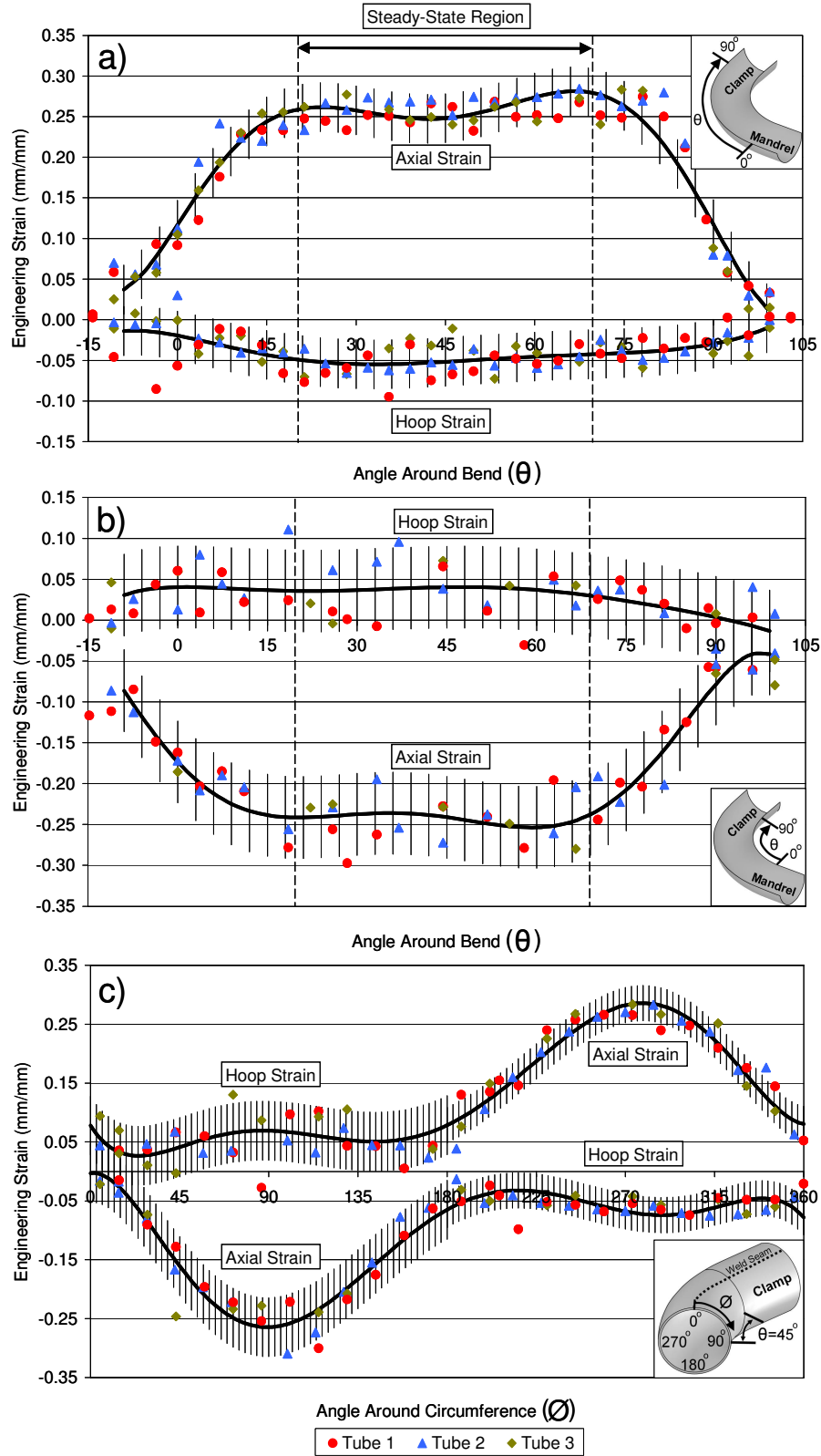
Figure 61: Strain distribution along a) outside of the bend b) inside of the bend and c) around the circumference for DP600 (MB)

Figure 61 illustrates the scatter of the strain grid measurement method, which is approximately ±0.03 strain at the outside of the bend and ±0.05 strain for the inside of the bend. The scatter was quantified in Figure 61 by inspection of the data points relative to the error bars (some points lay outside the error bars). A similar level of scatter was reported by Dyment (2004) for pre-bent AKDQ steel tubes. Note that the strains are plotted with respect to bend angle θ or circumferential angle ∅, as shown in the inset in Figure 61. The greater scatter for the inside of the bend distribution is attributed to poor circle grid quality caused by rubbing of the surface against the wiper die during bending. Due to the poor quality circle grids at the inside of the bend, the circumferential strain measurements have a scatter of ±0.05 for 0°<∅<180° and ±0.03 for 180°<∅<360°. The strain distribution scatter shown in Figure 61, was observed for both materials and all boost cases.

To assess the effect of bending boost on the strain distribution, a single average curve was constructed for each boost case for comparison purposes. For DP600, the measured results for three tubes (for each boost case) were averaged, while for the IF material only two tubes were measured (for each boost case) because the circle grid quality was better than that of the DP600 tubes. Using Figure 61 as an example, the measured results from the three different tubes were individually curve-fit with a 6th order polynomial (not shown). The three different polynomial curves were than averaged (polynomial constants) to produce a single 6th order polynomial curve which is shown as the solid black curve in each graph in Figure 61. Due to the good accuracy of the ultrasonic thickness measurement system, only one tube was measured for each of the DP600 and IF boost cases to determine the thickness distribution. As will be seen in the following, thickness distributions provide a more reliable method of evaluating the effect of bending boost.

At the outside of the bend region, the major (tensile) strain acts along the axial direction and is the sum of the membrane and bending strains. The minor (compressive) strain is aligned with the hoop direction of the tube and is a consequence of Poisson's effect and tube ovalization. For the inside of the bend, the tube experiences minor (compressive) strain in the longitudinal direction of the tube which is also the sum of the membrane and bending strain. The major (tensile) strain occurs in the hoop direction of the. Thinning occurs at the outside of

the bend due to the major tensile strain, while thickening occurs at the inside of the bend. The strain measured around the circumference of the tube at $\theta=45°$ shows a sinusoidal distribution that can be attributed to the bending component of axial strain. At $\theta=65°$, a distinct peak in strain is present for both boost conditions.

To quantify the effect of bending boost on strain and thickness at the outside and inside of the bend, the average strain (ε_{avg}) and thickness (t_{avg}) are calculated from the average curves. The average is taken from the data points within the steady-state region (where strains and thicknesses are approximately constant) which is $20°<\theta<70°$ for all bending cases. The results for each alloy are presented in the following sections.

4.2.2 DP600 Results

The strain and thickness distributions for the DP600 LB and MB boost cases are shown in Figure 62 and Figure 63, respectively. The average steady-state strain (ε_{avg}) and thickness (t_{avg}) are presented in Section 4.2.4. This section presents the general trends observed for the LB and MB strain and thickness distributions.
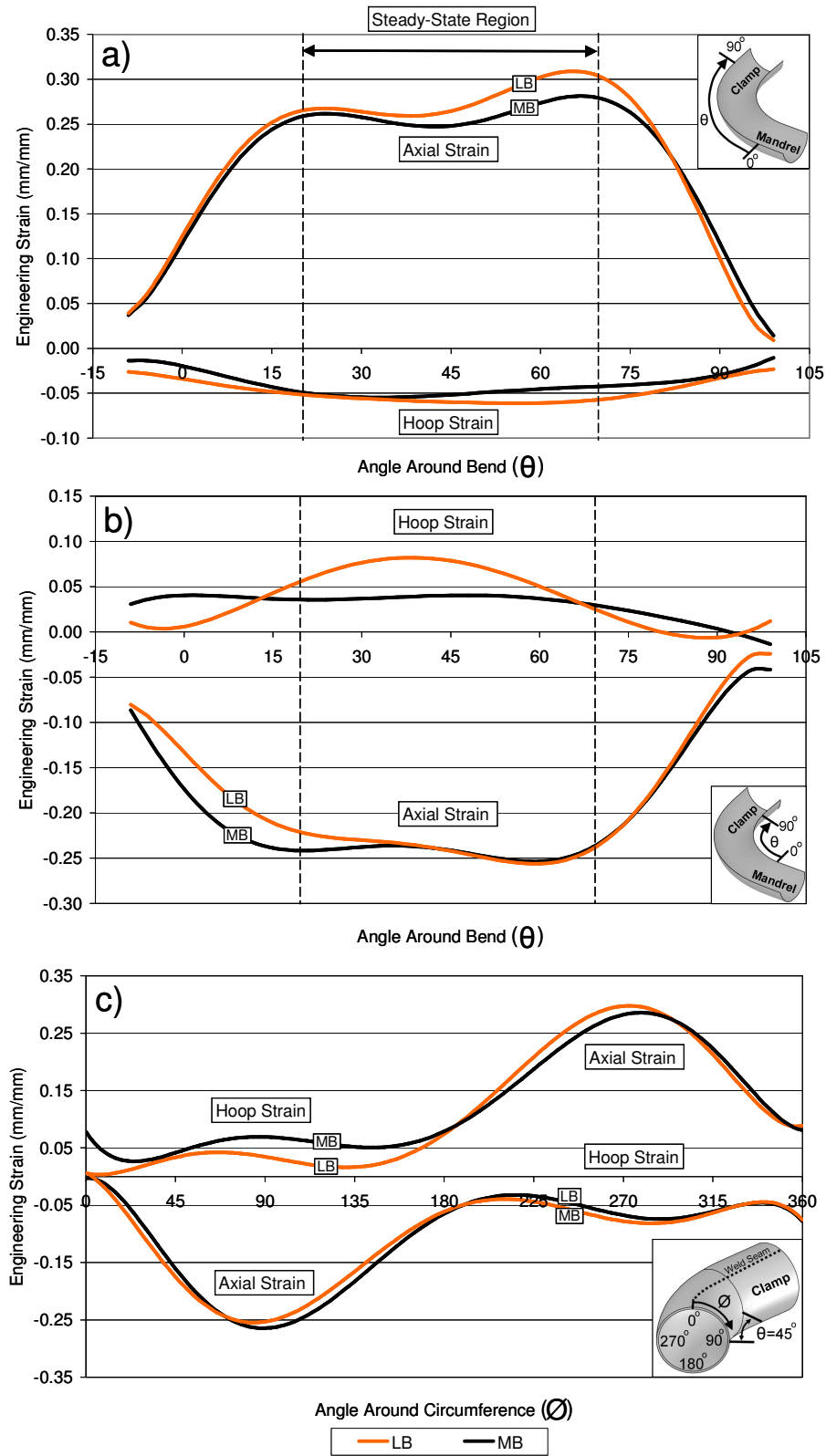
Figure 62: Measured strain for the DP600 tube a) outside of the bend b) inside of the bend c) around the circumference strain distribution for all boost cases

83

For the outside of the bend within the steady-state region (Figure 62a), the LB case has higher major strains than the MB case. During pre-bending, the longitudinal compressive strain increases as the boost level increases. This reduces the major tensile strain component (in longitudinal direction of the tube) at the outside of the bend. The minor strain is unaffected by boost within the steady-state region and is lower in magnitude than the major strains. At θ=65°, a distinct peak in the major strain distribution is present for both boost cases.

Due to poor circle grid quality, no boost effects could be discerned in the minor strains (compressive) along the inside of the bend (Figure 62b). Theoretically, higher boost will increase the minor compressive strain due to the additional compressive strain component along the longitudinal direction of the tube.

Around the circumference of the bend (Figure 62c), there is little discernable effect of boost on the major and minor strain distributions. The distributions in the range 0°<Ø<180° are not very reliable since the grids run against the wiper die. For 180°<Ø<360°, the major strain is generally less for the MB case, which expected.
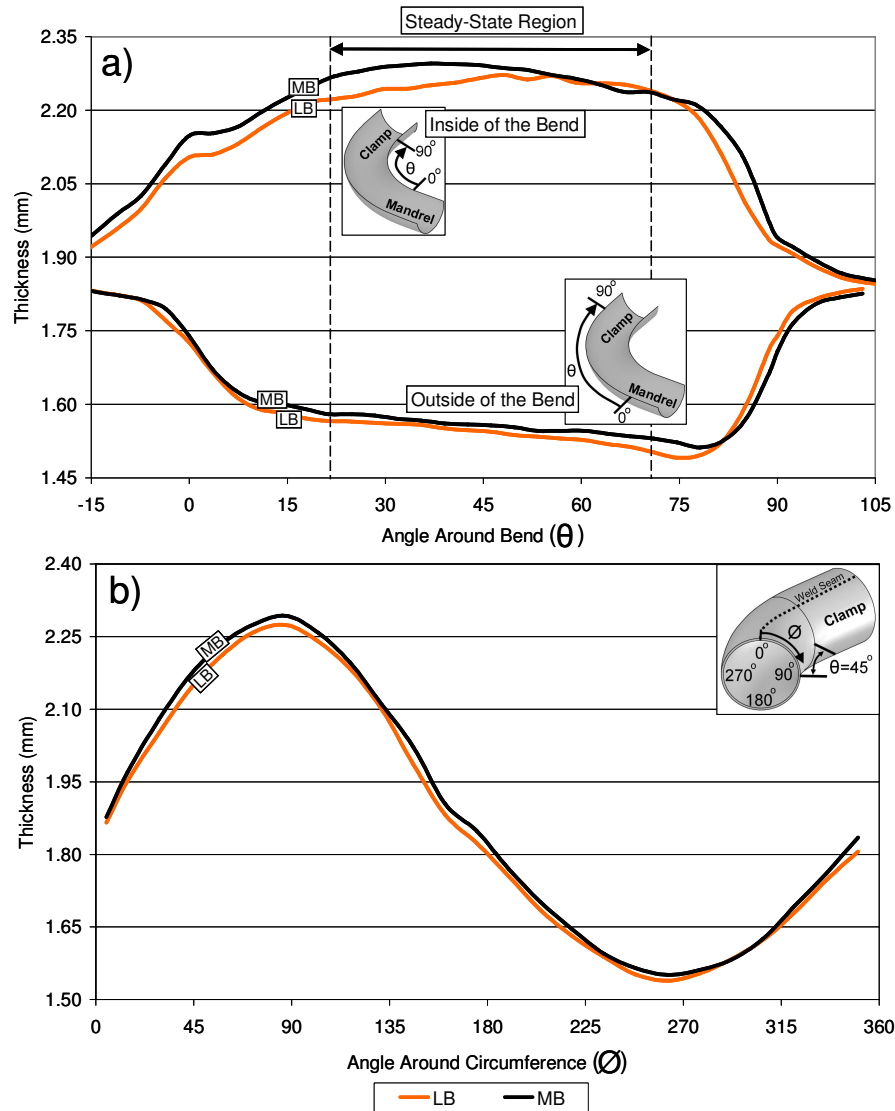
Figure 63: Measured thickness for the DP600 tube a) outside and inside of the bend b) around the circumference thickness distribution for all boost cases

Due to the large major (tensile) strains at the outside of the bend, thinning occurs, as shown in Figure 63a. The reduction in major strain (for increased boost) results in less thinning for the MB tube. The greatest difference in thinning between the LB and MB cases is at θ=75°, which corresponds approximately to the major strain distribution peaks in Figure 62a).

Thickening occurs at the inside of the bend due to the large minor (compressive) strains, as shown in Figure 63a. The poor quality grids at the inside of the bend hindered observation of a measurable difference in strain distribution between the two boost cases (Figure 62b), but the increased thickening of the MB tube (Figure 63a) supports the theory that greater minor strains occur for higher boost levels at the inside of the bend.

Around the circumference of the bend (Figure 63b), the thickness of the MB tube is greater for the entire range of the measurements (0°<Ø<360°). This is due to the additional longitudinal compressive stress component for increased boost level.

4.2.3 IF Results

The average strain and thickness distributions for the IF tube LB, MB and HB cases are shown in Figure 64 and Figure 65 respectively. The average steady-state strain (ε_{avg}) and thickness (t_{avg}) are presented in Section 4.2.4 along with the DP600 results.
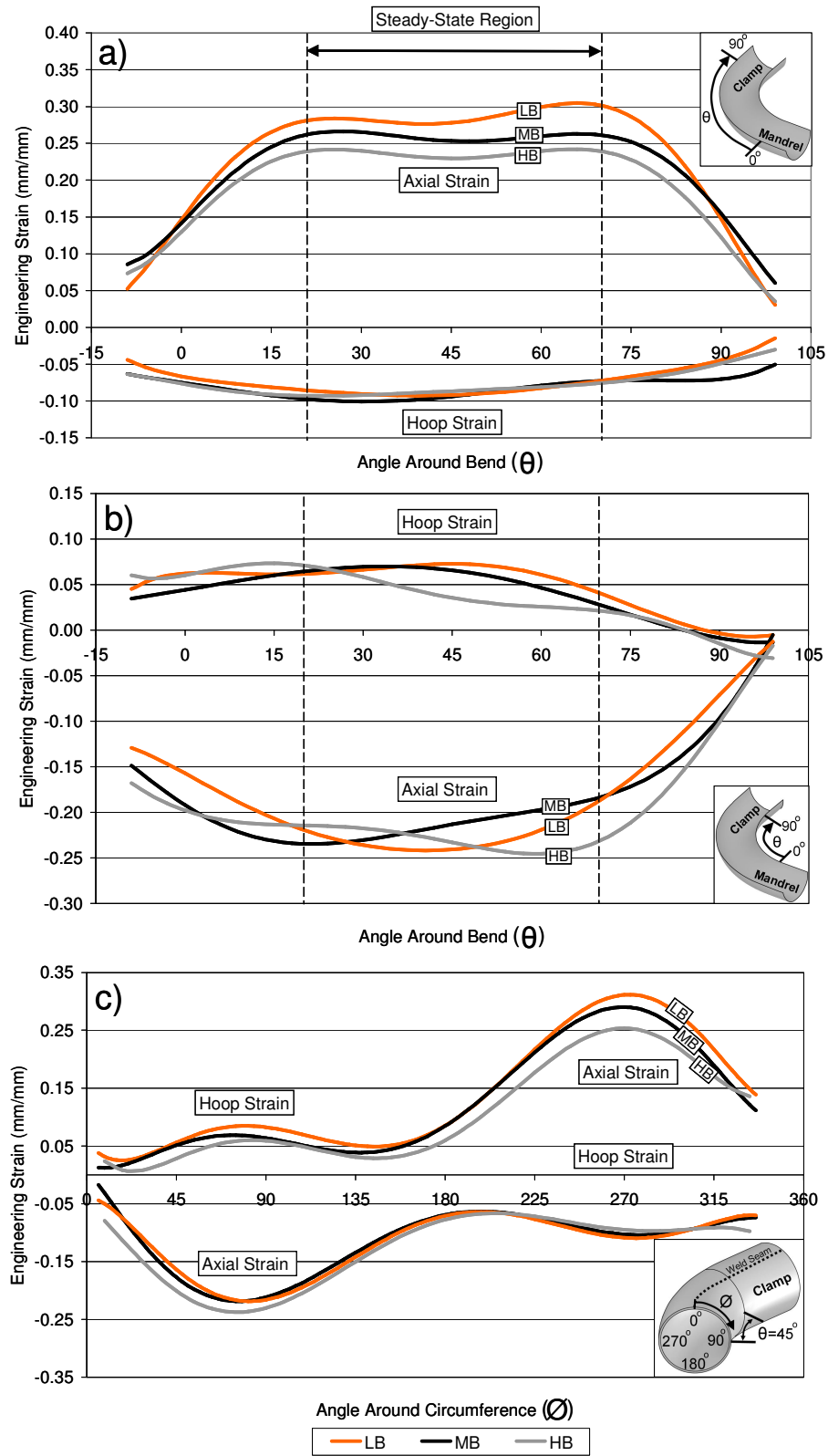
Figure 64: IF a) outside of the bend b) inside of the bend c) around the circumference strain distribution for all boost cases
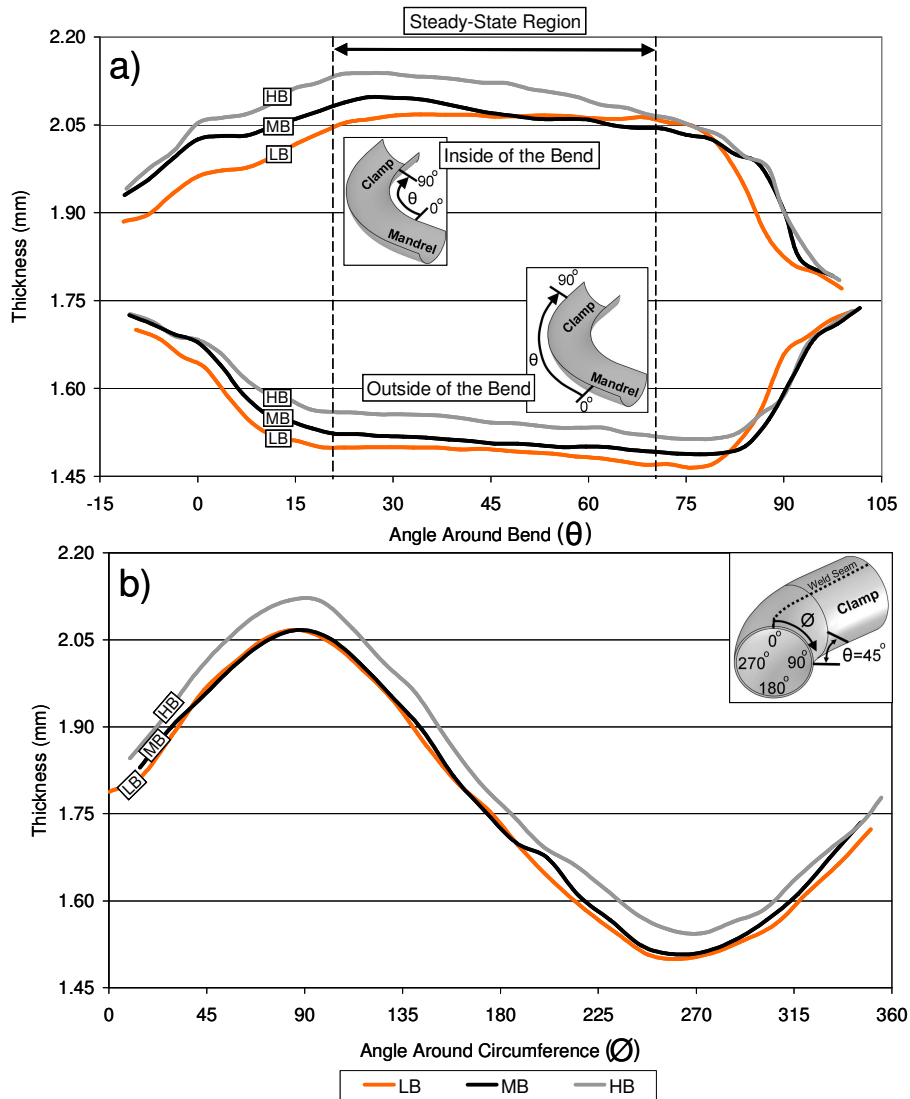
Figure 65: IF a) outside and inside of the bend b) around the circumference thickness distribution for all boost cases

For the outside of the bend steady-state region (Figure 64a), each increment in boost shows a distinct reduction in the major strains, with no effect on the minor strain distribution. Only the LB case shows a distinct peak in strain at $\theta=65°$. Less thinning is also observed with increasing boost (Figure 65a). The degree of thinning is generally greatest at $\theta=70°$.

As observed for the DP600 tubes, the strains at the inside of the bend (Figure 64b) do not exhibit significant boost effects, likely due to poor circle grid quality; however, the thickness distributions show a distinct increase in thickening between the MB and HB cases

(Figure 65a). The same trend is also followed by the LB case. Thickening is generally greatest at θ=20°.

Around the circumference of the bend (Figure 64c) at 0°<∅<180°, the HB case shows an increase in major (compressive) strain over the LB and MB cases which are roughly the same as one another. For 180°<∅<360°, the major (tensile) strain distributions show a reduction in strain for increasing boost. The thickness distribution shows more thickening (0°<∅<180°) and less thinning (0°<∅<360°) for the HB case around the entire cross-section when compared to the LB and MB cases.

4.2.4 Summary of Bending Deformation

Table 8 summarizes the average steady-state principal strain (major and minor), (ε_{avg}) and thickness (t_{avg}) at the outside and inside of the bend. The average values are calculated for 20°<θ<70°, the steady-state region. In addition to the average steady-state values, the minimum and maximum value of the average distribution curves are shown in the square parentheses. Figure 66, Figure 67 and Figure 68 present the average steady-state strain and thickness values in bar chart format. For the circumferential thickness distributions (Figure 63b and Figure 65b), an average circumferential thickness is calculated for 0°<∅<360° and is presented in Table 8. In addition to the average circumferential thickness, the percent increase in thickness (based on original tube thickness) is presented in the square brackets.

Table 8: Average steady-state strain and thickness summary

Material	Boost	Outside of the Bend			Inside of the Bend			Circum.
		Major Strain (Ten.) (mm) [min/max]	Minor Strain (Comp.) [min/max]	Thick. (mm) [min/max]	Minor Strain (Comp.) [min/max]	Major Strain (Ten.) [min/max]	Thick. (mm) [min/max]	Average Thickness (mm) [% increase]
DP600	LB	0.28 [0.26/0.31]	0.06 [0.05/0.06]	1.54 [1.51/1.57]	0.24 [0.22/0.26]	0.07 [0.03/0.08]	2.25 [2.22/2.27]	1.869 [1.0%]
	MB	0.26 [0.25/0.28]	0.05 [0.04/0.06]	1.56 [1.54/1.58]	0.24 [0.24/0.24]	0.04 [0.03/0.04]	2.27 [2.24/2.30]	1.885 [1.9%]
IF	LB	0.29 [0.28/0.31]	0.09 [0.07/0.09]	1.49 [1.47/1.50]	0.23 [0.19/0.24]	0.06 [0.04/0.07]	2.06 [2.05/2.07]	1.762 [1.3%]
	MB	0.26 [0.25/0.27]	0.09 [0.07/0.10]	1.51 [1.49/1.52]	0.21 [0.19/0.24]	0.06 [0.03/0.07]	2.07 [2.10/2.05]	1.771 [1.9%]
	HB	0.24 [0.23/0.24]	0.09 [0.08/0.09]	1.54 [1.52/1.56]	0.23 [0.22/0.25]	0.04 [0.02/0.07]	2.11 [2.07/2.14]	1.810 [4.0%]
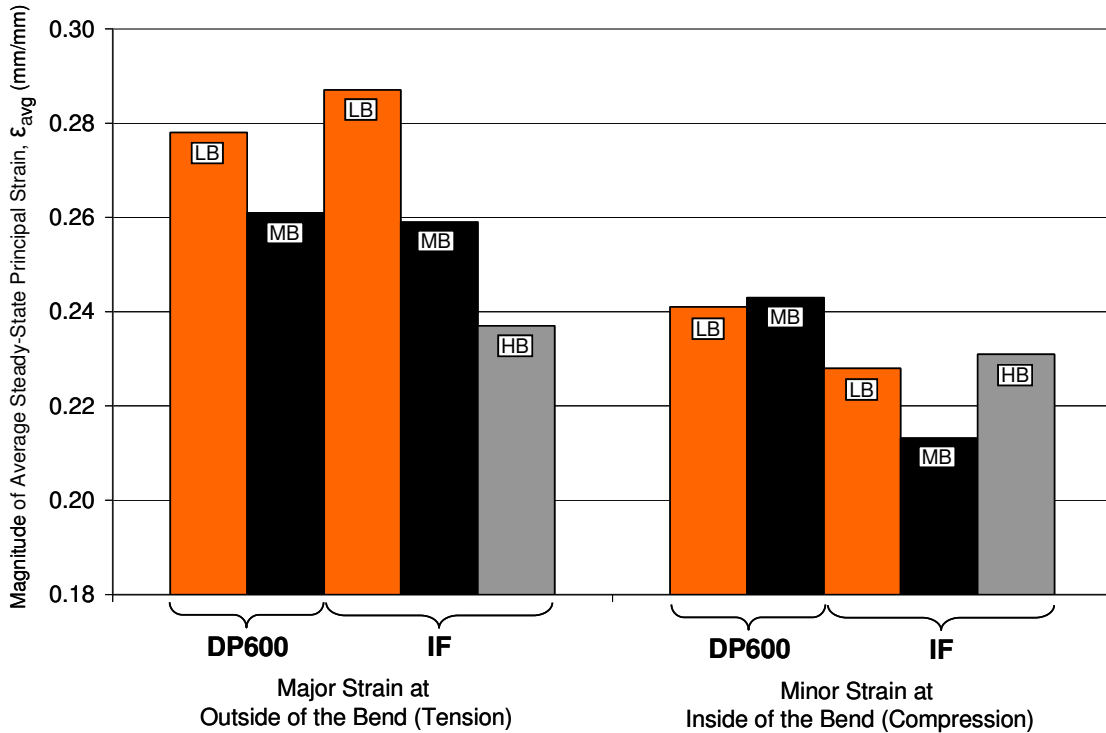
Figure 66: Magnitude of the measured average steady-state principal strain. The major component at the outside of the bend and the minimum component at the inside of the bend correspond to the bending and membrane strains.
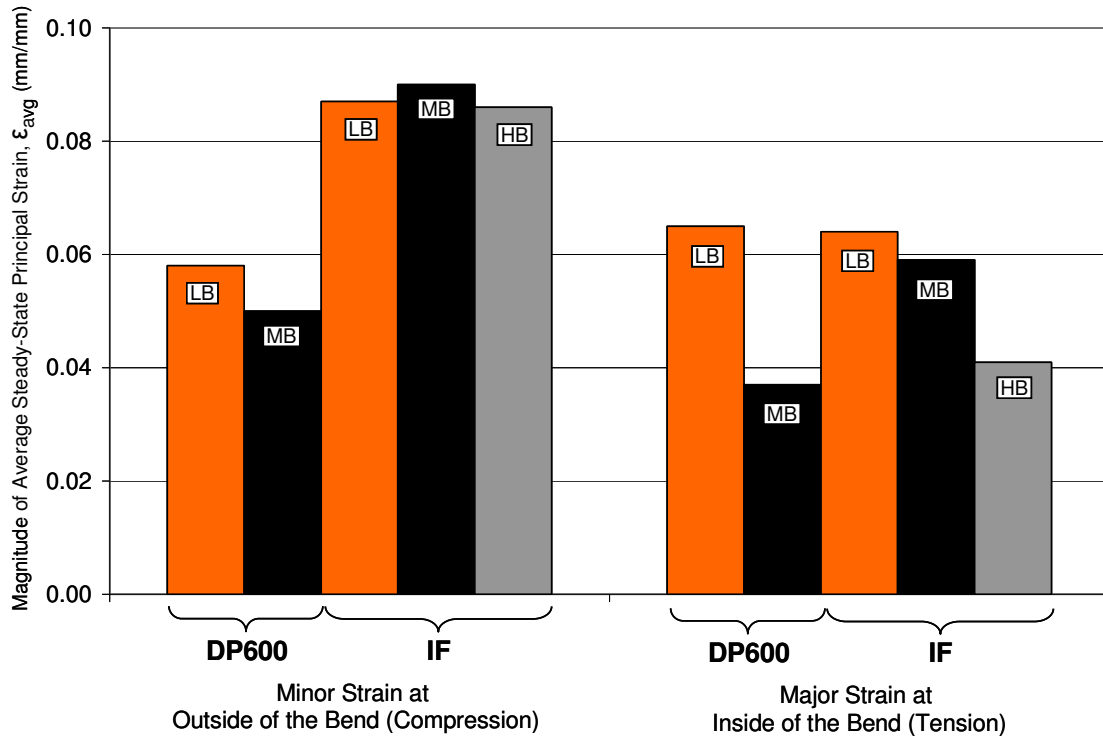
Figure 67: Magnitude of the predicted and measured average steady-state principal strain. The minor component at the outside of the bend and the major component at the inside of the bend correspond to the bending and membrane strains
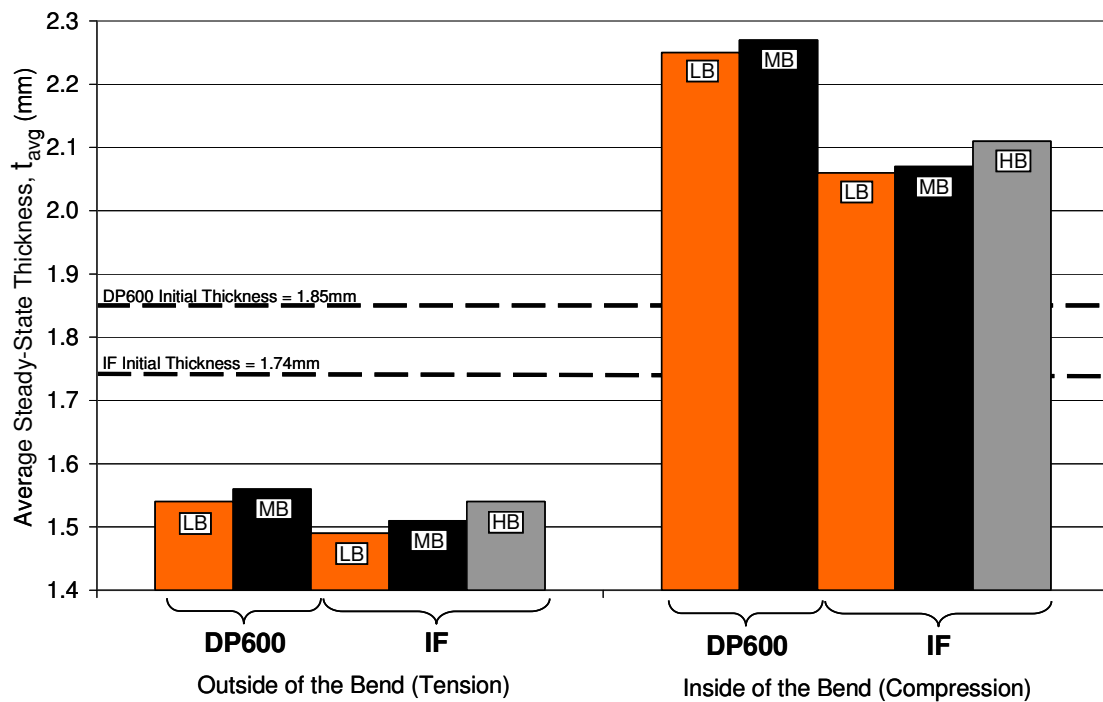
Figure 68: Average inside and outside of the bend thickness

For DP600, the average major (tensile) strain at the outside of the bend decreased from 0.28 (LB) to 0.26 (MB) which is a 6% decrease in total strain. The minor (compressive) strain is approximately the same at 0.06 for all boost cases. The thickness for LB is 1.54mm which corresponds to 17% thinning (compared to original tube thickness of 1.85mm) and 1.56mm for MB which represents 16% thinning. The IF major (tensile) strains were 0.29, 0.26 and 0.24 for LB, MB and HB, respectively. These correspond to a 17% total reduction in strain between the LB and HB case. Again, the minor (compressive) strains are approximately the same for all boost cases at 0.09. The thicknesses are 1.49mm, 1.51mm and 1.54mm for LB, MB and HB respectively. The LB thickness shows 14% thinning (compared to original tube thickness of 1.74mm) while HB shows 11% thinning.

Due to the strain measurement scatter (poor grids) at the inside of the bend for both the DP600 and IF tubes, no boost effects could be observed. The major (compressive) strain is the same for both boost cases at 0.24 while the minor (tensile) strain is 0.07 for LB and 0.04 for MB. The LB thickness is 2.25mm which corresponds to 22% thickening and 2.27mm for MB which is 23% thickening. For IF, the major (compressive) strain is approximately the same for all three boost cases at 0.22 while the minor (tensile) strain is approximately 0.05 for all boost cases. The IF thicknesses are 2.06mm, 2.07mm and 2.11mm for LB, MB and HB, respectively. The LB thickness shows 18% thickening while HB shows 21% thickening when compared to the original thickness of the tube.

The average circumferential thickness (Table 8) shows the same trend for both the DP600 and IF tubes, where the percent increase in circumferentially averaged thickness increases with increasing bending boost. Increased overall thickening is a result of more longitudinal compressive strain during bend for increased bending boost levels.

92

CHAPTER 5

EXPERIMENTAL RESULTS: HYDROFORMING

The results of the straight and pre-bend tube hydroforming experiments are presented in this chapter. The average burst pressure, corner-fill expansion (CFE), strain and thickness measurements are presented and summarized. The main goals of this chapter are to observe the effect of pre-bending, pre-bending boost and hydroforming end-feed (EF) on the hydroformability (formability during hydroforming) of DP600 and IF tubes.

5.1 Straight Tube Hydroforming

Straight tube hydroforming experiments were conducted on the DP600 and IF tubes to determine their hydroformability (without pre-bending). By comparing these results with the pre-bend hydroforming experiments, the amount of ductility/formability that is consumed by the pre-bending process can be quantified. Straight tubes represent an R/D ratio of infinity. Also, the effect of hydroforming end-feed (EF) on the hydroformability of the straight tubes is evaluated.

5.1.1 Results

The results of the straight tube hydroforming study are summarized in Table 9. For each of the DP600 test conditions, corresponding to zero, 67kN and 133kN end-feed (EF), four tubes were hydroformed to burst and the averaged burst pressure was calculated. For the 200kN EF (DP600) and zero EF (IF) cases, only one tube was tested because the maximum clamping capacity of the hydroforming press was reached and the tubes did not burst. Because the IF tube with zero EF did not burst, no additional EF cases were tested.

Due to the current design of the embedded displacement transducer (Section 3.2.6), corner-fill expansion (CFE) was not performed during tests loaded until burst because the transducer was being damaged at burst. In order to provide CFE data for each of the DP600

93

burst cases, an interrupted tests were performed in which tubes were deformed to 70% and 90% of the average burst pressures and then unloaded. Table 9 summarizes the test conditions and results.

The average end-feed (EF) displacement is also shown in Table 9 and is the average displacement of the two EF rams [(EF ram #1 disp. + EF ram #2 disp.)/2]. For the 67kN, 133kN and 200kN EF cases, real-time measurement of EF displacement (for each ram) is done through the control system. For the zero EF tests (DP600 and IF), the EF rams remain stationary. The tube shortens naturally during loading and the final EF displacement was determined by measuring the length of the tube after burst.

Table 9: Straight tube hydroforming results

Material	End-Feed (kN) [kip]	Number of Burst Tests	Average Burst Pressure (MPa) [psi]	Average End-Feed Displacement at Burst (mm) [in]	90% Interrupted Test CFE (mm) [in]	90% Interrupted Test CFE (%)
DP600	Zero	4	69.6 [10,092]	6.8 [0.266]	7.4 [0.290]	46%
	67 [15]	4	92.1 [13,359]	17.6 [0.692]	9.8 [0.385]	61%
	133 [30]	4	126.9 [18,405]	24.8 [0.975]	11.3 [0.447]	70%
	200 [45]	1	151.7* [22,000]	32.8 [1.292]	12.4** [0.490]	77%**
IF	Zero	1	151.7* [22,000]	11.5 [0.453]	13.3** [0.526]	83%**

* Burst was not achieved, maximum capacity of the press was reached
** Measured at final hydroforming pressure as shown in column 4

5.1.2 Burst Pressure and Corner-Fill Expansion

The effect of end-feed (EF) load on the average burst pressure can be seen in Figure 69. The repeatability of the burst tests is shown by the individual burst test data points which are closely clustered together. The corner-fill expansion (CFE) for 90% interrupted test is also shown for increasing levels of hydroforming EF load.
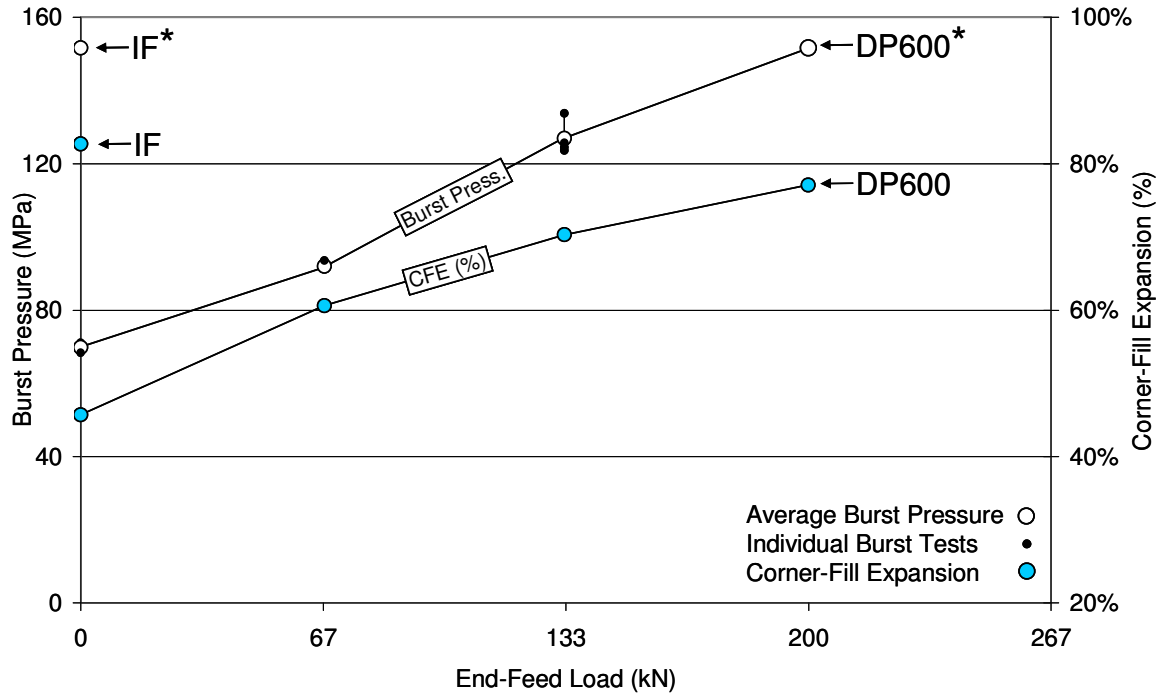
Figure 69: Burst pressure and CFE (90% interrupted) *vs.* internal pressure for DP600 and IF straight tube

For the DP600 tests, burst pressure increases with the application of EF. The corner-fill expansion (CFE) also increases with EF which is a result of the tube being able to sustain a higher internal pressure. For the zero EF IF test, the CFE reaches 83% at the maximum capacity of the press which occurs at 151.7MPa internal pressure. This CFE corresponds to the maximum CFE that can be accommodated in the current straight hydroforming die cross-section (Section 3.2.6) and indicates that the tube has fully expanded into the die cavity.

Real-time CFE measurements were recorded for each 90% interrupted test and are shown in Figure 70. The curves are constructed from the raw data measured by the data acquisition system and exhibit virtually no scatter. The CFE of the zero EF IF and DP600 tests greatly differ due to lower strength and higher formability of the IF material. The IF tube has much greater CFE than the DP600 tube and yielding begins at internal pressures of approximately 11MPa and 20MPa for the IF and DP600 tubes respectively. The hydroformability of the IF tube is very high because the CFE plateaus at approximately 100MPa, when the tube has fully filled the die cavity.

95
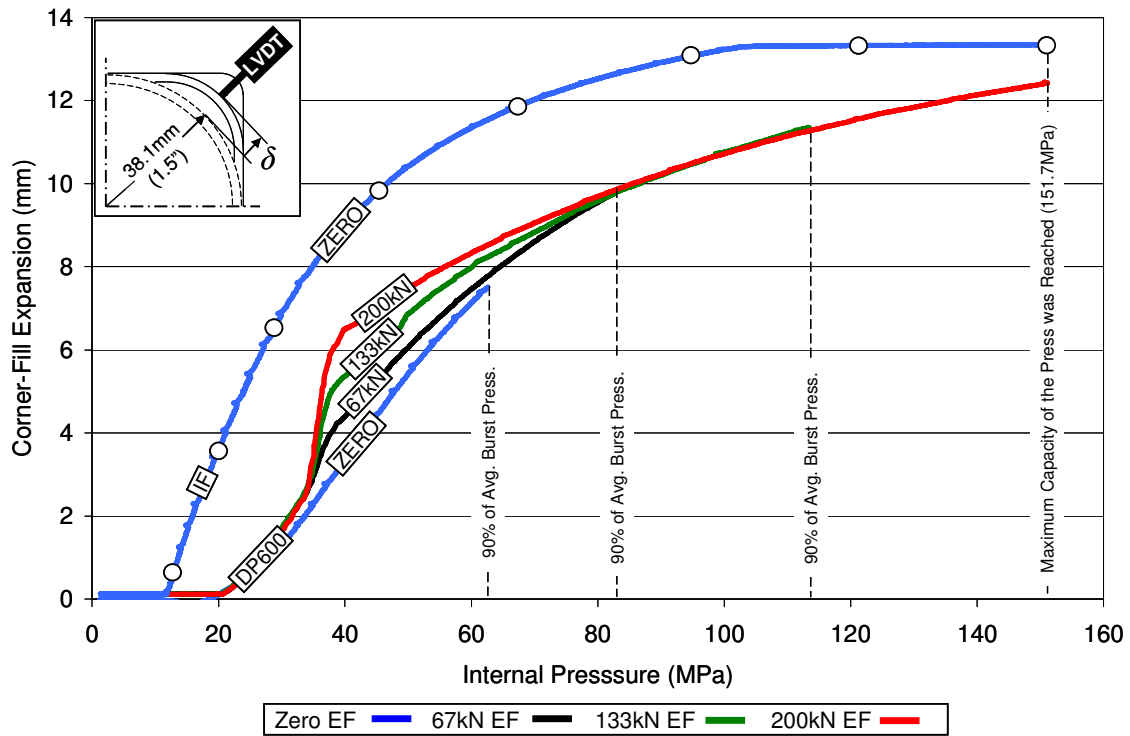
Figure 70: CFE *vs.* internal pressure, DP600 and IF straight tube

For the DP600 EF cases (67kN, 133kN and 200kN), the CFE curves show a large increase in CFE when the additional EF load is applied (35MPa to 38MPa). After 38MPa, the rate of CFE converges on to a single curve at approximately 80MPa internal pressure.

5.1.3 End-Feed Displacement

Load-control EF was applied during hydroforming, the displacement response of the EF rams is an important measure for the validation of the numerical models (to assess the COF and constitutive model selected for the numerical model). Figure 71 shows the average EF displacement [(EF ram #1 disp. + EF ram #2 disp.)/2] response for the DP600 and IF tests. Similar to the CFE results, the EF displacement curves are constructed from the raw data measured by the data acquisition system and show virtually no scatter.
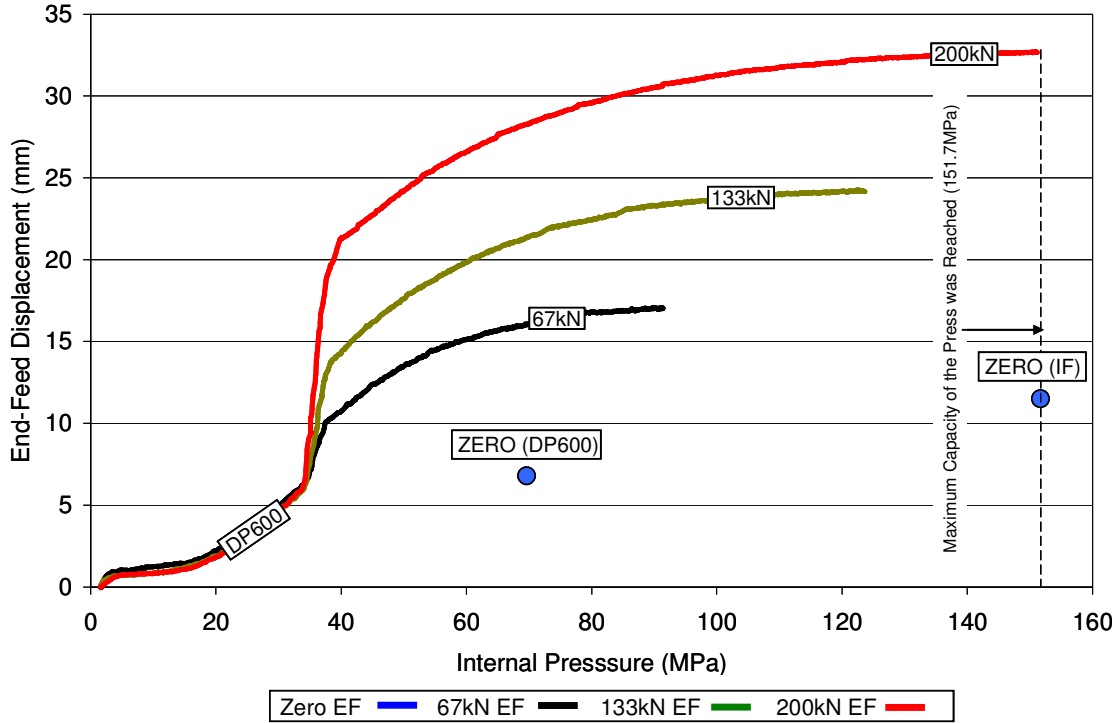
Figure 71: Average EF displacement *vs.* internal pressure for burst tests, DP600 and IF straight tube

For the DP600 and IF zero EF cases, the EF rams were stationary during the test and the change in length of the tube was measured manually to calculate the average EF displacement. When the additional EF load is applied during the 67kN, 133kN and 200kN EF tests a sudden increase in rate of EF displacement is observed at 35MPa, which is a result of the increase in axial load. After 38MPa, the rate of EF displacement decreases as the internal pressure in the tube increases. This reduction in the rate of EF displacement is due to increased friction between the tube and die as a result of the internal pressure increase, which retards the flow of the tube in the axial direction.

5.1.4 Strain and Thickness Measurement

The strain and thickness were measured for the 90% interrupted tests according to the procedure that was presented in Section 3.2.7. Figure 72 shows the measured strain and

thickness for the different end-feed (EF) cases shown in Table 9. The individual strain and thickness distribution plots for each EF case can be found in Appendix E.
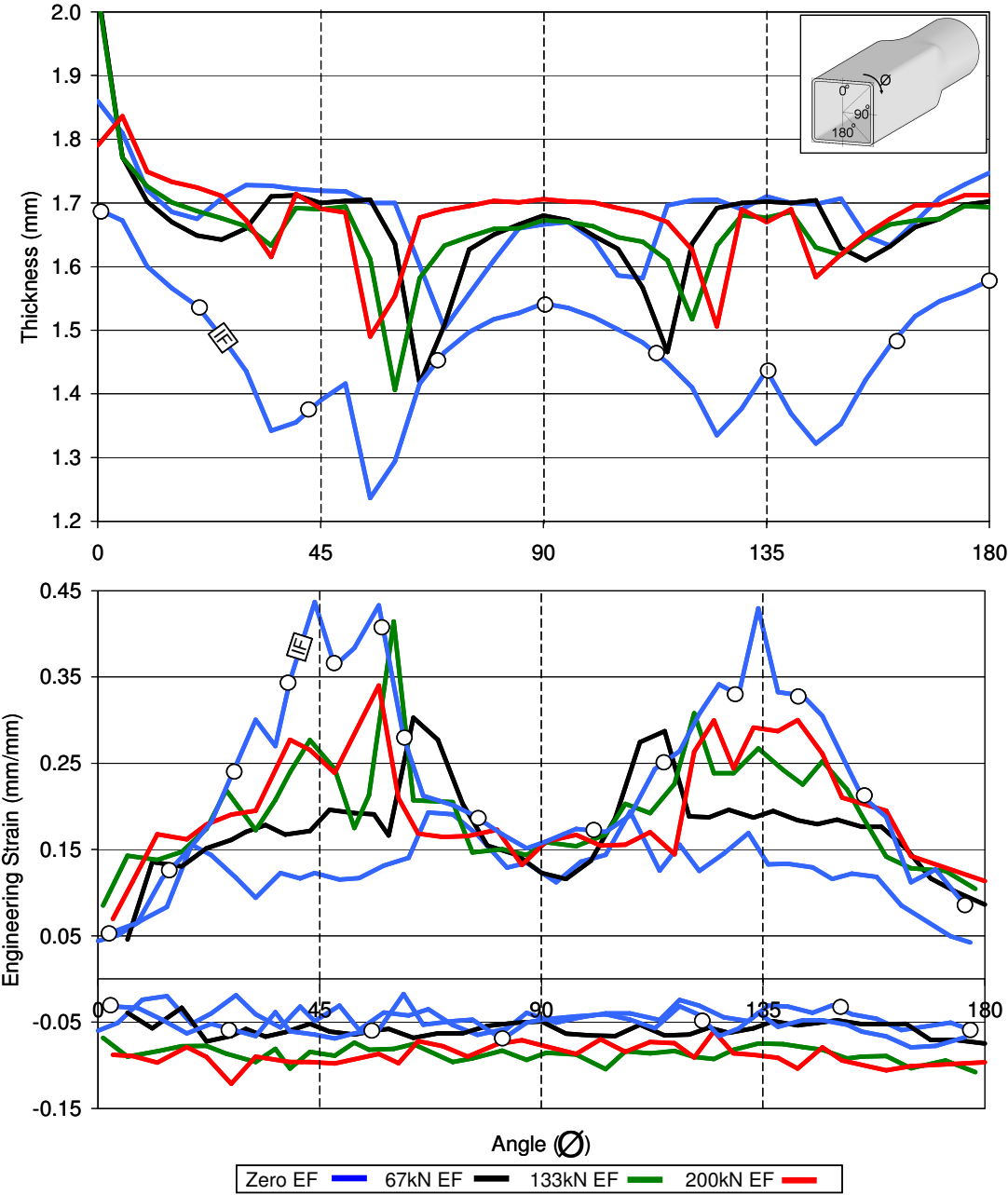
Figure 72: Measured strain and thickness distributions for DP600 and IF straight tube, 90% interrupted. See Appendix E for strain and thickness distributions plots for each EF case.

From the results shown in Figure 72, the following observation can be made on the effect of EF and tube material on the strain and thickness within the 90% interrupted straight tube hydroforming tests,

Thickness

The thickness at Ø=0° always corresponds to the weld seam, therefore the thickness is either greater or close to the initial thickness of the tube that is, 1.85mm for DP600 (all EF cases) and 1.74mm for IF. At Ø=180°, the DP600 thickness (for all EF cases) reduces to approximately 1.70mm (8%) while the IF thickness reduces to 1.58mm (9%).

An interesting observation can be made for all EF cases and both materials at Ø=45° and Ø=135° which represent the corners of the die. The thickness on either side of these two locations exhibits a sudden local drop (thinning). These locally thinned sections of the tube correspond to the transition from tube/die contact to the free expansion zone as illustrated shown in Figure 73 (a). The local thinning phenomenon is due to the friction between the tube and die. At high internal pressure, the friction between the tube and die pins the flow of the tube towards the corner of the die (sliding of the tube against die surface) which only allows tubular expansion in the free expansion zone (Figure 73). The expanding tube induces a large tensile load (hoop direction) at the transition zone and causes thinning. At the tube/die contact zone, it should be noted that a through-thickness stress component exists and is a result of the internal pressure which forces the tube against the die.
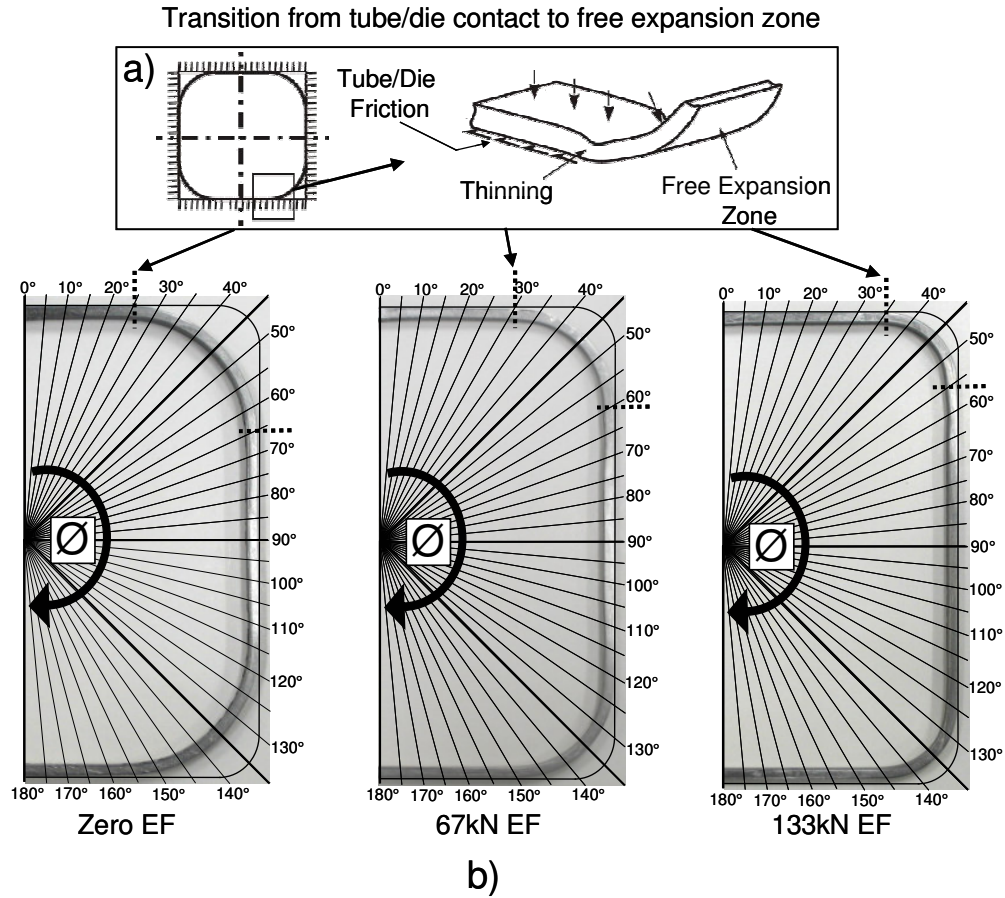
Figure 73: a) Transition from tube/die contact to free expansion zone (Simha *et al.*, 2006) b) Sections cut from 90% interrupted DP600 straight tubes

Although the IF tube did not burst because the maximum capacity of the press was reached, a large neck had developed in the transition zone and is shown in Figure 74. The good formability of the material allowed the tube to expand after the neck had initiated.
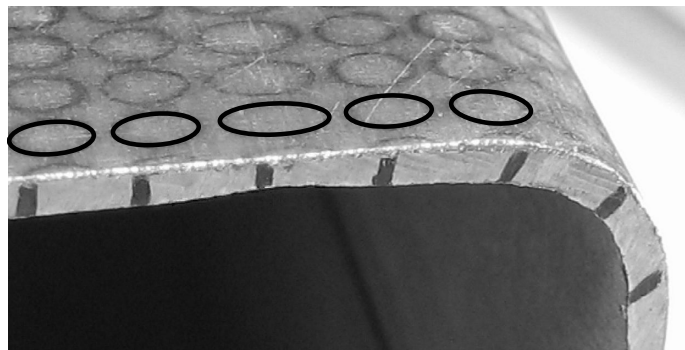
Figure 74: Neck in zero EF IF straight tube

100

Strain

In straight tube hydroforming, the major strain is tensile and in the hoop direction of the tube, while the minor in-plane strain component is compressive and oriented along the longitudinal direction of the tube. For all DP600 and IF end-feed (EF) cases, the general trends for the major strain distributions are consistent with the findings of the measured thickness distributions. Figure 72 shows that the peaks in major strain correspond to the same angular location where thinning occurs. Figure 74 illustrates this point since severely elongated grids correspond to the location of the neck. The major strain peaks increase in magnitude as end-feed (EF) increases.

The minor strain remains fairly constant over the entire measurement angle, Ø. For the DP600 tubes, the approximate minor strain increases in magnitude from -0.04 to -0.08 as the EF level increases from zero to 200kN. The IF tube average minor strain is -0.05 for the zero EF case. As EF increases, the minor strain becomes more negative because of the increase in compressive longitudinal stress.

5.2 Pre-Bend Tube Hydroforming

Hydroforming experiments were conducted on the pre-bent DP600 and IF tubes presented in Chapter 4. The main focus of this section is to evaluate the effect of bending, bending boost (a key pre-bending parameter) and hydroforming end-feed (EF) on the hydroformability of the two alloys.

5.2.1 Tube Movement during Hydroforming

Dyment (2004) showed that during hydroforming of pre-bent tubes with zero end-feed (EF), the tube lifts away from the inside of the bend and translates towards the outside of the bend. This movement causes the weld seam (neutral axis of as-bent tubes) to shift towards the outside of the bend, which can be observed in Figure 54. Hydroforming with EF causes this effect to be more pronounced because the EF force also causes the tube to be pushed towards

101

the outside of the bend region. It can also be observed that the unsupported tube at the inside of the bend begins to wrinkle or buckle; this was only observed for the 133kN EF case. As the tube expands to contact the inside of the bend, the wrinkles are ironed out by the internal pressure.
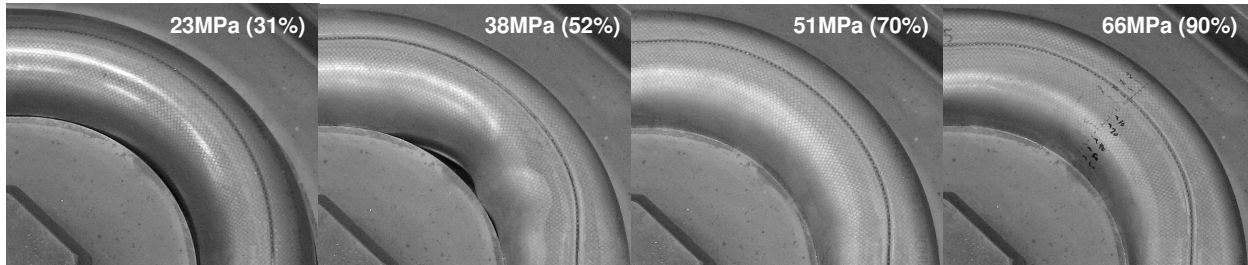
Figure 75: Series of DP600 samples interrupted at various pressures showing tube movement under 133kN EF

5.2.2 Results

The results of the pre-bent tube hydroforming study are summarized in Table 10. For all DP600 end-feed (EF) cases, multiple tubes were pressurized to burst and the average burst pressure was calculated. The IF tubes did not burst and were hydroformed to the pressures shown in column four of Table 10. For each of the DP600 burst tests, the average EF displacement [(EF ram #1 disp. + EF ram #2 disp.)/2] was measured. The average for each EF case was calculated and is shown in Table 10. The EF displacement for the IF zero EF cases was not measured and the average EF displacement was measured for IF 67kN EF cases.

As mentioned above, the IF tubes could not achieve burst because the maximum capacity of the press clamp force was reached. To observe the effect of bending boost, two tubes for each boost case were pressurized to 35MPa (5,000psi) with zero EF during hydroforming. In addition, a single 67kN EF test was conducted for each boost case to observe the effect of EF. As in the zero EF case, the maximum capacity of the press clamp was reached before burst occured.

A single interrupted test to 70% and 90% of the average burst pressure was conducted for the DP600 tubes for each EF condition in order to measure the inside and outside CFE

(with embedded displacement transducers). The CFE was measured at the final hydroforming pressure for all of the IF tests. Due to the non-symmetrical expansion of the inside and outside of the bend regions the CFE is presented as the inside, outside and average value as discussed in Section 3.2.6.

The overall thickness presented in Table 10 is the thickness averaged around the circumference of the DP600 (at 90% interrupted pressure) and IF (at final forming pressure) tubes for 0°<∅<360°. The thickness measurements were taken around the circumference of the hydroformed pre-bent tube as shown in Figure 54. The percent reduction is calculated by subtracting the average circumferential thickness from the as-tubed initial thickness.

Table 10: Pre-Bend tube hydroforming results

Material	Bending Boost Case	End-Feed (kN) [kip]	# of Burst Tests	Avg. Burst Press. (MPa) [psi]	Avg. End-Feed Disp. at Burst (mm) [in]	90% Intrpt. Test CFE (inside, outside, **average**) [in]	90% Intrpt. Test CFE (inside, outside, **average**) %	Overall Thick. (mm) [% Red.]
DP600	MB	Zero	3	45.0 [6,528]	5.4 [0.211]	-1.6, 4.4, **1.4** [-0.064,0.173, **0.055**]	-10%, 27%, **9%**	1.890 [-2.2%]
	MB	67 [15]	3	60.4 [8,756]	12.1 [0.478]	5.2, 7.5, **6.4** [0.207, 0.297, **0.252**]	33%, 47%, **40%*****	NA
	LB	67 [15]	5	54.6 [7,915]	10.8 [0.423]	4.4, 7.3, **5.9** [0.275, 0.353, **0.314**]	27%, 45%, **36%**	1.796 [2.9%]
	MB	133 [30]	4	73.4 [10,643]	17.6 [0.694]	7.0, 9.0, **8.0** [0.172, 0.288, **0.230**]	43%, 56%, **49%**	1.783 [3.6%]
IF	LB	Zero	2	34.5* [5,000]	NA	7.5, 8.2, **7.9**** [0.295, 0.323, **0.309**]	46%, 51%, **49%****	1.589 [8.7%]
	MB	Zero	2	34.5* [5,000]	NA	7.6, 8.2, **7.9**** [0.299, 0.323, **0.298**]	47%, 51%, **49%****	1.580 [9.2%]
	HB	Zero	2	34.5* [5,000]	NA	7.0, 8.1, **7.6**** [0.277, 0.320, **0.298**]	44%, 50%, **47%****	1.641 [5.7%]
	LB	67 [15]	1	151.7* [22,000]	18.8** [0.741]	13.7, 13.9, **13.8**** [0.540, 0.548, **0.544**]	85%, 86%, **86%****	1.498 [13.9%]
	MB	67 [15]	1	151.7* [22,000]	20.3** [0.800]	13.7, 13.9, **13.8**** [0.540, 0.548, **0.544**]	85%, 86%, **86%****	NA
	HB	67 [15]	1	151.7* [22,000]	18.5** [0.726]	13.7, 13.9, **13.8**** [0.538, 0.547, **0.542**]	85%, 86%, **85%****	1.540 [11.5%]

* Burst was not achieved
** Measured at final hydroforming pressure as shown in column 5
*** Tube burst at 87% of average burst pressure

5.2.3 Failure Location

The failure (burst) locations on the pre-bent tubes varied depending on the amount of EF applied during hydroforming and the bending boost case. Table 11 is a summary of failure locations for all of the DP600 pre-bend burst tests, while Figure 76 illustrates the different locations where failure occurred.

Table 11: All DP600 pre-bend tube failure (burst) locations

Bending Boost Case	End-Feed (kN) [kip]	# of Burst Tests	Failure Location, Inside of the Bend and Neutral Axis	# of Burst Tubes at Weld Seam and Opposite Weld Seam	Picture
MB	Zero	3	Inside of the Bend	0	-
			Neutral Axis	3 (Opposite Weld Seam)	
MB	67 [15]	3	Inside of the Bend	0	-
			Neutral Axis	1 (Weld Seam) 2 (Opposite Weld Seam)	
LB	67 [15]	5	Inside of the Bend	2	
			Neutral Axis	1 (Weld Seam) 2 (Opposite Weld Seam)	Similar to MB 67kN EF case
MB	133 [30]	4	Inside of the Bend	3	
			Neutral Axis	1 (Weld Seam)	Similar to MB 67kN EF case

The two dominant failure locations were at the neutral axis or at the inside of the bend. The neutral axis failures occurred within the parent metal adjacent to the weld seam or in the tube wall opposite to the weld seam (Figure 76). For the 67kN LB and MB cases, the neutral axis failures occurred at least once near the weld seam or opposite the weld seam, as shown in Table 11. This observation suggests that the weld seam was manufactured properly since no failures occurred directly within the weld metal. For the 67kN LB and MB tests, the MB tubes consistently burst either at the neutral axis while the LB tubes burst at the neutral axis or at the inside of the bend. The 133kN EF cases exhibited burst at the inside of the bend for the majority of the experiments. The results indicate a transition in failure location from the neutral axis to the inside of the bend as either boost changes of EF increases.
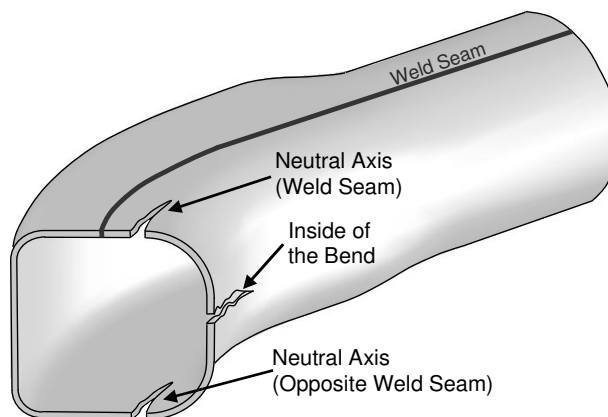
Figure 76: DP600 pre-bend failure location schematic

5.2.4 Burst Pressure and Corner-Fill Expansion

The effect of EF on the average burst pressure for the DP600 MB tests is shown in Figure 77. The repeatability of the burst tests is seen in the close proximity of the individual burst pressure data points. In addition to the DP600 results, only the MB 67kN end-feed (EF) IF test is shown because the results for the three IF boost cases did not vary significantly as shown in Table 10.
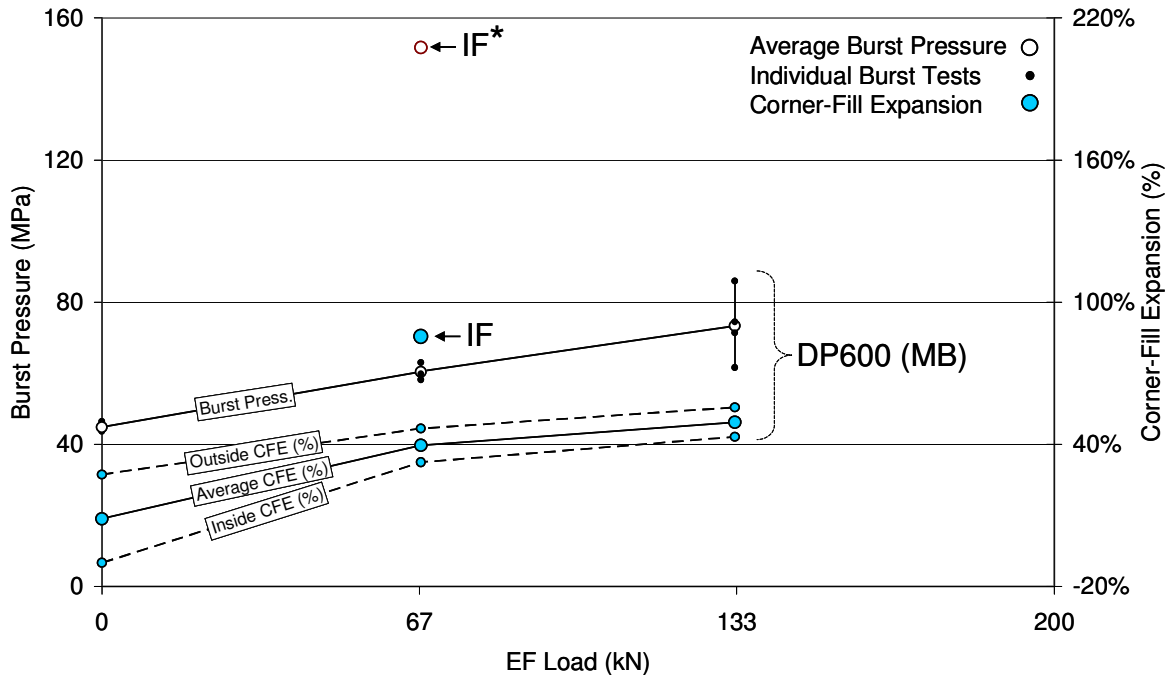
*Burst was not achieved since the maximum capacity of the press was reached. Since CFE results are similar for LB, MB and HB, only the MB average CFE is shown.

Figure 77: Burst pressure and CFE (90% interrupted) *vs.* end-feed, DP600 (MB) and IF pre-bent tube

The DP600 results show that an increase in EF delays the onset of failure which increases the burst pressure. Burst pressure repeatability is very good for the zero and 67kN EF cases, but the level of scatter increases for the 133kN EF case. As a result of the increase in burst pressure for greater EF levels, the tube is consequently allowed to form more and thus achieve a higher level of corner-fill expansion (CFE), as shown in Figure 77.

Real-time CFE measurements for the DP600 pre-bend tubes (90% interrupted tests) are shown in Figure 78. For each test, the inside and outside of the bend CFE is shown which allows the effect of bending boost and hydroforming EF to be analysed.
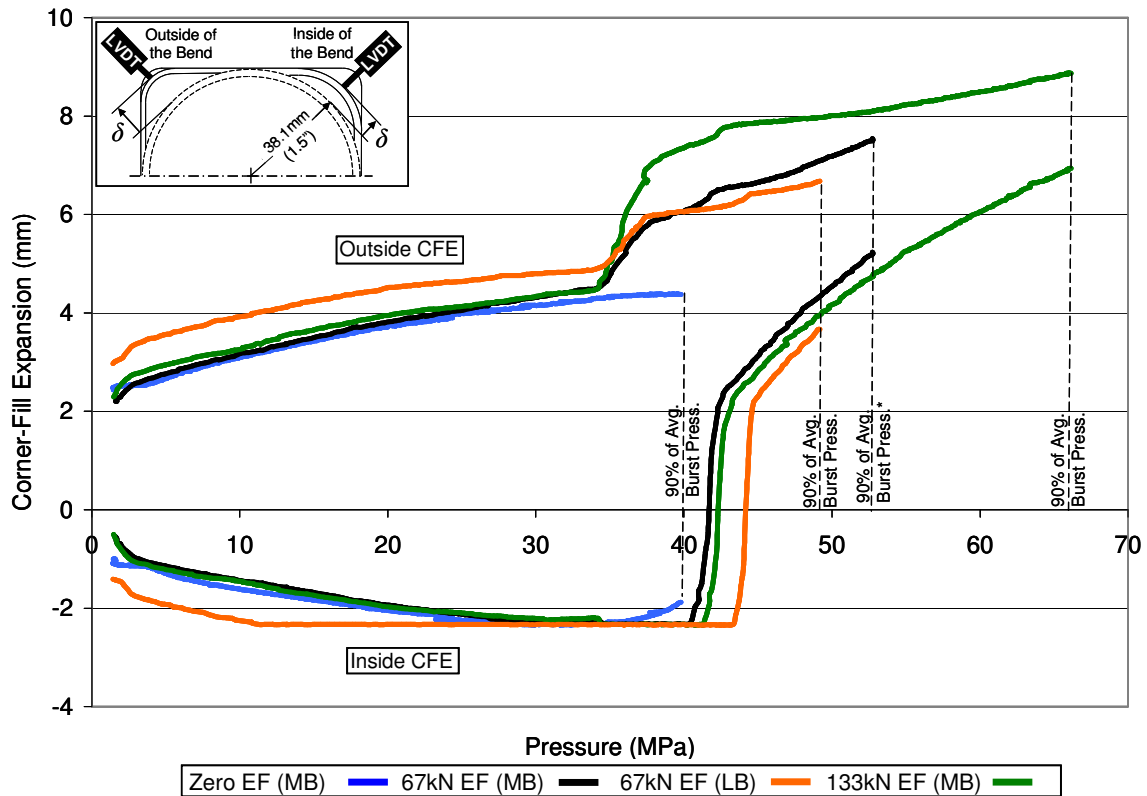
Figure 78: CFE *vs.* internal pressure, DP600 pre-bend tubes, 90% interrupted

* Tube burst at 87% of average burst pressure

The inside CFE for all EF cases begins at a value less than zero and the outside CFE is greater than zero. This is possibly due to a combination of hydroforming die clearance and ovalization that is induced on the tubes during pre-bending (Dwyer *et al.*, 2002; Dyment, 2004). Figure 79 illustrates how ovalization causes the initial inside CFE to be negative and outside CFE to be positive.
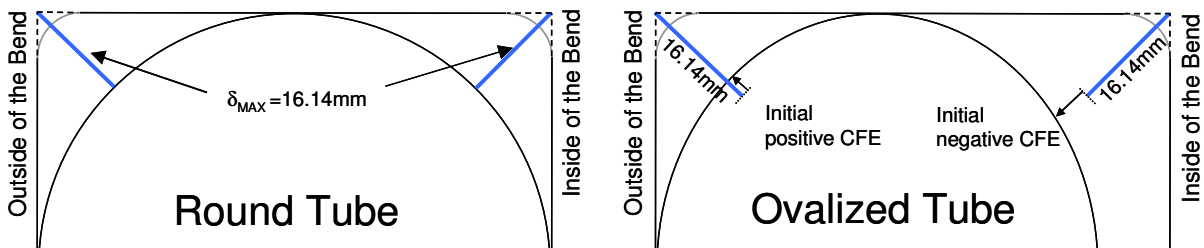
Figure 79: Effect of pre-bending ovalization on initial CFE measurements.

Due to the current embedded LVDT displacement transducer design, the inside corner-fill expansion (CFE) measurements are limited to negative 2.5mm because the probe reaches maximum extension and loses contact with the tube. After approximately 40MPa, the inside CFE begins to increase as the tube starts to form and expand into the die cavity, re-contacting the transducer. For the 67kN and 133kN EF cases, the inside CFE becomes positive at approximately 43MPa, which suggests that the tube has made contact with the die at the inside of the bend. The outside CFE gradually increases until 35MPa. The rate of CFE increases when the EF load is applied (35MPa to 38MPa). A constant and lower rate of outside CFE increase occurs after 38MPa internal pressure.

An effect of bending boost can be seen for the 67kN EF (LB and MB) cases in Figure 78. After EF is applied (35MPa to 38MPa), there is little difference between the outside and inside CFE for the two boost cases. It is the delay of failure (burst) of the MB tube which allows it to form more than the LB tube and ultimately exhibit a higher formability.

The CFE measurements for the IF zero and 67kN EF cases are shown in Figure 80 and Figure 81 respectively. Similar to the DP600 results, both EF cases show that the initial inside CFE is negative and the outside CFE is positive. For both sets of tests (zero and 67kN EF), the effect of boost on the CFE curves is insignificant after 20MPa of internal pressure. After 20MPa internal pressure, the LB and MB curves are almost the same, with the HB case displaying a slightly lower CFE for both the zero and 67kN EF cases. Because burst was not achieved for the zero and 67kN EF cases, no significant observations can be made on the effect of boost and EF on the formability of IF tubes.
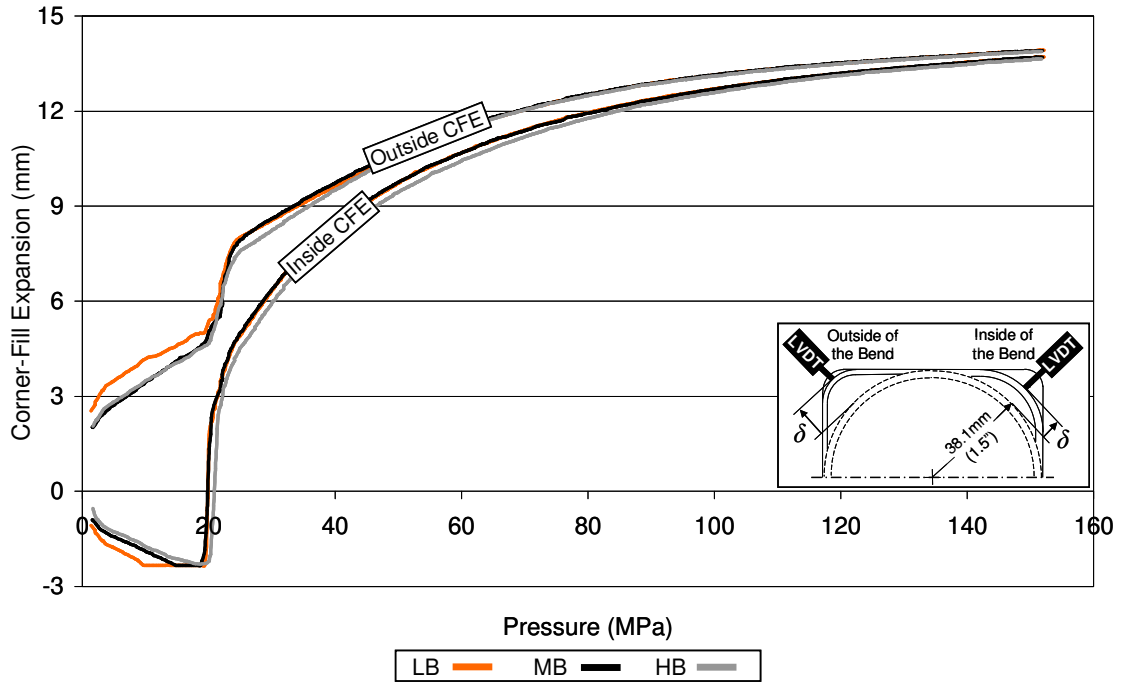
Figure 80: CFE *vs.* internal pressure, IF pre-bend tubes, 67kN EF
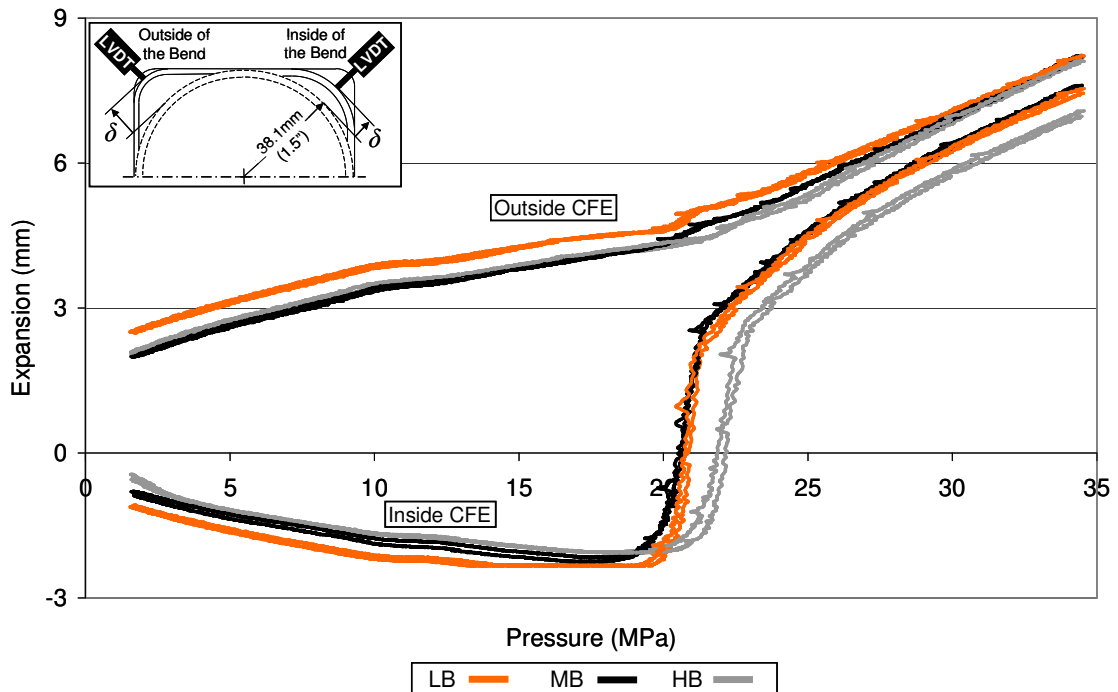
Figure 81: CFE *vs.* internal pressure, IF pre-bend tubes, zero EF

109

5.2.5 End-Feed Displacement

Figure 82 shows the end-feed (EF) displacement *versus* pressure response for the DP600 burst tests and the 67kN EF IF tests. The DP600 curves shown in Figure 82 are for a single "median" burst test from the group of burst tests (for a given EF case). (Appendix F shows all of the individual burst test EF displacement curves for each EF case, and shows the good repeatability of the EF displacement results). For the zero EF displacement result, the data point is the average of the EF displacements from Table 10.
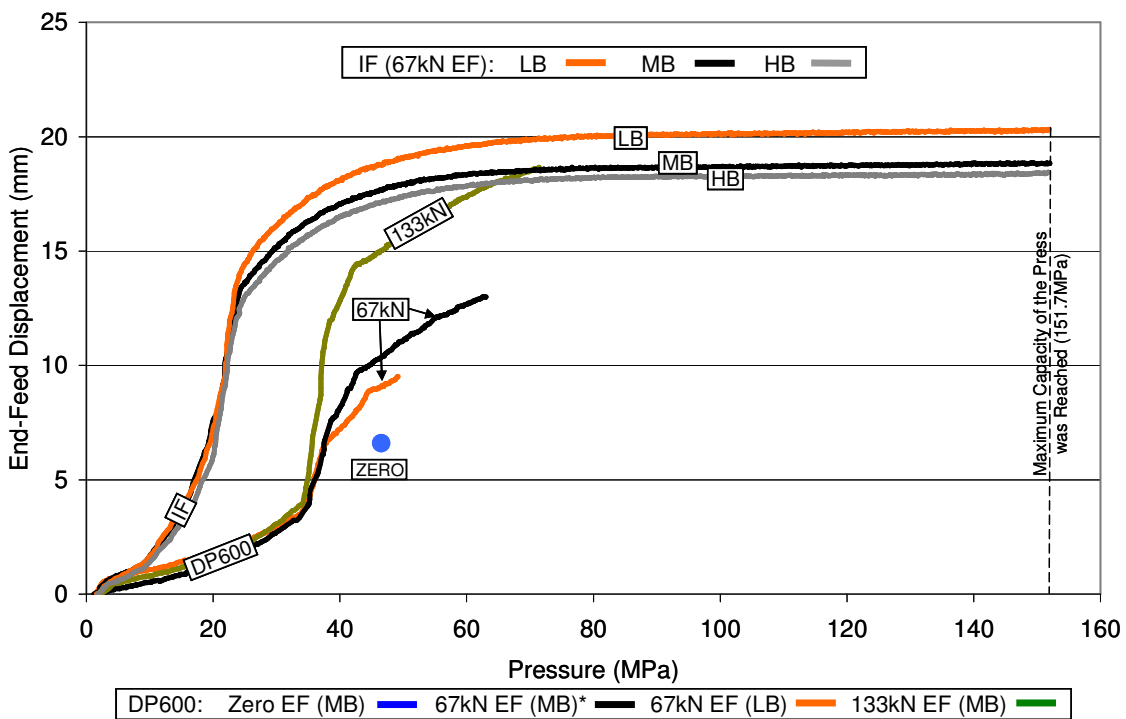
* Tube burst at 87% of average burst pressure

Figure 82: EF displacement *vs.* internal pressure for DP600 burst tests and IF pre-bend tubes

For all of the DP600 results, a rapid increase in EF displacement occurs between 35MPa and 38MPa, which is the pressure range when EF is applied. A more constant and steady increase in EF displacement occurs after 38MPa. For the IF tests, EF is applied between 20MPa and 23MPa. After 23MPa, the EF displacement rate decreases until it eventually plateaus at approximately 70MPa pressure.

5.2.6 Strain and Thickness Measurement

The strain and thickness was measured for the DP600 tests following the procedure outlined in Section 3.2.7. As indicated in the footnote to Table 10 (***), the 90% interrupted 67kN EF MB case actually burst prematurely at 87%, therefore only a portion of the strain and thickness distribution was measured due to high post fracture deformation. Figure 83 shows the measured strain and thickness distribution for the DP600 90% interrupted MB tests. Due to the poor quality of the circle grids on the LB tube, there was no strain measured. Since a true 90% interrupted 67kN EF MB test was not available, the thickness distribution of the 70% interrupted LB and MB tests is shown in Figure 84. The dashed lines in the strain and thickness plots are the as-bent strain and thickness distributions. The measured strain and thickness distributions for individual EF and boost cases can be found in Appendix F.
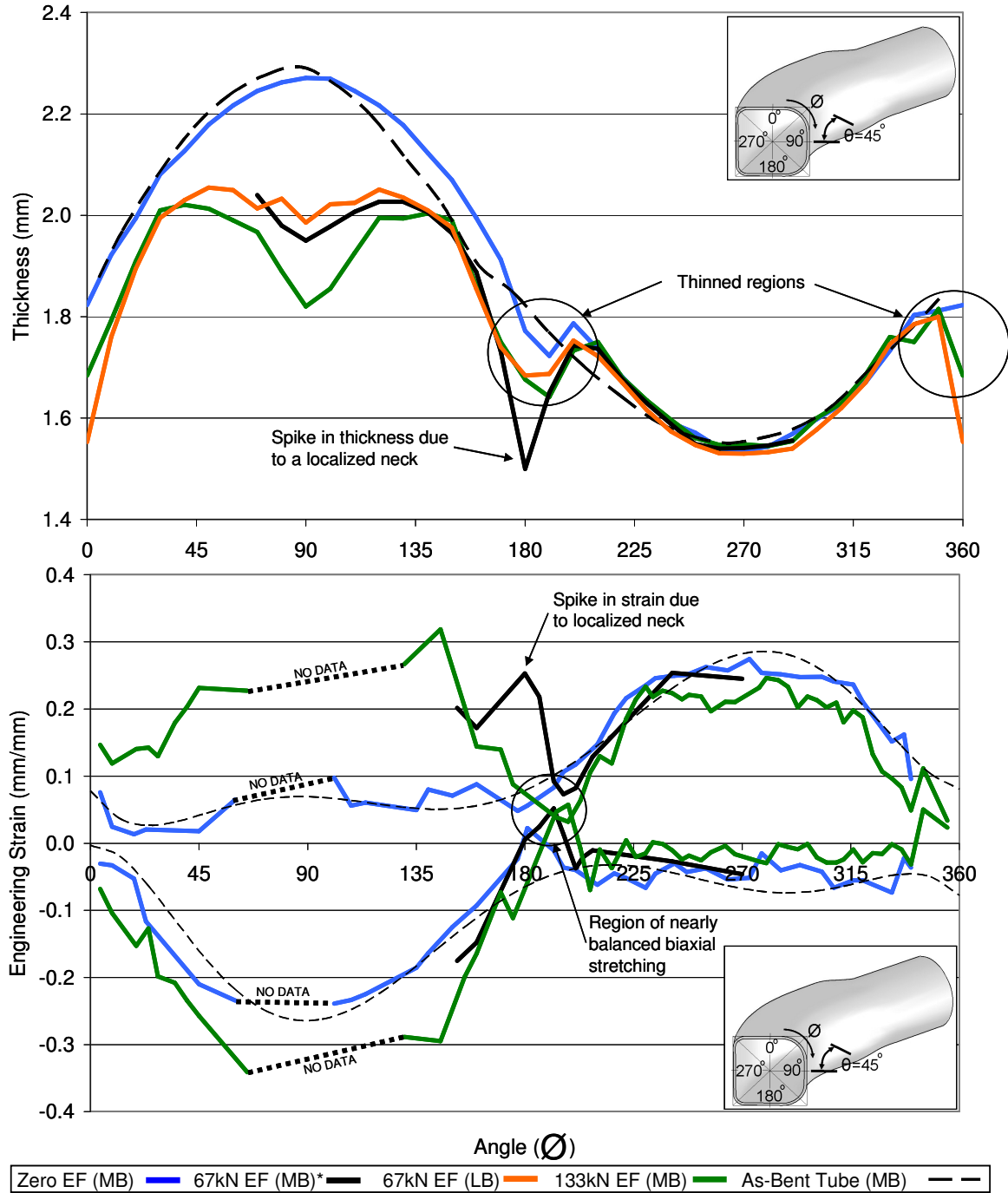
Figure 83: Measured thickness and strain distribution for DP600 (MB) pre-bend tubes, 90% interrupted. See Appendix F for strain and thickness distributions plots for each EF case.

* Tube burst at 87% of average burst pressure
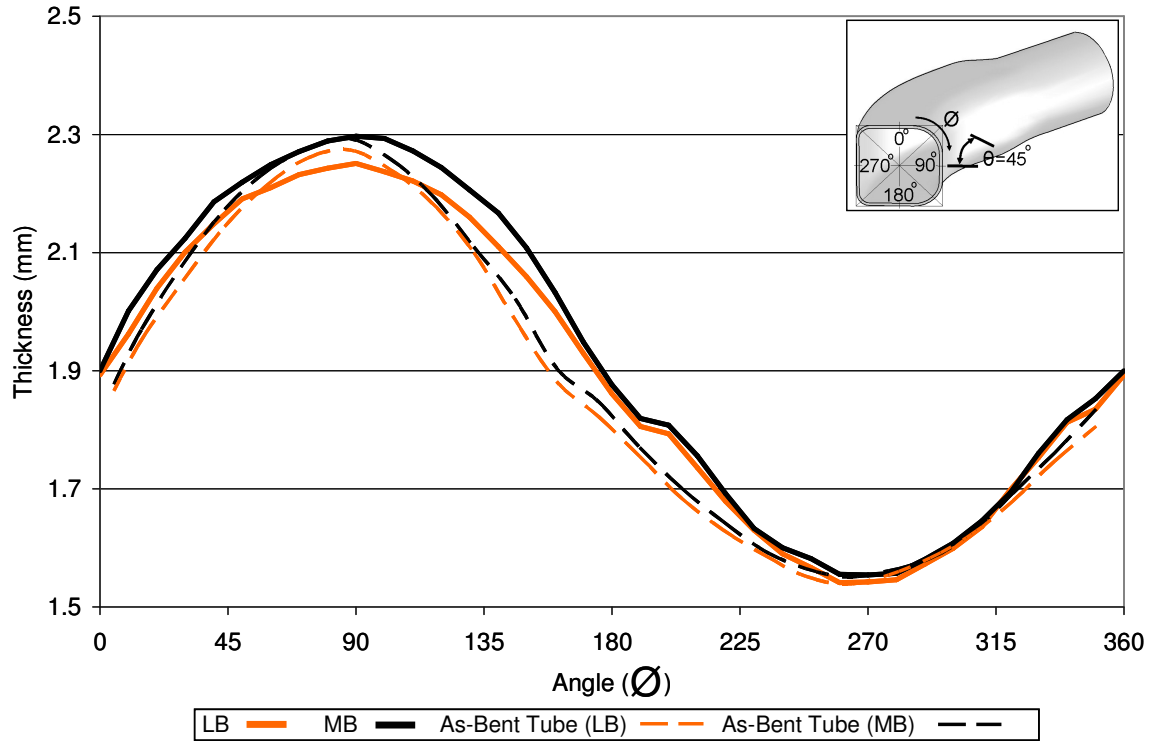
Figure 84: Measured thickness distributions for DP600 pre-bend tube, 70% interrupted

Due to pre-bending and hydroforming, the circle grids were worn off of all IF tubes and strain was not measurable. Thickness distributions for the zero EF tests are shown in Figure 85 and the thickness distributions for the 67kN EF tests are shown in Figure 86.
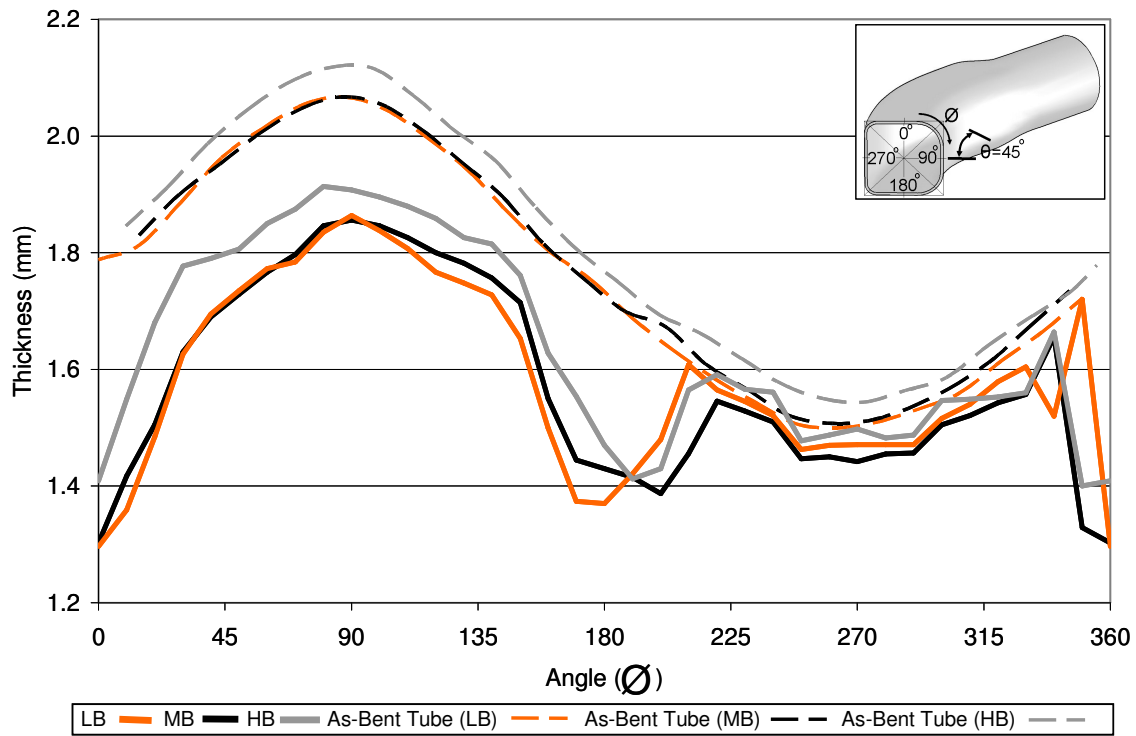
Figure 85: Measured thickness distributions for IF pre-bend tube, zero EF, stopped at 34.5MPa
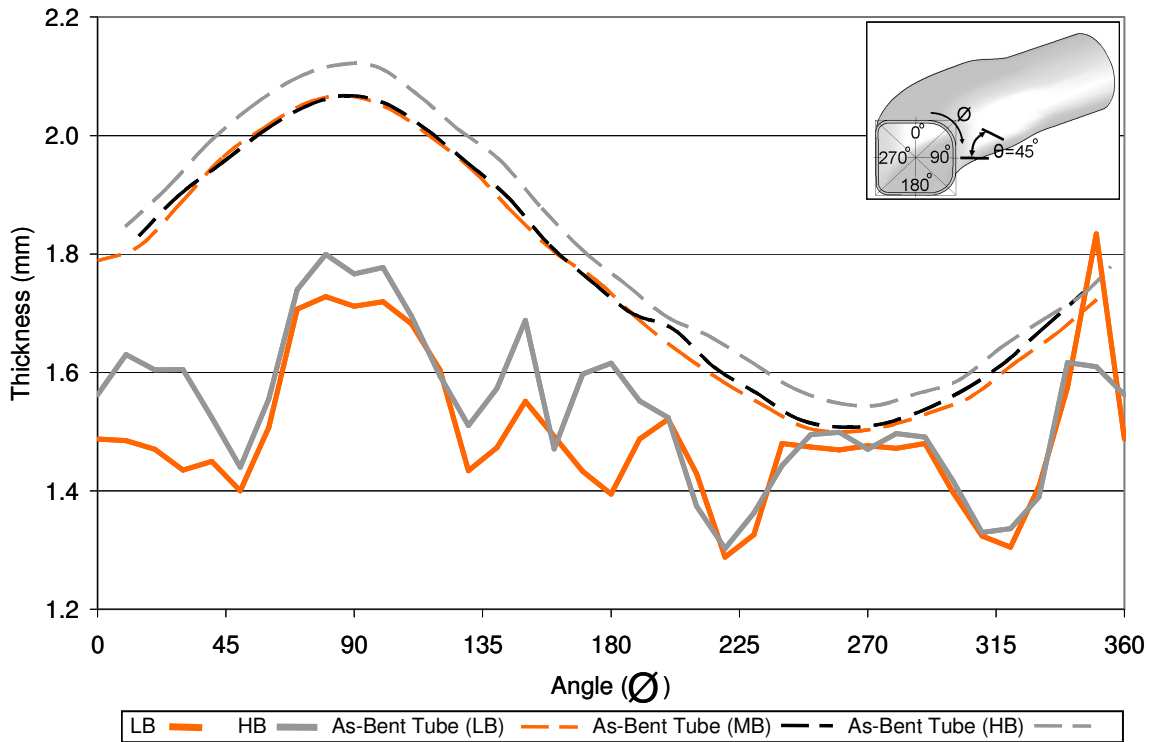
Figure 86: Measured thickness distributions for IF pre-bend tube, 67kN EF, stopped at 151.7MPa (maximum capacity of press)

The following observation can be made on the effect of EF and tube material on the strain and thickness distributions,

Strain

Strain distributions were difficult to measure for the DP600 tubes because of the excessive circle grid wear during pre-bending and hydroforming. This effect was worse for the inside of the bend region which corresponds to $45° < \emptyset < 135°$ and results in missing data for the zero and 133kN end-feed (EF) cases (Figure 83). Circle grid wear was so poor for the LB 67kN EF test, that no strains were measured around the circumference. Because the MB 67kN EF tube actually burst at 87%, many of the grids could not be measured due to the tube post-burst deformation. Furthermore, the spike in major strain was a result of a localized neck that would not have been present if the tube did not burst.

The zero EF test did not have a significant change in strain distribution from the strains measured for the as-bent tube which are shown as a dashed line in Figure 83. The main difference between the hydroformed and as-bent strain distribution occurs at $225° < \emptyset < 315°$, where the tube is in contact with the die at the outside of the bend. Here, the strain distribution is fairly constant at 0.28 strain. For $180° < \emptyset < 360°$, the minor strain is close to the as-bent strain distribution.

Major differences in strain distribution between the as-bent and 133kN EF hydroformed tube were observed in Figure 83. At the inside of the bend $(0° < \emptyset < 180°)$, the major (tensile) strain increases from 0.10 to approximately 0.25. The increase in major strain from the as-bent condition is in the hoop direction of the tube and is due to circumferential expansion. The minor strain for this region is compressive and acts along the longitudinal direction of the tube. The minor strain becomes more compressive, which is due to the compressive EF load in the longitudinal direction and natural draw-in of the material (Poisson's effect) during circumferential expansion. It should be noted that no strain was measured from $65° < \emptyset < 130°$, due to poor circle grid quality. Similar to the zero EF case, the major strain distribution is flat for $225° < \emptyset < 315°$. The flat distribution has an approximate

115

value of 0.22 strain, which is less than the zero EF case. The reduction in major strain (longitudinal direction) is due to the compressive longitudinal load from EF during hydroforming. The minor strain for 180°<∅<360° is fairly constant and less than the zero EF case.

For 180°<∅<200°, all of the major and minor strain curves show the same trend (Figure 83). Major strain is similar to the as-bent strain, while the minor strain becomes positive and tensile. Because the major and minor strain are close in magnitude and positive (tensile), it appears that the tube is in a state of balanced biaxial stretching within 180°<∅<200°. This may also occur at ∅=0°, but not enough strain data was available. Thickness measurements will help to confirm this conjecture.

Thickness

For the zero end-feed (EF) case, the thickness distribution coincides with the strain distribution of the as-bent tube (dashed line) and is shown in Figure 83. For 180°<∅<200°, there is a definite decrease in thickness (thinning) which coincides with the observed change in strain (biaxial tension) for 180°<∅<200°. The thinned area is also consistent with the burst locations that are presented in Table 11.

The 67kN EF (LB and MB) and 133kN EF thickness distributions show similar trends. The greatest difference (from the zero EF case) occurs at the inside of the bend region (30°<∅<150°), where the thickness drops considerably compared to the as-bent thickness distribution. For the 67kN EF LB and MB case, the thickness drops from a maximum as-bent thickness of 2.3mm to approximately 2.05mm, which represents a reduction of 11%. Both the LB and MB cases show a local drop in thickness at ∅=90°. The 133kN EF case shows a similar drop in thickness for 30°<∅<150°, but a considerably more pronounced local reduction in thickness at ∅=90°. The thickness at ∅=90° is 1.8mm and represents a 22% reduction in thickness. For both EF cases, the thinning at ∅=90° is due to the high circumferential (hoop)

116

expansion that is shown by the increase in hoop (major) and longitudinal (minor) strain (Figure 83). Similar to the zero EF case, the 67kN (LB and MB) and 133kN EF thickness distributions show a drop in thickness at Ø=180°. There is also a drop in thickness at the Ø=0°/360°.

Because the DP600 67kN EF MB test (90% interrupted) burst prematurely, it is difficult to compare the effect of bending boost on thickness distribution during hydroforming. In order to observe the effect of bending boost on the thickness of the tubes during hydroforming, the 67kN EF LB and MB hydroforming tests were conducted to 70% of their average burst pressures. Figure 84 shows the measured thickness distribution of the 70% interrupted LB and MB tests. At the 70% interrupted pressure, both tubes have just made contact with the die at the inside of the bend. For 0°<Ø<360°, the LB tube is thinner than the MB tube. This difference is most obvious from 0°<Ø<180°. Although the difference in thickness is not great, the thicker MB tube can support a higher internal pressure and exhibit greater formability by achieving more corner-fill expansion (CFE).

Figure 85 and Figure 86 also serve to verify the bending boost effects for the IF tests. In both figures, the HB thickness distribution is generally greater than the LB and MB cases. For zero EF (Figure 85), the LB and MB thickness are similar for the majority of the distribution, which is a result of their similar as-bent thickness distributions. For the 67kN EF case (Figure 86), the MB tube was not available for measurement, but is expected to behave similarly to the LB case. For 0°<Ø<180°, the HB thickness is consistently greater than the LB case.

The shape of the IF thickness distributions are considerably different from the DP600 thickness distributions. For the zero EF case (Figure 85), the entire 0°<Ø<180° thickness distribution appears to shift down from the as-bent distribution. A much larger degree of thinning occurs at the Ø=180° and Ø=0° locations. The high formability of the IF material allows the tubes to thin much more than the DP600 tubes before failure occurs. For 67kN EF, the IF tubes (LB and HB) have a drop in thickness at the four corners of the die (Ø=45°, 135°, 225° and 315°). This is considerably different than the DP600 tubes, which thin only slightly,

117

if at all at these locations. Thinning at $\varnothing=0°$ and $\varnothing=180°$ occurs for the IF tubes and was also observed for the DP600 67kN EF tests.

Table 10 presents the overall average circumferential thickness for the DP600 (90% interrupted) and IF (at final pressures) tubes. Thickness is calculated by averaging the circumferential thickness measurements for $0°<\varnothing<360°$ and the percent reduction is calculated by subtracting the average circumferential thickness from the as-tubed initial thickness. The DP600 tests indicate that overall circumferential thinning increases as EF increases for a given bending boost level. Also, the IF results indicate that increased boost reduces thinning for a given EF level.

5.3 Experimental Results Summary

The main findings of the hydroforming experimental study are presented in this section. Specifically, the effect of bending boost and end-feed (EF) on the average circumferential thickness, burst pressure, and corner-fill expansion (CFE) are analyzed for the DP600 and IF tests. The differences between straight and pre-bend hydroforming is also be highlighted.

Figure 87 shows the averaged thickness around the circumference of the straight tubes (as-tubed), after pre-bending and after hydroforming (90% interrupted, unless otherwise noted). The effect of hydroforming EF on thickness is shown for the DP600 results, while the effect of bending boost on thickness is shown by the IF results.
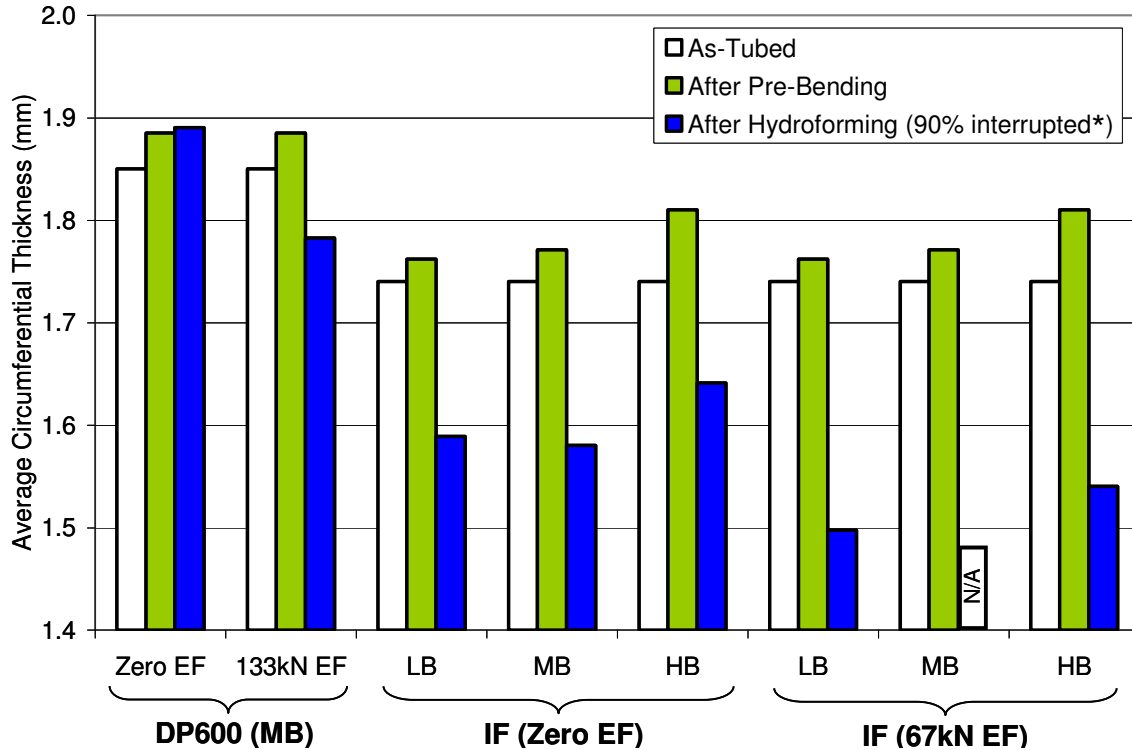
* For DP600. IF tubes were measured at the pressures specified in Table 10, column 5.

Figure 87: Effect of bending boost and hydroforming EF on thickness after hydroforming

Figure 87 shows that an increase in EF from zero to 133kN reduces the average circumferential thickness (of 90% interrupted tests) from 1.89mm to 1.78mm which is a 6% decrease This shows that increased EF during hydroforming allows a tube to thin more just prior to failure. The increase in thinning is a result of an increase in strain, which suggests that EF allows a tube to sustain greater deformation (strain) during hydroforming.

Because the IF LB and MB pre-bending average circumferential thickness are very similar, the zero EF tests show little difference between the LB and MB thickness after hydroforming. The HB bending case shows a 0.05mm thicker (3% increase) average circumferential thickness compared to the LB and MB cases and is a result of the greater average circumferential thickness after pre-bending. A similar trend is shown for the IF 67kN EF case, where the HB tube is 0.04mm thicker (3% increase) than the LB tube (Note that the MB test was not available). Although none of the IF hydroforming tests were taken to burst,

the increased average circumferential thickness of the higher boost tubes suggests that a higher internal pressure and expansion could be supported.

Burst pressures for the DP600 straight and pre-bend tube experiments are presented in Figure 88. Burst pressure is dependent on the amount of EF for both straight and pre-bent tubes. The burst pressure is also dependent on the amount of boost applied during pre-bending.
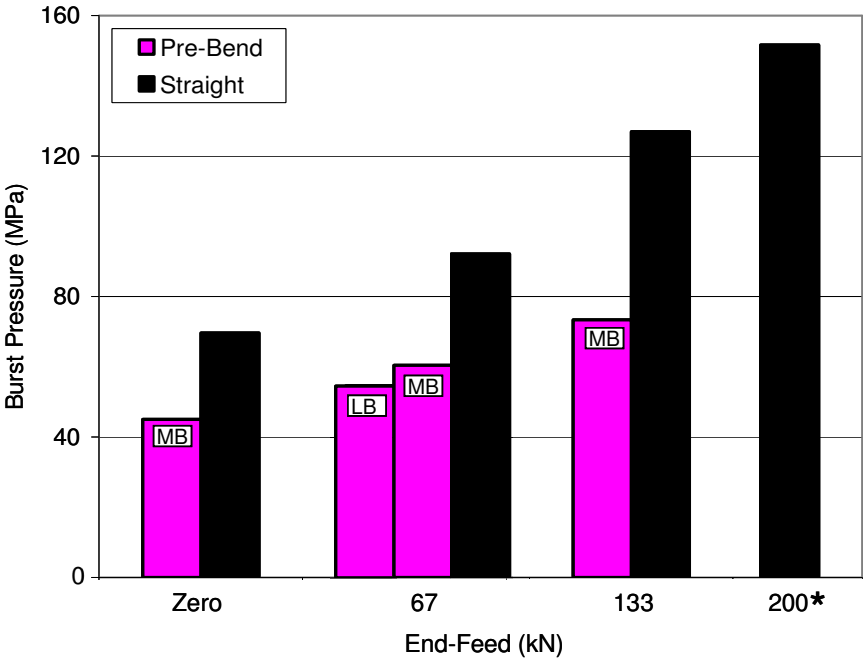
* Burst was not achieved because the maximum capacity of the press was reached (151.7MPa)

Figure 88 Effect of EF on burst pressure for 90% interrupted DP600 straight and pre-bend tubes

There is a considerable increase in straight tube burst pressure for increased EF, while the difference is more subtle for the pre-bent tubes. The straight tube burst pressure increases by 57MPa (82% increase) for an increase in EF from zero to 133kN, while the pre-bent tube burst pressure increases by 28MPa (63% increase) for the same increase in EF. For the zero EF case the pre-bent tube burst pressure is 25MPa less (35% reduction) than the straight tube burst pressure. For the 133kN EF case, the pre-bent tube burst pressure now becomes 54MPa less (42% reduction) relative to the straight tube burst pressure. The lower burst pressure of

120

the pre-bent tubes is a result of the loss in ductility (formability) that was consumed during pre-bending.

The effect of bending boost is also shown for the 67kN EF case. The MB tubes have a 10MPa greater burst pressure than the LB tubes, which is attributed to the MB tubes being thicker after pre-bending.

The DP600 pre-bent tube corner-fill expansion (CFE) results are summarized in Figure 89 and Figure 90. Figure 89 shows that increased EF results in greater hydroformability (by increasing the CFE). Application of 133kN of EF, improves the average CFE by 41% (difference in total CFE) over the zero EF case. Figure 89 also shows that increasing the bending boost from LB to MB (67kN EF case), increases the average CFE by 3%. EF increases the CFE by delaying failure (fracture) during hydroforming, while bending boost increases CFE by increasing the thickness of the tube during pre-bending and therefore allowing the tube to achieve a higher internal pressure. Increasing EF also causes the difference between the outside and inside CFE to reduce as shown in Figure 89. This is important for manufacturing a more square (similar inside and outside CFE) pre-bent part.
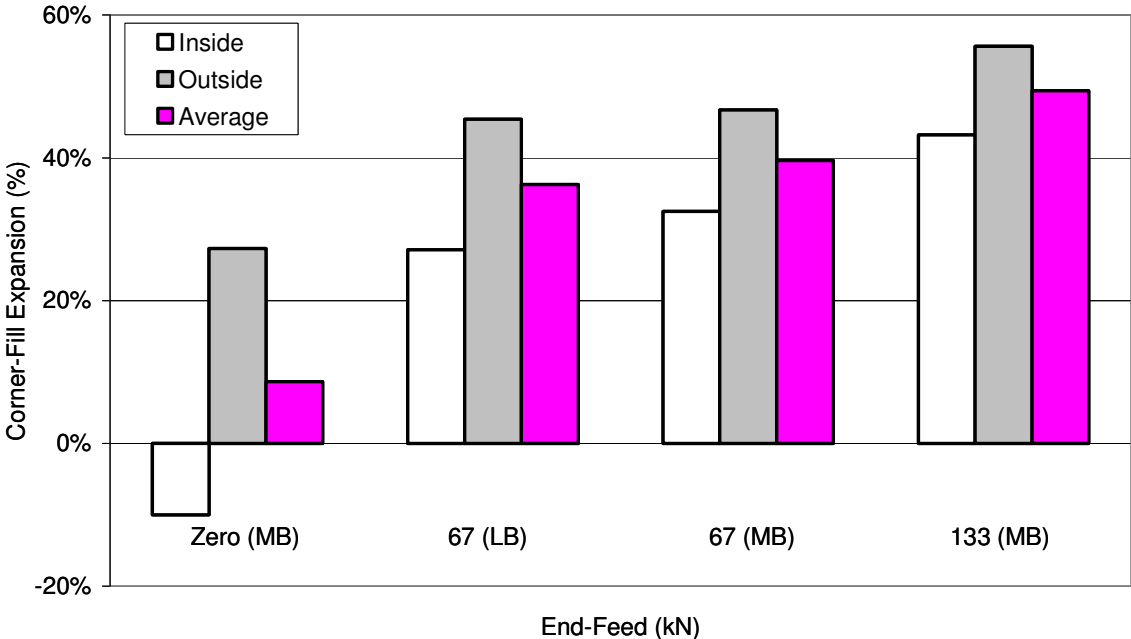
Figure 89: Effect of EF on inside and outside CFE for 90% interrupted DP600 pre-bend tubes

Figure 90 serves to illustrate the effect of pre-bending on the hydroformability (CFE) of the DP600 tubes by contrasting the results of the straight and pre-bend experiments. For the zero EF case, the difference in CFE between the straight and pre-bend tube is very significant, even though the difference in burst pressure is not as drastic (Figure 88). The overall percentage reduction in zero EF CFE between the straight (45% average CFE) and pre-bent tubes (9% average CFE) is 80%. This is a significant decrease in CFE which is a result of the formability consumed during the pre-bending process. For the 133kN EF case, the pre-bent CFE (49%) is 30% less than the straight tube CFE (70%) and indicates that the formability which is consumed during pre-bending can be compensated for by application of end-feed.
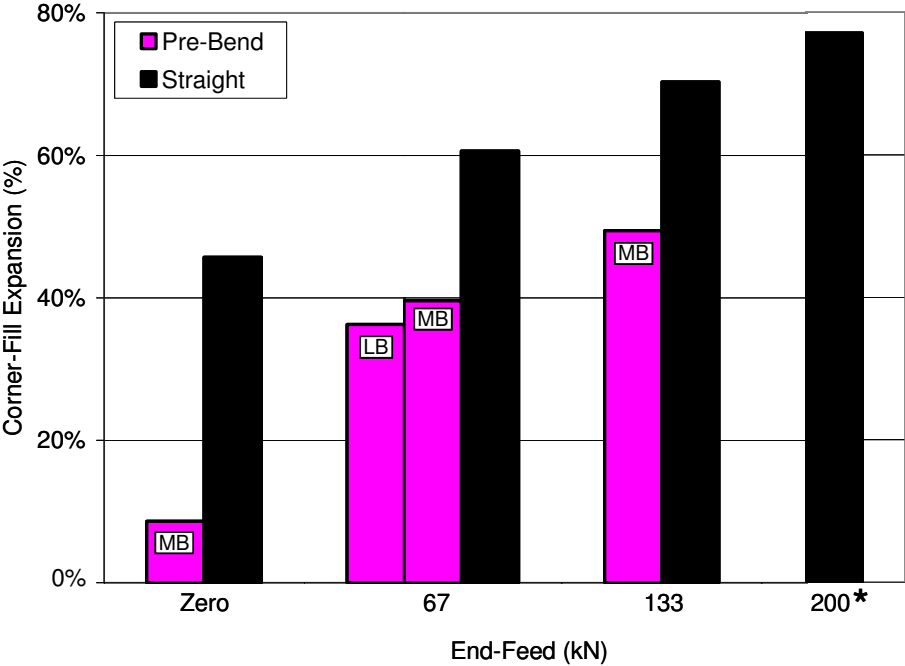
* Burst was not achieved because the maximum capacity of the press was reached (151.7MPa)

Figure 90: Effect of EF on DP600 and IF tube CFE. Average CFE is plotted for the pre-bent tubes.

CHAPTER 6

NUMERICAL MODELING PROCEDURE

Finite element (FE) models were used to simulate the pre-bending and hydroforming operations. For straight tube hydroforming, a single model was run, while the pre-bend hydroforming process was simulated with the following models:

1. Pre-Bending
2. Springback after pre-bending
3. Hydroform die closure and end-feed ram insertion
4. Hydroforming with end-feed

6.1 Finite Element Formulation

The finite element (FE) models presented in this thesis were solved using the dynamic explicit formulation within LS-DYNA (Hallquist, 2003). The springback numerical models were solved using the static implicit formulation within LS-DYNA. A 24 processor Linux cluster with 3.06 Ghz Pentium-4 processors was used for all of the models.

The geometry for the hydroforming tools (Section 3.2.4 and 3.2.5) was developed in solid model format using SolidWorks 2004. The FE meshes of the tubes and various tooling components for the bending and hydroforming models were created with Altair Hypermesh v5.0. LS-PREPOST was the post-processor software used to analyze the results.

The DP600 and IF flow stress curves that were generated from the uniaxial tensile tests discussed in Section 2.1.2, and shown in Figure 33, were used to define the constitutive model of the tubes which obeyed the Von-Mises yield criterion.

6.2 Pre-Bending Simulation

6.2.1 Finite Element Mesh

The finite element (FE) meshes for the bend tooling and deformable tube are shown in Figure 91 (a) and (b). A half-symmetry model (about the Z-X plane) was used to reduce computational time. All of the tool surfaces were meshed with four-noded quadrilateral shell elements with a rigid material model, adopted for its computational efficiency. The tube was modeled with five though-thickness eight-noded constant-stress brick elements. Although brick elements are less efficient than shell elements, they are required for the implementation of the XSFLC failure criterion, which utilizes the three principal stress components. The element density along the length of the tube is "fine" within the bend region and "coarse" along the unbent region for computational efficiency (Figure 91 b).

The "fine" mesh adopted for the simulation of the DP600 tubes consists of 2.34mm x 2.37mm x 0.37mm (longitudinal x hoop x thickness) elements, while the "coarse" mesh elements are 7.02mm x 2.37mm x 0.37mm. The elements for the IF tube have the same longitudinal and hoop dimensions, but have a thickness of 0.35mm due to the lower tube wall thickness. A total of 77,520 elements were used for the tube. The number of elements used to mesh each of the pre-bending tools is shown in Table 12.
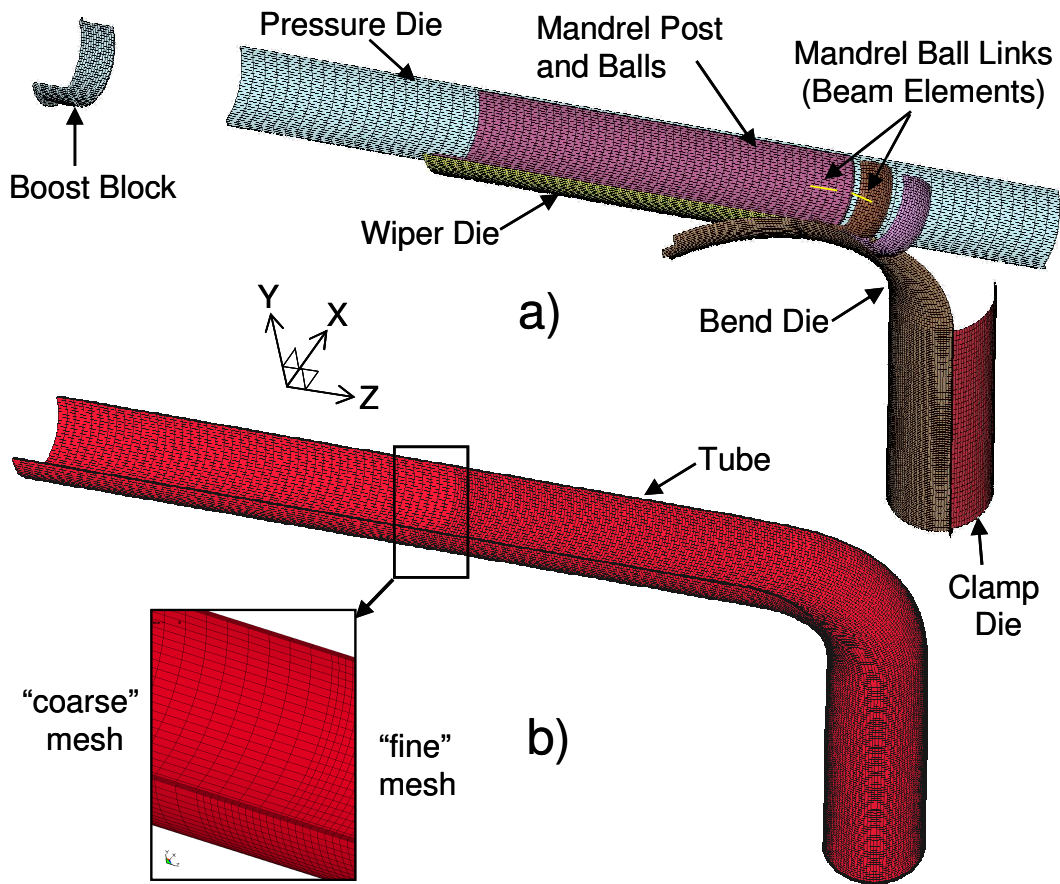
Figure 91: a) The R/D=2.0 pre-bend tooling meshes (shell elements) b) Tube mesh (brick elements) showing the "fine" and "coarse" regions (shown at a bend angle of 70°)

Table 12: The number of elements, active degrees of freedom and coefficient of friction characteristics used for the pre-bending model

Mesh	Number of Elements	Active Degrees of Freedom	Twist Compression Test Coefficient of Friction	Increased Coefficient of Friction Values
Bend Die	6,699	Y-Rotation	0.08	0.13
Pressure Die	2,240	X and Z-Translation	0.08	0.13
Boost Block	928	X and Z-Translation	0.08	0.13
Clamp Die	1,280	X and Z-Translation	0.08	0.13
Wiper Die	4,972	No active degrees of freedom (fixed)	0.06	0.08
Mandrel	4,290	X and Z-Translation	0.04	0.08

In order to accurately simulate the mandrel assembly kinematics (Figure 91 a), rigid beam elements were used to connect the balls and post following the approach of Dyment (2004). The boost block assembly, shown in Figure 42 and Figure 43, was considered in all of the tube bending simulations. The boost block is rigidly attached to the pressure die. The wiper die rake angle is set to 0.3 degrees, which replicates the measured rake angle from the experiments.

6.2.2 Contact and Friction

The surface-to-surface, penalty stiffness-based contact algorithm was implemented to model the contact between the tube and all of the tube bender tools. The static and dynamic coefficients of friction (COF) between the bending tools and tube were measured using the twist compression test (Section 2.2.2) and are shown in Table 12. In addition to the COF determined from the twist compression test, the MB bending simulation was also run with the increased COF values shown in Table 12. This model was run to observe the effects of increased COF on the prediction of the pre-bending process variables and the strain and thickness distributions of the bent tubes.

6.2.3 Constraints, Prescribed Motions and Loads

Table 12 summarizes the active degrees of freedom for the individual tools. These degrees of freedom are the same as those in the experiments. There are no boundary conditions or constraints imposed on the tube other than those imposed through the contact-friction interferences defined with the tooling and those imposed through the symmetry plane. The tube bending simulation run time is 30 milliseconds and requires roughly 16.5 hours to solve using a four-processor (parallel) run.

Dyment (2004) found that the simulation time affected the prediction of the pre-bending process variables because of dynamic effects introduced during acceleration and deceleration of the tools. Through trial and error, the simulation times were optimized for the computational time with the least level of dynamic effects.

Figure 92 shows the prescribed load and displacement time-history curves used for the pre-bending simulation. The y-axis magnitude of each tool shown in Figure 92 is scaled from 0 to 1. A magnitude of 1 represents the full prescribed load or displacement applied in the experiments. The magnitude of the prescribed loads and displacements are shown in Table 3. During the first 3 milliseconds of the simulation, the clamp die closes 1mm in the x-direction using displacement control and remains closed for the entire simulation. The pressure die also closes in the x-direction in the first 6 milliseconds, but acts under load control. After 6 milliseconds, the pressure die x-load remains constant for the entire simulation. At 6 milliseconds, the bend die begins to rotate about the y-axis and the pressure die (and boost block) begins to displace in the z-direction. At 28 milliseconds (corresponds to an 85° bend angle), the mandrel displaces in the negative z-direction under displacement control, again matching the experiments in which the mandrel is withdrawn from the tube near the end of the bend.
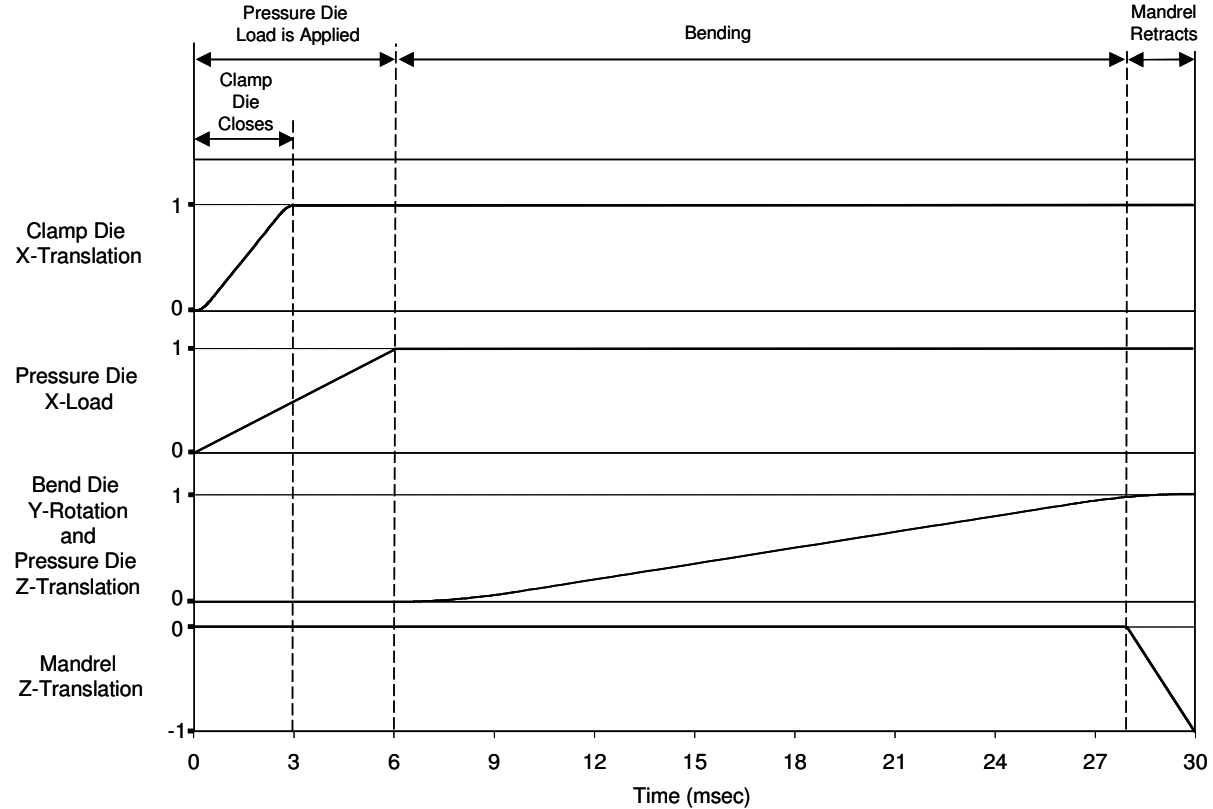
Figure 92: Tube bending tool prescribed load and displacement time histories

127

6.2.4 Springback

To account for the deformation accumulated during the pre-bending simulation, a file which contains the final workpiece geometry, stress and strain tensors and selected tool meshes is generated after the final time step of the pre-bending simulation. The springback simulation uses this file as input. This procedure is repeated for the die close and hydroforming simulations.

The nodes at the end of the tube, shown in Figure 93 (a), were fully constrained during the springback simulation. After springback was simulated, the post-springback angle of the tube was checked against the hydroforming die mesh.

Nodes along the edge of the tube are fully constrained during springback

Zoom-in

a)

Before Springback

After Springback

Springback Angle

b)
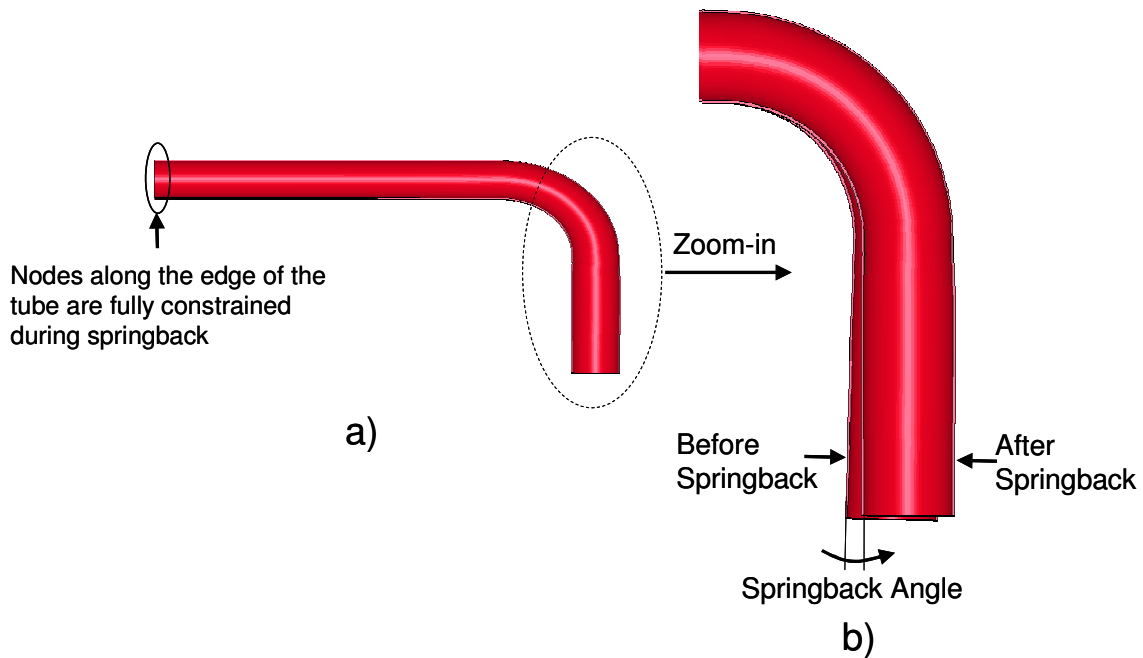
Figure 93: a) Screen capture of the pre-bent tube, showing the constrained nodes b) Overlaid images of the tube before and after springback

6.3 Die Close Simulation

In order to prepare the pre-bent tube (after springback) for hydroforming, the tube is trimmed and the die closure operation is simulated. The tube mesh is trimmed of the "coarse" elements (new element count is 62,160) to fit the hydroforming die, as shown in Figure 94 (a). After the tube is trimmed, a null (zero thickness) shell mesh is created at the inside surface of the tube and used to define the internal surface to which the pressure is applied during the hydroforming simulation. The hydroforming die and EF rams were meshed with quadrilateral elements and were assigned a rigid material model (Figure 94 b). The number of elements used to mesh the die closure tools are shown in Table 13.
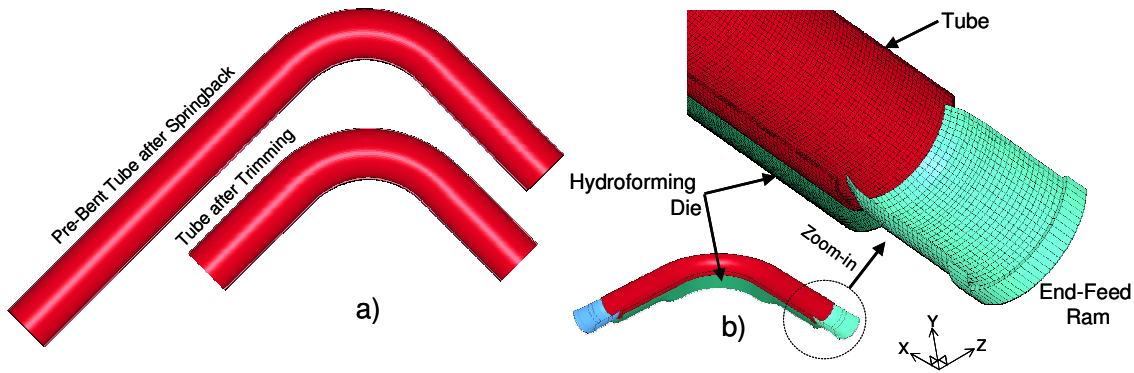
Figure 94: a) Image of pre-bent tube and trimmed tube b) Image of mesh applied to the end-feed ram

Table 13: The number of elements, active degrees of freedom and coefficient of friction characteristics used for the die closure model

Tool	Number of Elements	Active Degrees of Freedom	Twist Compression Test Coefficient of Friction
Hydroforming Die	29,467	Y-Translation	0.035
Null Shell	10,800	Constrained to the nodes on the internal surface of the tube	0.0
End-feed Ram (Mandrel)	945	Z -Translation	0.08
End-feed Ram (Clamp)	945	X -Translation	0.08

For the die close simulation, a surface-to-surface, penalty stiffness-based contact algorithm was used to model the contact between the hydroforming tools and tube. The coefficient of friction (COF) between the tube and hydroforming die was measured using the twist compression test (Section 2.2.2) and is shown in Table 13. The COF between the rams and inside of the tube was not tested, but was set to 0.08.

The die close simulation is 4 milliseconds in duration and requires roughly 13.8 hours to solve with a single processor. The simulation begins with the die moving in the y-direction (closing) under displacement control (during the first 2 milliseconds). After the die closes, the EF rams are inserted into the tube under displacement control, as shown in Figure 95.
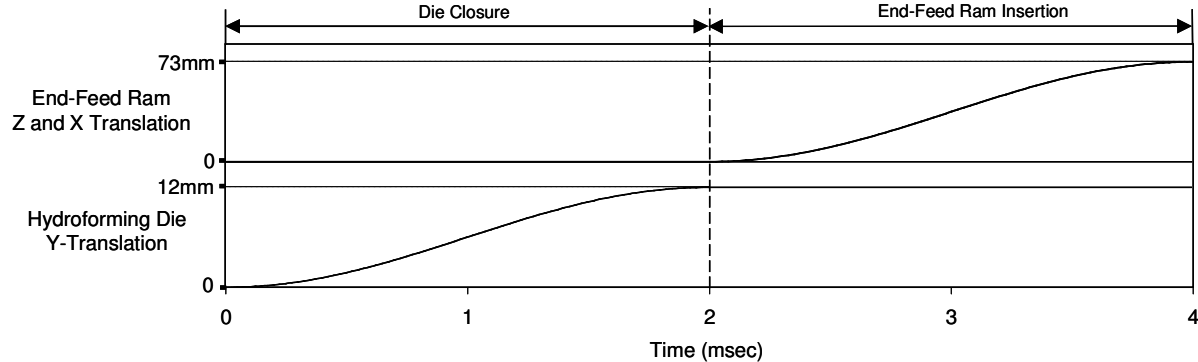
Figure 95: Die close tool prescribed displacement time-history curves

6.4 Straight and Pre-Bend Tube Hydroforming Simulations

After die closure, the pre-bend tube hydroforming simulation proceeds. The straight tube hydroforming simulation does not require a die close simulation; therefore it is run in a single step.

6.4.1 Finite Element Mesh

The pre-bend hydroforming mesh is the same as the mesh after the die closure simulation and is shown in Figure 96 (a). Also shown in Figure 96 is the 1/8th-symmetry

straight tube hydroforming mesh. The tube, in the straight tube hydroforming model, is modeled with 80,000 eight-noded constant stress brick elements. The DP600 straight tube element dimensions are 1.97mm x 0.07mm x 0.37mm (longitudinal x hoop x thickness). The IF tube mesh elements have a thickness of 0.35mm. Similar to the pre-bend tube, the straight tube hydroforming die and end-feed (EF) rams are modeled with quadrilateral shell elements and a rigid material model. The number of elements used to mesh the pre-bend and straight tube hydroforming tools are shown in Table 13.
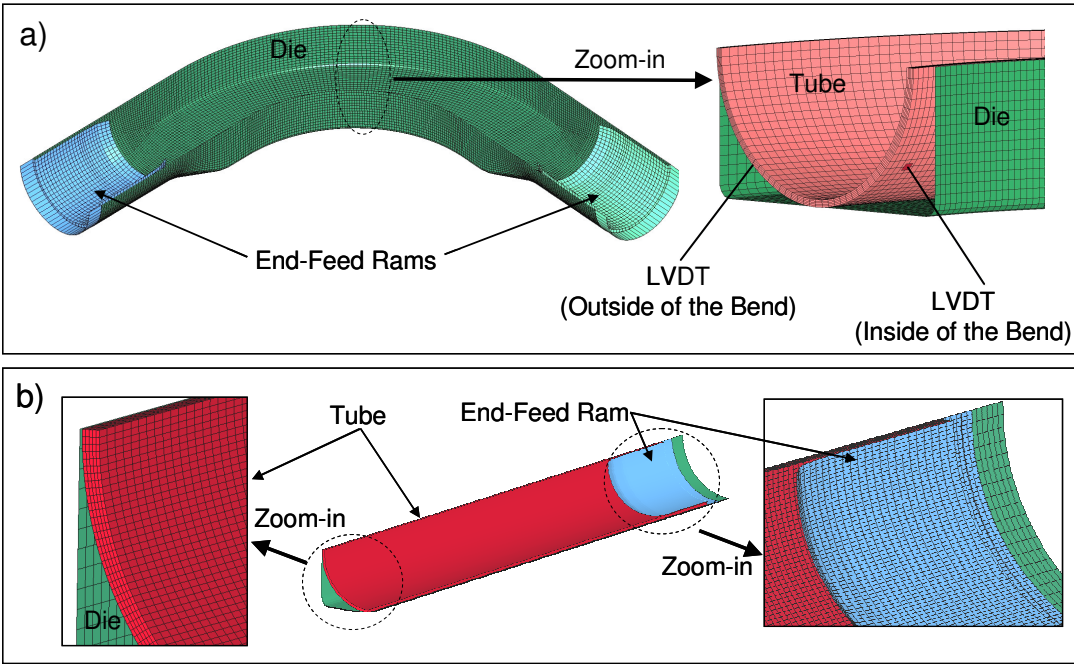
Figure 96: a) 1/8th-symmetry straight tube hydroforming model showing the mesh b) 1/2-symmetry pre-bent hydroforming model showing the mesh

Table 14: The number of elements, active degrees of freedom and coefficient of friction characteristics used for the hydroforming models

Tool	Number of Elements	Active Degrees of Freedom	Twist Compression Test Coefficient of Friction	Increased Coefficient of Friction Values
Pre-Bend - Die	29,467	No active degrees of freedom (fixed)	0.035	0.07
Pre-Bend – End-Feed Ram (Mandrel)	945	Z -Translation	0.08	0.08
Pre-Bend – End-feed Ram (Clamp)	945	X -Translation	0.08	0.08
Straight Tube - Die	7,054	No active degrees of freedom (fixed)	0.035	0.07
Straight Tube – End-feed Ram	3,600	Z-Translation	0.08	0.08

At the beginning of the pre-bend hydroforming simulation, two beam and shell elements are defined and used to simulate the LVDT displacement probes used in the experiments. For each LVDT, a shell is connected to a beam and is used to contact the outer surface of the tube as shown in Figure 96 (a). Only one LVDT is used in the straight tube hydroforms.

6.4.2 Contact and Friction

For both hydroforming simulations, a surface-to-surface penalty stiffness-based contact algorithm was once again used to model the contact between the tube and the die, rams and LVDT displacement probes. The coefficient of friction (COF) between the tube and hydroforming die was measured using the twist compression test (Section 2.2.2) and used as an input to the model. The COF between the rams and inside of the tube was not tested and the value analyzed is given in Table 14. A COF of zero was used to model the contact between the LVDT probe and tube. In addition to the COF determined from the twist compression test, the straight and pre-bend (MB) 67kN end-feed hydroforming simulations were run with an increased COF, as shown in Table 14. This model was run to observe the effects of increased COF on the prediction of formability during hydroforming. One should

note that for the pre-bent hydroforming simulation with the increased COF, the pre-bend simulation was run with the twist compression test COF values.

6.4.3 Constraints, Prescribed Motions and Loads

Table 14 summarizes the active degrees of freedom for the hydroforming die and EF ram meshes. There are no boundary conditions or constraints imposed on the tube other than those imposed through the contact-friction interferences defined with the tooling and those imposed through the symmetry plane(s). The straight and pre-bend hydroforming simulations have a run time of 60 and 30 milliseconds respectively. The longer straight tube run time was necessary to overcome dynamic effects which were a result of the difference between the straight and pre-bent tube geometry. The computational time for the straight and pre-bend hydroforming simulations was roughly 49.3 hours (4 processor parallel run) and 139.8 hours (single processor) respectively. The pre-bend simulation could not be solved with a multi-processor parallel simulation due to unexplainable contact problems between the tube and hydroforming die.

Figure 97 shows the prescribed load and displacement time-history curves used for both the straight and pre-bend hydroforming simulations. During the first 2 milliseconds, the LVDT displacement probes are activated by applying a small load of 85N to hold the probes against the tube. At 2 milliseconds, the internal pressure (which acts on the null shell mesh at the inside of the tube) pre-pressurizes the tube (no EF is applied) up to 3 milliseconds. After 3 milliseconds, the pressure is constantly increased to the maximum hydroforming pressure of 151.7MPa (22,000psi). Just before 2 milliseconds, the EF ram load is ramped up slightly (using load-control) and held constant to simulate the EF pre-load during ram insertion. At 3 milliseconds (when pre-pressurization is complete) the full EF load is applied up to 4 milliseconds and held constant for the remainder of the simulation. The maximum EF load scale in Figure 97 is set to the values shown in Table 5 for the different EF cases.

133
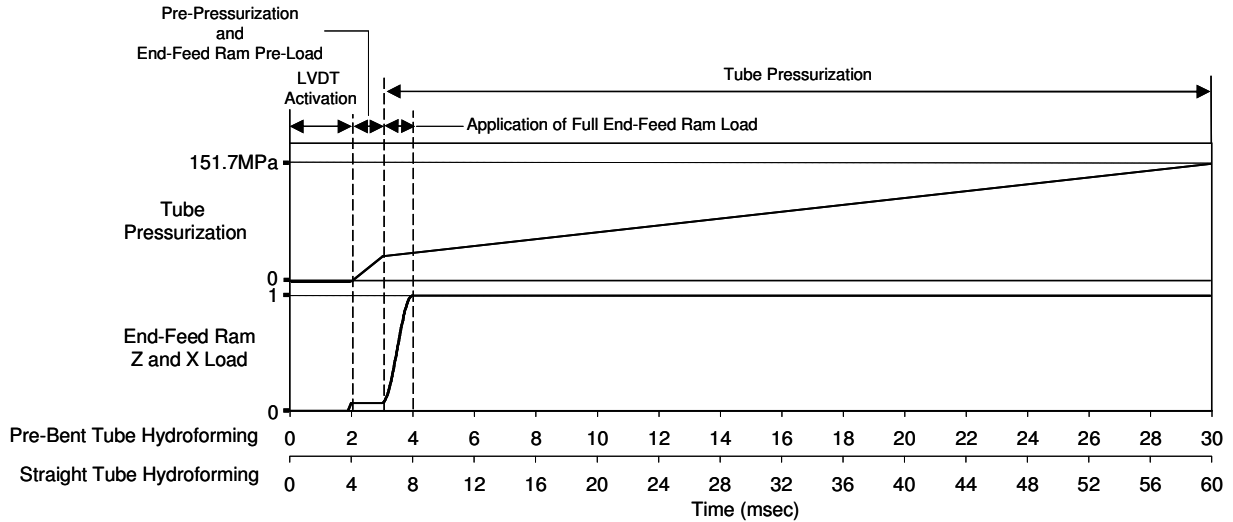
Figure 97: Prescribed end-feed ram load and internal pressure time-histories

6.5 XSFLC Failure Criteria Implementation and Evaluation

The formability of the tubes was predicted using the extended stress-based forming limit curve (XSFLC) failure criterion due to Simha *et al.* (2006). To implement the XSFLC failure criterion, a subroutine was developed and used to track the proximity of the effective and mean stress path to the XSFLC curve for each element at each time step (Figure 98 a). A material input file is used by the subroutine to define the XSFLC curve (in effective and mean stress space) and the material flow stress curve. A binary history variable (γ) is introduced to track the proximity of each element to the XSFLC curve. If γ is greater than or equal to 1, then that element has crossed the XSFLC curve and is considered to have "necked", as shown in Figure 98 (b). It should be noted that necking failure in a tube is predicted to occur only after all of the elements through-the-thickness have crossed the XSFLC curve.

134
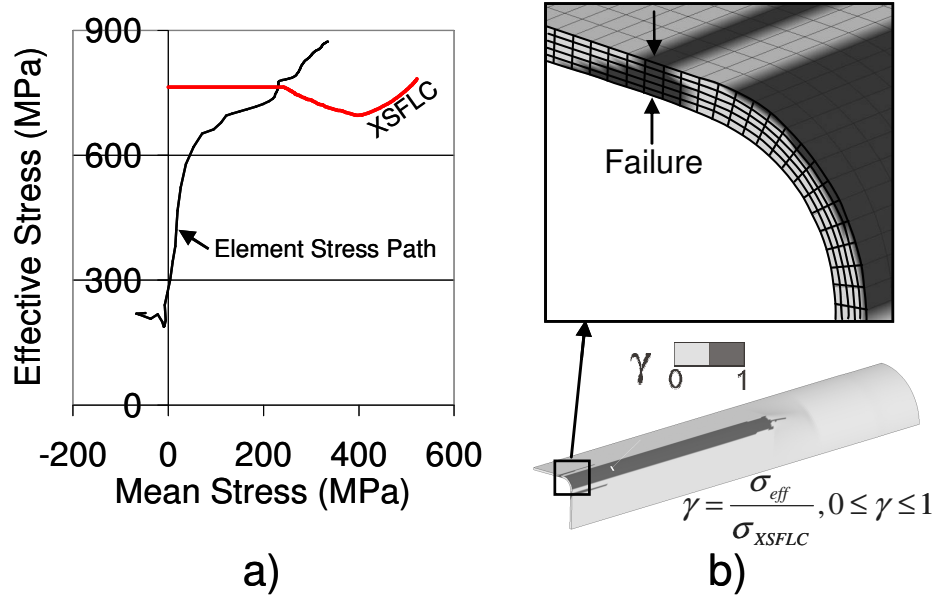
Figure 98: XSFLC failure analysis method

At the end of the pre-bending simulation, the subroutine generates an output file that is used as an input for the hydroforming simulation. This file is used to adjust the XSFLC curve based on the degree of tensile or compressive pre-strain experienced during pre-bending. For greater detail on the XSFLC subroutine, refer to Simha *et al.* (2006).

CHAPTER 7

NUMERICAL SIMULATION OF THE TUBE BENDING EXPERIMENTS

This chapter presents the application of the finite element (FE) models used to simulate the pre-bending process and comparison of these predictions with the experimental results presented in Chapter 4. First, the process variables are shown after which the strain and thickness distributions are assessed. A final summary of this validation exercise is presented at the end of this chapter.

7.1 Process Variables

The accuracy of the pre-bending models is evaluated through comparison with the measured process variables, namely pressure die load, mandrel load and bend die torque. The predicted and measured process variables are compared for both materials and all boost conditions considered in the experiments. Note that the DP600 HB bending case was not tested in the experiments due to equipment limitations; therefore for the DP600 HB case, only the predicted results are presented. For the DP600 MB bend case, an additional simulation was performed using increased frictional coefficients and was also compared to the measured results.

7.1.1 Process Variable: Pressure Die Boost Load

The DP600 and IF pressure die boost load predictions are shown in Figure 99. The load corresponds to the z-direction reaction force (Figure 91) of the coupled pressure die and boost block within the numerical models. The dashed lines indicate the region of steady-state bending condition for both the experiments and simulations.
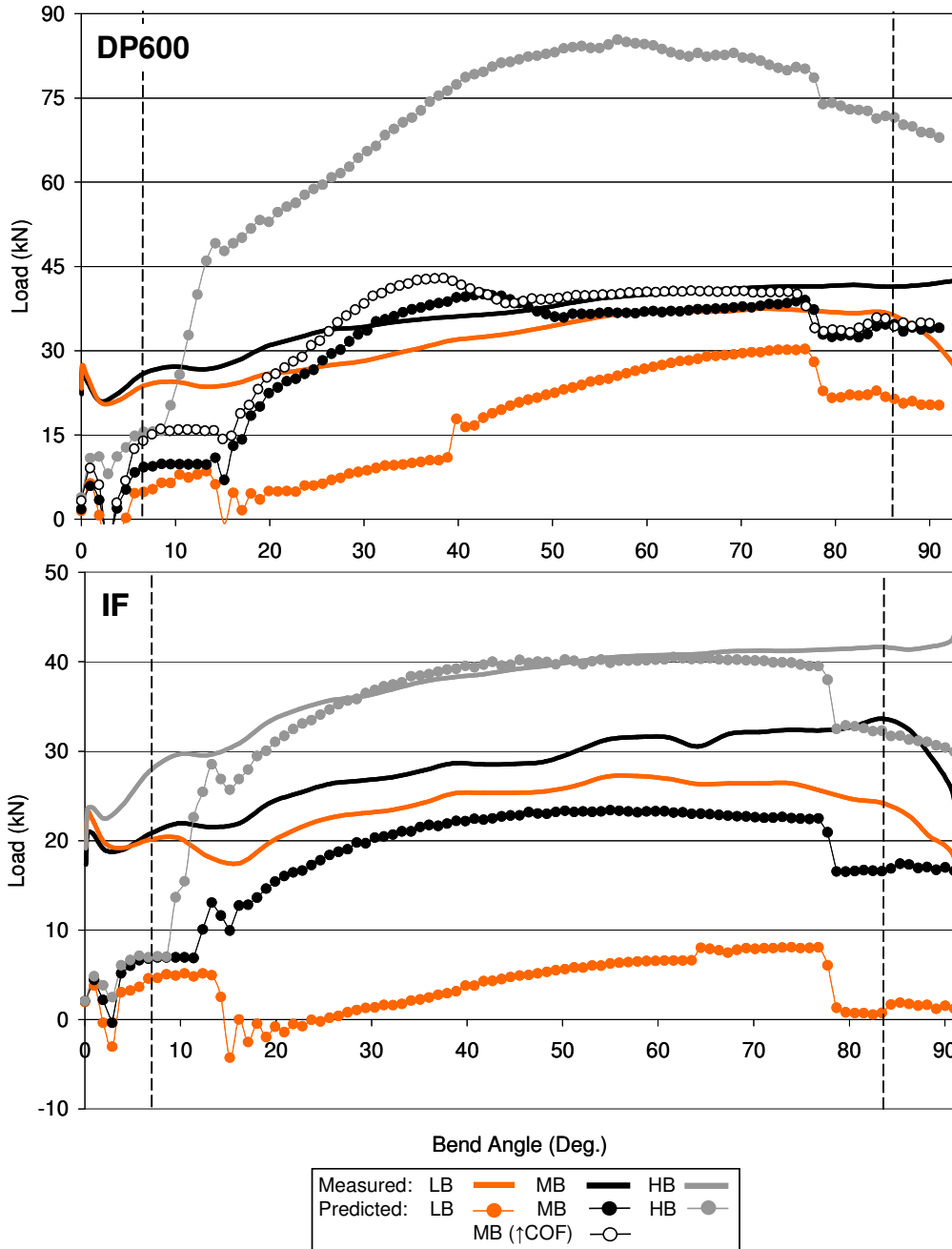
Figure 99: Predicted and measured pressure die boost loads for the DP600 and IF tubes. Note that the MB (↑COF) prediction compared to these using an elevated friction coefficient. Note also that no HB DP600 experiments were performed

At the beginning of the DP600 simulation, the predicted boost loads begin at approximately zero, while the measured boost loads begin at approximately 25kN. Within the steady-state region, the DP600 predictions show a similar trend to the measured results, with

the MB results matching better than the LB results. The predicted HB boost load has a maximum peak at 85kN, which is approximately twice that of the MB bending case. There is little difference between the MB predictions using the measured or "high" friction coefficients, which is a result of the limited sliding between the tube and pressure die.

For the IF tube bending simulations, the predicted pressure die boost loads also begin at zero, while the measured boost loads begin at approximately 20kN. The trends of the predicted boost loads are very close to those of the measured loads, but only the HB case matches well with the measured boost load. The predicted MB boost load is also close, while the LB boost load is approximately one third of the measured load.

The "calibration test" pressure die boost load presented in Figure 57 of Section 4.1.2, of the experimental chapter, suggested that approximately 11.8kN of boost load was required to overcome the internal friction within the system. The addition of 11.8kN boost load to the predicted results in Figure 99 would improve the accuracy of the DP600 and IF model predictions.

7.1.2 Process Variable: Mandrel Load

The predicted and measured mandrel load for the DP600 and IF bends are shown in Figure 100. The total mandrel load is the sum of the z-direction force components of the mandrel balls and post.
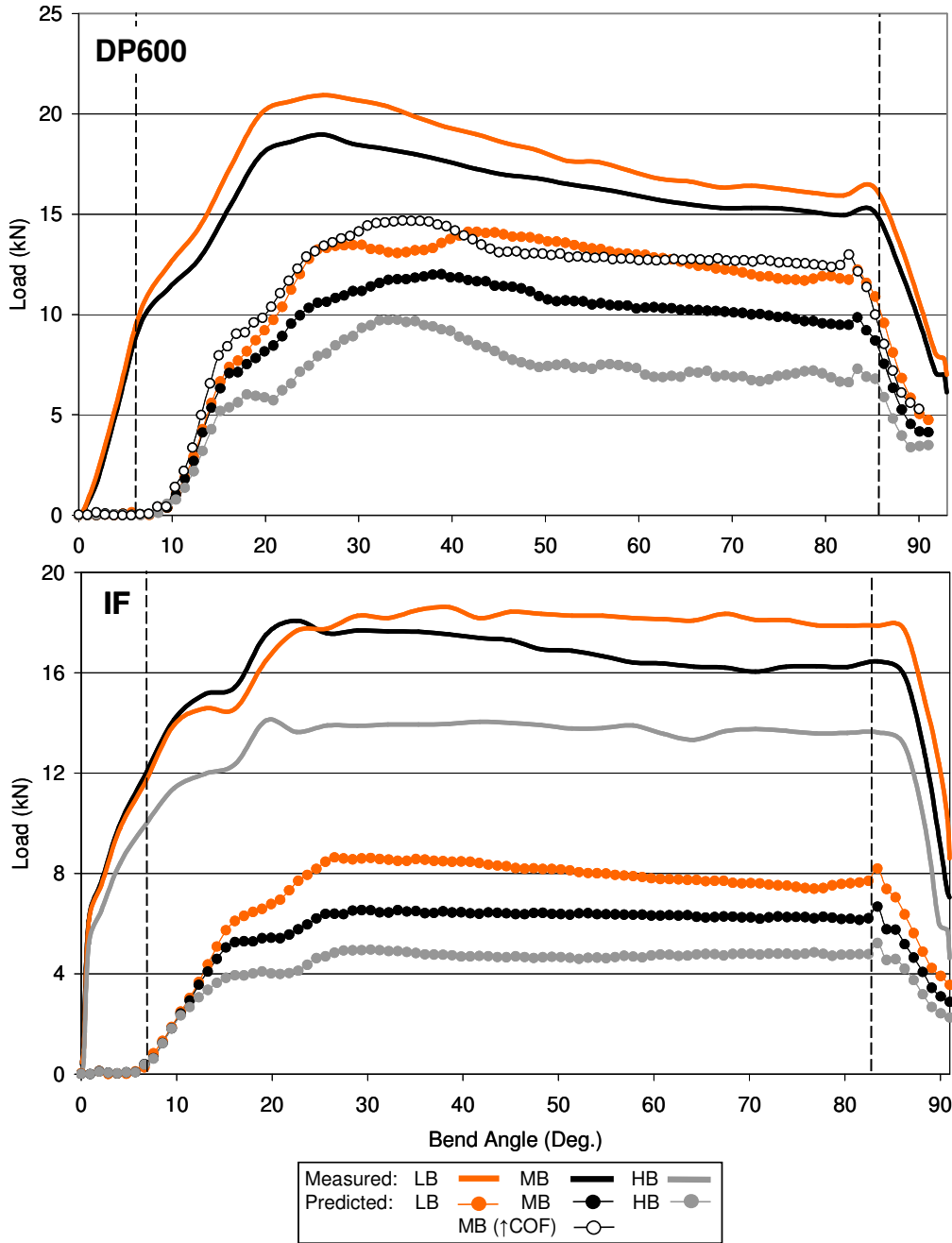
Figure 100: Predicted and measured mandrel loads for DP600 and IF. Note that the MB (↑COF) prediction compared to these using an elevated friction coefficient. Note also that no HB DP600 experiments were performed

For both the DP600 and IF tubes, the predicted mandrel load trends match relatively well with the measured results. Although the trends are similar between the predicted and measured results, the magnitude of the predicted mandrel loads is approximately two thirds

and one third of the measured value for the DP600 and IF tubes, respectively. By increasing the coefficient of friction between the mandrel and tube ($\uparrow$COF prediction), the predicted mandrel load is closer in magnitude to the measure magnitude for the DP600 MB case. This indicates that the COF selected for the mandrel assembly may be too low.

The measured mandrel load for the "dry run" (Figure 58 of Section 4.1.3) was insignificant and would not affect the overall prediction for either DP600 or IF.

7.1.3 Process Variable: Bend Die Torque

Dyment (2004) used a numerical technique to couple the clamp die to the bend die for a more accurate method of predicting the bend die torque. This technique was attempted, but did not function as a result of using brick elements to mesh the tube (Dyment used shell elements for the tube). For this reason, the total predicted bend die torque is the sum of the bend die and clamp die y-axis moments. Due to strong oscillations present in the predicted moments, a 4-point average filter was applied to smooth out the results. The unfiltered predictions can be found in Appendix G. The predicted bend die torques for the DP600 and IF bends are shown in Figure 101.
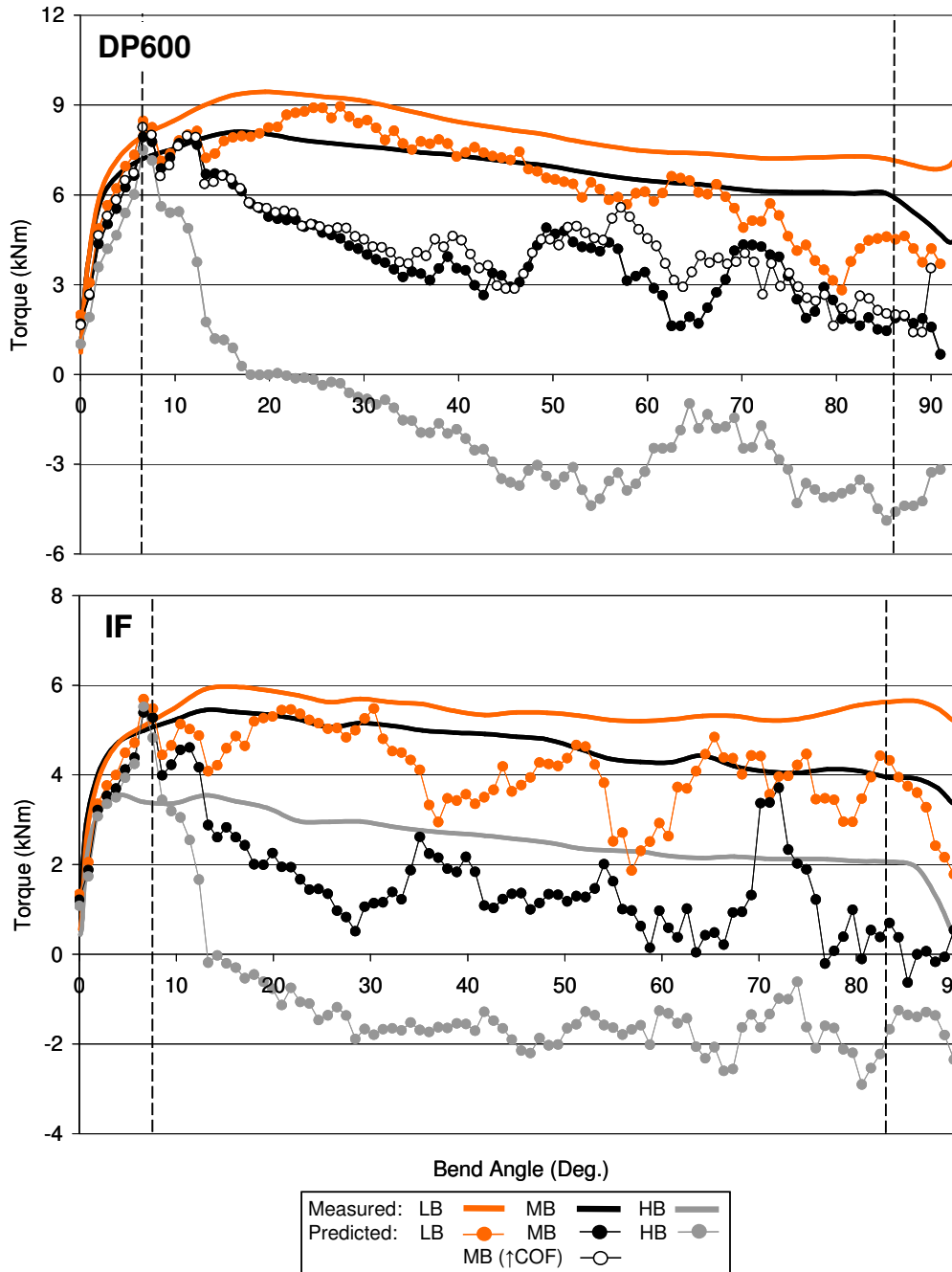
Figure 101: Predicted and measured bend die torque for DP600 and IF. Note that the MB (↑COF) prediction compared to these using an elevated friction coefficient. Note also that no HB DP600 experiments were performed

The DP600 LB bend die torque prediction is close in both trend and magnitude to the measured torque, while the MB trend fluctuates and is approximately one-half the magnitude of the measured torque. The HB torque is mostly negative and indicates that the bend die

torque is acting opposite to the bending direction. The effect of varying the coefficient of friction between the tube and bend tools on the predicted bend torque is negligible. The measured IF HB case shows that the bend die torque is not negative, therefore making the HB prediction questionable.

The "calibration test" bend die torque was 1.2kNm and is shown in Figure 59 of Section 4.1.4. The addition of 1.2kNm bend die torque to the predicted results in Figure 101 would slightly improve the accuracy of the DP600 and IF model predictions.

7.1.4 Summary

Table 15 summarizes the predicted average steady-state values for the pressure die boost load, mandrel load and bend die torque. The average steady-state values are an average of the predicted results within the steady-state region shown by the dashed lines in Figure 99, Figure 100 and Figure 101. In addition to the predicted average values, the measured average steady-state values from Table 7 are presented for comparison. Figure 102 is a plot of the average loads (measured and predicted) in a bar chart to compare the models to the experiments.

Table 15: Average steady-state process variable summary, predicted and measured

Material	Boost	Average Predicted Pressure Die Boost Load (kN), [Measured]	Average Predicted Mandrel Load (kN), [Measured]	Average Predicted Bend Die Torque (kNm), [Measured]
DP600	LB	17.2 [31.7]	11.3 [17.5]	6.8 [8.2]
	MB	31.3 [35.9]	9.4 [16.1]	4.1 [7.1]
	MB ($\uparrow$COF)	34.5 [35.9]	11.6 [16.1]	4.5 [7.1]
	HB	NA [69.2]	NA [6.9]	NA [-1.4]
IF	LB	4.0 [23.9]	7.3 [17.4]	4.2 [5.5]
	MB	19.4 [28.0]	5.8 [16.5]	1.7 [4.8]
	HB	35.2 [37.4]	4.4 [13.4]	-1.1 [2.7]
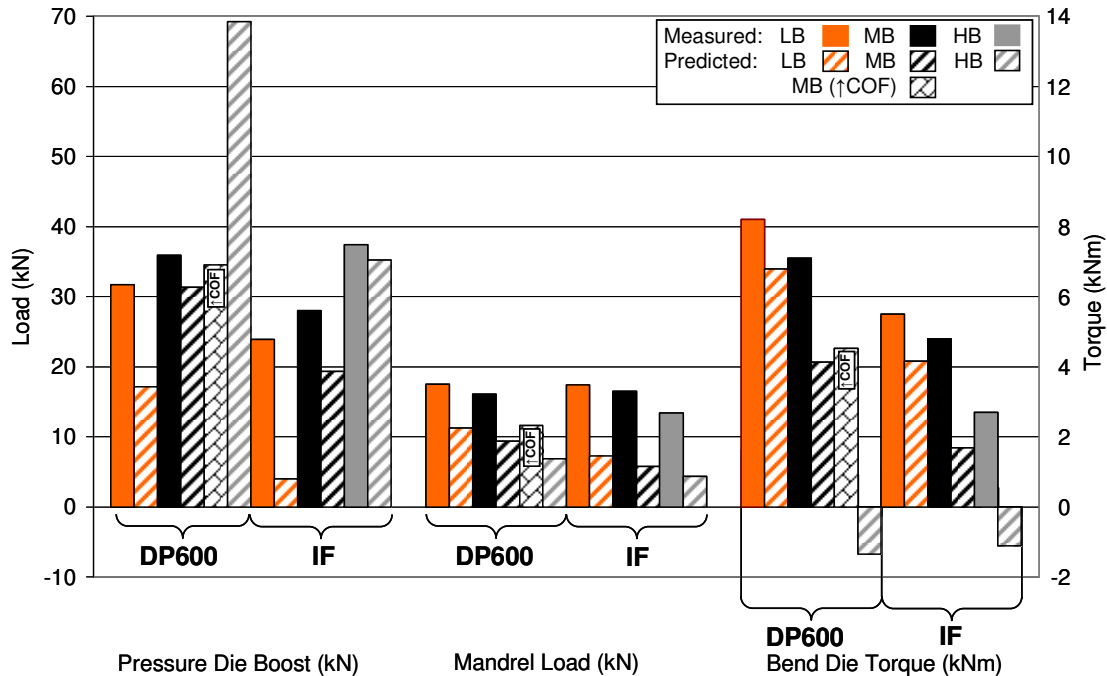
Figure 102: Average predicted and measure process variable bar graph

For both the DP600 and IF tubes, all of the predicted process variables show the same trends (increase or decrease) with respect to the boost level, although the magnitudes are always less than the measured values.

Both the DP600 and IF models are able to predict the trend of increased pressure die boost load for increased bending boost. Generally, the predicted mandrel loads for both materials show the same trends as the measured results, but are considerably less in magnitude than the measured values.

One possible source of the discrepancy in the measured loads is the internal friction within the tube bender. The "calibration test" experiment presented in Sections 4.1.2, 4.1.3 and 4.1.4 showed that the average boost load and torque required to overcome the internal friction within the bender was 11.8kN and 1.2kNm, respectively. The addition of the 11.8kN and 1.2kNm loads to the predicted average values in Figure 102 would considerably improve the agreement with the measured values.

7.2 Strain and Thickness

The results of the numerical model strain and thickness predictions are presented in this section and compared to those measured in Section 4.2. A summary is also included to compare the predicted and measured average steady-state values.

7.2.1 Predicted Strain and Thickness Measurement Technique

The predicted strain and thickness results were extracted from the models after the springback simulation. The engineering strain was calculated as the surface strain using the post-processor LS-PREPOST. Thickness was calculated as the distance between element nodes. For the inside and outside of the bend, a 5° measurement interval was used while the measurement frequency around the circumference of the bend was 10°, Figure 47.

7.2.2 DP600 Results

Figure 103 shows the effective strain contour plot for LB and HB pre-bent tubes. The effect of increased boost can be seen in the decreased strain at the inside of the bend and increased strain at the outside of the bend.
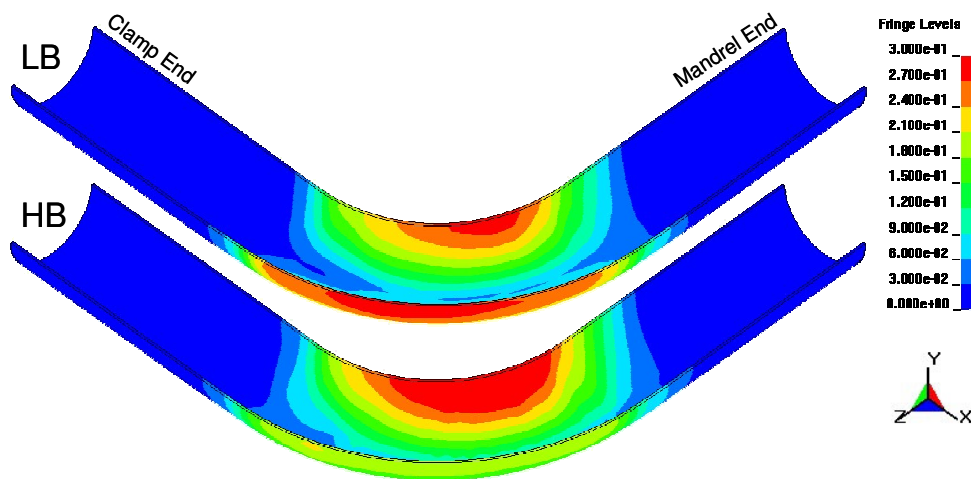
Figure 103: Contours of effective plastic strain for DP600 pre-bend tubes

The predicted strain and thickness distributions for the DP600 tubes are shown in Figure 104 and Figure 105, respectively. These include the predictions for the MB case with an increased coefficient of friction (↑COF). The figures also show the measured strain and thickness distributions. The steady-state region shown in Figure 104 and Figure 105 corresponds to 20°<θ<70°.
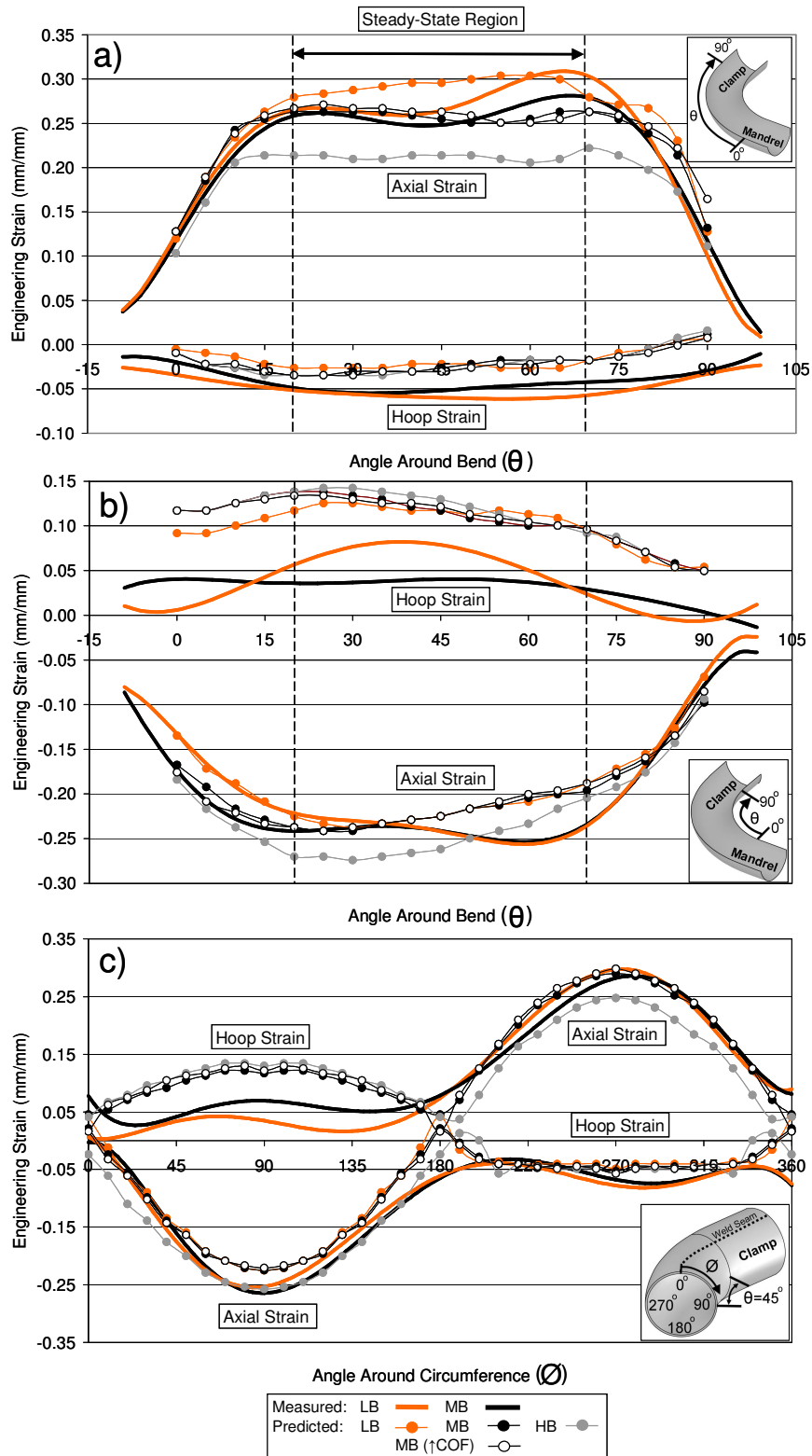
Figure 104: Predicted and measured strain for the DP600 tube a) outside of the bend b) inside of the bend c) around the circumference strain distribution for all boost cases. Note that the MB (↑COF) prediction compared to these using an elevated friction coefficient. Note also that no HB DP600 experiments were performed

For the region in the steady-state region at the outside of the bend (Figure 104 a), the LB and MB models predict the trends and magnitudes of the measured strains which have a scatter of ±0.03 strain (Section 4.2.1). The LB model is not able to capture the peak in major strain distribution at θ=70°, rather a drop in the distribution is shown. The HB prediction shows a distinct reduction in major strain distribution. The minor strain is unaffected by boost or increased COF.

At the inside of the bend (Figure 104 b), larger compressive minor strains are predicted for increased bending boost levels. The predicted strains are close to the measured strains which have a scatter of ±0.05 strain (Section 4.2.1). The predicted major strain is similar for all boost cases and friction coefficients; however the magnitude is over predicted.

Around the circumference of the bend (Figure 104 c), the trends for the entire distribution (0°<∅<360°) are predicted relatively well. For 0°<∅<180°, the major strains are over predicted and the minor strains are slightly under predicted. There is almost no difference between the LB and MB predictions. The HB predictions exhibit a noticeable increase in minor strain distribution for 0°<∅<180° and a decrease in major strain for 180°<∅<360°, relative to the lower boost case.

The predicted strain distribution for the increased coefficient of friction MB model (↑COF) shows little difference from the baseline MB model predictions.

Figure 105: Predicted and measured thickness for the DP600 tube a) outside of the bend b) inside of the bend c) around the circumference strain distribution for all boost cases. Note that the MB (↑COF) prediction compared to these using an elevated friction coefficient. Note also that no HB DP600 experiments were performed.

Thickness changes are predicted well by the models for the inside and outside of the bend region, as shown in Figure 105 (a). At the outside of the bend, the predicted thickness distribution shows less thinning for increasing boost level and more thickening for increased boost level at the inside of the bend. The HB model predicts considerably less thinning at the outside of the bend and more thickening at the inside of the bend.

Around the circumference of the bend (Figure 105 b), the predicted thickness distribution trends and magnitudes agree well with the measured results. The LB model predicts more thinning than the MB model, although the difference is insignificant for $0°<\varnothing<180°$. The HB model predicts a thicker distribution over the entire circumference.

Figure 105 (a) and (b) indicate little difference in the predicted thickness between the MB friction cases.

7.2.3 IF Results

The predicted strain and thickness distributions for the IF tubes are shown in Figure 106 and Figure 107, respectively. The figures also show the measured strain and thickness distributions.
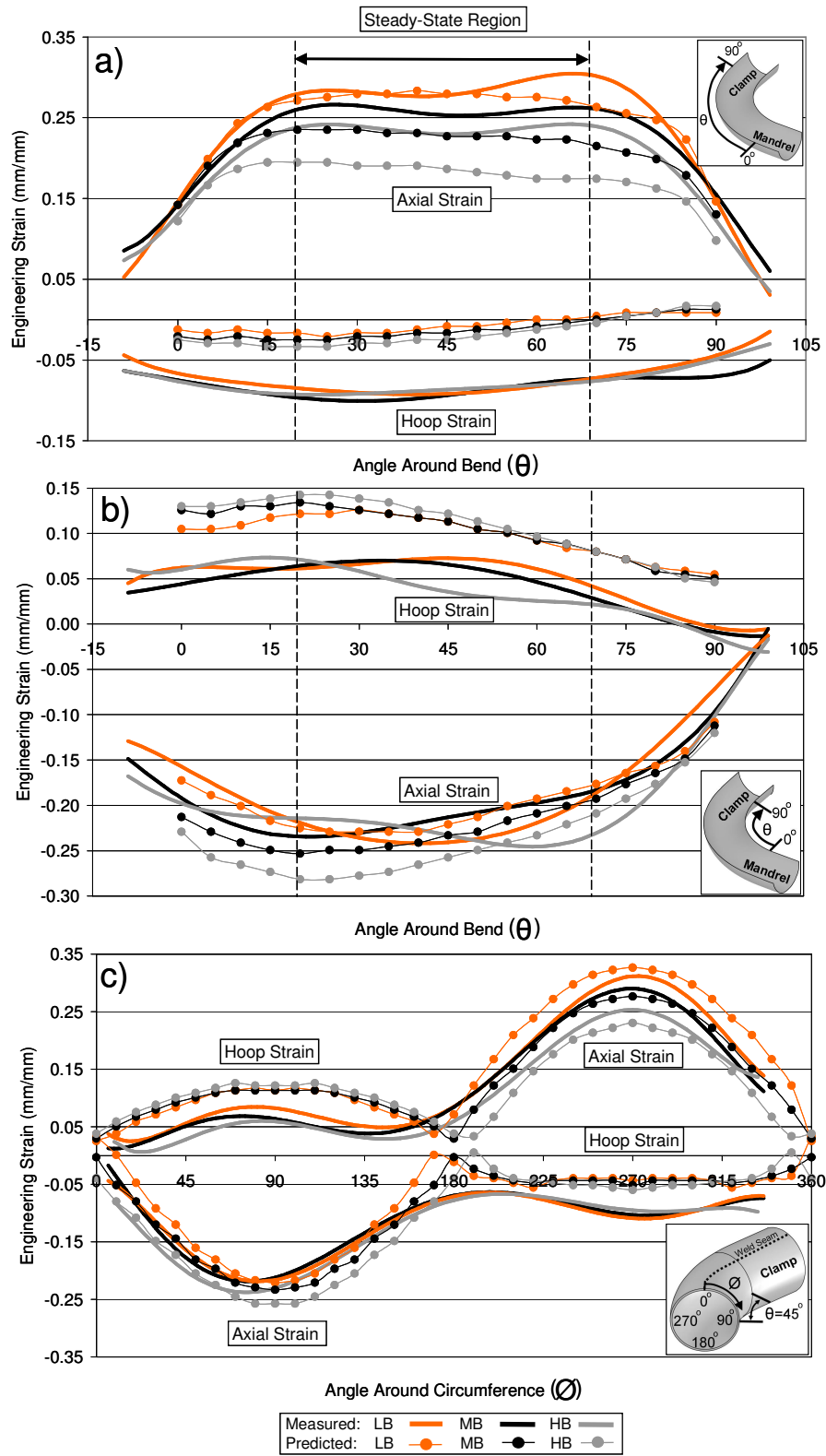
Figure 106: Predicted and measured strain for the IF tube a) outside of the bend b) inside of the bend c) around the circumference strain distribution for all boost cases
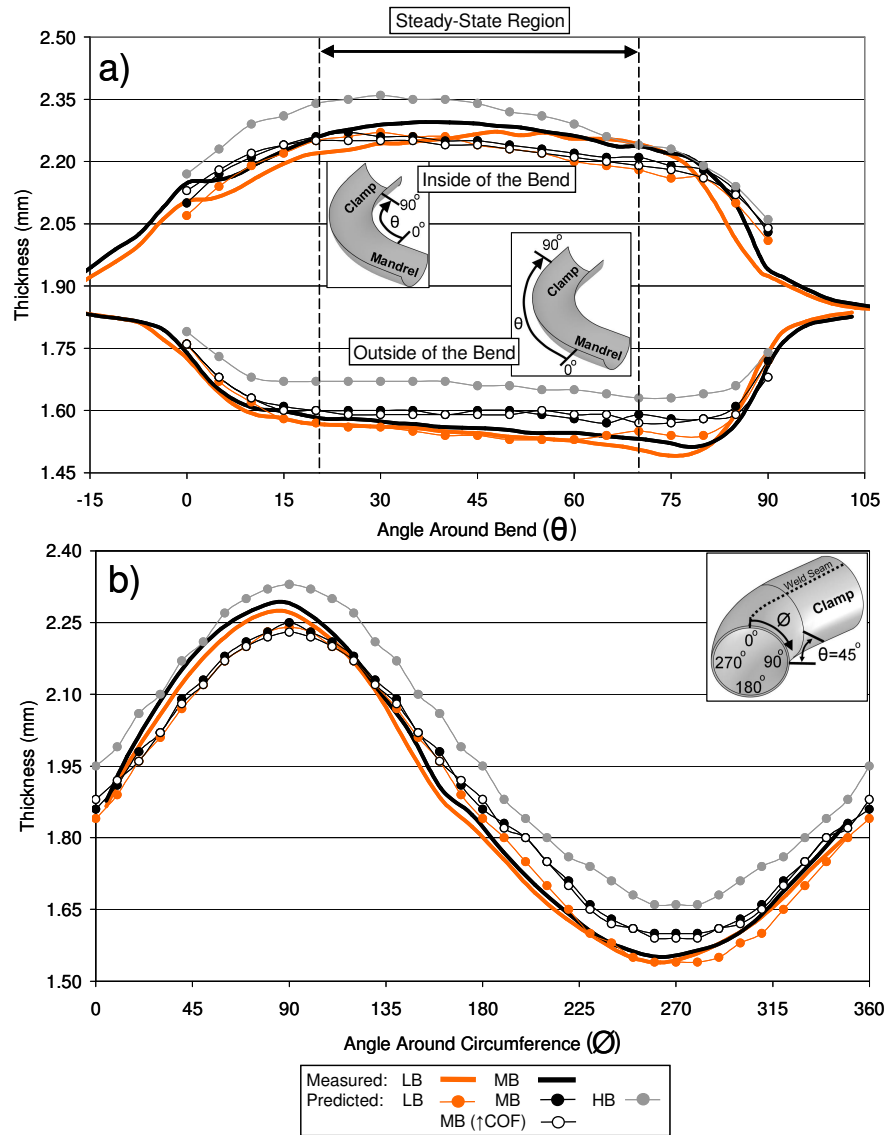
150
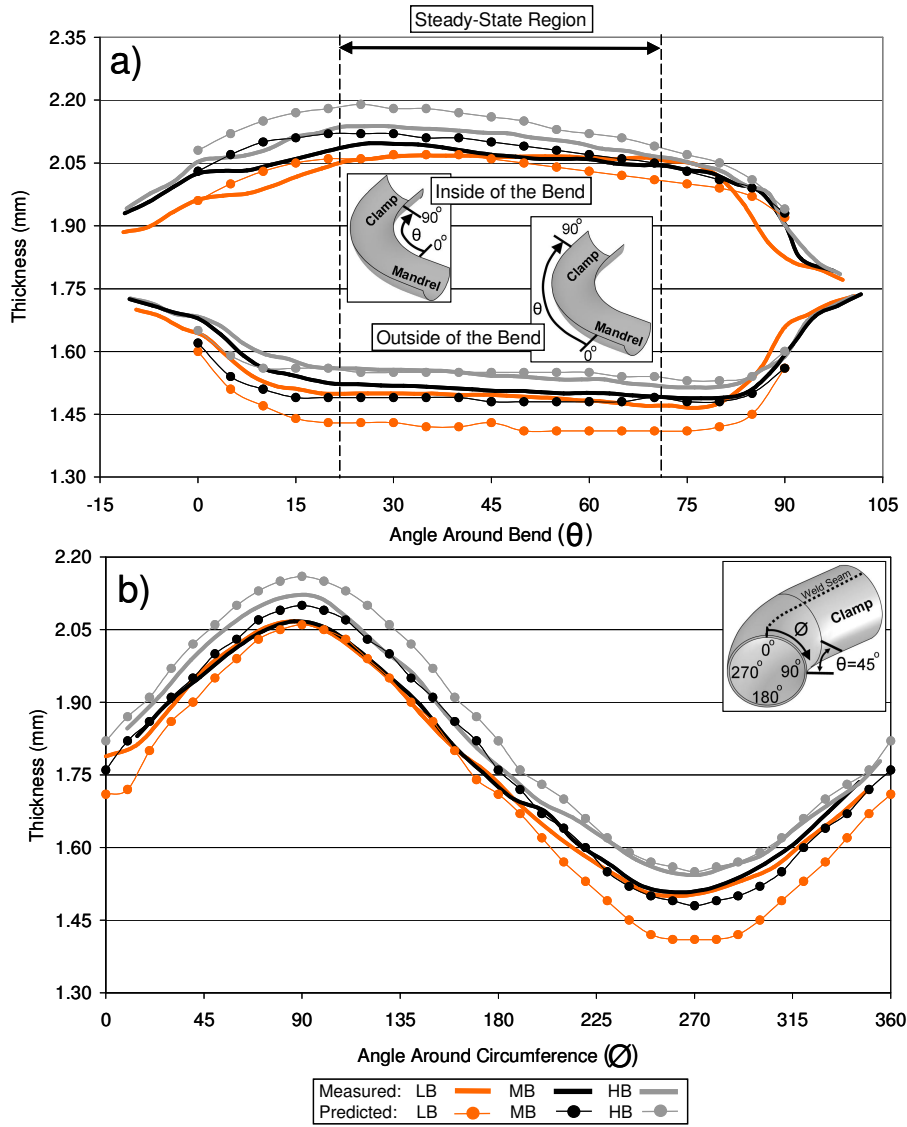
Figure 107: Predicted and measured thickness for the IF tube a) outside of the bend b) inside of the bend c) around the circumference strain distribution for all boost cases

For the LB and MB cases at the outside of the bend region (Figure 106 a), the predicted major strain distributions are similar to the measured distributions which have a scatter of ±0.03 strain. The HB prediction lies outside the measured strain distribution scatter. The models under predict the strain distribution magnitudes more as the boost level increases. The minor strains are under predicted and unaffected by the boost level. The thinning trend is also

captured accurately by the models (Figure 107 b), with the prediction becoming more accurate as the boost level increases.

At the inside of the bend (Figure 106 a), the models capture the expected trend of larger compressive minor strain for increased levels of bending boost. The predictions are within the ±0.05 strain scatter of the measured distributions. Similar to the DP600 predictions, the major strain is over predicted by the models. Thickening is captured well by the models (Figure 107 a) and shows better agreement with the measured results as the boost level decreased.

The trend in major and minor strain distributions around the circumference of the bend (Figure 106 c) are captured well by the models. For 0°<Ø<180°, the major strains are over predicted and the minor strains are accurately predicted. The major strain predictions for 180°<Ø<360° are close to the measured results while the minor strains are under predicted. The predicted thickness distributions (Figure 107 b) are more accurate for decreased boost levels for 0°<Ø<180°, and for 180°<Ø<360°, the models predict the measured results better for increased boost levels.

7.2.4 Summary

Average values of principal strain (major and minor), (ε_{avg}) and thickness (t_{avg}) were calculated at the inside and outside of the bend for 20°<θ<70°, the steady-state region. These were determined for both the predicted and measured data and the results are summarized in Table 16. Figure 108, Figure 109 and Figure 110 present this data in bar chart format.

Table 16: Average steady-state strain and thickness summary, predicted and measured

Material	Boost	Outside of the Bend			Inside of the Bend		
		Predicted Major Strain (Ten.) [Measured]	Predicted Minor Strain (Comp.) [Measured]	Predicted Thick. (mm) [Measured]	Predicted Minor Strain (Comp.) [Measured]	Predicted Major Strain (Ten.) [Measured]	Predicted Thick. (mm) [Measured]
DP600	LB	0.29 [0.28]	0.02 [0.06]	1.55 [1.54]	0.22 [0.24]	0.12 [0.07]	2.23 [2.25]
	MB	0.26 [0.26]	0.03 [0.05]	1.59 [1.56]	0.22 [0.24]	0.12 [0.04]	2.24 [2.27]
	MB (↑COF)	0.26 [NA]	0.03 [NA]	1.59 [NA]	0.22 [NA]	0.12 [NA]	2.23 [NA]
	HB	0.21 [NA]	0.03 [NA]	1.66 [NA]	0.25 [NA]	0.12 [NA]	2.32 [NA]
IF	LB	0.28 [0.29]	0.01 [0.09]	1.42 [1.49]	0.21 [0.23]	0.11 [0.06]	2.05 [2.06]
	MB	0.23 [0.26]	0.01 [0.09]	1.49 [1.51]	0.23 [0.21]	0.11 [0.06]	2.09 [2.07]
	HB	0.18 [0.24]	0.02 [0.09]	1.55 [1.54]	0.25 [0.23]	0.12 [0.04]	2.15 [2.11]
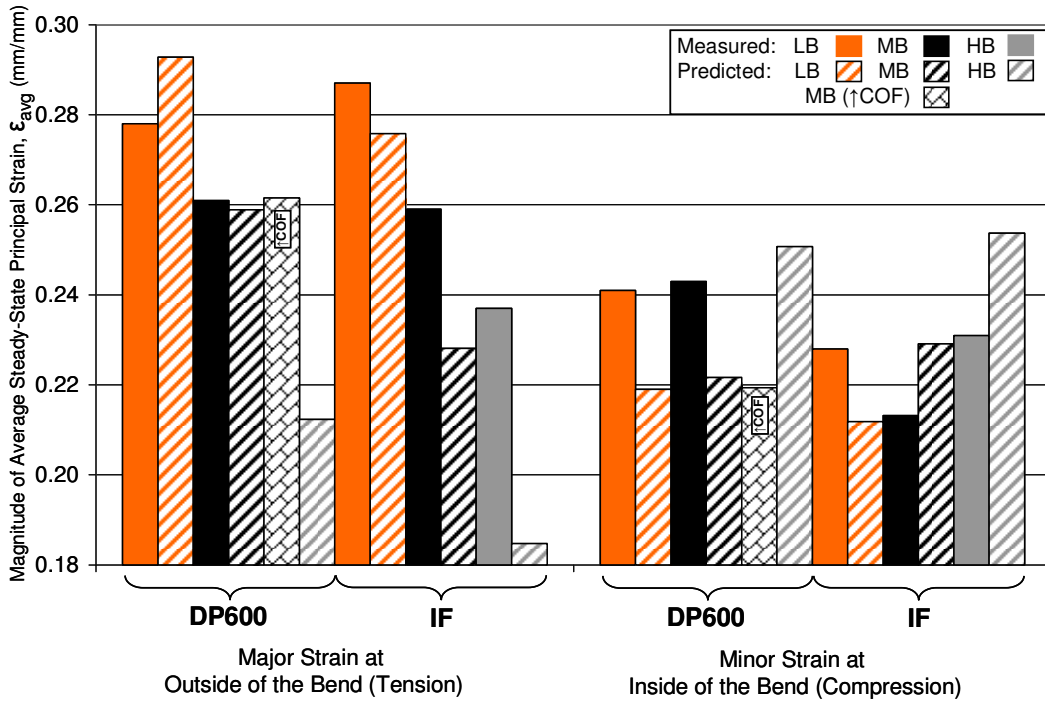
Figure 108: Magnitude of the predicted and measured average steady-state principal strain. The major component at the outside of the bend and the minimum component at the inside of the bend correspond to the bending and membrane strains
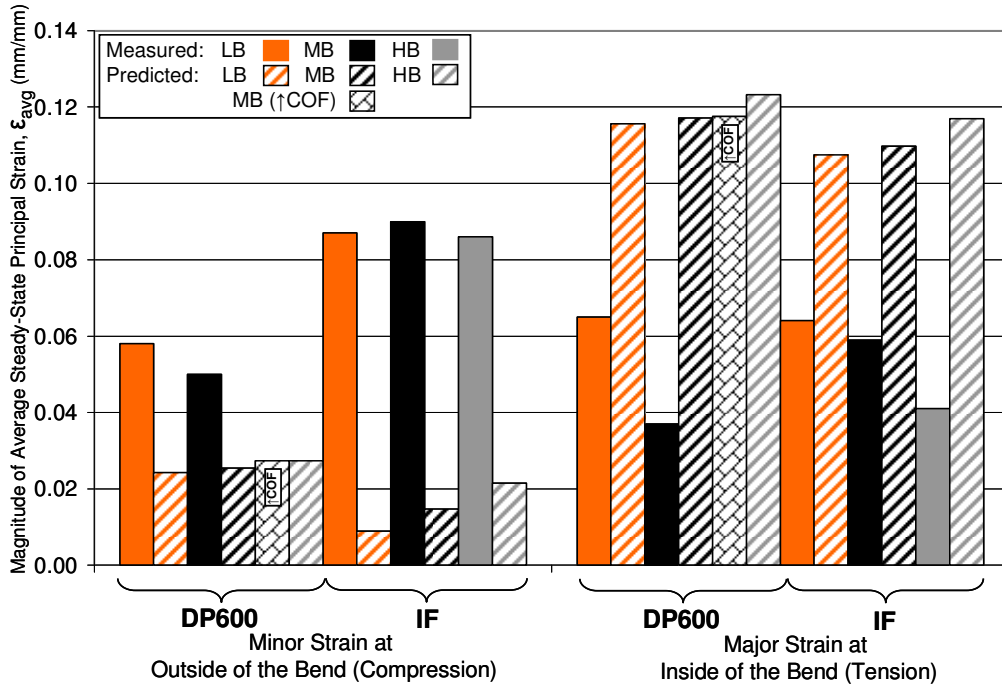
Figure 109: Magnitude of the predicted and measured average steady-state principal strain. The minor component at the outside of the bend and the major component at the inside of the bend correspond to the bending and membrane strains
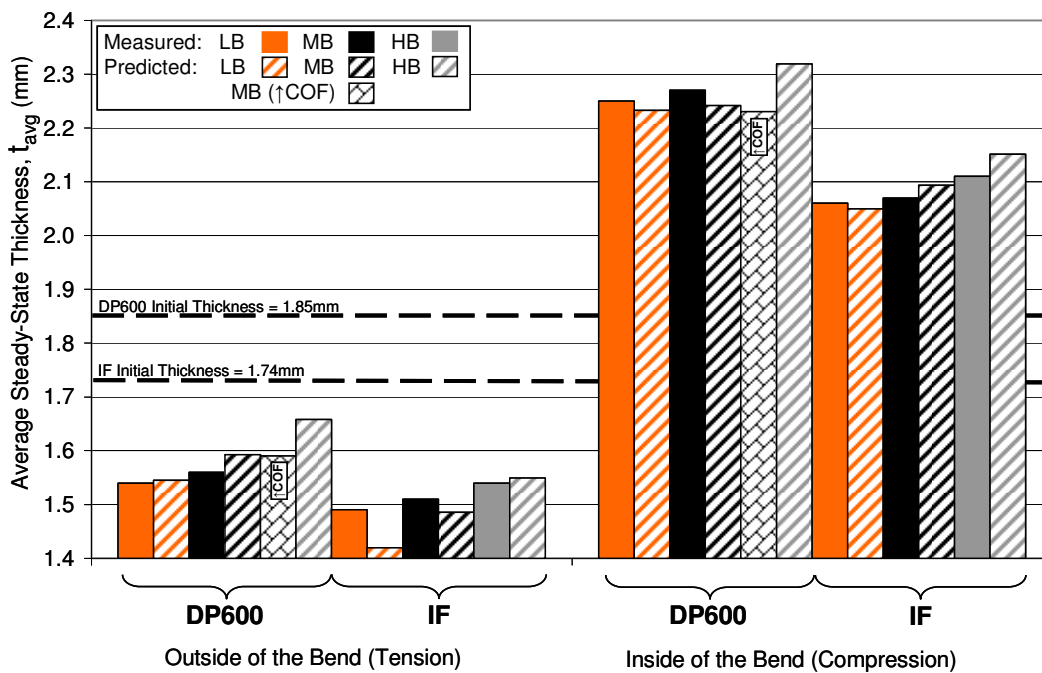
Figure 110: Average outside and inside of the bend steady-state thickness, predicted and measured

For the predictions at the outside of the bend, both the DP600 and IF models show a decrease in major strain for an increase in boost level. The magnitude of the predicted major strain (ε_{avg}) agrees well with the measured results for the DP600 tubes. The IF predictions are close to the measured results for decreasing levels of boost. The DP600 and IF models accurately capture the trend of reduced thinning for increased boost levels.

At the inside of the bend region, the predicted minor strains show a mild increase in magnitude (more compressive) for increasing boost levels. The magnitudes of the minor strains are within the scatter of the measured strains (±0.05 strain). The predicted major strains for the DP600 and IF tubes at the inside of the bend are generally higher in magnitude than the measured strains and lie outside of the scatter (±0.05 strain) of the measured results.

The increased coefficient of friction MB model ($\uparrow$COF) did not show a significant difference (compared to normal MB model) in the predicted strain or thickness values for the outside and inside of the bend regions. This indicates that the selected COF (within a reasonable range) for the tube bending model does not have a significant impact on the strain and thickness of the tube. This result is not overly surprising since the strains are largely controlled by the bend tooling geometry and level of boost.

CHAPTER 8

NUMERICAL SIMULATION OF THE TUBE HYDROFORMING EXPERIMENTS

The results from finite element (FE) models used to simulate the straight and pre-bend tube hydroforming processes are presented along with the experimental results presented in Chapter 5. The corner-fill expansion (CFE), end-feed (EF) displacement and strain and thickness (post hydroforming) are compared to the measured values from the experiments. The predictive ability of the XSFLC failure criterion is also assessed through comparison with the measured hydroforming burst pressures. The results of this straight and pre-bend tube hydroforming model validation exercise are presented in a summary at the end of this chapter.

8.1 Straight Tube Hydroforming

The results from straight tube hydroforming finite element (FE) models are presented in this section. The effect of hydroforming end-feed (EF) on the corner-fill expansion (CFE) and EF displacement is presented for both the DP600 and IF tubes. Also, the extended stress-based forming limit curve (XSFLC) failure criterion is evaluated.

8.1.1 Corner-Fill Expansion and End-Feed Displacement

Table 17 summarizes the predicted corner-fill expansion (CFE), end-feed (EF) displacement and extended stress-based forming limit curve (XSFLC) failure predictions. Figure 111 and Figure 112 show the predicted and measured CFE for the DP600 and IF straight tubes that were interrupted prior to failure (tested to 90% of burst pressure). For all levels of EF and both materials, the hydroforming model is able to accurately predict the measured CFE *vs.* internal pressure (Figure 111). For the increased coefficient of friction (↑COF) DP600 67kN EF case, the CFE is slightly under predicted by the model during expansion, but agrees with the experiment at the final pressure. Figure 112 shows the

predicted CFE at the final pressure to which the tubes were formed (90% interrupted). The agreement is excellent, even for the elevated friction (↑COF) model.

Table 17: Predicted and measured straight tube hydroforming results

Material	End-Feed (kN) [kip]	Measured Average Burst Pressure (MPa) [psi]	Predicted XSFLC Failure (Necking) Pressure (MPa) [psi]	Measured Average End-Feed Disp. at Burst (mm) [in]	Predicted End-Feed Disp. at Burst Press. (mm) [in]	Measured CFE at 90% Interrupted Test Press. (mm)[in]	Predicted CFE at 90% Interrupted Test Press. (mm) [in]
DP600	Zero	69.6 [10,092]	87.8 [12,732]	6.8 [0.266]	10.6 [0.417]	7.4 [0.290]	7.7 [0.302]
	67 [15]	92.1 [13,359]	107.1 [15,528]	17.6 [0.692]	16.2 [0.638]	9.8 [0.385]	9.56 [0.376]
	67 (↑COF) [15]	NA	78.9 [11,477]	NA	13.1 [0.516]	NA	9.6 [0.379]
	133 [30]	126.9 [18,405]	138.8 [20,132]	24.8 [0.975]	22.1 [0.870]	11.3 [0.447]	11.2 [0.441]
	200 [45]	151.7* [22,000]	NA	32.8** [1.292]	28.2** [1.110]	12.4** [0.490]	12.3** [0.484]
IF	Zero	151.7* [22,000]	NA	11.5** [0.453]	12.1** [0.476]	13.3** [0.526]	13.5** [0.531]

* Burst was not achieved, maximum capacity of the press was reached
** Measured at experimental hydroforming pressure as shown in column 3
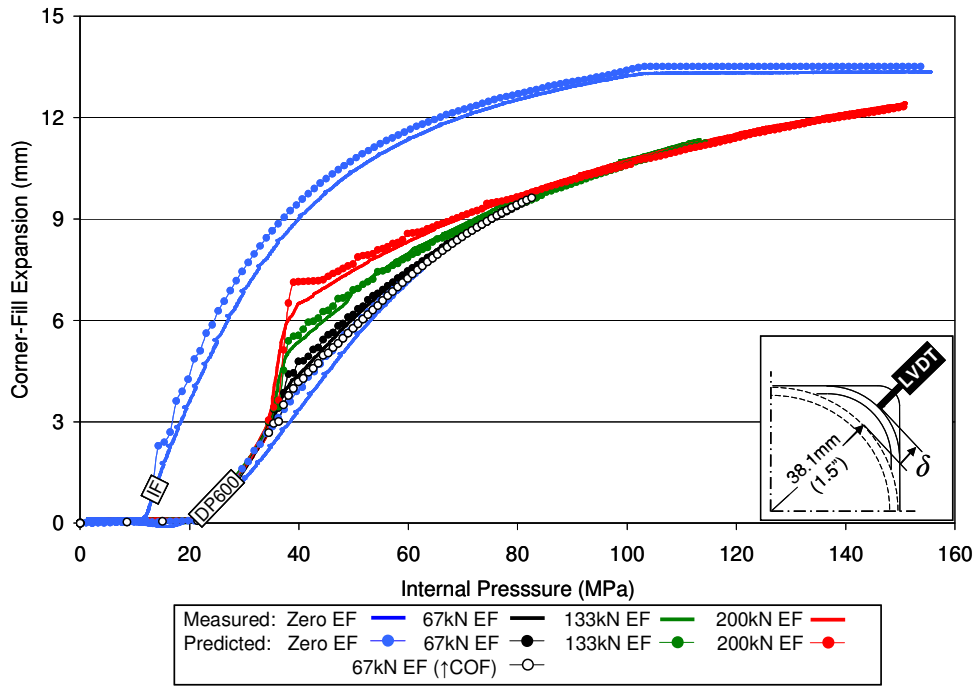
Figure 111: Predicted and measured CFE *vs.* internal pressure, DP600 and IF straight tube at 90% interrupted pressure
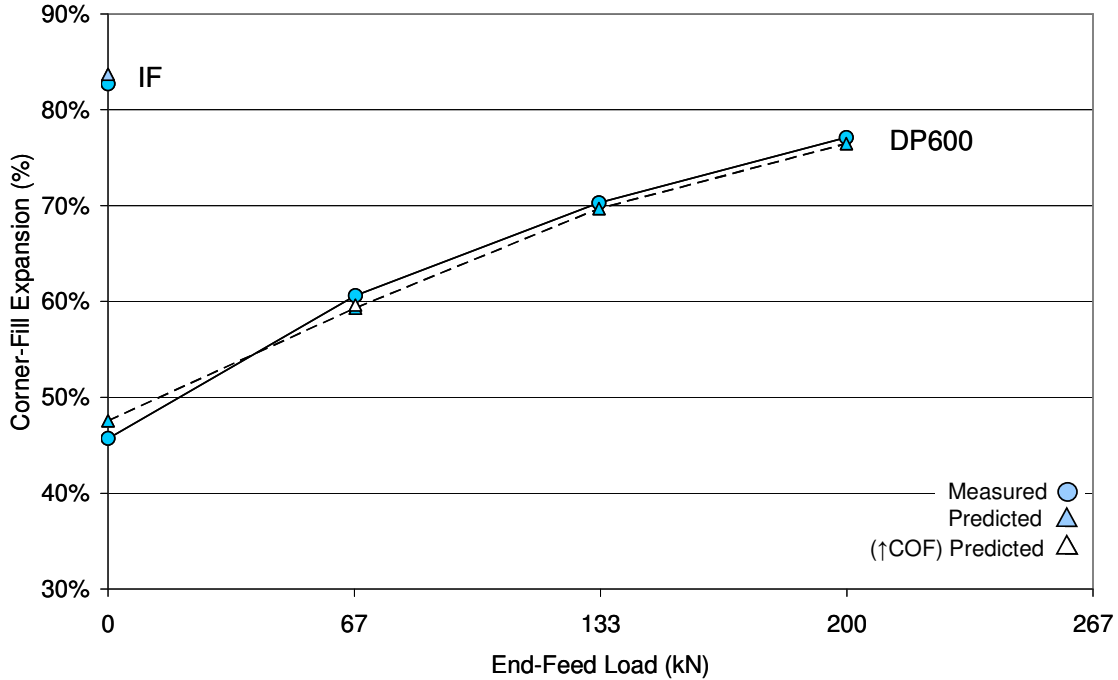
Figure 112: CFE *vs.* EF load for DP600 and IF straight tube at 90% interrupted pressure

Figure 113 shows the predicted and measured end-feed (EF) displacement *vs.* the internal pressure for the DP600 and IF tubes tested to burst. The measured curves in the figure are median curves from the set of burst test results. For the DP600 67kN, 133kN and 200kN EF cases, the models under predict the measured EF displacement, with the disagreement increasing as the EF force increases. The DP600 zero EF model over predicts the EF displacement, while the IF zero EF model predicts the correct EF displacement (recall that zero EF refers to EF force and that the tubes naturally draw-in resulting in a positive EF displacement). The increased coefficient of friction DP600 67kN EF model (↑COF) under predicts the EF displacement more than the baseline model which used the COF measured with the twist compression test. This result supports the use of the twist compression test for measuring the COF and uniaxial tension test to define the constitutive material model.
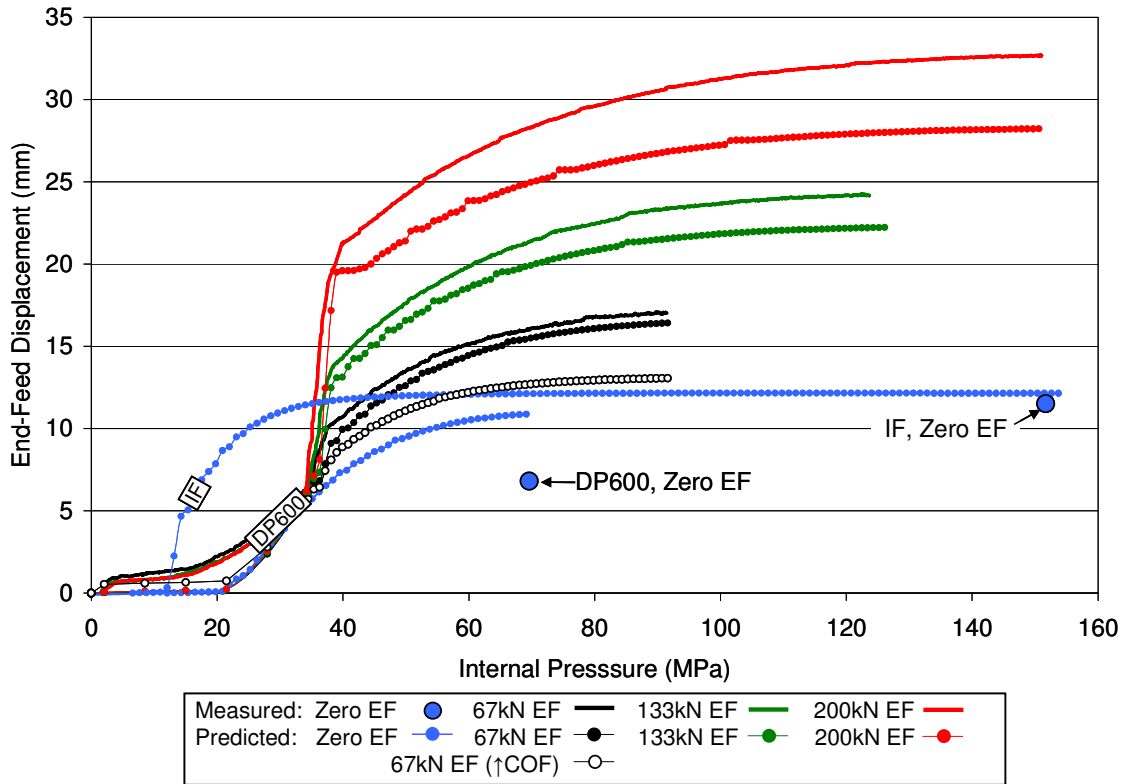
Figure 113: Predicted and measured EF displacement *vs.* internal pressure for DP600 and IF straight tube

8.1.2 Strain and Thickness Validation

Figure 114 shows predicted contours of effective plastic strain plots for DP600 under zero and 200kN EF. It can be seen that increased EF allows the tube to flow more readily into the corners and to better distribute the strains within the tube. The plots are shown for a pressure level corresponding to the burst pressure in the experiments for each load case.
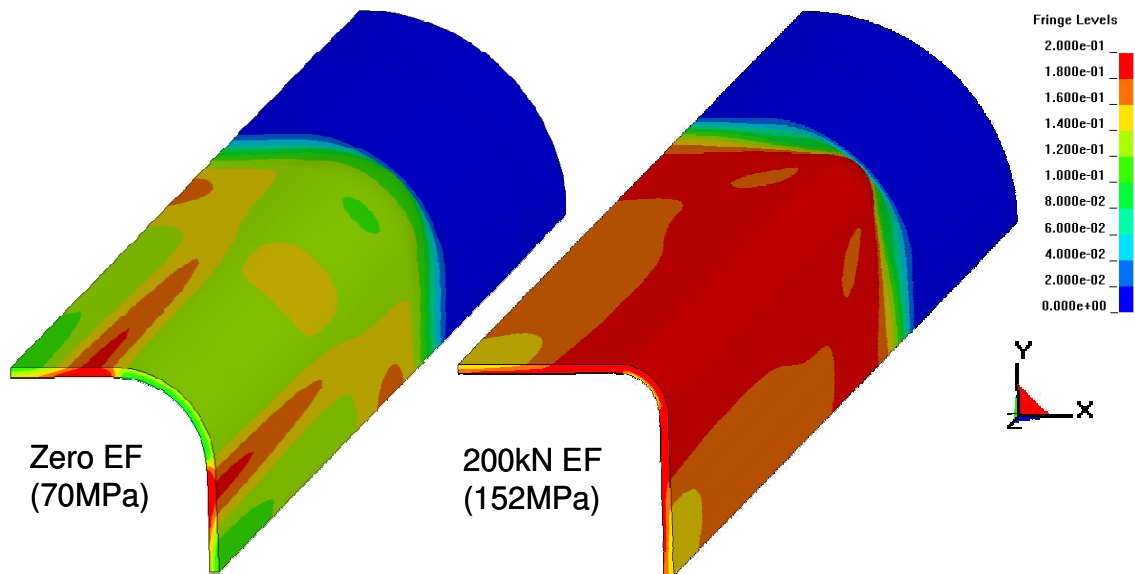
Figure 114: Contours of effective plastic strain at measured burst pressure for DP600 zero and 200kN EF models

The predicted strain and thickness distributions were measured at the same pressure that the tubes reached during the experiments. The strain and thickness was measured at a 5° interval around the circumference. Figure 115 shows all of the predicted and measured strain and thickness distributions for the DP600 and IF straight tube hydroforming cases. Appendix E contains the individual strain and thickness graphs for each of the EF cases.
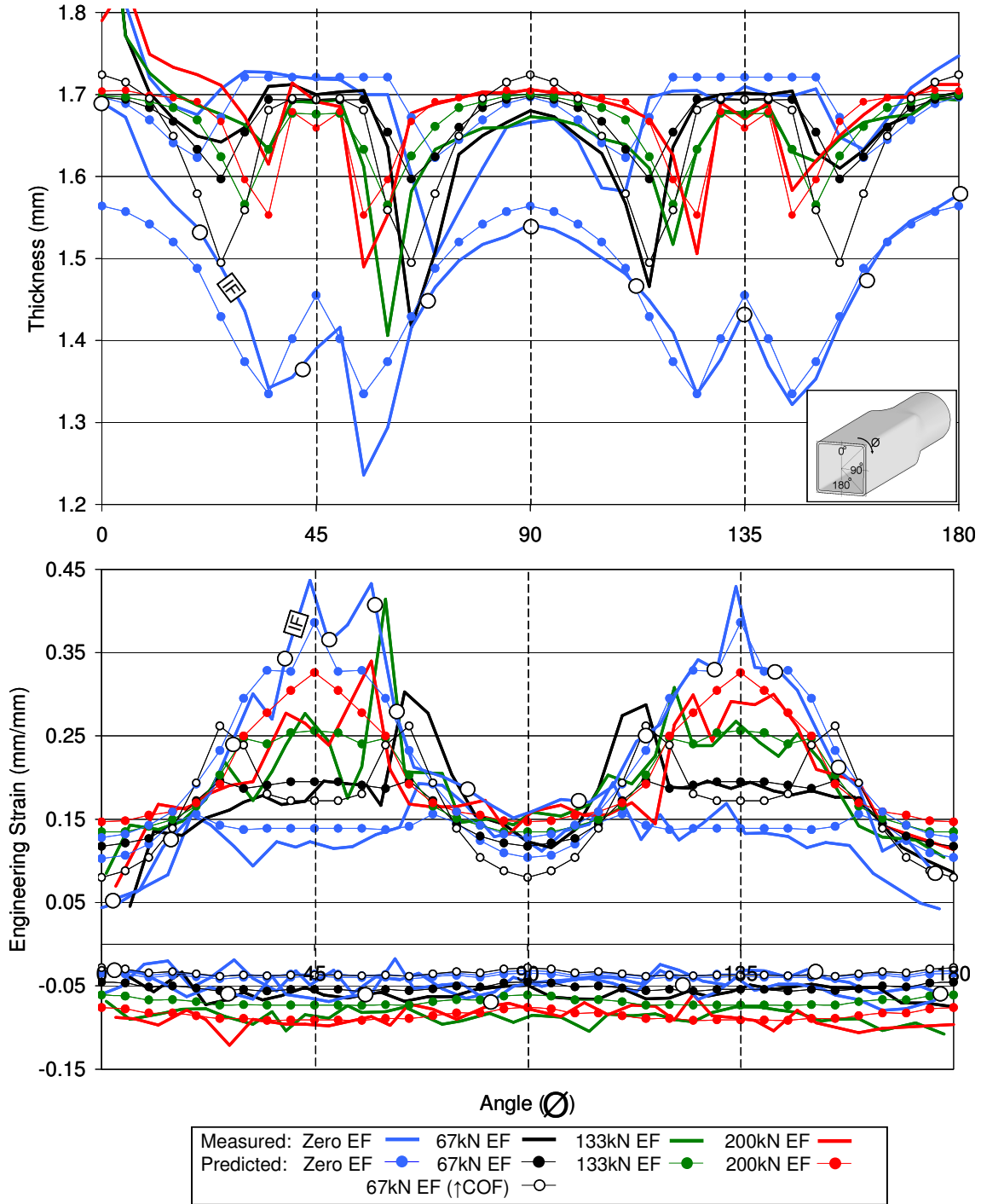
Figure 115: Predicted and measured strain and thickness distributions for DP600 and IF straight tube. See Appendix D for strain and thickness distributions plots for each EF case.

For both materials and all end-feed (EF) cases, the FE models accurately predict the measured strain and thickness distributions. The major and minor strain predictions agree very

well with the measured values for all EF cases. The thickness predictions are able to capture the distinct thinned portions of the measured cross-section. The DP600 67kN EF model was also run with an increased coefficient of friction (↑COF) between the tube and the hydroforming die. The high friction model predicts greater thinning than the normal model and consequently, stronger peaks in major strain. This is a result of the increased frictional force between the tube and die, which reduces sliding of the tube during expansion and induces greater tensile strain in the free expansion corners.

8.1.3 XSFLC Failure Criteria Validation

The extended stress-based forming limit curve (XSFLC) failure criterion was used to predict the onset of necking in the straight tube hydroforming models. Because the IF tube was not able to reach failure (burst), the XSFLC was only applied to the DP600 models. Figure 116 shows the XSFLC predicted failure (necking) pressure for the DP600 straight tubes. The XSFLC failure criteria consistently over predicts the failure pressures for all EF cases. The reason for the over predicted failure pressure is possibly due to the Keeler-Brazier approximation of the strain-based forming limit curve (εFLC), which ultimately controls the XSFLC failure curve in stress-space. By shifting the εFLC (down) along the major strain axis, the resultant XSFLC curve would predict failure at a lower pressure. It should be noted that the Keeler-Brazier approximation was derived for sheet material, not tubular material. The over predicted failure pressures suggest that the Keeler-Brazier approximation may not be applicable for approximating the εFLC of a tube. Recently, Sorine *et al.* (2006) used free expansion hydroforming burst tests to calibrate the εFLC. They found that the plane strain intercept (FLC_o) determined by the experiments was much lower (along the major strain axis) than the FLC_o predicted by the Keeler-Brazier approximation (using tubular *n* value).

For the high friction 67kN EF model (↑COF), the XSFLC under predicts the failure pressure, which shows that the failure criteria is sensitive to the COF used in the models. The XSFLC under prediction is due to the greater major strain peaks (compared to normal model) as shown in Figure 115 and Appendix E. These larger peaks in major strain result in a greater

effective stress, which causes the stress-path to cross the XSFLC curve. The measured and predicted failure pressure values can be found in Table 17.
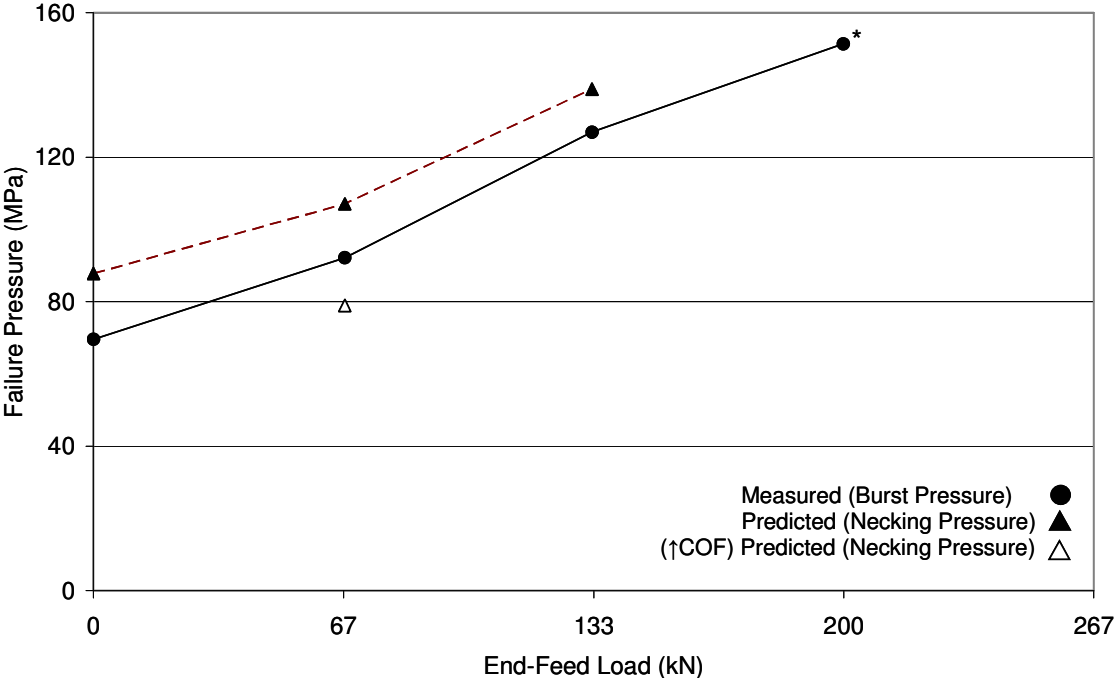
* 200kN EF tube did not burst (maximum capacity of press reached), therefore XSFLC could not predict failure

Figure 116: XSFLC predicted failure for DP600 straight tube hydroforming

Figure 117 shows XSFLC contour plots at the pressure when failure (necking) occurred for different EF cases. Photographs of the failed experimental tubes are also shown. Although the failure pressure is over predicted by the XSFLC, the correct failure location is captured. For all three DP600 EF cases (zero, 67kN and 133kN EF), the models predict failure in the transition between the tube/die contact zone and the free expansion zone. This transition zone is in a state of tri-axial stress, because a through-thickness stress component exists in the tube wall. It was also shown in the previous section (and Appendix E), that both the models and measured results indicate thinning in the regions that the XSFLC predicts failure (indicated by a star in Figure 117).
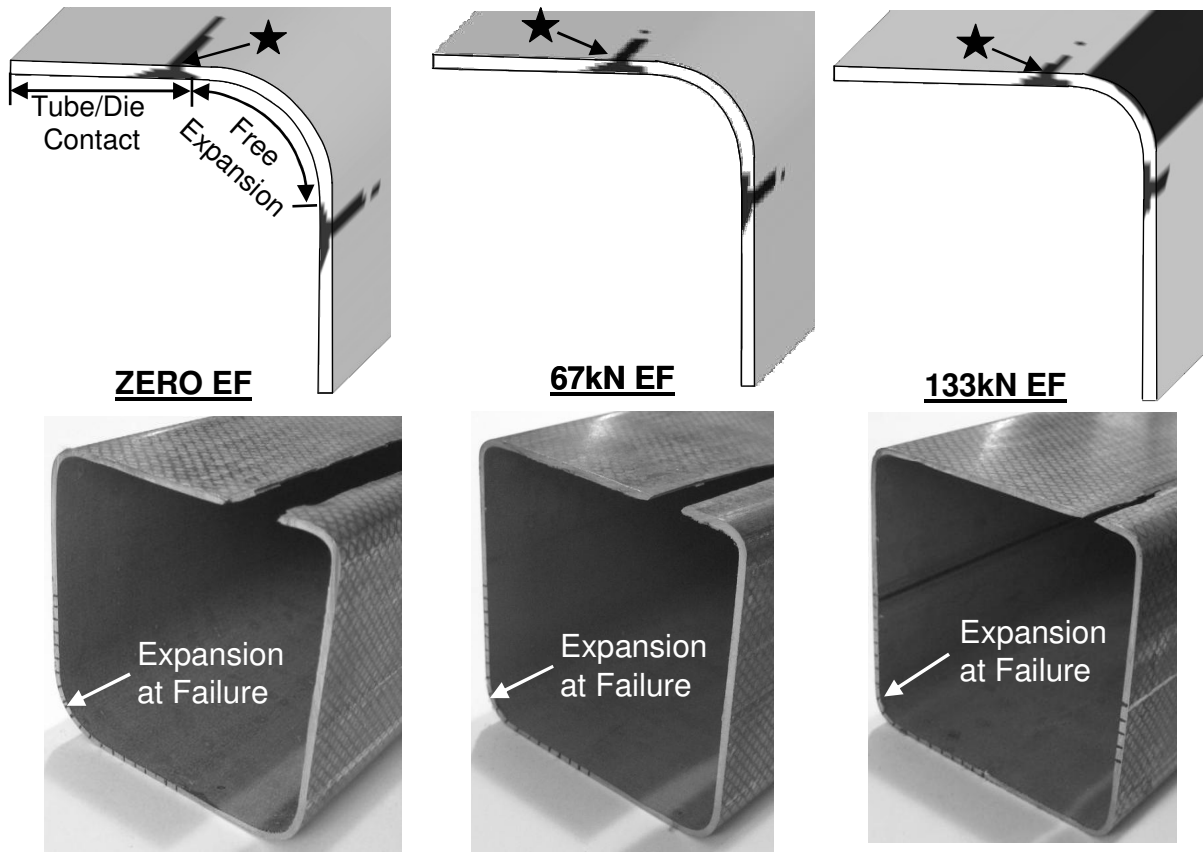
Figure 117: XSFLC straight tube DP600 failure location predictions. Dark grey contours are for elements for which stress path has crossed the XSFLC, with the star indicating complete through thickness failure (necking). Photographs of the corresponding failed tubes are shown as well.

8.2 Pre-Bend Tube Hydroforming

The predictions from the pre-bend tube hydroforming finite element (FE) models are examined in this section. The effect of bending boost and hydroforming end-feed (EF) on the corner-fill expansion (CFE) and EF displacement is presented for the DP600 and IF pre-bent tubes. In addition, the extended stress-based forming limit curve (XSFLC) failure criterion is evaluated.

164

8.2.1 Tube Movement

As shown in Section 5.2.1, the tube moves away from the inside of the bend region during hydroforming. Figure 118 shows a series of deformed mesh plots from the DP600 MB, 133kN end-feed (EF) model. At 38MPa internal pressure, the tube is the furthest away from the inside of the bend region. At this pressure, the EF load is being applied. After the full EF load has been applied (at 41MPa), the tube shows wrinkling/buckling as in the experiment. As the pressure increases, the tube eventually makes contact with the inside of the die and continues to expand circumferentially. The models predict that tube movement away from the die increases for greater levels of hydroforming EF, as in the experiments.
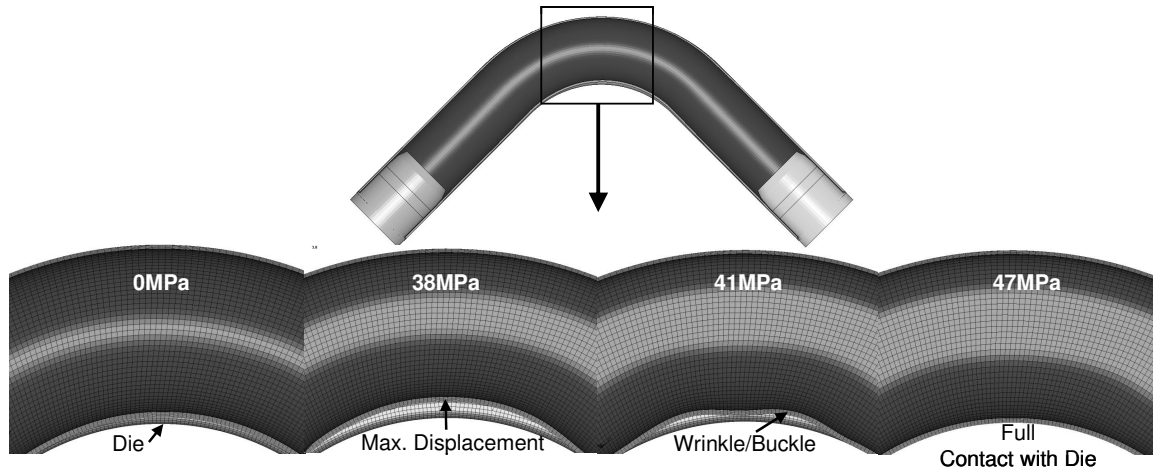
Figure 118: Predicted tube movement during hydroforming of DP600, 133kN EF tube

8.2.2 Corner-Fill Expansion and End-Feed Displacement

Table 18 summarizes the predicted corner-fill expansion (CFE) and end-feed (EF) displacement results for the DP600 and IF tubes. Figure 119 and Figure 120 show the predicted and measured CFE for the DP600 pre-bend tubes. The models are able to capture the overall trends in the measured CFE *vs.* internal pressure. For all EF levels, the models under predict the magnitude of the outside CFE (Figure 119) up to an internal pressure of approximately 35MPa, which corresponds to the pressure when the EF load is applied. After

165

35MPa, the models closely predict the outside CFE. Three modifications to the hydroforming model (increased simulation time, increased pre-load on EF actuators and increased coefficient of friction between the tube and die) were made in an attempt to correct the under prediction of the outside CFE. All of the modified models showed the same under prediction shown in Figure 119. For the inside CFE, the opposite trend exists, where the models closely predict the CFE magnitude up to 35MPa internal pressure, but under predict the magnitude after 35MPa internal pressure. Note that the measured inside CFE can reach only a minimum of -2.5mm due to the limitation of the LVDT displacement transducer. None of the modified models corrected the under prediction of the inside CFE. Appendix F contains the CFE *vs.* internal pressure graphs for the individual EF cases (zero, 67kN and 133kN).

Figure 120 shows the predicted and measured average CFE *vs.* EF load for the DP600 MB tubes. The measured and predicted CFE were recorded at a pressure of 90% of the burst pressure. The models accurately predict the correct trend, but under predict the magnitude for all three EF levels. The under prediction is due to the inability of the models to capture the inside CFE (at 90% interrupted pressure), as shown in Figure 119.

The increased coefficient of friction model (↑COF) for the DP600 67kN EF case deviates from the baseline case only after a pressure of 35MPa. The model under predicts the magnitude of the CFE. The under prediction is due to the reduction in the effect of the 67kN EF load on the tube, because of the increase in frictional force between the tube and the die, which resists tube movement in the longitudinal direction.

The DP600 LB and IF tube results are presented in Section 8.2.4, which focuses on the effect of bending boost on the prediction of CFE and EF displacements.

Table 18: Predicted and measured pre-bend tube hydroforming results

Material	Bending Boost Case	End-Feed (kN) [kip]	Measured Avg. Burst Press. (MPa) [psi]	Measured Average End-Feed Disp. at Burst (mm) [in]	Predicted End-Feed Disp. at Burst Press. (mm) [in]	Measured CFE at 90% Int. Test Press. (in, out, avg.) (mm) [in]	Predicted CFE at 90% Int. Test Press. (in, out, avg.) (mm) [in]
DP600	MB	Zero	45.0 [6,528]	5.4 [0.211]	4.1	-1.6, 4.4, **1.4** [-0.064,0.173, **0.055**]	-3.1, 4.1. **0.5** [-0.122, 0.161, **0.020**]
	MB	**67 [15]**	60.4 [8,756]	12.1 [0.478]	11.5	5.2, 7.5, **6.4** [0.207, 0.297, **0.252**]	3.1, 6.9, **5.0** [0.122, 0.272, **0.197**]
	MB (↑COF)	**67 [15]**	NA	NA	9.5	5.2, 7.5, **6.4** [0.207, 0.297, **0.252**]	3.1, 6.1, **4.6** [0.122, 0.240, **0.181**]
	LB	**67 [15]**	54.6 [7,915]	10.8 [0.423]	11.0	4.4, 7.3, **5.9** [0.275, 0.353, **0.314**]	2.3, 6.8, **4.6** [0.090, 0.269, **0.181**]
	MB	133 [30]	73.4 [10,643]	17.6 [0.694]	17.6	7.0, 9.0, **8.0** [0.172, 0.288, **0.230**]	5.0, 9.0, **7.1** [0.197, 0.354, **0.280**]
IF	LB	Zero	34.5* [5,000]	NA	NA	7.5, 8.2, **7.9**** [0.295, 0.323, **0.309**]	6.2, 6.5, **6.3** [0.244, 0.256, **0.248**]
	MB	Zero	34.5* [5,000]	NA	NA	7.6, 8.2, **7.9**** [0.299, 0.323, **0.298**]	5.8, 7.8, **6.8** [0.228, 0.307, **0.268**]
	HB	Zero	34.5* [5,000]	NA	NA	7.0, 8.1, **7.6**** [0.277, 0.320, **0.298**]	5.3, 7.7, **6.5** [0.209, 0.303, **0.256**]
	LB	67 [15]	151.7* [22,000]	18.8 [0.741]	15.4	13.7, 13.9, **13.8**** [0.540, 0.548, **0.544**]	13.0, 12.3, **12.6** [0.512, 0.483, **0.498**]
	MB	67 [15]	151.7* [22,000]	20.3 [0.800]	17.5	13.7, 13.9, **13.8**** [0.540, 0.548, **0.544**]	12.7, 13.7, **13.2** [0.500, 0.541, **0.521**]
	HB	67 [15]	151.7* [22,000]	18.5 [0.726]	18.6	13.7, 13.9, **13.8**** [0.538, 0.547, **0.542**]	12.5, 13.7, **13.1** [0.492, 0.541, **0.516**]

* Burst was not achieved
** Measured at final hydroforming pressure as shown in column 4
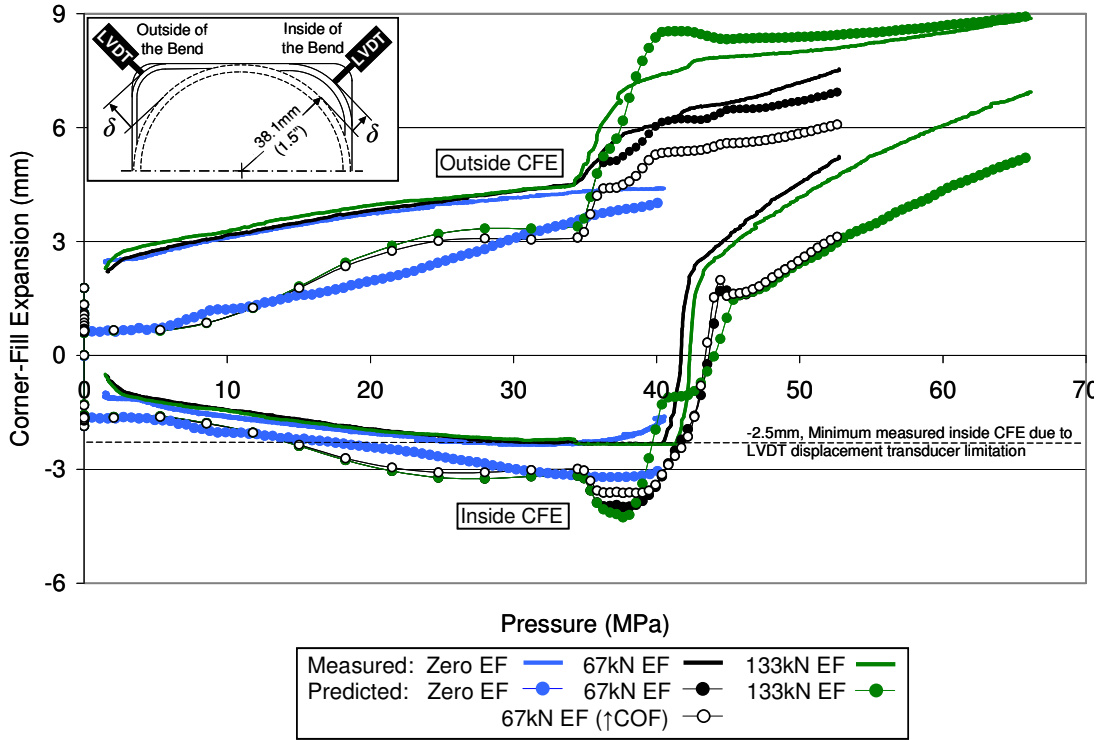
Figure 119: Predicted and measured DP600 CFE *vs.* internal pressure, pre-bend tube hydroforming
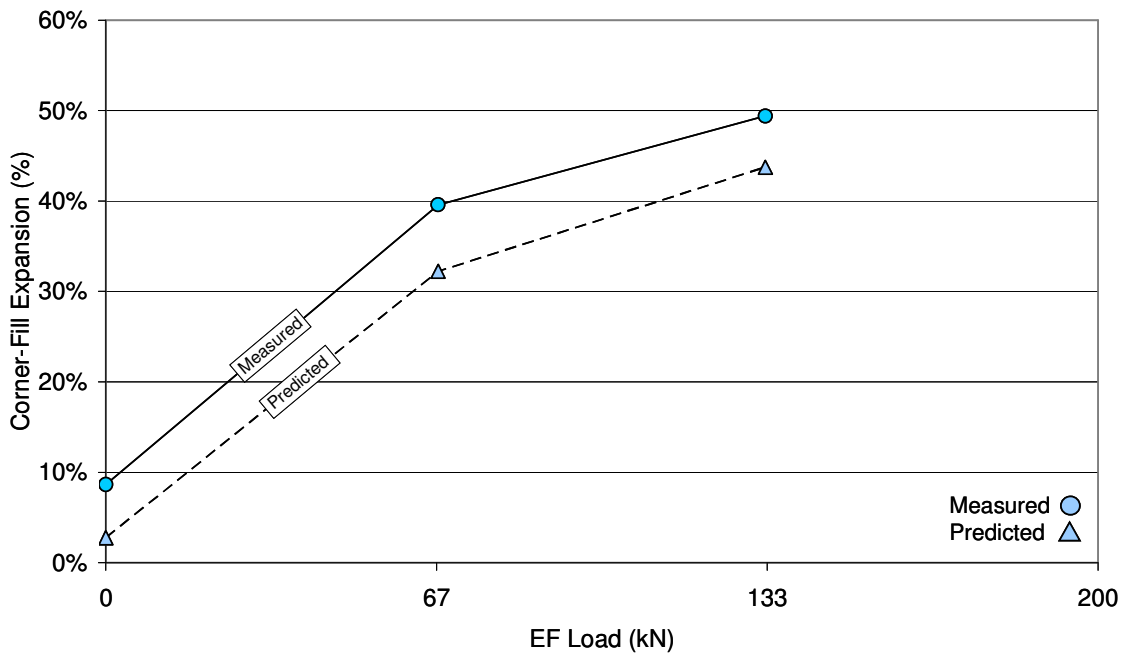
Figure 120: Predicted and measured average CFE at 90% of burst pressure *vs.* EF load for DP600 pre-bend tubes

Figure 121 shows the predicted and measured average EF displacement (average of both EF ram displacements) at the average measured burst pressure shown in Table 18. The measured curves shown are the median curves from the set of burst tests (see Appendix F). The models closely predict the EF displacement for all three of the EF cases.

The 67kN EF model was run with an increased coefficient of friction (↑COF) between the tube and die. The model under predicted the measured EF displacement because the increased frictional force between the tube and the die retards the axial movement of the tube within the die.
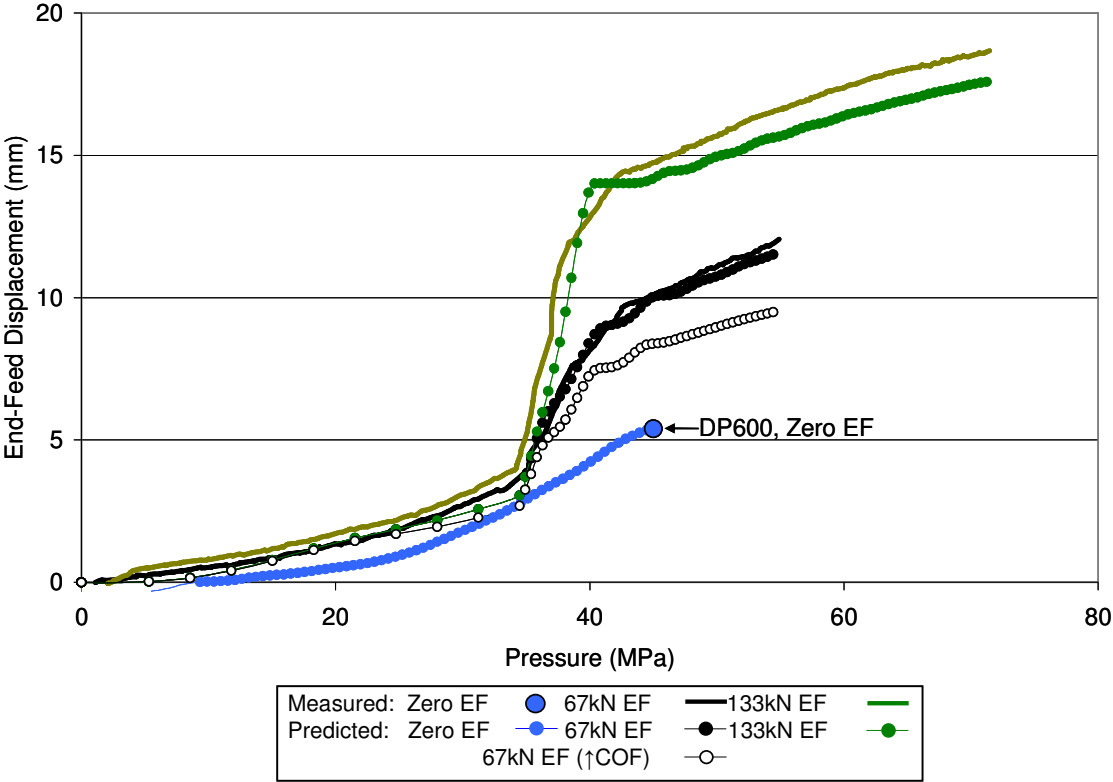
Figure 121: Predicted and measured EF displacement *vs.* internal pressure for DP600 pre-bend tubes (burst tests)

8.2.3 Strain and Thickness

Figure 122 shows the contour plots (at burst pressure) of effective plastic strain in the DP600 MB tubes for the zero and 133kN EF case. Similar to the straight tube contour plots,

the 133kN EF model shows that the tube can withstand a greater amount of strain (at burst) than the zero EF case.
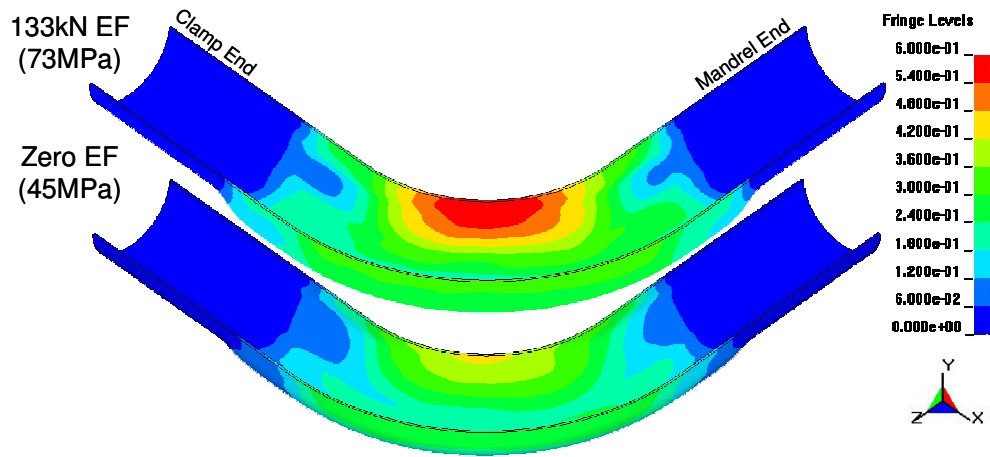
Figure 122: Contours of effective plastic strain at burst pressure for DP600 MB (Zero and 133kN EF)

The predicted strain and thickness distribution around the circumference of the hydroformed pre-bend tube was output at 10° intervals. As in the case of the straight tubes, the predicted results are presented at the same internal pressure as the experiments (90% of the burst pressure). Figure 123 shows the predicted and measured strain and thickness distributions for the DP600 tubes. Appendix F contains the individual strain and thickness plots for each EF case.
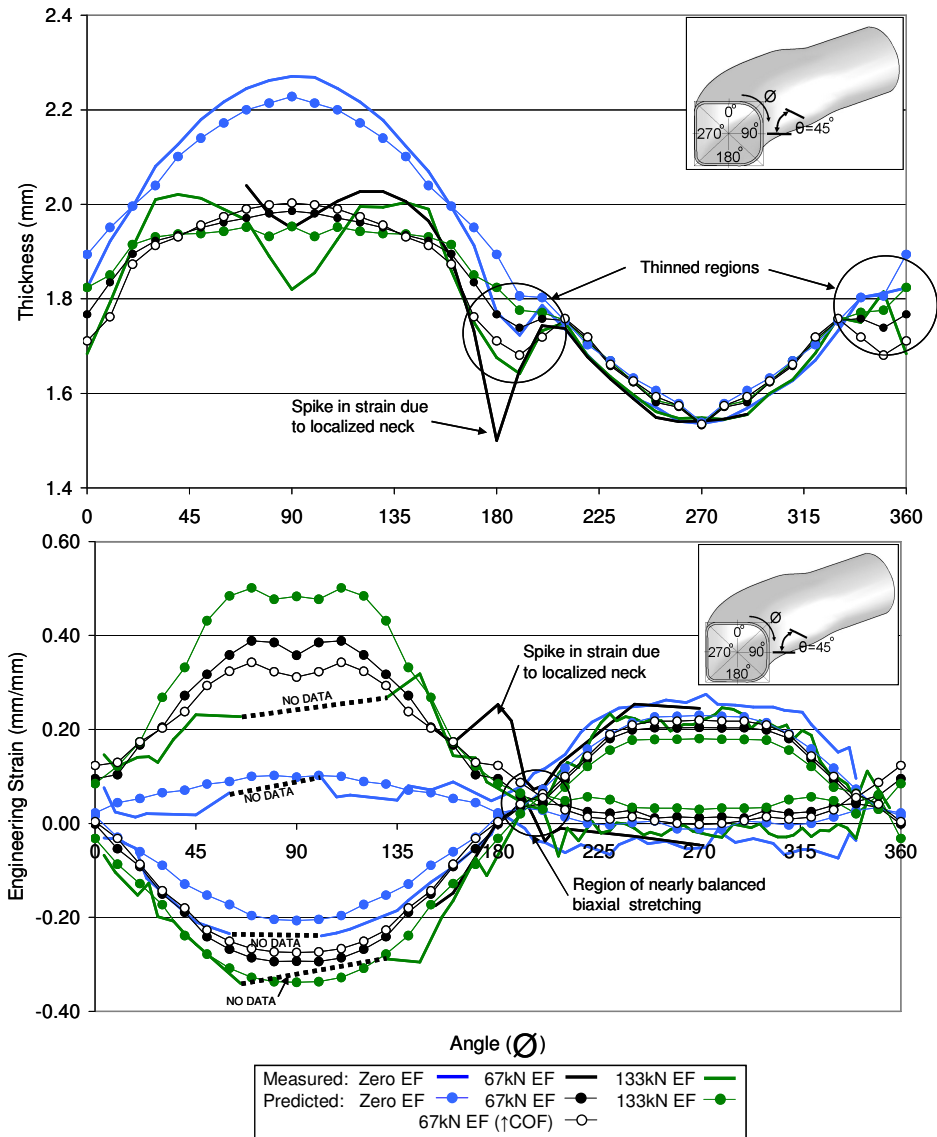
Figure 123: Predicted and measured strain and thickness distribution for DP600 pre-bend tubes. See Appendix F for strain and thickness distributions plots for each EF case.

The models accurately capture the thickness distributions seen in the measured results. The increased coefficient of friction 67kN MB model (↑COF) predicts a similar thickness distribution as the baseline model which uses the COF from the twist compression test. The main difference between the two models occurs at the thinned regions, where the ↑COF model predicts more thinning.

8.2.4 Effect of Bending Boost on Pre-Bend Hydroforming

The predicted effect of bending boost on the corner-fill expansion (CFE), end-feed (EF) displacement and the strain and thickness distribution are presented in this section. The results focus on the DP600 tubes because the same trends are present for the IF models. The IF results can be found in Appendix H. Figure 124 shows the CFE *vs.* internal pressure for the 67kN EF case. After an internal pressure of 35MPa, the predicted outside and inside CFE is similar for the LB and MB cases, although the measured results show a difference between the inside LB and MB results. The predicted HB CFE results are slightly less than the MB case for the outside CFE and noticeably less for the inside CFE after 35MPa.
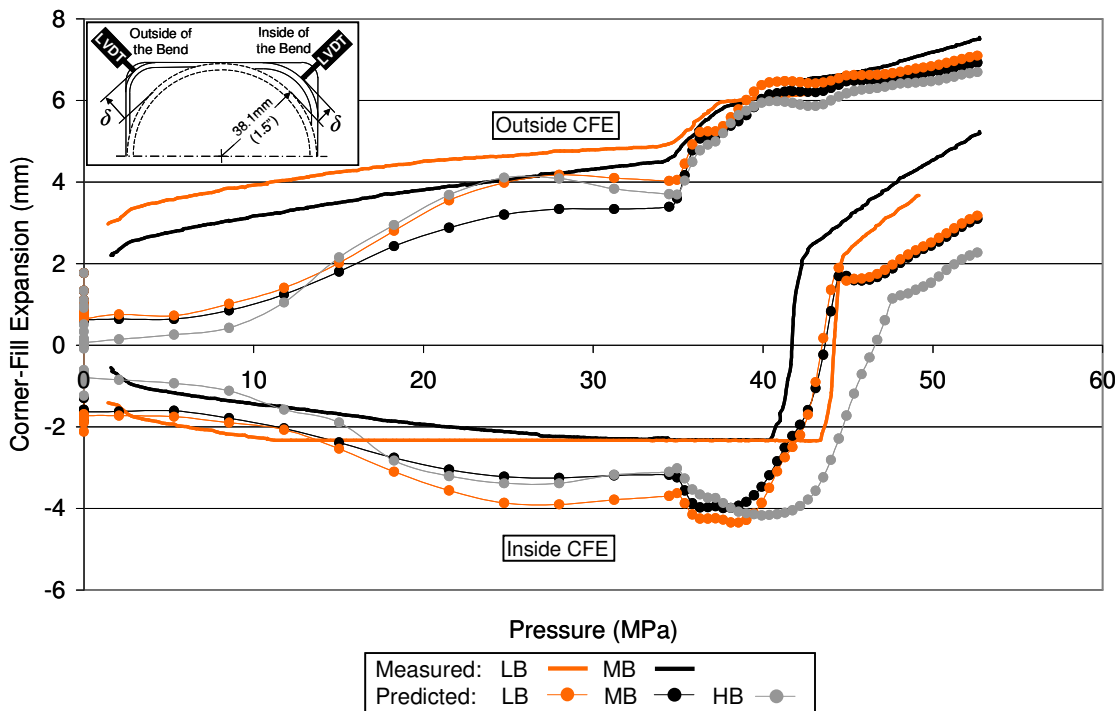
Figure 124: Predicted and measured DP600 CFE *vs.* internal pressure, 67kN EF case, pre-bend tube hydroforming

Figure 125 shows the predicted and measured end-feed (EF) displacement for the 67kN EF case. The measured curves are so-called median curves from the group of tests (see Appendix F). The MB models show a very similar EF displacement to the measured results,

but over predict the EF displacement for the LB case. The HB model predicts a slightly greater EF displacement than the MB and LB cases.
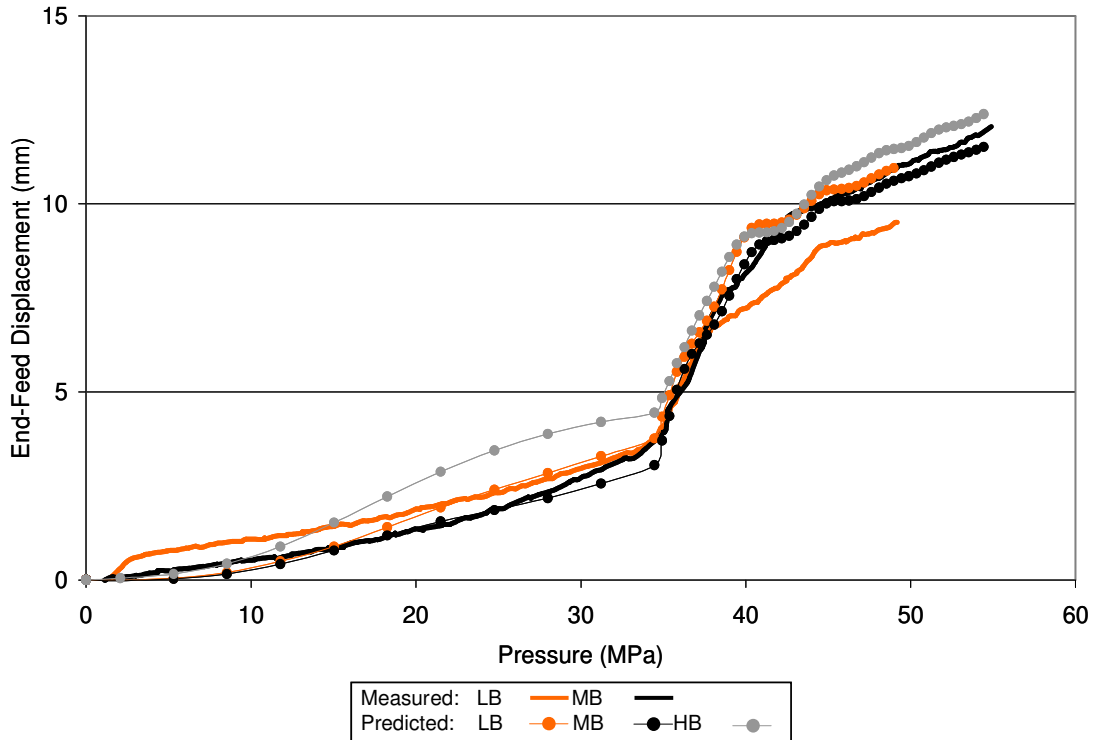
Figure 125: Predicted and measured DP600 EF displacement *vs.* internal pressure, 67kN EF case, pre-bend tube hydroforming

Figure 126 shows the predicted strain and thickness distributions at 54MPa (7,830psi) for all of the boost cases, which is the average burst pressure of the MB 67kN EF tests. The models show that increasing boost levels reduce the amount of thinning in the hydroforming process. All three boost cases capture the thinned regions in the distribution at Ø=180°, 360°. For 0°<Ø<180°, the strain distribution shows that increased boost reduces the major strain and decreases (makes more compressive) the minor strain. This is a result of the HB tube having a greater as-bent thickness than the LB and MB tubes. For 180°<Ø<360°, there is a distinct reduction in major strain between all three boost cases. The HB tube has a considerably lower major strain distribution than the LB tube. For this region of the tube, the minor strain is only slightly affected, with the HB tube having a greater minor strain component than the LB and MB tubes.

173
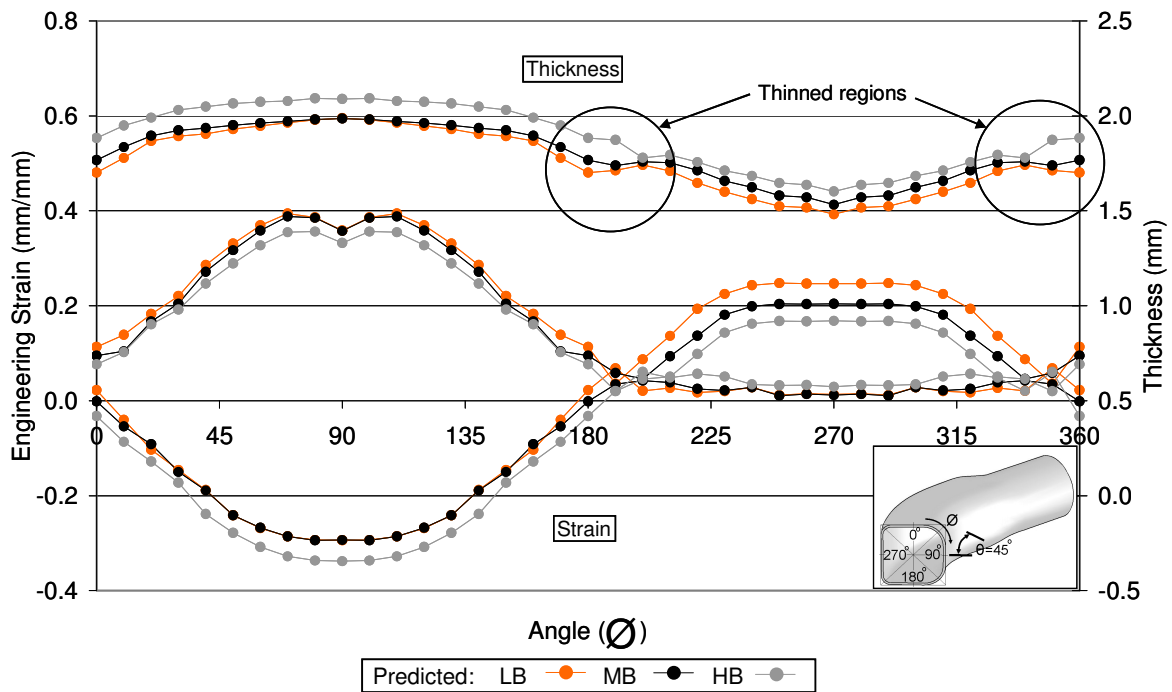
Figure 126: Predicted strain and thickness for all boost cases, DP600 67kN EF, at 54MPa pressure, pre-bend tube hydroforming

8.2.5 XSFLC Failure Prediction

The extended stress-based forming limit (XSFLC) failure criterion was used to predict necking in the DP600 pre-bend hydroforming models. The IF models were not analyzed with the XSFLC because the hydroforming experiments did not achieve burst (due to the high formability of the IF material).

Table 19 shows the results of the predicted failure pressure for the DP600 models and Figure 127 shows the three different failure locations which occurred in all of the models. The predicted failure pressures presented in Table 19 are for the "correct" and "first" failure locations. For the "correct" location results, the XSFLC failure location matched the burst location from the experiment (Table 11), even though failure may have been predicted at a lower pressure for another location. The "first" location results are for the first (lowest) predicted failure pressure, even if the predicted and experimentally observed burst locations

174

did not match. Figure 127 shows the three distinct locations where all of the pre-bend hydroforming models predicted failure (at different internal pressures).

Table 19: XSFLC failure prediction in pre-bend hydroforming summary

Material	Bending Boost Case	End-Feed (kN) [kip]	Measured Avg. Burst Press. (MPa) [psi] Failure Location	Predicted Failure, Correct Location (MPa) [psi] Failure Location	Predicted Failure, First Location (MPa) [psi] Failure Location
DP600	MB	Zero	45.0 [6,528] Neutral Axis	52.7 [7,643] Neutral Axis	46.7 [6,773] Outside of the Bend
	MB	67 [15]	60.4 [8,756] Neutral Axis	78.9 [11,443] Neutral Axis	49.0 [7,107] Inside of the Bend
	MB (↑COF)	67 [15]	NA	63.5 [9,211] Neutral Axis	NA
	LB	67 [15]	54.6 [7,915] Neutral Axis*	72.5 [10,515] Neutral Axis*	49.0 [7,107] Inside of the Bend
	MB	133 [30]	73.4 [10,643] Inside of the Bend*	45.8 [6,643] Inside of the Bend	42.7 [6,193] Outside of the Bend

* Selected because more tubes burst at this location, see Table 11
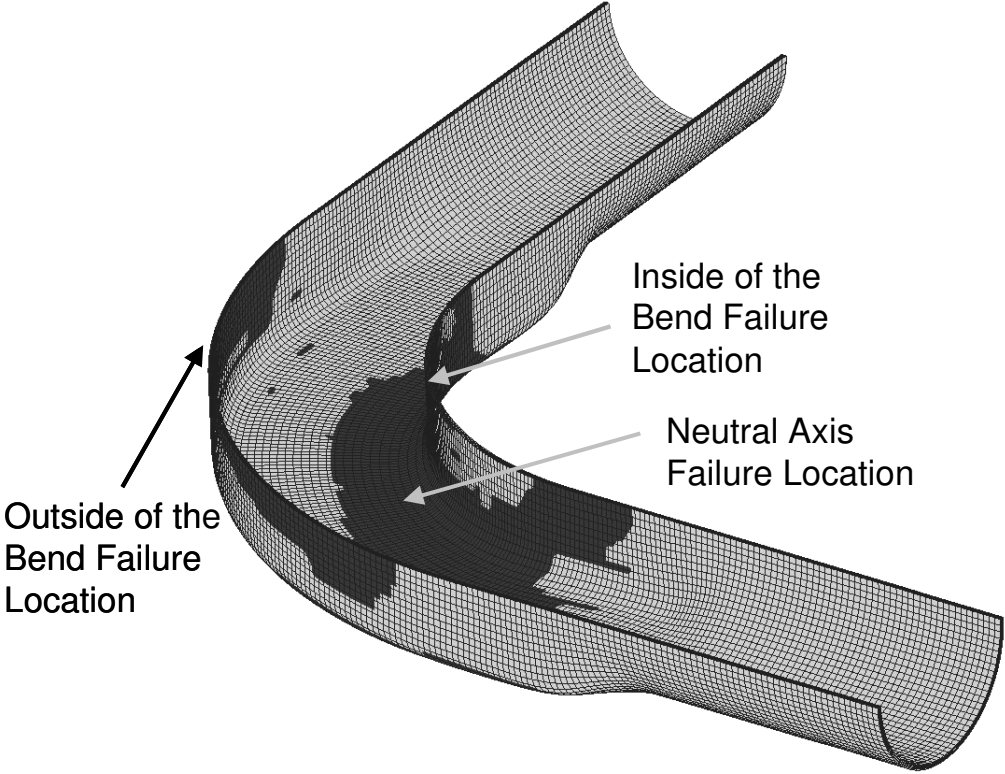
Figure 127: Common XSFLC failure locations for pre-bend hydroforming models

Figure 128: Predicted and measured failure pressures.
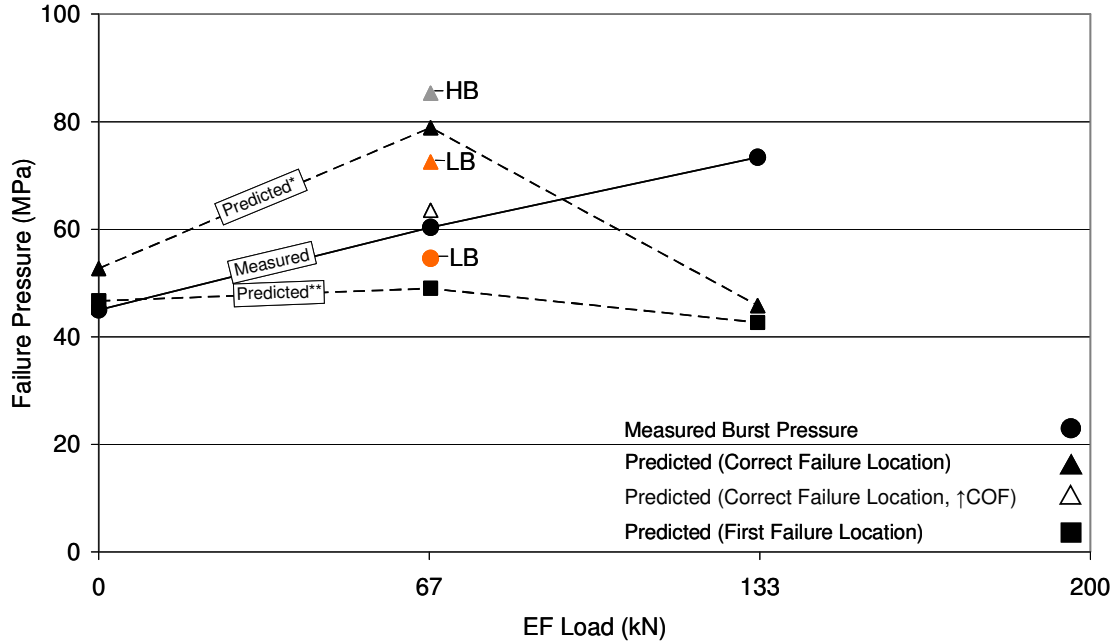
*   At the same failure locations as in the experiments
** At the first failure location predicted by the XSFLC

Figure 128 presents the measured (burst) and predicted XSFLC (necking) failure pressures from Table 19. The predictions at the same failure location as in the experiments ("correct") show an over prediction for the zero and 67kN EF case and a significant under prediction for the 133kN EF case. None of "first" failure locations that are predicted by the XSFLC agree with the experiments and consequently, the failure pressures do not agree with the experiments. Consistently, the "first" failure locations predicted by the XSFLC occur at either the inside or outside of the bend locations, not in the correct neutral axis location observed in the experiments. A possible reason why the XSFLC predicts premature failure at the inside and outside of the bend locations is the assumption made (within the method) which takes into account the tensile and compressive pre-strain created by the pre-bending operation Simha *et al.* (2006). Further investigation is required to validate this work.

Although the XSFLC failure criteria over predicts the "correct" failure pressure for the 67kN EF case, it is able to capture the effect of bending boost on failure pressure. The predicted LB failure pressure is less than the predicted MB case, which is also shown by the

measured burst pressures in Figure 128. The predicted HB failure pressure is greater than the MB case, which is expected due to the increased thickness of the HB tube after pre-bending.

The MB 67kN EF model was also run with an increased coefficient of friction (↑COF) for the tube/die contact definition. The high coefficient model predicts a lower failure pressure for the "correct" failure location. The predicted "correct" failure pressure more accurately predicts the measured failure pressure. A more in-depth study into the effect of COF on failure prediction in pre-bend hydroforming needs to be conducted.

8.3 Numerical Validation Summary

This section summarizes the corner-fill expansion (CFE) and extended stress-based forming limit curve (XSFLC) failure predictions. Figure 129 presents the measured and predicted effect of bending boost and hydroforming end-feed (EF) on the failure pressure for the straight and pre-bend hydroforming experiments. For the straight tube hydroforming models, the XSFLC predicts an increase in burst pressure for increased EF levels, but consistently over predicts the magnitude. The correct failure location is also predicted by the models. It was also show (Figure 116) that the XSFLC is sensitive to the coefficient of friction used in the models. By increasing the coefficient of friction from 0.035 to 0.07, the XSFLC under predicted the failure pressure. The pre-bend failure predictions do not agree with the measured burst pressures or burst locations. When failure is predicted for the "correct" location as in the experiments, the model fails to accurately predict the burst pressure and the trend of increased burst pressure for increasing EF level. The "first" locations to fail in the models do not agree with the burst locations from the experiments. A possible reason for the inaccurate failure prediction for pre-bend hydroforming is the assumptions made for the XSFLC method, which account for the pre-strain after bending.

Figure 129: Effect of hydroforming EF on failure pressure for DP600, predicted and measured
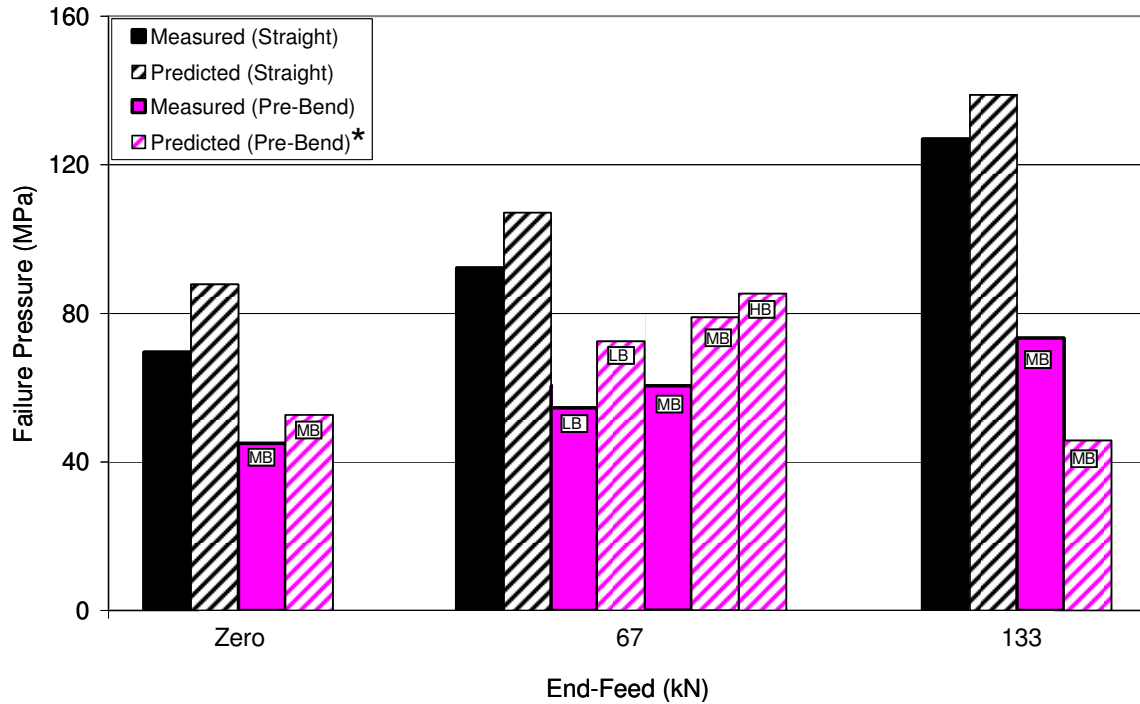
* "Correct" failure location, see Figure 128

Figure 130 presents the effect of bending boost and hydroforming end-feed (EF) on the corner-fill expansion (CFE) during straight and pre-bend tube hydroforming. The straight tube models accurately predict the CFE trend of increased CFE for increased EF level. The magnitude of the CFE is also predicted very closely. For pre-bend tube hydroforming, the models are able to capture the increase in CFE for increased levels of EF as well. The magnitude of the predicted CFE is consistently less than the measured values. The under predicted CFE is a result of the models inability to capture the inside CFE (Figure 119). The effect of bending boost on CFE was also captured by the LB and MB 67kN EF models. The MB model showed a greater CFE than the LB model.
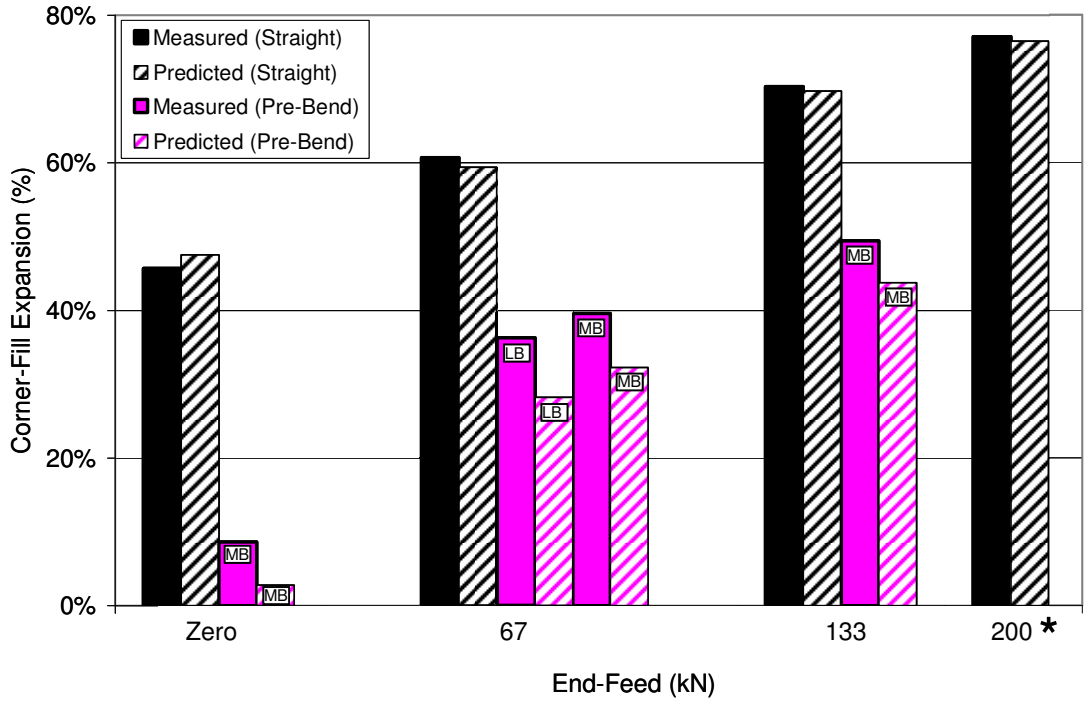
* Burst was not achieved because the maximum capacity of the press was reached (151.7MPa)

Figure 130: Effect of hydroforming EF on CFE for 90% interrupted DP600 tubes, measured and predicted

CHAPTER 9

CONCLUSIONS AND RECOMMENDATIONS

9.1 Conclusions

Based on the work presented in this thesis, the following conclusions can be made:

1. Pre-bending consumes a considerable fraction of ductility of the DP600 tubes. A zero end-feed straight tube had a corner-fill expansion (CFE) of 48%, while the equivalent pre-bent tube had a CFE (average) of 9%. The addition of 133kN EF, resulted in a straight tube CFE of 70%, while the pre-bent tube had a CFE of 49%.

2. Increased hydroforming end-feed delays the onset of fracture (burst) in both the straight and pre-bend hydroforming processes. The delay in fracture increases the burst pressure, which in turn results in greater corner-fill expansion (CFE). For the DP600 material, the application of a 133kN end-feed load during hydroforming increased the average burst pressure from 67MPa to 127MPa for straight tube hydroforming and from 45MPa to 73MPa for pre-bend tube hydroforming. This results in an increase in CFE from 46% to 70% in straight tube hydroforming and an increase from 9% to 49% in pre-bend tube hydroforming. The failure location also changes for different EF levels in pre-bend hydroforming.

3. The effect of increased bending boost on pre-bent tubes results in a decrease in the major (tensile) strain and thinning at the outside of the bend and an increase in minor (compressive) strain and thickening at the inside of the bend. The average thickness around the circumference of the tube also increases with increased bending boost.

4. The effect of increased bending boost in pre-bend hydroforming increases the burst pressure and CFE of the tubes due to the greater thickness of the as-bent tubes. For the DP600 tubes, an increase from 100% bending boost to 105% bending boost (LB to MB), resulted in an increase in average burst pressure from 55MPa to 60MPa. As a result of the increase in burst pressure, the CFE also increased from 36% to 40%. The failure location also changes for different bending boost levels. The failure location also changes for different boost levels in pre-bend hydroforming.

5. The numerical models of the pre-bending and hydroforming process accurately predict the CFE and EF displacement well.

6. The extended stress-based forming limit curve (XSFLC) failure criterion accurately predicts the straight tube hydroforming failure pressure trend, but over predicts the magnitude. This outcome suggests that the approximated (Keeler-Brazier) strain-space forming limit curve (εFLC) is too high along the major strain axis. This suggestion is supported by the findings of Sorine *et al.* (2006), who showed that the εFLC derived from free expansion burst tests was actually lower (along the major strain axis) than the εFLC predicted by the Keeler-Brazier approximation. One should also be aware of the potential effect that the extrapolated constitutive model (flow stress curve) may have on ability of the XSFLC to predict failure.

7. For pre-bend hydroforming, the XSFLC fails to predict the measured trend or magnitude, but captures the change in failure pressure due to pre-bend *versus* straight tube hydroforming. Further investigation into the assumptions made to account for the pre-strain during bending is required.

8. The XSFLC failure predictions are sensitive to the coefficient of friction (COF) used in the model, with a lower failure pressure when the COF is increased.

9.2 Recommendations

The following recommendations should be considered to expand upon the work completed for this thesis:

1. A conventional steel (such as AKDQ) tube with the same wall thickness as the DP600 tube would provide a better comparison for the investigation of the hydroformability of advanced high strength steel. The study should also be expanded to investigate other advanced high strength steels such as DP800, TRIP and TWIP steels.

2. The DP600 HB boost condition should be examined experimentally to strengthen the conclusions made for the effect of increased bending boost on hydroformability. Recently, the torque capacity of the tube bender at the University of Waterloo was upgraded to achieve the HB condition for DP600 tubes.

3. An optimized end-feed load schedule during hydroforming should be modeled and tested experimentally to determine the maximum burst pressure and corner-fill expansion that can be achieved.

4. The strain-space forming limit curve (εFLC) and constitutive model (flow stress curve) for the DP600 tubes should be measured experimentally with the free-expansion burst test to further validate the extended stress-based forming limit curve (XSFLC) failure criterion.

5. The current study should be extended to further examine the effect of pre-bending R/D ratio on hydroformability.

6. A better circle grid etching technique which resists erosion due to pre-bending and hydroforming would provide more accurate measured strain distributions to validate the models.

REFERENCES

Advanced High-Strength Steels (2006) [online]. [Accessed March 21st, 2006]. Available from World Wide Web: < http://ussautomotive.com/auto/tech/grades/complex_phase.htm>

Ahmetoglu, M., Sutter, K., Li, X.J., Altan, T., 2000. Tube hydroforming: current research, applications and need for training. *bb*, vol. 98, 224-231.

Al-Qureshi H.A., 1999. Elastic-plastic analysis of tube bending. *Machine Tools and Manufacture*, vol. 39, 87-104.

Altan, T., 1999. Formability and design issues in tube hydroforming. *Hydroforming of Tube, Extrusions and Sheet Metal*, vol. 1, 105-121.

Arrieux, R., Bedrin, C., Boivin, M., 1982. Determination of an intrinsic forming limit stress diagram for isotropic sheets. *Proceedings of the 12th Biennial Congress IDDGR*, 61-71.

Asnafi, N., 1999. Analytical modeling of tube hydroforming. *Thin-Walled Structures*, vol. 34, 295-330.

Asnafi, N., Skogsgardh, A., 2000. Theoretical and experimental analysis of stroke-controlled tube hydroforming. *Material Science & Engineering A*, vol. A279, 95-110.

Asnafi, N., Nillson, T., Lassl, G., 2003. Tubular hydroforming of automotive side members with extruded aluminum profiles. *Journal of Materials Processing Technology*, vol. 142, 93-101.

Bardelcik, A., Worswick, M.J., 2006. Numerical investigation into the effects of bending boost and hydroforming end-feed on the hydroformability of DP600 tube. *SAE 2005 Transactions: Journal of Materials and Manufacturing*, 41-51.

Carleer, B., van der Kevie, G., de Winter, L., van Velhuizen, B., 2000. Analysis of the effect of material properties on the hydroforming process of tubes. *Journal of Materials Processing Technology*, vol. 104, pp. 158-166.

Chen, K.K., Chen, J.J., Chen, X.M., 2005. Plane strain simulation for corner fill of hydroforming tubes in oversized die. *Proceedings of 2005 SAE World Congress: Sheet/Hydro/Gas Forming Technology and Modeling*, 83-93.

Chow, C.L., Yang, X.J., 2002. Bursting of fixed tubular and restrained hydroforming. *Journal of Materials Processing Technology*, vol. 130-131, 107-114.

Dohda, K., Kawai, N., 1990. Correlation for tribological indices for metal forming. *Journal for the Society of Tribologists and Lubrication Engineers*, vol. 46, 727-734.

Dohmann, F., Hartl, C., 1997. Tube hydroforming – research and practical application. *Journal of Materials Processing Technology*, vol. 71, 174-186.

Dwyer, N., Worswick, M.J., Gholipour, J., Xia, Z.C., Khodayari, G., 2002. Pre-Bending and subsequent hydroforming of tube: Simulation and experiment. *Proceedings of NUMISHEET* 2002, 447-452.

Dyment, J., 2002. User manual for TubeBend Software, Internal report, University of Waterloo.

Dyment, J., Worswick, M.J., Formani, F., Oliveira, D.A., Khodayari, G., 2003. Effect of endfeed on the strains and thickness during bending and on the subsequent hydroformability of steel tubes. *Proceedings of IBEC 2003 Conference*, 717-722.

Dyment, J., 2004. MASc Thesis: Effect of bending process on the hydroformability of steel tubes. University of Waterloo.

Fretty, P., 2001. Case study: Hydroforming reshapes BMW. *Advanced Manufacturing Magazine*, November.

Fuchizawa, S., Takeyama, H., 1979. Study of bulge forming of thin-walled cylinder. *Journal of Japan Society of Precision Engineering*, vol. 45, 106-111.

Fuchizawa, S., 1984. Influence of strain hardening exponent on the deformation of thin-walled tube of finite length subjected to hydrostatic internal pressure. *Proceedings of Advanced Technology of Plasticity*, vol. 1, 297-302.

Fuchizawa, S., 1987. Influence of plastic anisotropy on deformation of thin-walled tubes in bulge forming. *Proceedings of Advanced Technology of Plasticity*, vol. 2, 297-302.

Gholipour, J., Worswick, M.J., Oliveira, D.A., Khodayari, G., 2004. Severity of the bend and its effects on the subsequent hydroforming process for aluminum alloy tube. *Proceedings of Numiform 2004*, 1089-1094.

Gao, L., Strano, M., 2004. FEM analysis of tube pre-bending and hydroforming. *Journal of Materials Processing Technology*, vol. 151, 294-297.

Goodarzi, M., Kuboki, T., Murata, M., 2005. Deformation analysis for the shear bending process of circular tubes. *Journal of Materials Processing Technology*, vol. 162-163, 492-497.

Goodwin, G.M., 1968. Application of strain analysis to sheet metal forming in the press shop. *SAE Paper*, #680093.

Graf, A., Hosford, W., 1994. The influence of strain-path changes on forming limit diagrams in Al 6111 T4. *International Journal of Mechanical Sciences*, vol. 36, 897-910.

Green, D., Stoughton, T.B., 2004. Hydroforming severity using stress-based forming limits. *Proceedings of the 2nd Annual North American Hydroforming Conference and Exhibition*.

Grey, J.E., Devereaux, A.P., Parker, W.N., 1939. Apparatus for making wrought metal T's. US Patent 2,203,868.

Gupta, A.K., Kumar, D.R., 2006. Formability of galvanized interstitial-free steel sheets. *Journal of Materials Processing Technology*, vol. 172, 225-237.

Hallquist, J., 2003. LS-DYNA Theoretical Manual, *Livermore Software Technology Corporation.*

Hill, R., 1948. A theory of the yielding and plastic flow of anisotropic metals. *Proceeding of the Royal Society of London A193,* 281-297.

Hill, R., 1950. The mathematical theory of plasticity, *Oxford University Press*.

Hokook L., Van Tyne, C.J., Field, D., 2005. Finite element bending analysis of oval tubes using rotary draw bender for hydroforming applications. *Journal of Materials Processing Technology,* vol. 168, 327-335.

Inoue, K., Mellor, P.B., 1979. Radial-draw bending of stainless steel tube. *Journal of Mechanical Working Technology*, vol. 3, 151-166.

International Iron and Steel Institute, 2005. Advanced high strength steel (AHSS) application guidelines. March.

Interstitial Free (IF) Steel (2005) [online]. [Accessed March 21st, 2006]. Available from World Wide Web: < http://www.krakatausteel.com/product/ifsteel/index.asp>

Jirathearanat, S., Hartl, C., Altan, T., 2004. Hydroforming of Y-shapes - product and process design using FEA simulation and experiments. *Journal of Materials Processing Technology*, vol. 146, 124-129.

Johnson, K.I., Nguyen, B.N., Davies, R.W., Grant, G.J., Khaleel, M.A., 2004. A numerical process control method for circular-tube hydroforming prediction. *International Journal of Plasticity*, vol. 20, 1111-1137.

Kawai, N., Dohda, K., 1987. A new lubricity evaluation method for metal forming by a compression-twist type friction testing machine. *ASME Transactions: Journal of Tribology*, vol. 109, 343-350.

Keeler, S.P., Backhofen, W.A., 1964. Plastic instability and fracture in sheet stretched over rigid punches. *ASM Transactions Quarterly*, vol. 56, 25-48.

Keeler, S.P., Brazier, W.G., 1975. Relationship between laboratory materialcharacterization and press-shop formability. *Proceedings of MicroAlloying 75,* 517-528.

Khodayari, G., Reid, J.V., Garnett, M., 2002, Tubes, lubes, dies and friction. *The Tube and Pipe Journal*, vol. 13, 72-74.

Kim, J., Lei, L., Hwang, S., Kang, S., Kang, B., 2002. Manufacture of an automobile lower arm by hydroforming. *International Journal of Machine Tools & Manufacture*, vol. 42, 69-79.

Kim, S., Kim, Y., 2002. Analytical study for tube hydroforming. *Journal of Materials Processing Technology*, vol. 128, 232-239.

Kirdli, G.T., Bao, L., Mallick, P.K., Tian, Y., 2003. Investigation of thickness variationand corner filling in tube hydroforming. *Journal of Materials Processing Technology*, vol. 133, 287-296.

Kleemola, H.J., Pelkkikangas, M.T., 1977. Effect of predeformation and strain path on the forming limits of steel copper and brass. *Sheet Metal Industries*, vol. 63, 591-599.

Koc, M., Altan, T., 2001. An overall review of the tube hydroforming (THF) technology. *Journal of Materials Processing Technology*, vol. 108, 384-393.

Koc, M., Altan, T., 2002. Application of two dimensional (2D) FEA for the tube hydroforming process. *International Journal of Machine Tools & Manufacture*, vol. 42, 1285-1295.

Koc, M., 2003a. Investigation of the effect of loading path and variation in material properties on robustness of the tube hydroforming process. *Journal of Materials Processing Technology*, vol. 133, 276-281.

Koc, M., 2003b. Tribological issues in the tube hydroforming process – Selection of a lubricant for robust process conditions for an automotive structural frame rail. *ASME Transactions: Journal of Manufacturing Science and Engineering,* vol. 125, 484-492.

Konieczny, A., Chen, X.M., Witmer, D.A., Shi, M.F., Hayashida, Y., Omiya, Y., 2005. Hydroforming performance of laser welded and electric resistance welded high strength steel tubes. *Proceedings of 2005 SAE World Congress: Sheet/Hydro/Gas Forming Technology and Modeling*, 17-25.

Lee, Y. 2001. MASc Thesis: Formability of tailor welded blanks. University of Waterloo.

Lei, L., Kim, J., Kang, B., 2000. Analysis and design of hydroforming process for automobile rear axle housing by FEM. *International Journal of Machine Tools & Manufacture*, vol. 40, 1691-1708.

Li, H.Z., Fagerson, R., Stelson, K.A., 1994. A method of adaptive control of rotary-draw thin-walled tube bending with springback compensation. *NAMRI/SME Transactions*, vol. 22, 25-28.

Limb, M.E., Chakrabarty, J., Graber, S., Roberts, W.T., 1976. Hydraulic forming of tubes. *Sheet Metal Industries*, 418-424.

Lou, H., Stelson, K.A., 2001. Three-dimensional tube geometry control for rotary draw tube bending, Part 1: Bend angle and overall tube geometry control. *ASME Transactions: Journal of Manufacturing Science and Engineering*, vol. 123, 258-265.

Lou, H., Stelson, K.A., 2001. Three-dimensional tube geometry control for rotary draw tube bending, Part 2: Statistical tube tolerance analysis and adaptive bend control. *ASME Transactions: Journal of Manufacturing Science and Engineering*, vol. 123, 266-271.

Manabe, K., Nishimura, H., 1983. Influence of material properties in forming of tubes. *Proceedings of Bander Bleche Rohre* 9, 266-269.

Manabe, K., Mori, S., Suzuki, K., Nishimura, H., 1984. Bulge forming of thin walled tubes by micro-computer controlled hydraulic press. *Advanced Technology of Plasticity*, vol. 1, 279-284.

Manabe, K., Amino, M., 2002. Effects of process parameters and material properties on deformation process in tube hydroforming. *Journal of Materials Processing Technology*, vol. 123, 285-291.

Mortimer, J., 2001. BMW breaks new ground with hydroforming. *Assembly Automation*, vol. 21, no. 4, 317-320.

Nautiyal, P.C., Schey, J.A., 1990. Transfer of aluminum to steel tin sliding contact: Effects of lubricant. *ASME Transactions: Journal of Tribology*, vol. 112, 282-287.

Ngaile, G., Jaeger, S., Altan, T., 2004a. Lubrication in tube hydroforming (THF) Part I. Lubrication mechanisms and development of model tests to evaluate lubricants and die coatings in the transition and expansion zones. *Journal of Materials Processing Technology.* vol. 146, 108-115.

Ngaile, G., Jaeger, S., Altan, T., 2004b. Lubrication in tube hydroforming (THF) Part II.Performance evaluation of lubricants using LDH test and pear-shaped tube expansion test. *Journal of Materials Processing Technology.* vol. 146, 108-115.

Normani, F., 2004. MASc Thesis: Analytical modeling of tube bending with hydroforming. University of Waterloo.

Ososkov, Y., Jain, M., Wilkinson, D., Inal, K., Neal, K.W., 2005. Experimental and FEA investigation of tensile behaviour of high strength dual-phase DP600 steel. *Proceedings of 2005 SAE World Congress: Sheet/Hydro/Gas Forming Technology and Modeling*, 1-9.

Paulsen, F., Welo, T., 1996. Application of numerical simulation in the bending of aluminum alloy profiles. *Journal of Material Processing Technology*, vol. 58, 274-285.

Prier, M., Schmoeckel, D., 1999. Tribology of Internal-High-Pressure-Forming. *Proceedings of The International Conference on Hydroforming*, 379-390.

Rege, J.S., Inazumi, T., Nagataki, Y., Urabe, T., Smith, G., Zuidema, B., Denner, S., 2002. Development of HDGI/HDGA dual phase steel family (DP500, DP600, DP800, DP1000) at national steel corporation. *Proceedings of 44th MWSP*, vol. 40, 391-404.

Rimkus, W., Bauer, H., Mihsein, M.J.A., 2000. Design of load-curves for hydroforming applications. *Journal of Materials Processing Technology*, vol. 108, 97-105.

Rípodas Agudo, F.P., 2003. Technical article: Manufacturing tubes for hydroforming applications. *Tube and Pipe Technology Magazine*, May.

Rodriguez, J.N., Schlatter, D., 1999. Contribution of a booster device on tube rotary draw bending experimental and finite element analysis. *Proceedings of Stainless Steel '99: Science and Market*, 229-236.

Schey, J.A., Nautiyal, C., 1990. Effects of surface roughness on friction and metal transfer in lubricated sliding of aluminum alloys against steel surfaces. *Wear*, vol. 146, 37-51.

Simha, C.H.M, Gholipour, J., Bardelcik, A., Worswick, M.J., 2005. Application of an extended stress-based flow limit curve to predict necking in tubular hydroforming. *Proceedings of NUMISHEET 2005*, 511-516.

Simha, C.H.M, Gholipour, J., Bardelcik, A., Worswick, M.J., 2006. Prediction of necking in tubular hydroforming using an extended stress-based forming limit curve. Accepted for Publication in *ASME Transactions: Journal of Engineering Materials and Technology*

Singh, H., 2003. Fundamentals of hydroforming, Society of Engineers.

Sorine, M., Worswick, M.J., Oliveira, D.A., 2006. Effect of end-feed in hydroforming of straight and pre-bent high strength and advanced high strength steel tubes. *Proceedings of SAE 2006 World Congress*, paper #2006-01-0544.

Speich, G.R., 1990. Dual-phase steels. *In: Metals Handbook*, ASM International.

Stoughton, T.B., 2000. A general forming limit criterion for sheet metal forming. *International Journal of Mechanical Sciences*, vol. 42, 1-27.

Tang, N.C., 2000. Plastic-deformation analysis in tube bending. *International Journal of Pressure Vessels and Piping*, vol. 77, 751-759.

Thiruvarudchelvan, S., Seet, G.L., Ang, H.E., 2003. Computer-monitored hydraulic bulging of tubes. *Journal of Materials Processing Technology*, vol. 57, 182-188.

Tirosh, J., Neuberger, A., Shirizly, A., 1995. On tube expansion by internal fluid pressure with additional compressive stress. *International Journal of Mechanical Sciences*, vol. 38, 839-851.

Toyoda, S., Suzuki, K., Sato, A., 2004. High strength steel tubes for automotive suspension parts –High strength steel tubes with excellent formability and forming technology for light weight automobiles. *JFE Technical Report*, No. 4., 32-37.

Utsumi, N., Sakaki, S., 2002. Countermeasures against undesirable phenomena in the draw-bending process for extruded square tubes. *Journal of Materials Processing Technology*, vol. 123, 264-269.

Vollertsen, F., Plancak, M., 2002. On possibilities for the determination of the coefficient of friction in hydroforming of tubes. *Journal of Materials Processing Technology*, vol. 125-126, 412-420.

Wang, X., Cao, J., 2001. Wrinkling limit in tube bending. *ASME Transactions: Journal of Engineering Materials and Technology*, vol. 123, 430-435.

Winkler, S.L., Bardelcik, A., Worswick, M.J., Ososkov, Y., Wilkinson, D., Jain, M., 2005. Damage and formability of AKDQ and high strength DP600 steel tubes. *Proceedings of*

2005 SAE World Congress: Sheet/Hydro/Gas Forming Technology and Modeling, 75-83.

Woo, D.M., Hawkes, P.J., 1968. Determination of stress/strain characteristics of tubular materials. *Journal of the Institute of Metals*, vol. 96, 357-359.

Woo, D.M., Lua, A.C., 1978. Plastic deformation of anisotropic tubes in hydraulic bulging. *ASME Transactions Journal of Engineering Materials and Technology*, vol. 100, 421-425.

Xia, Z.C., 2001. Failure analysis of tubular hydroforming. *ASME Transactions: Journal of Engineering Materials and Technology*, vol. 123, 423-429.

Xing, H.L., Makinouchi, A., 2001. Numerical analysis and design for tubular hydroforming. *International Journal of Mechanical Sciences*, vol. 43, 1009-1026.

Yang, J., Jeon, B., Oh, S., 2001. The tube bending technology of a hydroforming process for an automotive part. *Journal of Materials Processing Technology*, vol. 111, 175-181.

Zhan, M., Yang, H., Jiang, Z.Q., Zhao, Z.Q., Lin, Y., 2002. A study on a 3D FE simulation mothod of the NC bending process of thin-walled tube. *Journal of Materials Processing Technology*, vol. 129, 273-276.

Zhang, S.H., 1999. Developments in hydroforming. *Journal of Materials Processing Technology*, vol. 91, 236-244.

APPENDICES

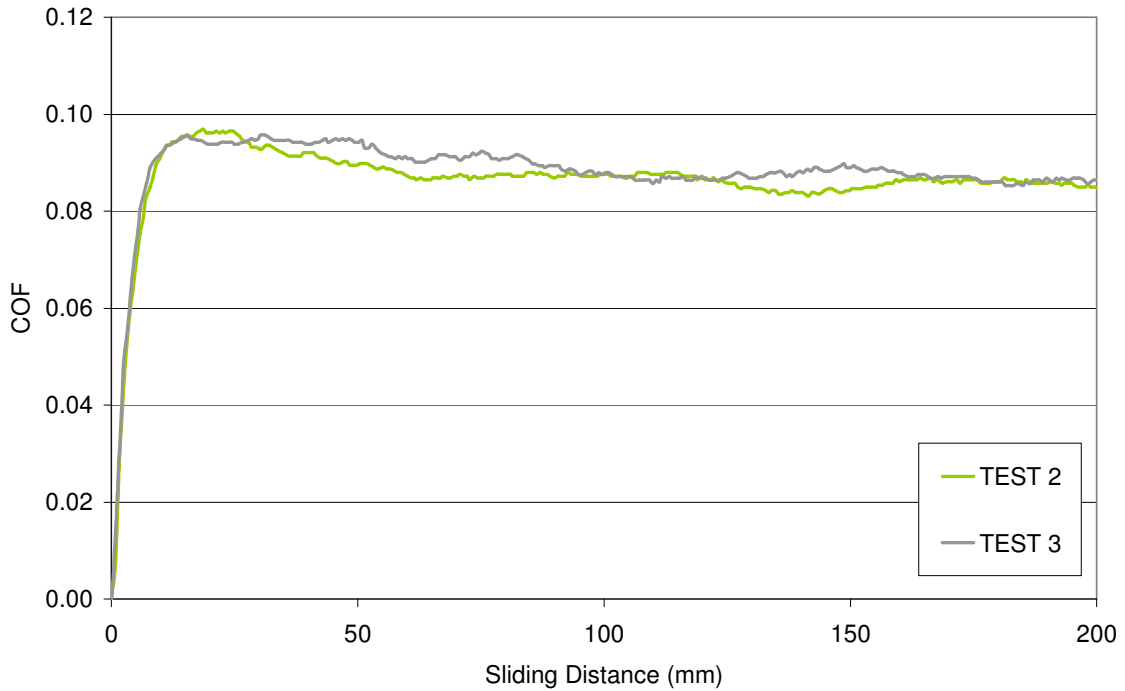# APPENDIX A

DP600 Twist Compression Test Results
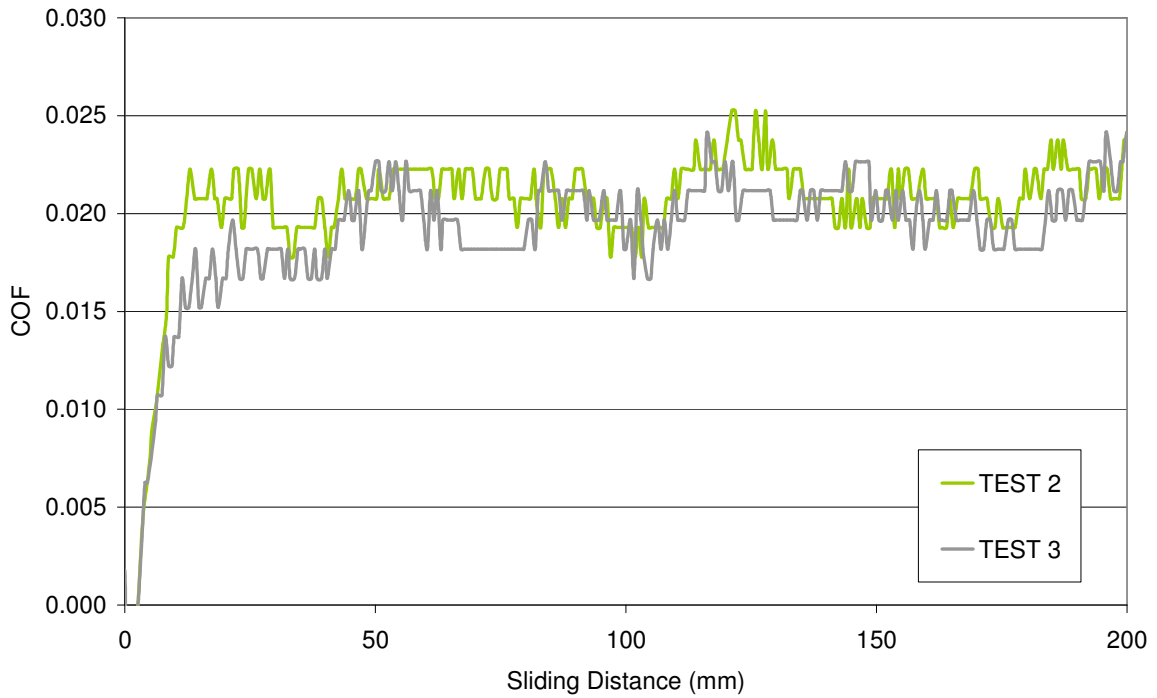
Figure A.1: TCT results for wiper tool at 21MPa (3,000psi) interfacial pressure

Figure A.2: TCT results for wiper tool at 83MPa (12,000psi) interfacial pressure
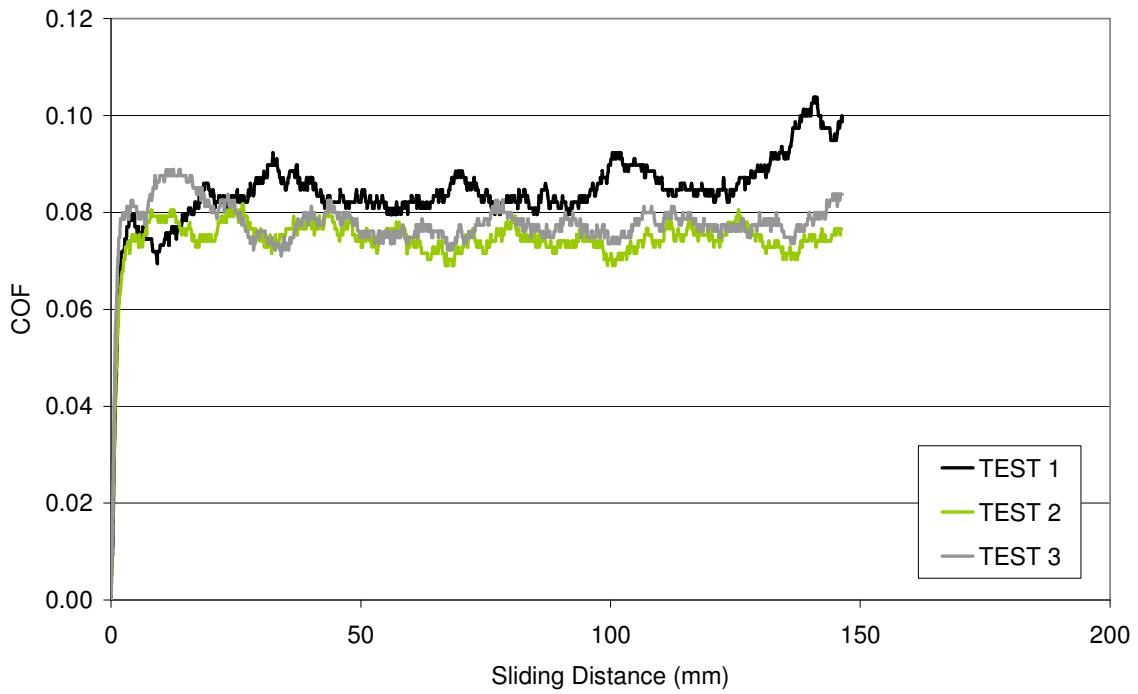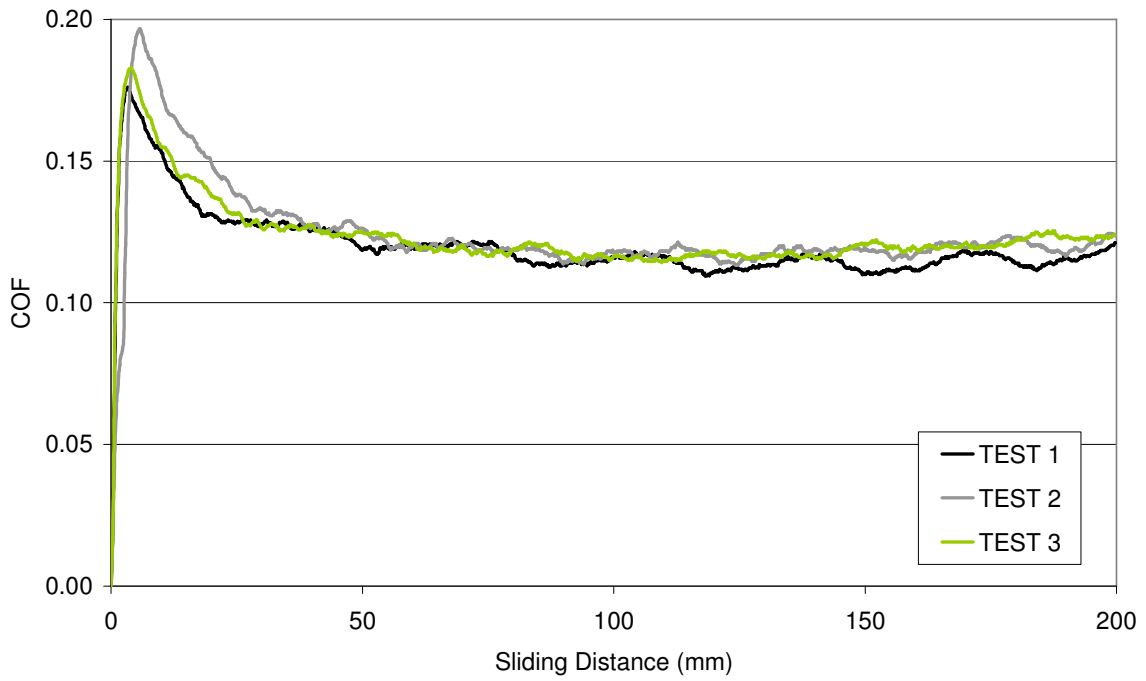
Figure A.3: TCT results for bend, pressure and clamp tool at 24MPa (3,500psi) interfacial pressure
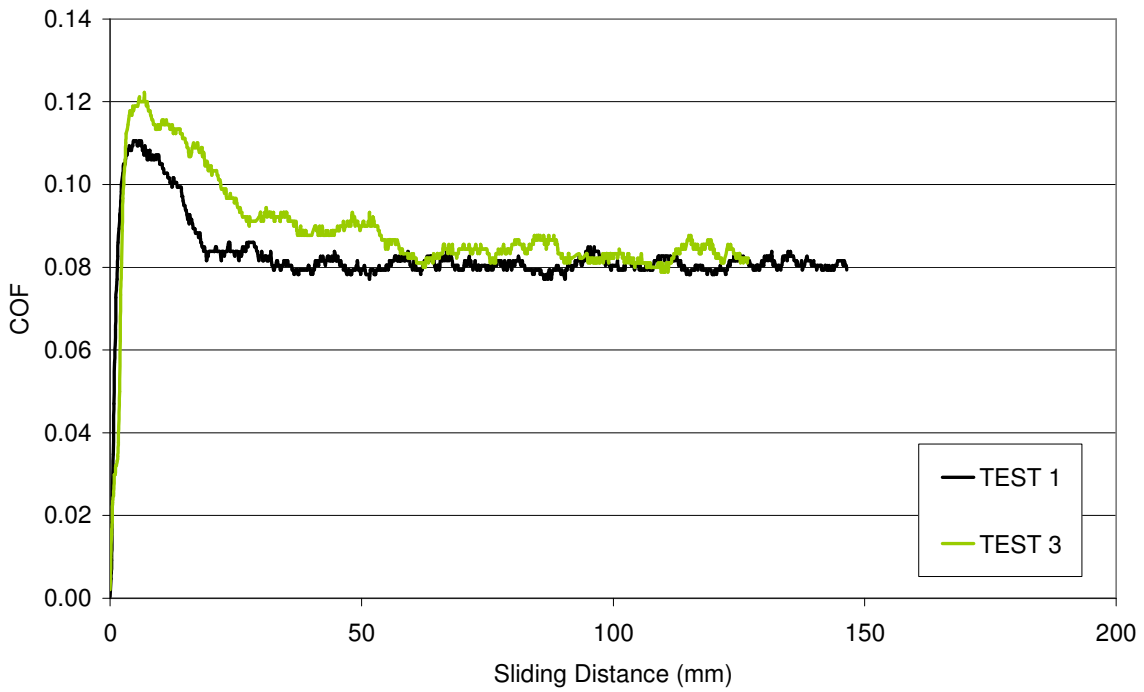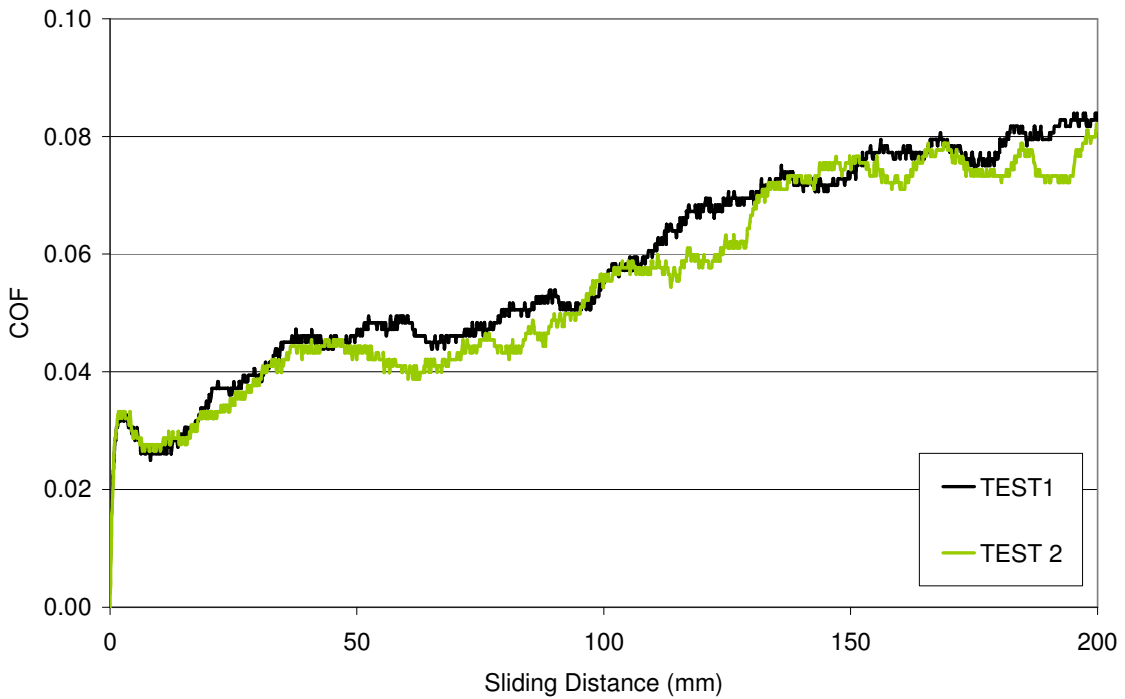

NOTE: Test 2 deviated significantly and was not considered

Figure A.4: TCT results for bend, pressure and clamp tool at 28MPa (4,000psi) interfacial pressure
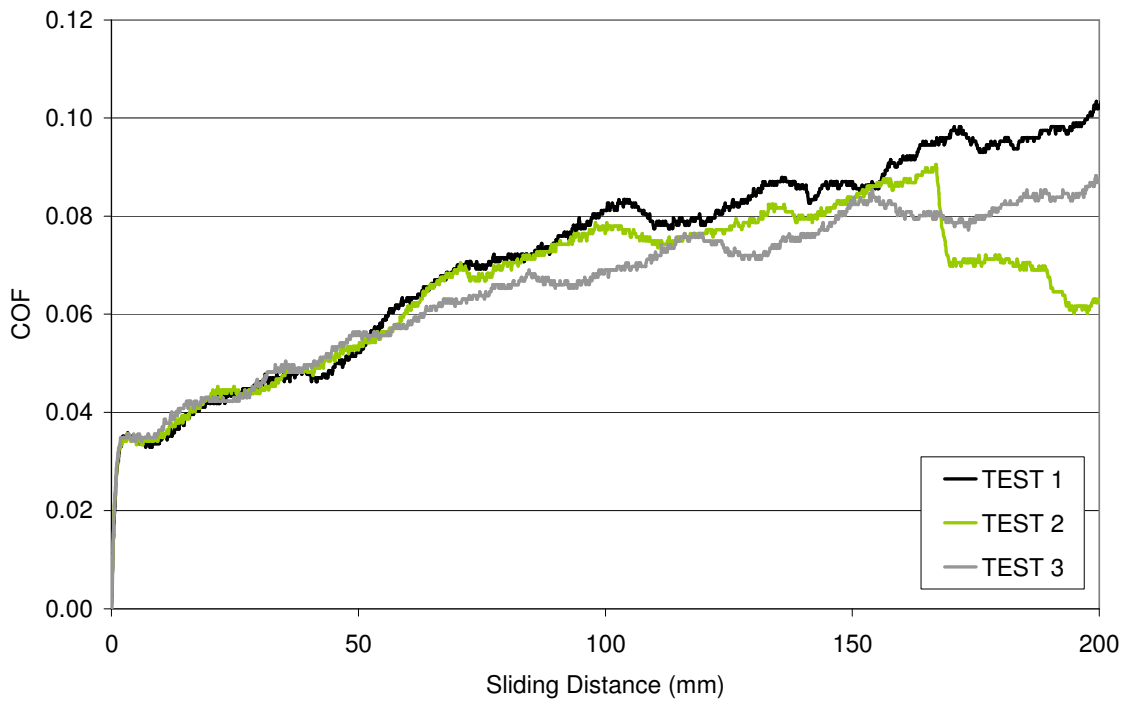
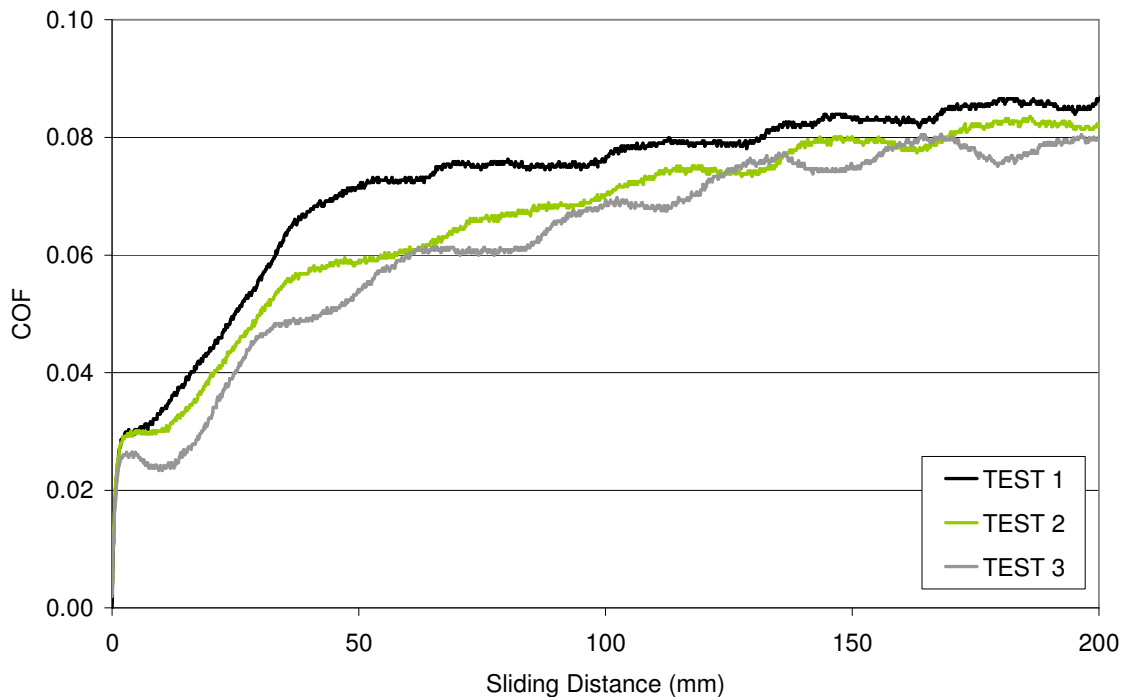**Figure A.5:** TCT results for bend, pressure and clamp tool at 69MPa (10,000psi) interfacial pressure

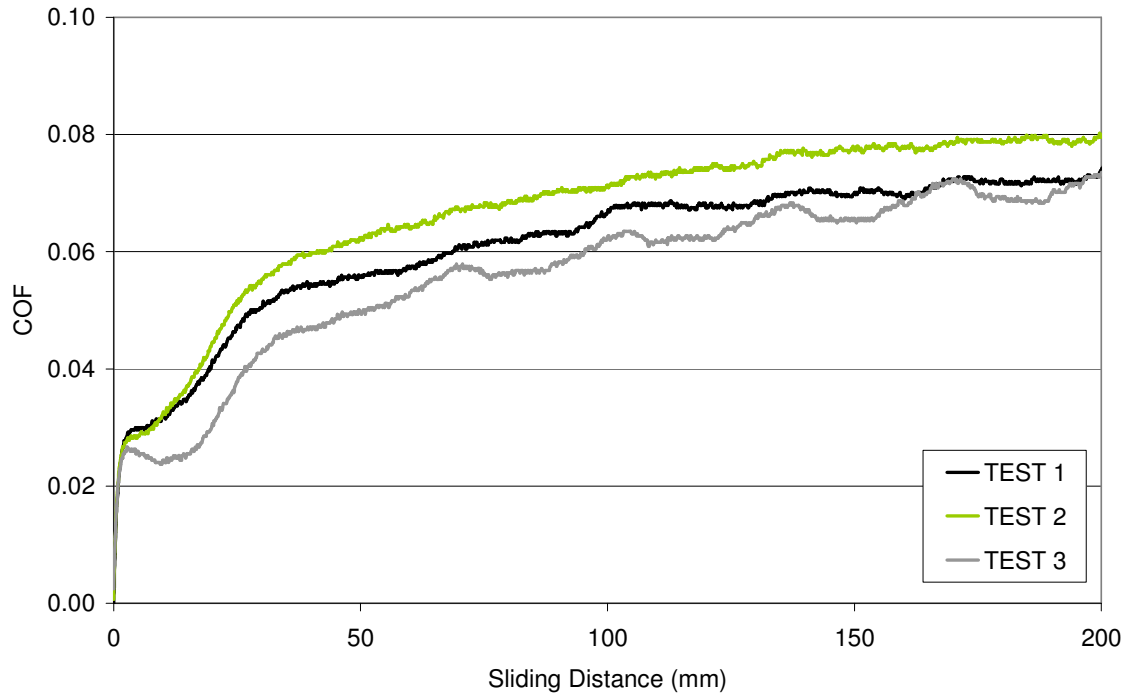NOTE: Test 3 deviated significantly and was not considered

Figure A.6: TCT results for hydroforming tool at 28MPa (4,000psi) interfacial pressure

Figure A.7: TCT results for hydroforming tool at 41MPa (6,000psi) interfacial pressure

Figure A.8: TCT results for hydroforming tool at 69MPa (10,000psi) interfacial pressure

Figure A.9: TCT results for hydroforming tool at 83MPa (12,000psi) interfacial pressure

APPENDIX B

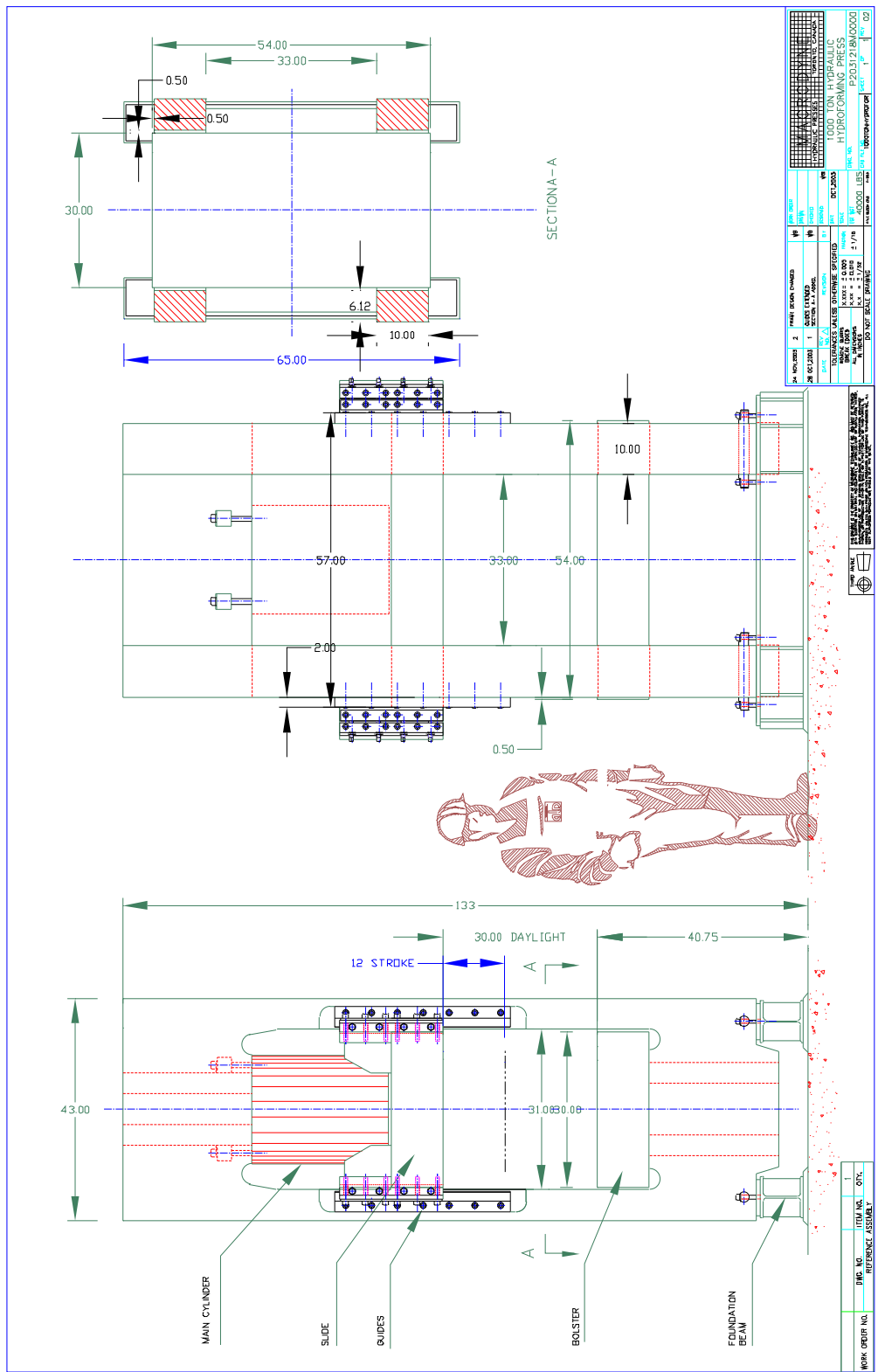Macrodyne Hydroforming Press and Pre-Bend Hydroforming Die

CAD Drawings
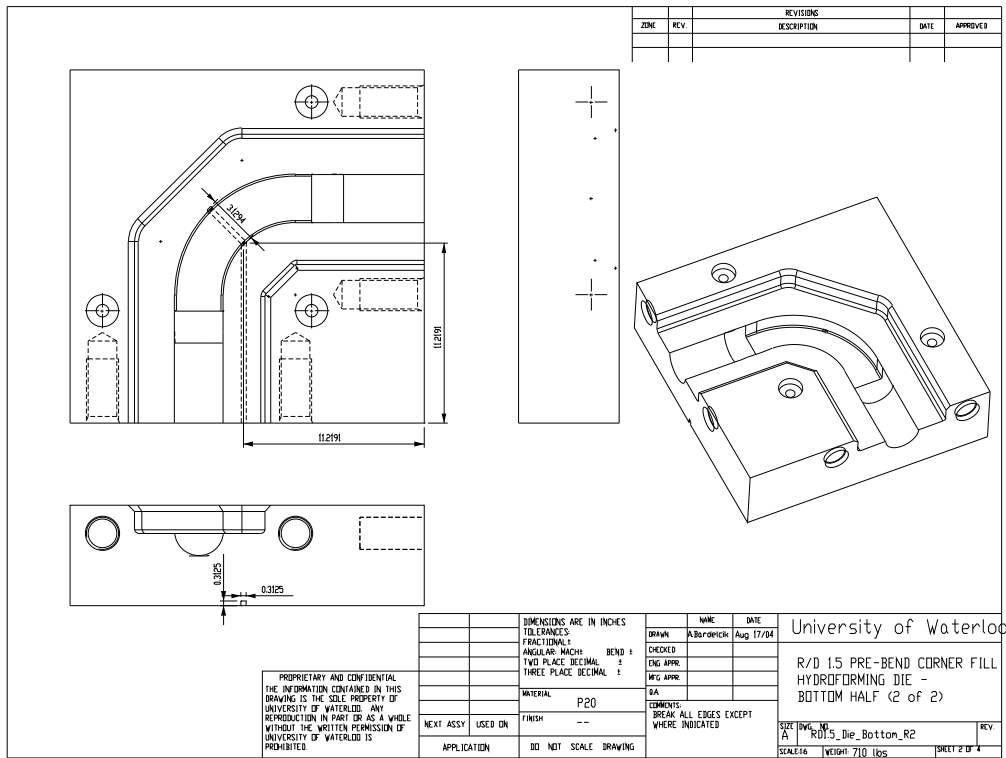
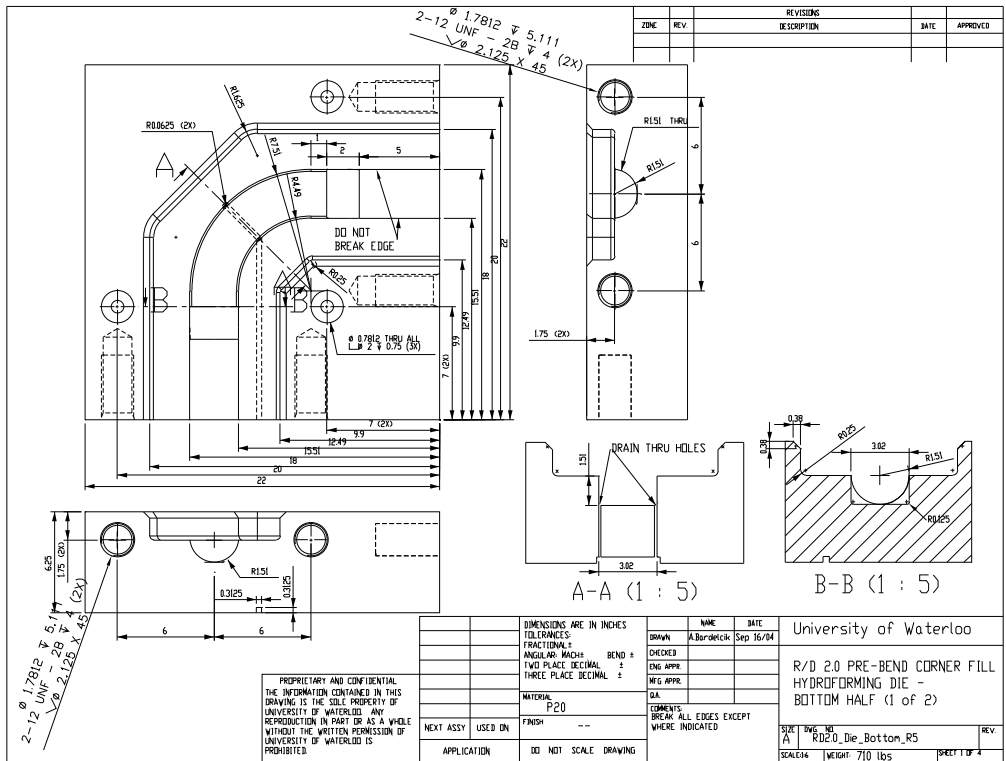**Figure B.1:** Macrodyne 1,000Ton hydroforming press

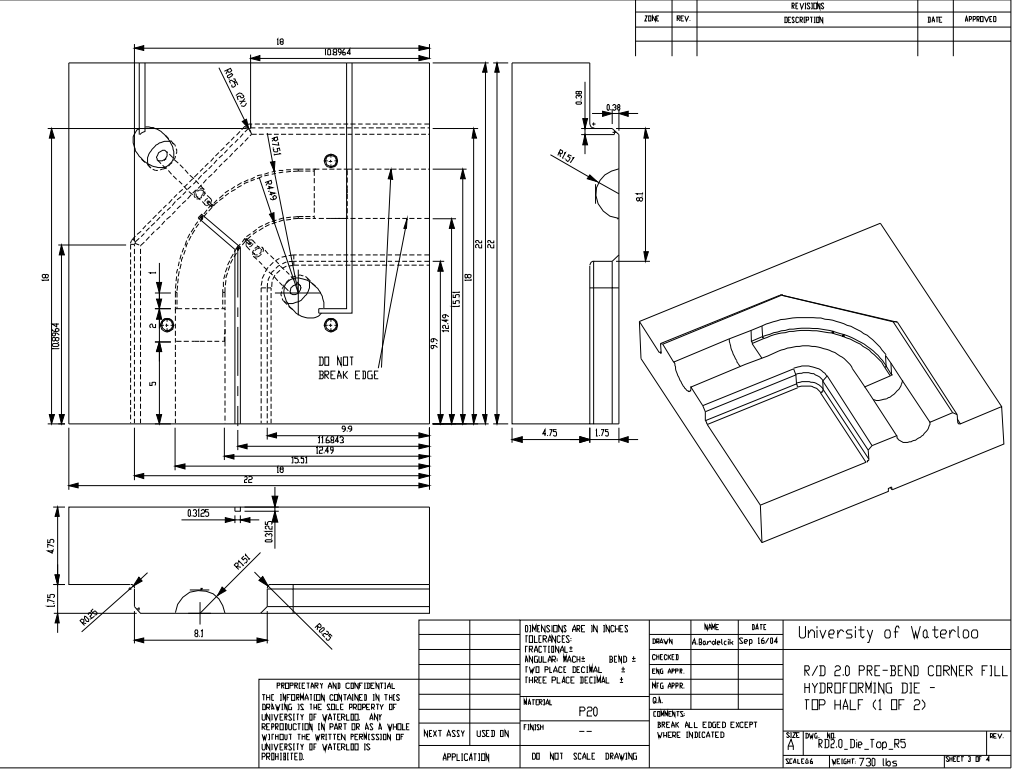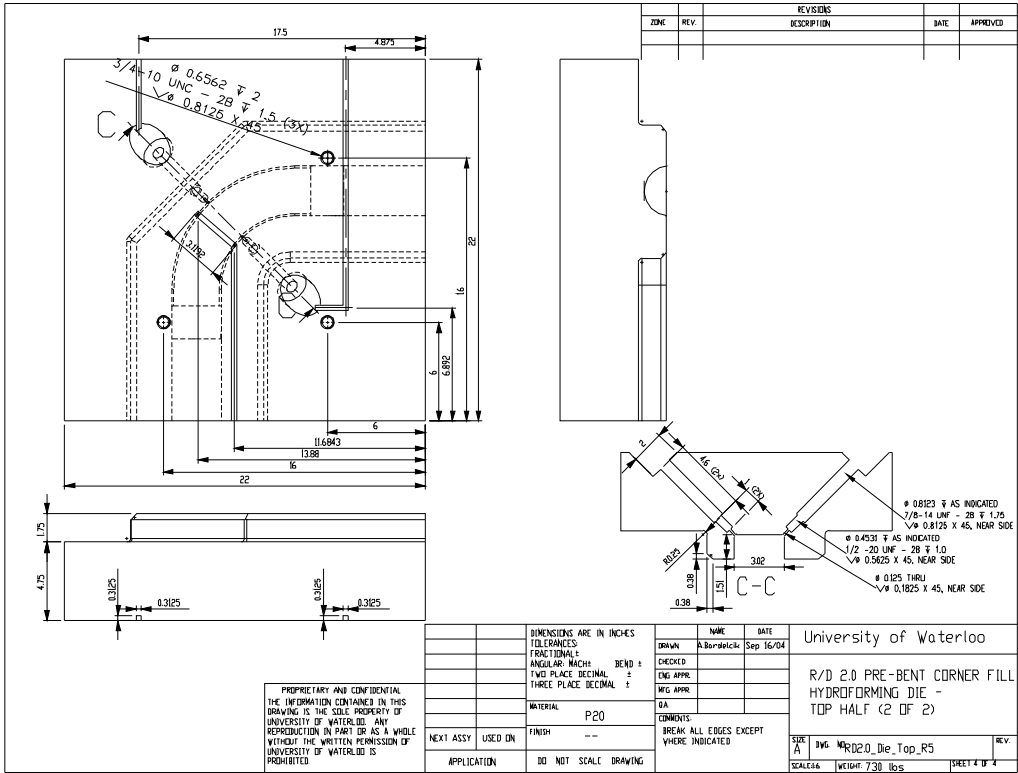**Figure B.2:** As-built CAD drawing of R/D 2.0 pre-bend hydroforming die (part 1)

Figure B.3: As-built CAD drawing of R/D 2.0 pre-bend hydroforming die (part 2)

APPENDIX C

Hydroforming Test Procedure

START OF DAY

1) Enter 'Valve Control', close HP1
2) Turn on water valve to intensifier
3) Empty air water filter(s)

START OF TEST

1) Computer: Enter 'Valve Control' and close HP1
2) Computer: Return to *main menu*
3) Remove yellow safety columns
4) Computer: Enter 'Die Closure'
5) On 1,000 ton cylinder 406 unit, ensure error on XDCR1 valve is zero
6) Turn on 'Low' then 'High' pressure to hydraulics
7) Plug in high pressure check valve
8) Computer: Uncheck '*Low Pressure Die Closure' box*
9) Computer: Set selection to *'move manually'*
10) Computer: Move toggle to move down position
11) Computer: Set displacement rate to 1 mm/s
12) Computer: Activate cylinder and close die. Pressure should rise to about 2,200 psi (wait about 5 seconds) then *'stop cylinder'*
13) Hold reset button on 1,000 tonne cylinder 406 and unplug check valve
14) Computer: Return to *main menu*

Move End-Feed Actuators

1) Make sure both the EF#1 and EF#2 actuators are fully retracted. Check, to ensure the 'Anlg In' signals are zero on both EF#1 and EF#2 Flextest units (do not turn on if not ~0). Turn on 'low' pressure to EF#1 Flextest, then 'high' pressure. Press the run button on both EF#1 and EF#2 Flextest units. (Note: EF#1 controls the hydraulic power to both actuators)
2) Computer: Enter 'End-Feed Actuators'
3) Computer: Set selection to *'move manually'*
4) Computer: Select 'Advance', 'Retract', or 'Hold Postion' for EF#1 and EF#2. Set the displacement rate in mm/s. Activate the cylinder(s). Stop cyclinder(s) when the load on each tube is approximately -1.5 kip (–'ve is for compression). This might take several tries with a displacement rate of ~0.1 mm/s.
5) Computer: Return to *main menu*

GENERATING A VACUUM AND TUBE FILL

1)   Computer: Enter 'Valve Control'
2)   Computer: Press automated sequence button and follow instructions
3)   Computer: Return to main menu

Build Initial Pressure in Tube and Pressurize the 1000 Tonne Cyclinder

1) ENTER 'DIE CLOSURE', TURN ON HYDRAULICS FOR INTENSIFIER – 'UPDATE'

PRESSURE TO 250 PSI

2) INCREASE PRESSURE TO '10,000 PSI' BY USING THE

PRESSURE/HOLD/RELEASE SWITCH

FORMING TUBE

1)   Computer: Enter 'Pressure Intensifier'
2)   Computer: Change file name
3)   Computer: Under *Form tube to: (select)* tab, select '*specified maximum pressure'* or
      '*burst*'. If '*specified maximum pressure*' was selected then enter the maximum pressure.
4)   Computer: Under *Make selection* tab, select '*No End-Feed*', '*End-Feed – Displacement
      Control*', or '*End-Feed – Force Control*'
5)   The plots on the screen **_must_** contain the proper curves before starting the test. 'Retrieve'
      the appropriate .csv file and make sure the curves are correct.
6)   Computer: Press '*Start*' to start the test and the green light will turn on. When test is
      finished the green light will turn off. If the tube does not burst, then the tube slowly de-
      pressurizes. Note that the green light must turn off before the program can be controlled
      again. Open HP3 once internal pressure is below 8,000 psi
7)   Turn the *pressure intensifier* 406 to 'low' pressure and then off
8)   Computer: Return to main menu

REMOVE END-FEED ACTUATORS FROM TUBE

1)   Enter 'Valve Control", close HP1
2)   Enter 'End-Feed Actuators'
3)   Select 'Retract' and set displacement rate → Activate cyclinders

4) When actuators are fully retracted to 0 mm, turn off Hydraulic to EF#1 and press the stop button on the program cylinder on both EF#1 and EF#2 controllers

DIE OPENING

1) Release pressure from the 1000 tonne cylinder by switching control to 'release'. Wait until pressure drops below 2200 psi and then move switch to 'hold'.
2) Computer: From *main menu* enter the *'Die Closure'*
3) Hold reset button on 1,000 tonne cylinder 406 and plug in check valve
4) Computer: Set displacement rate to 1 mm/s and move toggle to *move up* position
5) Computer: Move cylinder up to -120 mm
6) Unplug check valve
7) Place safety columns on die
8) In 'Valve Control', close HP#1, open HP#3 (to bleed off all pressure)
9) Turn off all hydraulics

END OF DAY

1) Close water valve to intensifier, turn off all hydraulics, and make sure all lights on the blue box are ***off*** by using 'Valve Control'

APPENDIX D

DP600 and IF Bend Process Data

DP600 and IF Process Variable Results

DP600 bending process data

DP600

MB

	BOOST	Clamp Slip	Bend Ang	Mandrel
MB16	99.6	7.4	93	0
MB17	99.4	7.2	93.1	0.4
MB18	99.5	6.6	93.1	0.2
MB19	99.3	8.1	93.1	0.2
MB20	99.4	6.5	93.1	0
MB21	99.4	6.7	93	0.5
MB22	99.4	6.7	93	0
MB23	99.4	7.2	93	0.1
MB24	99.6	7.5	93	0
MB25	99.4	6.4	93	0.3
MB26	99.6	7.1	93	0.4
MB27	99.3	7.4	93	0.4
MB28	99.5	7.1	93	0.1
MB29	99.3	7.2	93	0.3
MB30	99.5	6.2	93	0
MB31	99.5	6.4	93	0.1
MB32	99.4	6.9	93	0.5
MB33	99.2	7.2	93	0.2
MB34	99.9	7.9	93	0.3
MB35	99.7	6.2	93	0
MB36	99.8	7.2	93	0.3
MB37	99.7	6.9	93	0.4
MB38	99.5	5.8	93	0.5
MB39	98.1	10.2	93	0.3
MB40	98	10.8	93	0.4
MB41	100	6.8	93	0.5
MB42	99.7	6.5	93	0.3
MB43	99.7	5.8	93	0
MB44	99.6	6.6	93	0
MB45	99.9	6.7	93	0.5
MB46	99.5	6.4	93	0.4
MB47	99.5	6.4	93	0.2
MB48	99.6	6.7	93	0.5
MB49	99.8	6.2	93	0.5
MB50	99.8	7.2	93	0.3
MB51	99.6	6.5	93	0.6
MB52	99.8	5.8	93	0.2

AVG:	99.48	6.98	93.01	0.27

LB

	BOOST	Clamp Slip	Bend Ang	Mandrel
LB12	95.5	na	93	3
LB13	95.9	14.2	93	3
LB14	95.9	13.1	93.1	3
LB15	95.9	12.7	93.1	2.9
LB16	na	na	na	na
LB17	95.9	12.9	92.9	3
LB18	96	12.2	93	3
LB19	96	13.7	93	3
LB20	96	12.5	93	2.9
LB21	96.2	13	93	3.1
LB22	96	13.1	93	3.2
LB23	96	11.8	93	3

AVG:	95.94	12.92	93.01	3.01

IF bending process data

IF

MB

	BOOST	Clamp Slip	Bend Ang	Mandrel
MB7	100.3	1.4	90.9	0.35
MB8	100.3	1.9	90.9	0.49
MB9	100.3	2.3	90.9	0.5
MB10	100.3	1	90.9	0.46
MB11	100.1	1.2	90.9	0.75
MB12	100.3	1.5	90.9	0.12
MB14	100.5	2.2	90.9	0.03
MB15	100.2	3.7	90.8	0.08
MB16	100.2	2.5	90.9	0.23
MB17	100.2	2.9	90.9	0.28
MB18	100.3	1.4	90.9	0.39
MB19	100.3	1.5	90.9	0.08
MB20	100.3	2.2	90.9	0.12
MB21	100.3	1.5	90.9	0.04
MB22	100.3	2.4	90.9	-0.04
MB23	100.3	2.3	90.9	0.03
MB24	100.3	2.1	90.9	0.03
MB25	100.3	1.4	90.9	0.25
MB26	100.3	1.6	90.9	0.14
MB27	100.3	1.6	90.9	0.09
MB28	100.3	1.3	90.9	0.31
MB29	100.3	1.4	90.9	0.37
MB30	100.3	1.7	90.9	0.16
MB31	100.3	2.5	90.9	0.09
MB32	100.3	2.1	90.9	0.29
MB33	100.3	2.1	90.9	0.12
MB34	100.3	2.7	90.9	0.07
MB35	100.3	3.2	90.9	0.19
MB36	100.3	1.6	90.9	-0.01
MB37	100.3	2.1	90.9	0.17
MB38	100.3	2.9	90.9	0.12
MB39	100.3	3	90.9	0.02
MB40	100.3	1.7	90.9	-0.08
MB41	100.3	2	90.9	0.07
MB42	100.3	3.4	90.9	0.08
MB43	100.3	2.6	90.9	0.22

| AVG: | 100.29 | 2.08 | 90.90 | 0.18 |

LB

	BOOST	Clamp Slip	Bend Ang	Mandrel
LB1	95.3	na	90.8	0.28
LB2	95.3	4.1	90.8	0.2
LB3	95.4	6.3	90.8	0.25
LB5	95.4	10	90.8	0.18
LB6	95.4	10.7	90.8	0.13
LB7	95.4	10.9	90.8	0.13
LB8	95.4	10.4	90.8	0.23
LB9	95.4	11.2	90.8	0.26
LB10	95.4	12.7	90.8	0.19
LB11	95.4	10.1	90.8	0.1
LB12	95.4	11.7	90.8	0.33

| AVG: | 95.38 | 9.81 | 90.80 | 0.21 |

HB

	BOOST	Clamp Slip	Bend Ang	Mandrel
HB4	104.5	0.6	90.8	0.4
HB5	104.7	0.5	90.8	0.41
HB6	104.3	0.6	90.8	0.5
HB7	104.5	0.6	90.8	0.45
HB8	104.4	0.6	90.9	0.49
HB9	104.4	0.7	90.8	0.44
HB10	104.4	0.7	90.8	0.45
HB11	104.4	0.6	90.8	0.41
HB12	104.3	0.1	90.8	0.31
HB13	104.5	0.2	90.8	0.5
HB14	104.6	0.7	90.8	0.21
HB15	104.2	0.4	90.8	0.39

| AVG: | 104.43 | 0.53 | 90.81 | 0.41 |
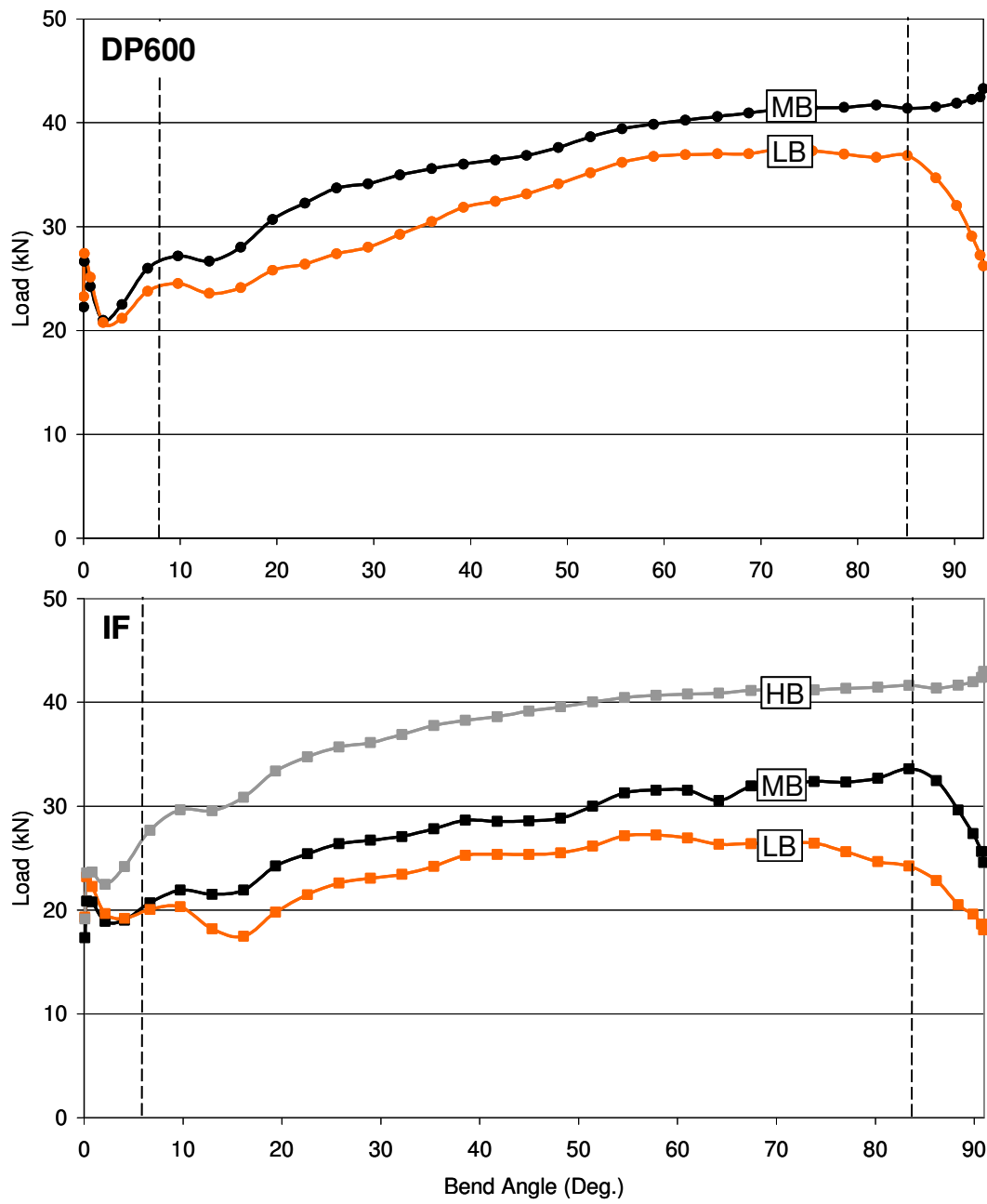
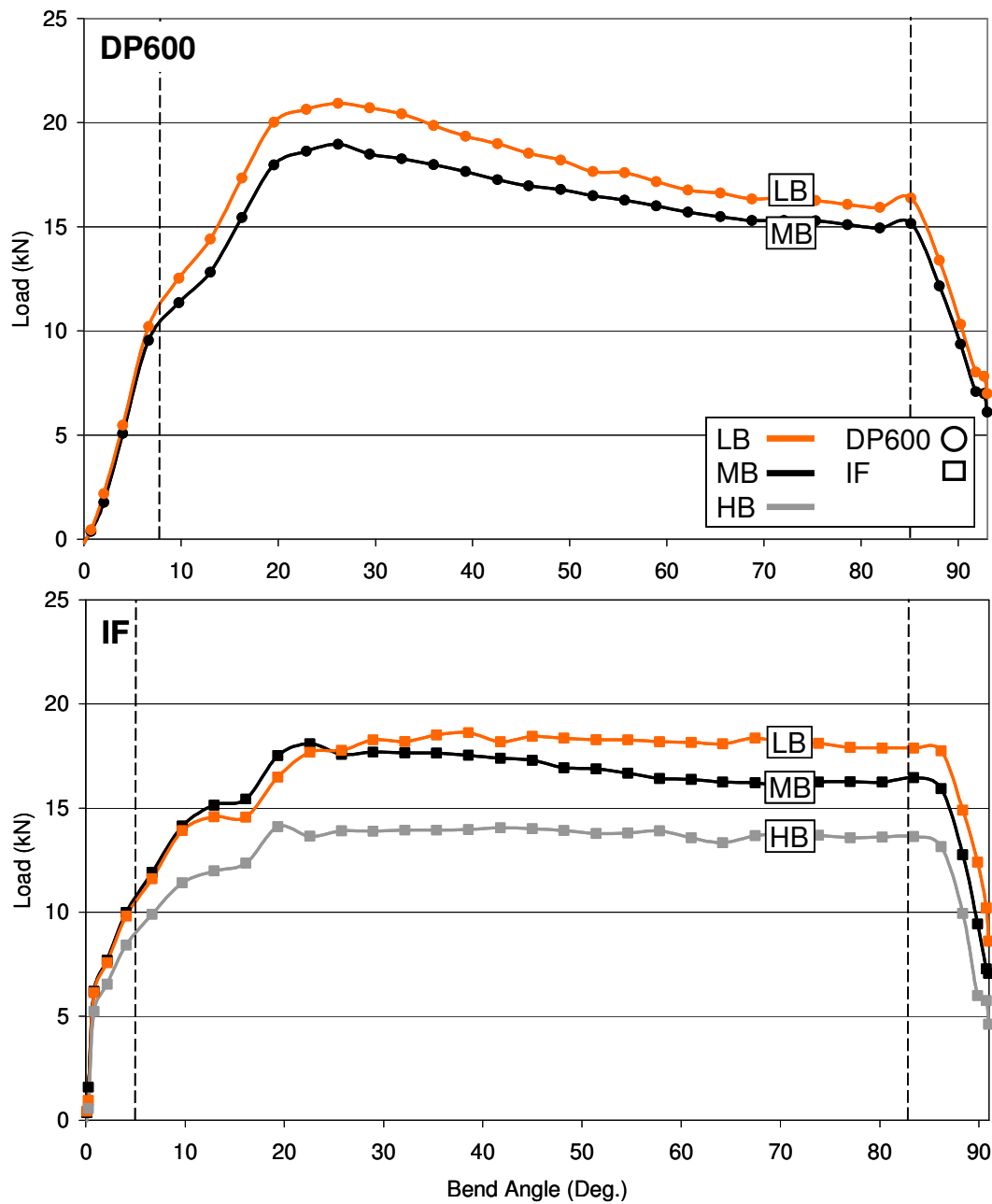**Figure D.1:** Average DP600 and IF pre-bending pressure die boost load

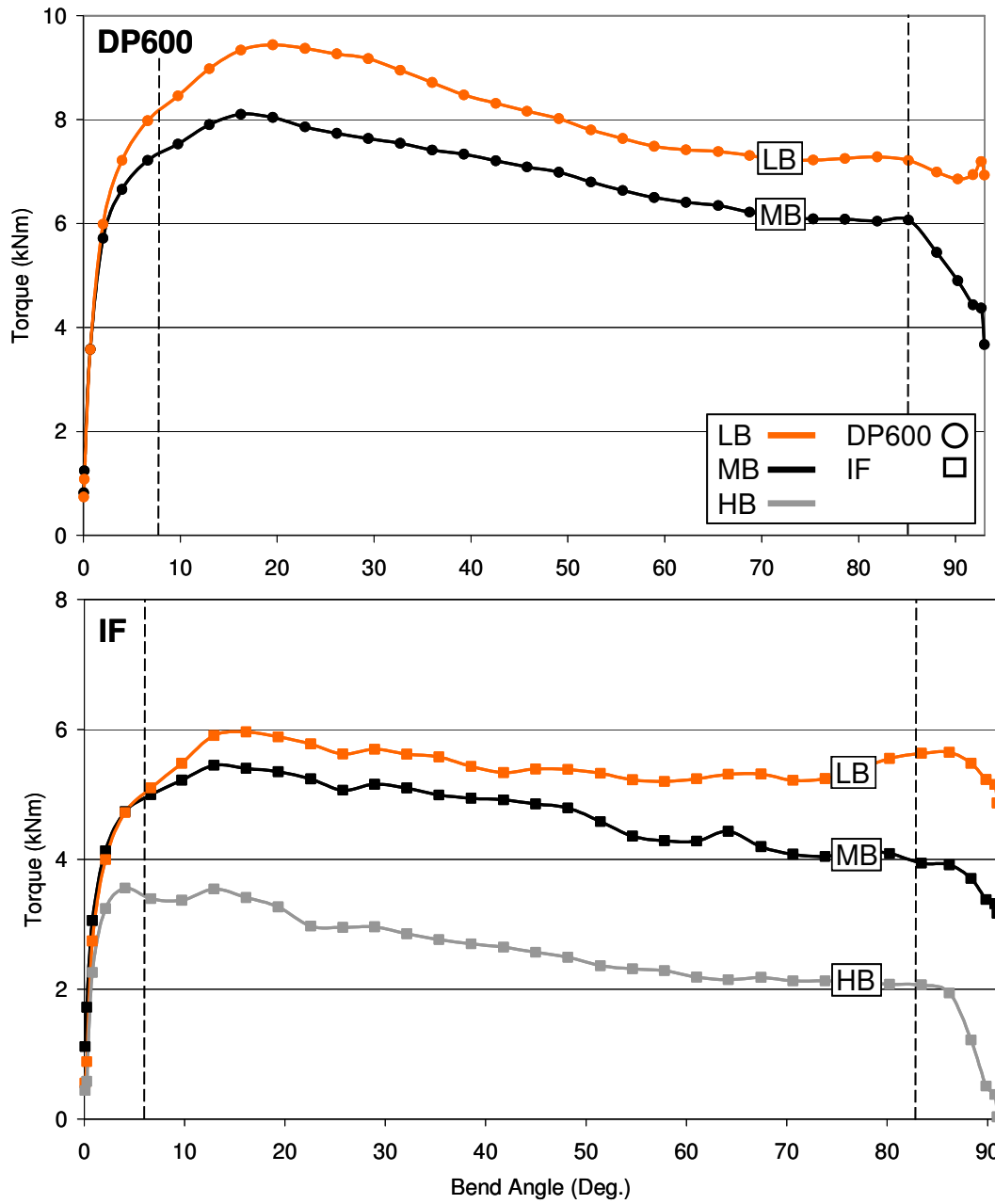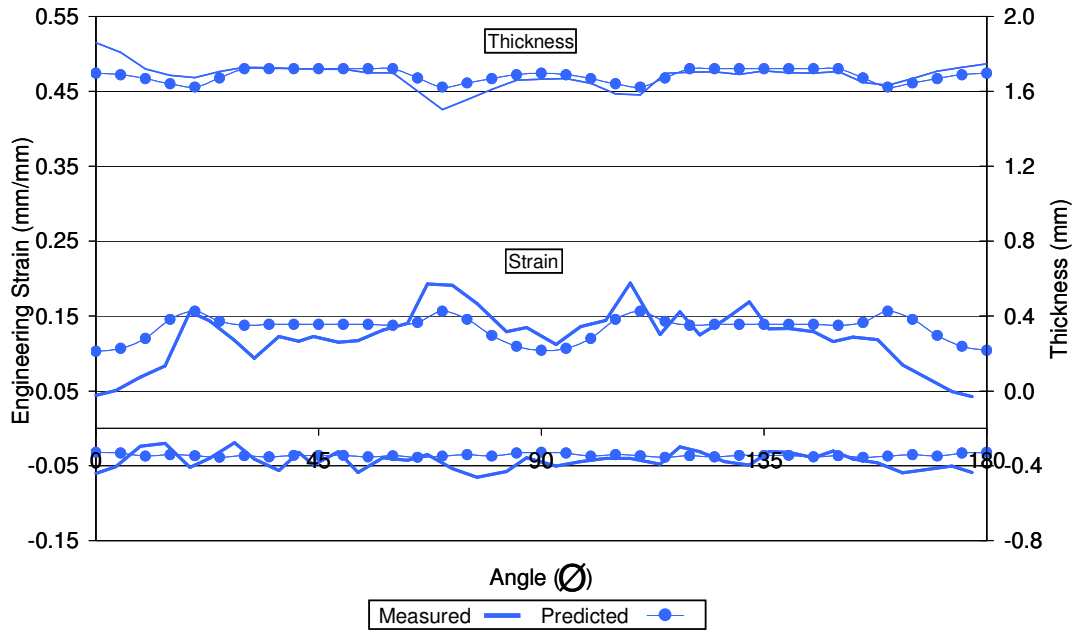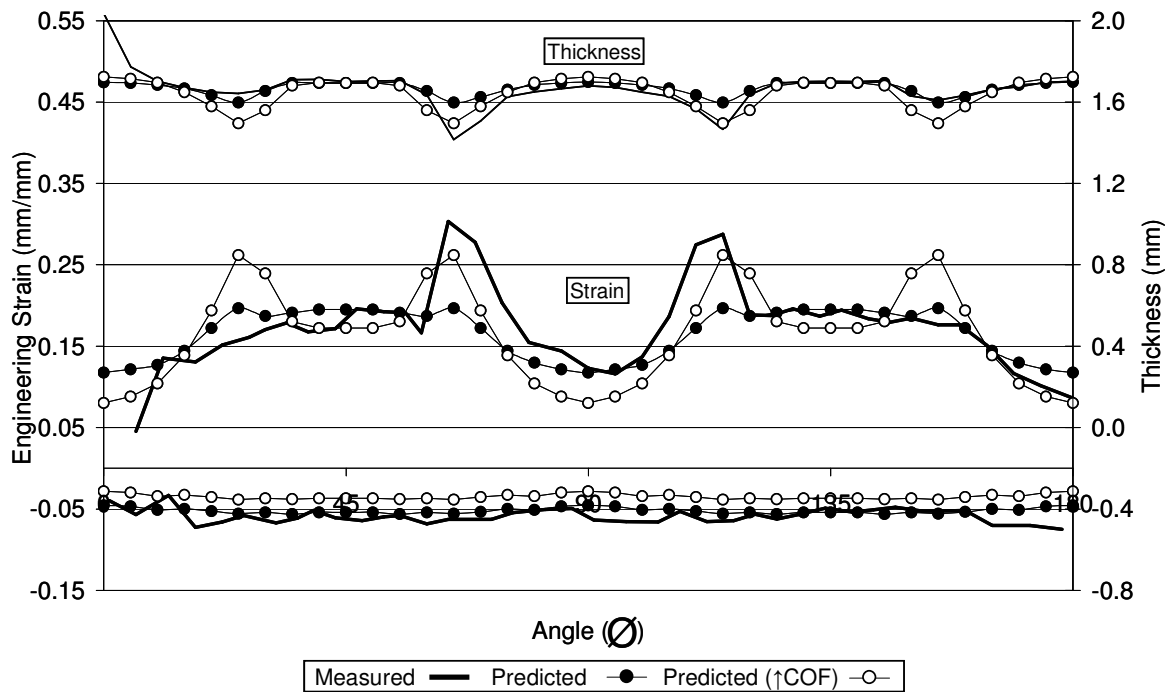**Figure D.2:** Average DP600 and IF pre-bending mandrel load

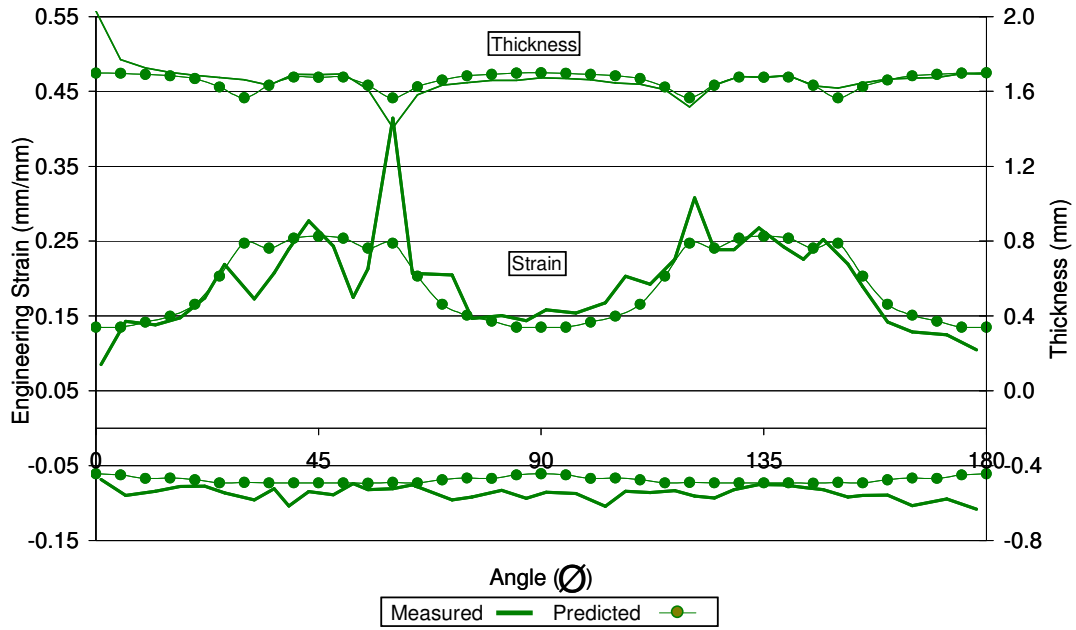**Figure D.3:** Average DP600 and IF pre-bending bend die torque

APPENDIX E

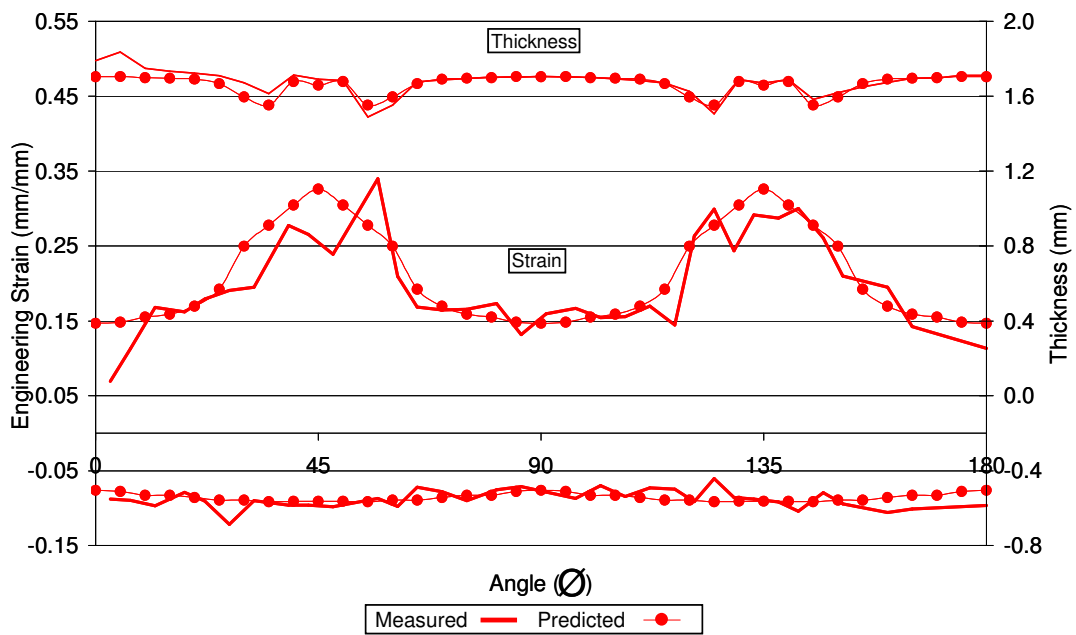DP600 and IF Straight Tube Hydroforming Strain and Thickness

Distributions

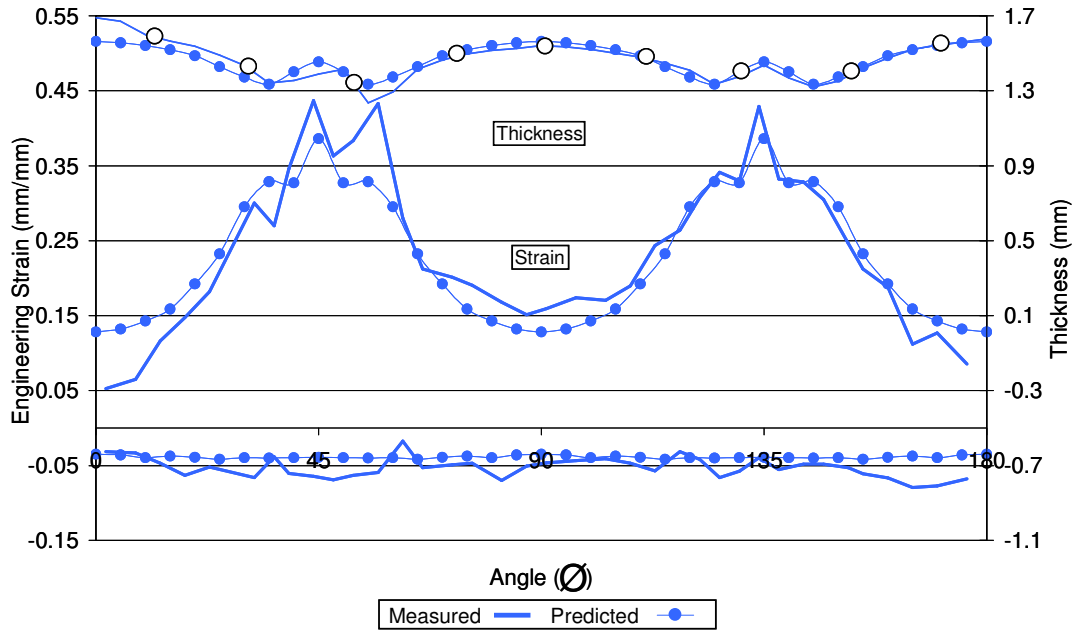**Figure E.1:** Measured strain and thickness distributions for DP600 straight tube, 90% interrupted, zero EF

Figure E.2: Measured strain and thickness distributions for DP600 straight tube, 90% interrupted, 67kN EF

Figure E.3: Measured strain and thickness distributions for DP600 straight tube, 90% interrupted, 133kN EF

Figure E.4: Measured strain and thickness distributions for DP600 straight tube, at final pressure of 151.7MPa, 200kN EF

Figure E.5: Measured strain and thickness distributions for IF straight tube, at final pressure of 151.7MPa, zero EF

APPENDIX F

DP600 Pre-Bend Tube Hydroforming End-Feed Displacement Results

DP600 Pre-Bend Tube Hydroforming Corner-Fill Expansion Results

DP600 Pre-Bend Tube Hydroforming Strain and Thickness

Distributions
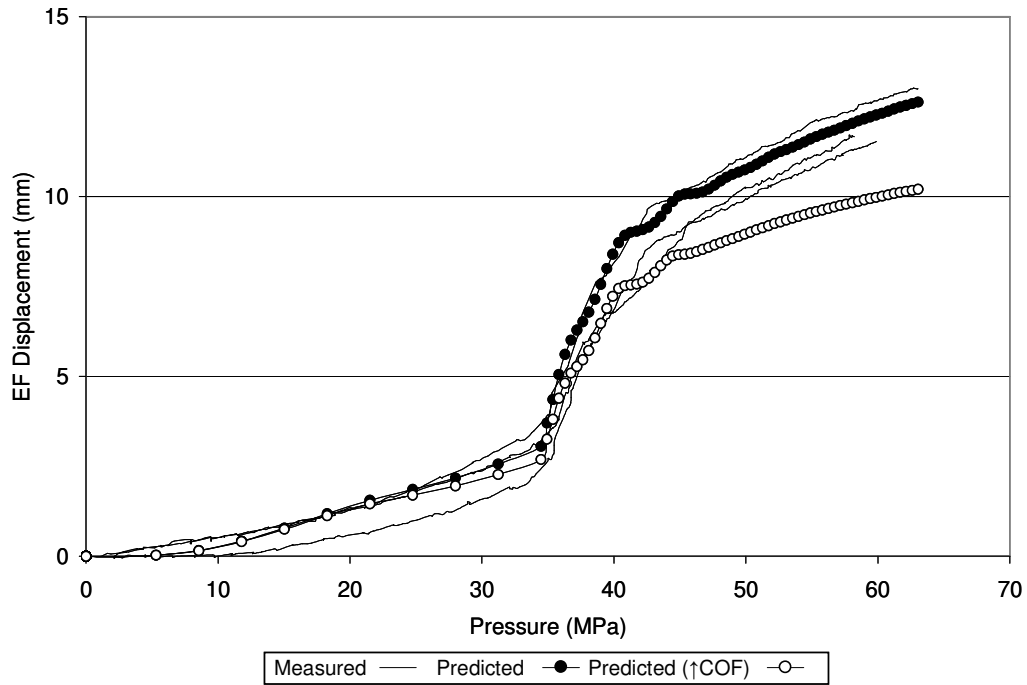
Figure F.1: Measured and predicted average EF displacement for DP600 MB 67kN pre-bend tubes
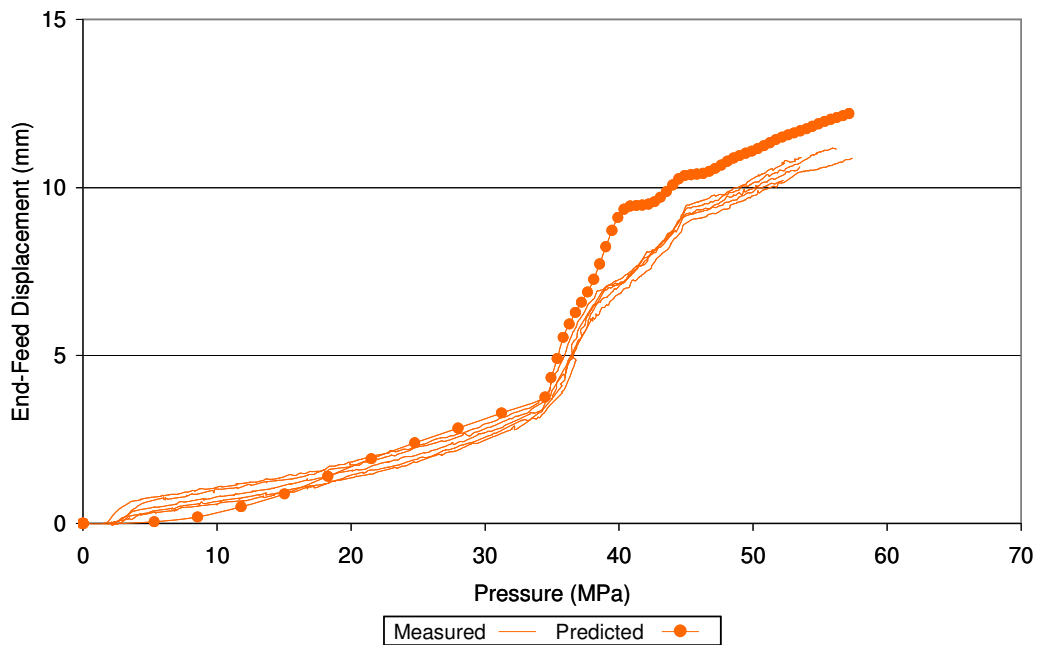
Figure F.2: Measured and predicted average EF displacement for DP600 LB 67kN pre-bend tubes
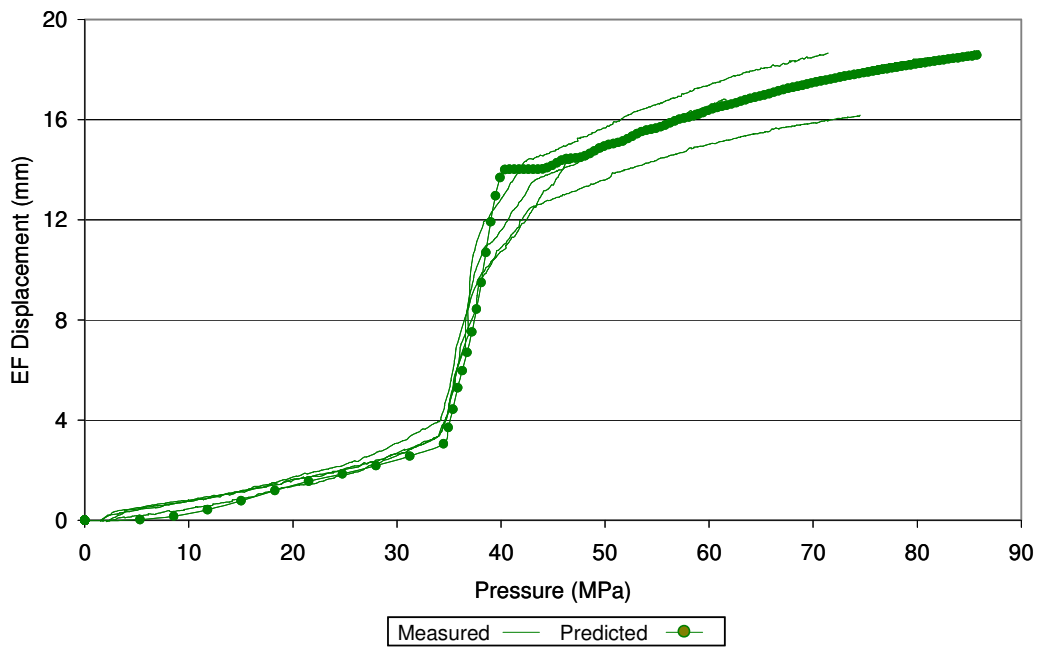
Figure F.3: Measured and predicted average EF displacement for DP600 MB 133kN pre-bend tubes
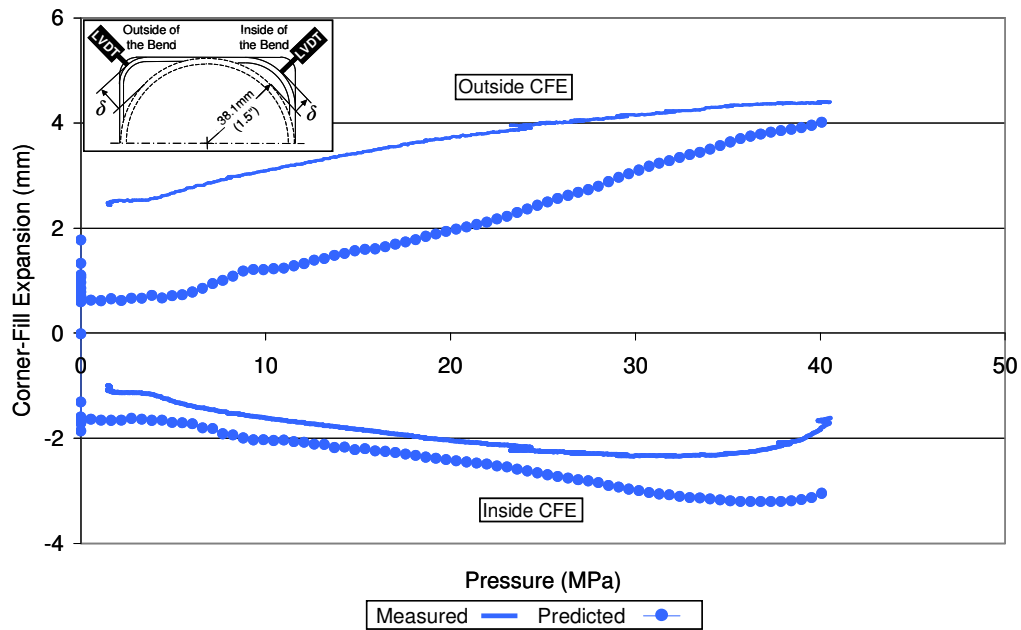
Figure F.4: Measured and predicted CFE for DP600 MB zero EF pre-bend tube

218
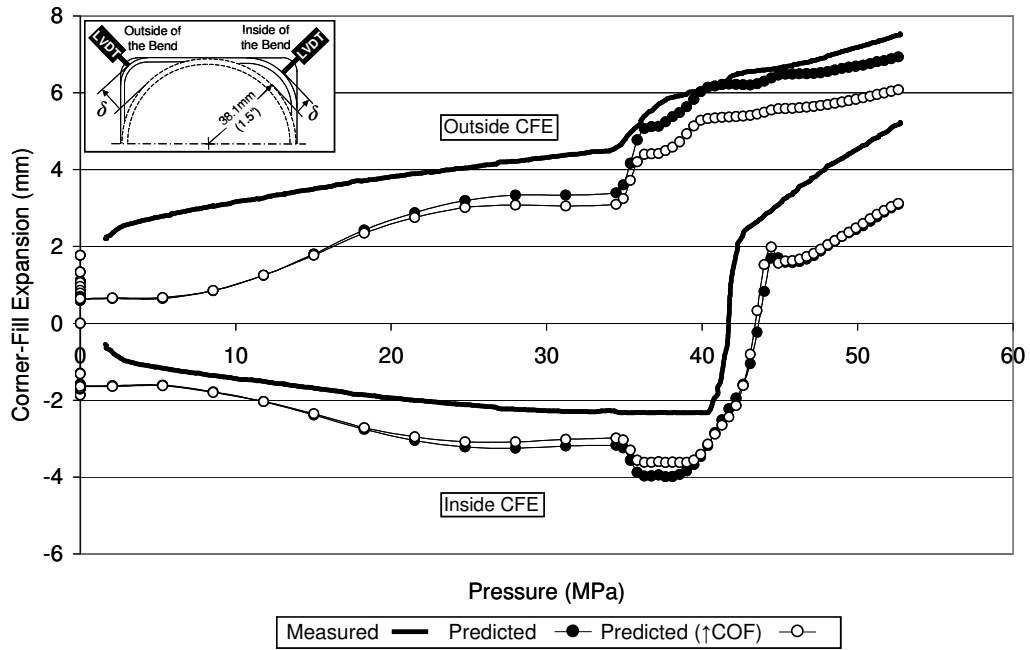
**Figure F.5:** Measured and predicted CFE for DP600 MB 67kN EF pre-bend tube
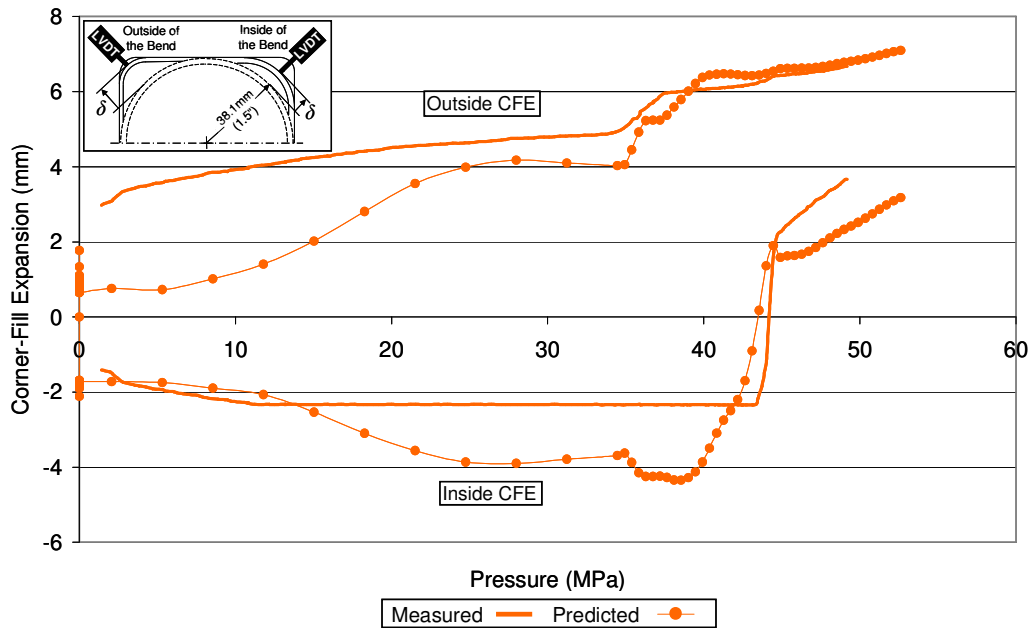
Figure F.6: Measured and predicted CFE for DP600 LB 67kN EF pre-bend tube
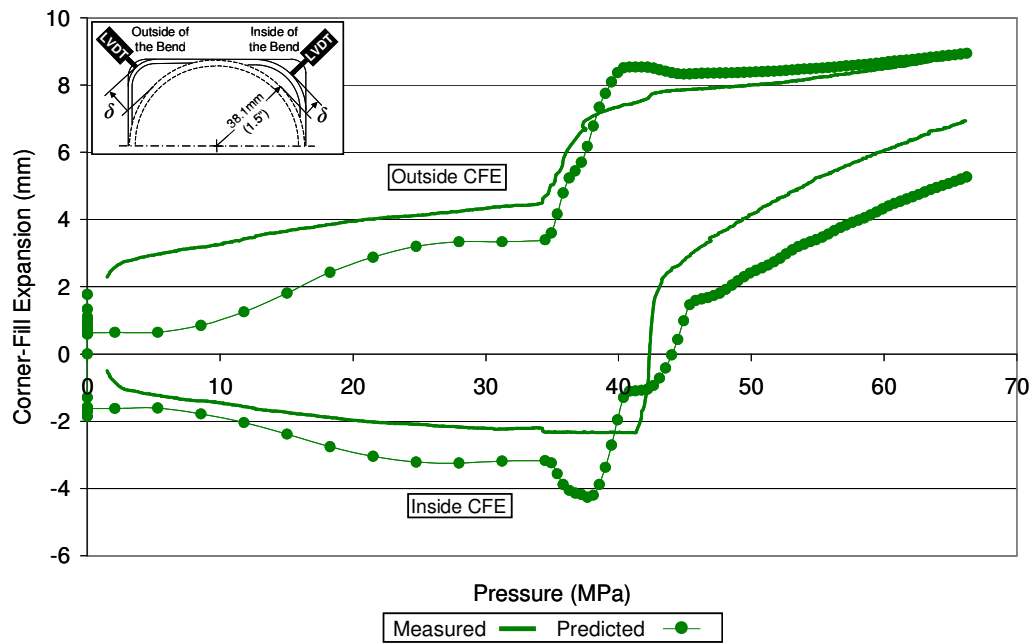
**Figure F.7:** Measured and predicted CFE for DP600 MB 133kN EF pre-bend tube
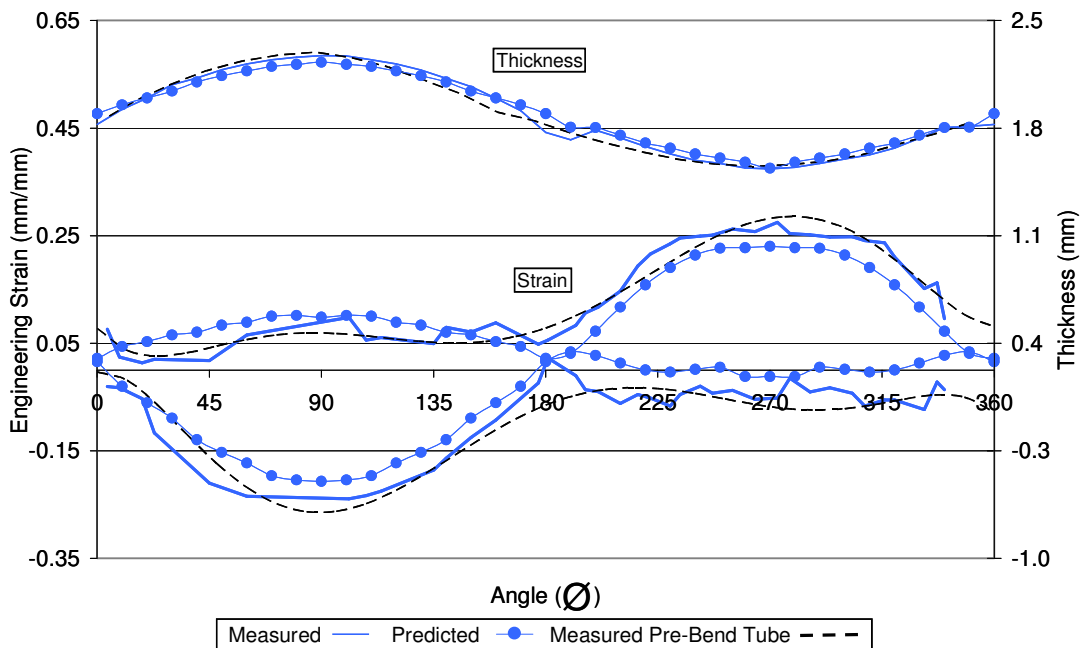
Figure F.8: Measured strain and thickness distributions for DP600 (MB) pre-bend tube, 90% interrupted, zero EF
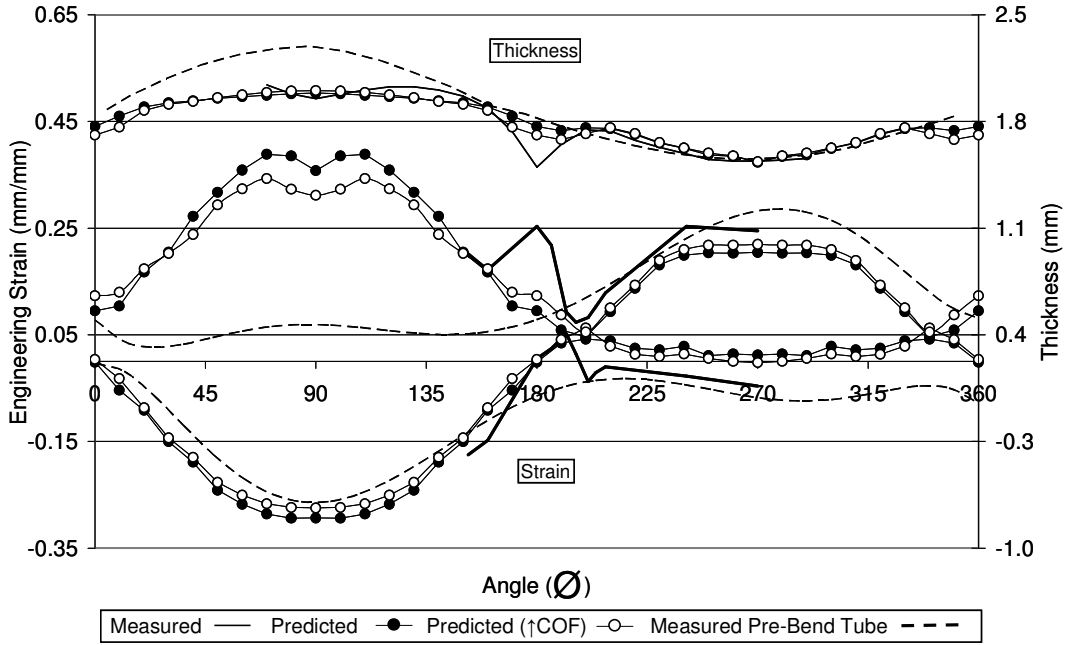
Figure F.9: Measured strain and thickness distributions for DP600 (MB) pre-bend tube, 90% interrupted, zero EF (burst at 87%)
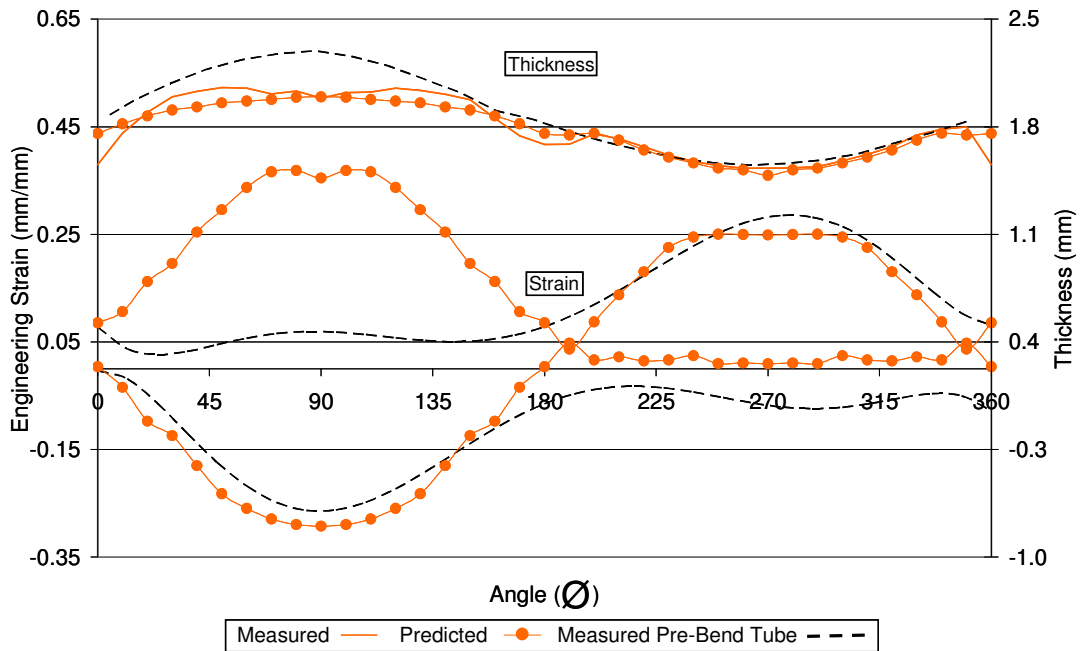
Figure F.10: Measured strain and thickness distribution for DP600 (LB) pre-bend tube, 90% interrupted, 67kN EF
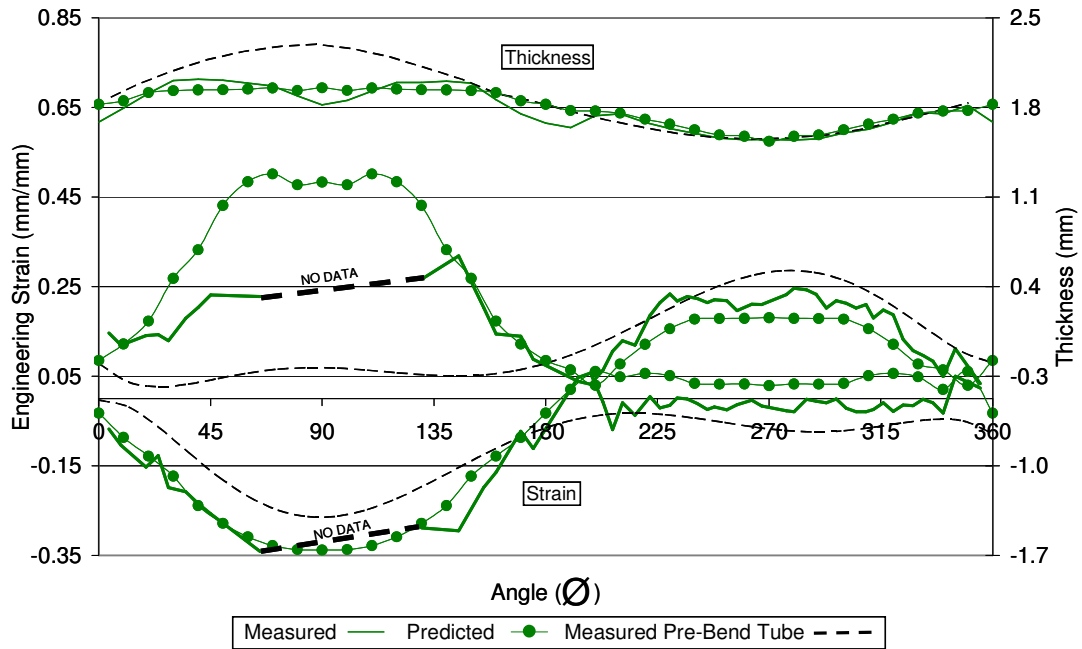
Figure F.11: Measured strain and thickness distribution for DP600 (MB) pre-bend tube, 90% interrupted, 133kN EF

APPENDIX G

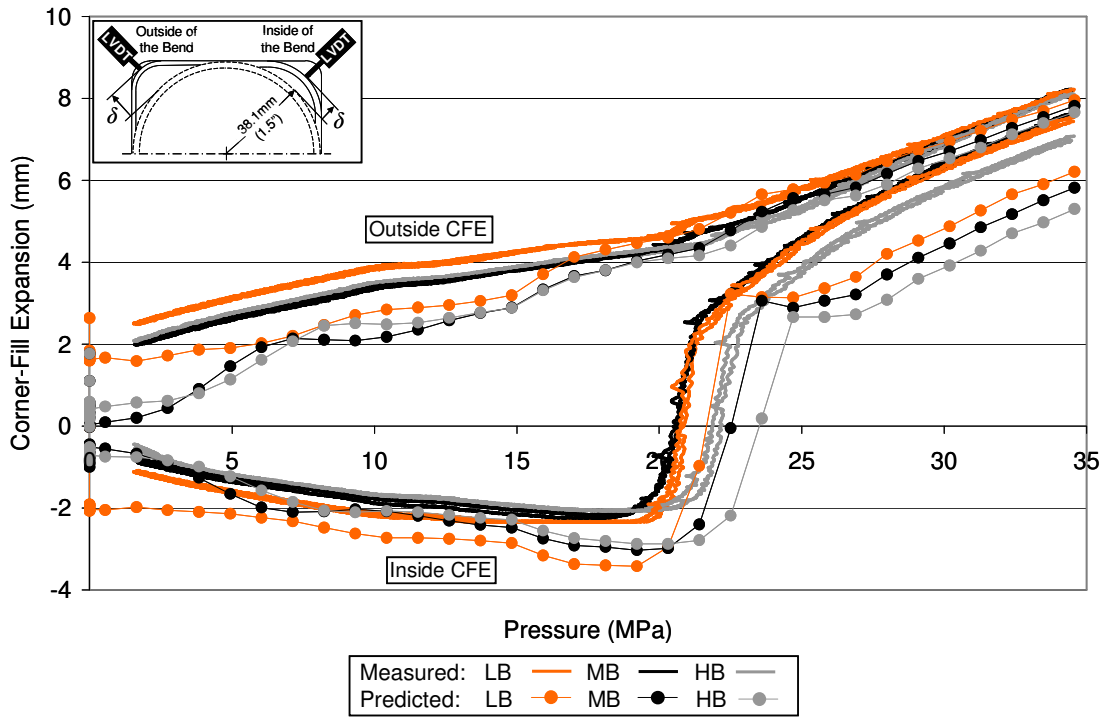DP600 and IF Predicted Bend Die Torque (Raw Data and 4-Point Average)
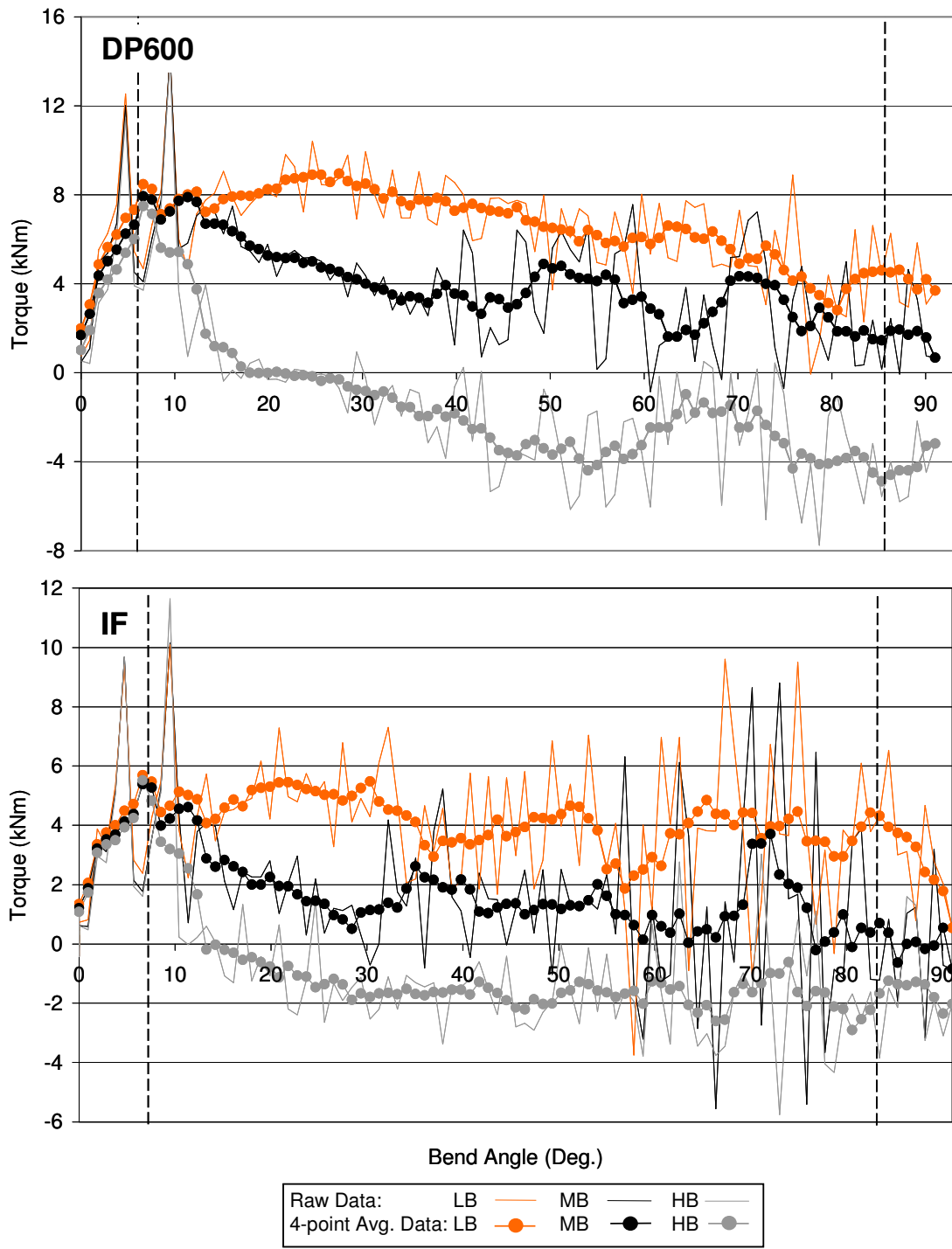
Figure G.1: Raw and 4-point average filter results for the predicted bend die torque
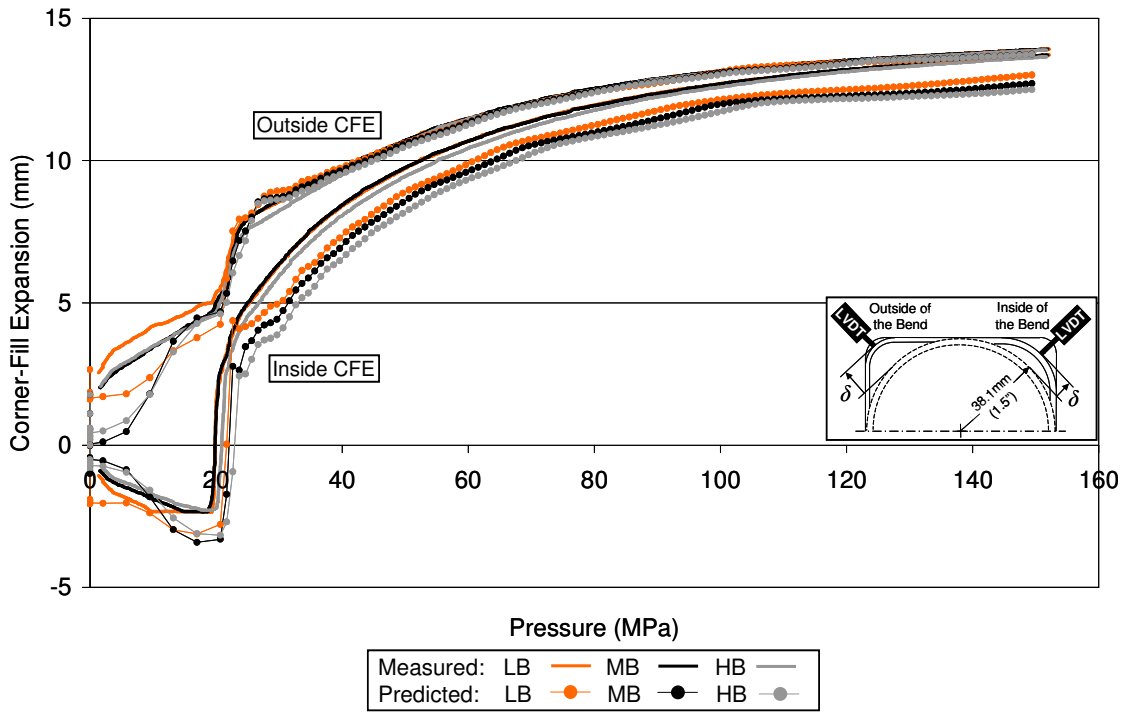
APPENDIX H

Predicted IF Corner-Fill Expansion Results
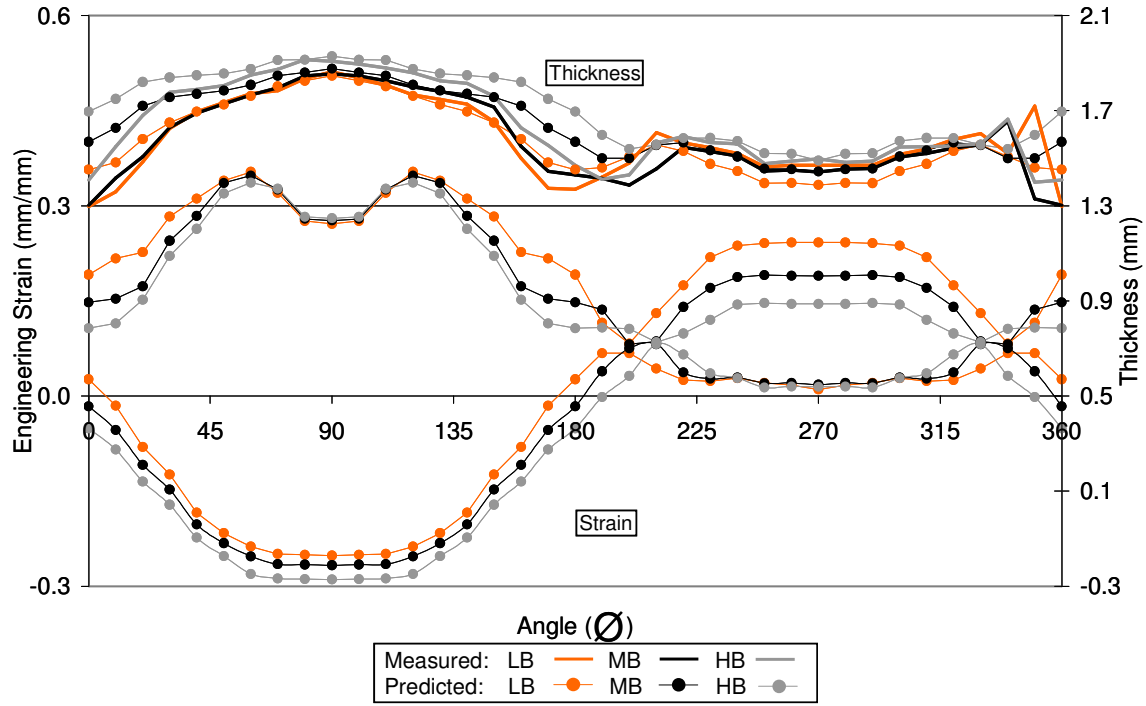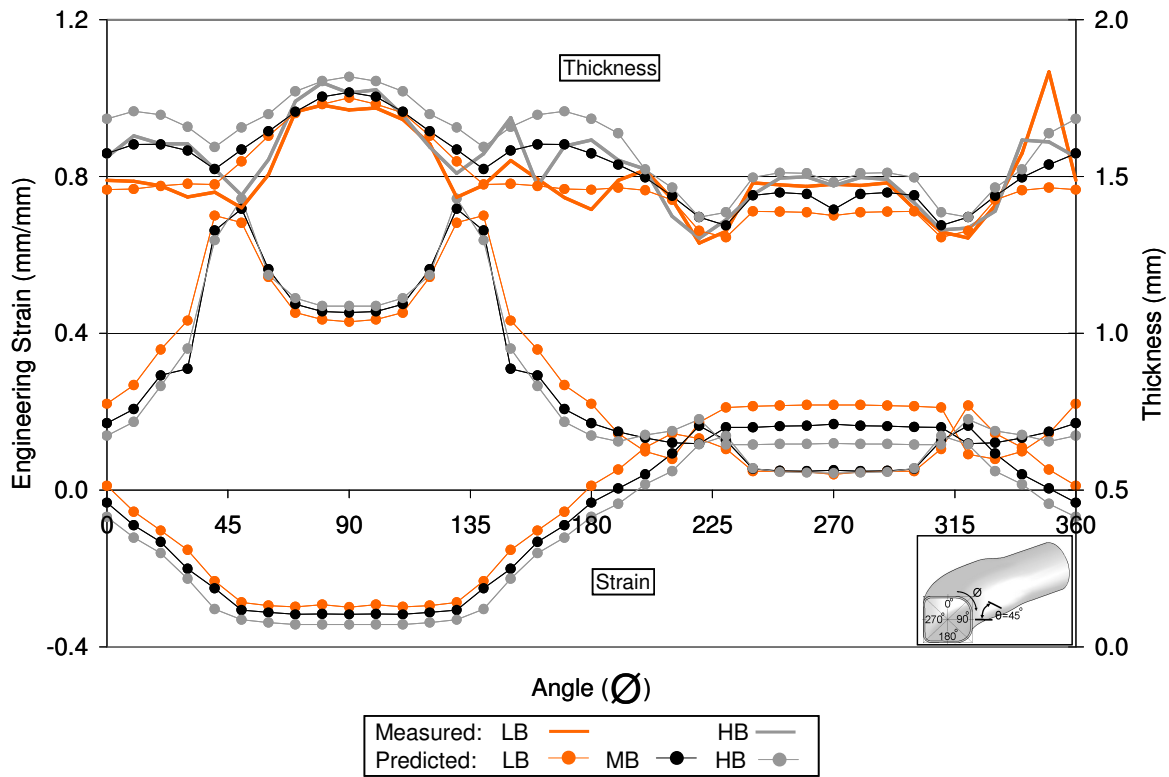
Predicted IF Strain and Thickness Distributions

Figure H.1: Predicted and measured IF CFE *vs.* internal pressure, Zero EF case, pre-bend tube hydroforming

Figure H.2: Predicted and measured IF CFE *vs.* internal pressure, 67kN EF case, pre-bend tube hydroforming

Figure H.3: Predicted and measured IF strain and thickness distribution for zero EF case, pre-bend tube hydroforming

Figure H.4: Predicted and measured IF strain and thickness distribution for 67kN EF case, pre-bend tube hydroforming